Order Number 9312215

1–5 Micron imaging of deeply embedded young stellar objects

Ressler, Michael Elvin, Ph.D.

University of Hawaii, 1992

U·M·I

300 N. Zeeb Rd.
Ann Arbor, MI 48106

1 – 5 MICRON IMAGING OF DEEPLY EMBEDDED YOUNG STELLAR OBJECTS

A DISSERTATION SUBMITTED TO THE GRADUATE DIVISION OF THE UNIVERSITY OF HAWAII IN PARTIAL FULFILLMENT OF THE REQUIREMENTS FOR THE DEGREE OF

DOCTOR OF PHILOSOPHY

IN

ASTRONOMY

DECEMBER 1992

By

Michael Elvin Ressler

Dissertation Committee:

Mark Shure, Chairman
Alan Tokunaga
George Herbig
Gerard Luppino
Paul Lucey

Abstract

Spectral energy distributions (SEDs) are one of the primary tools for analyzing the natures of young stellar objects. Theoretical models of SEDs have achieved some success over a wide frequency range (e.g., Adams *et al.* 1987, ApJ 312, 788); however, the models often underpredict the near-infrared (NIR, 1 – 5 μm) fluxes observed with single-element photometers by more than an order of magnitude. This observed "extra" flux is generally thought to be radiation which is scattered into the observer's beam from anisotropically distributed material surrounding the protostar. I explore a sample of well-known protostars with a seeing-matched InSb photodiode array camera; fourteen objects have been imaged in the J through M broadband filters, and many of these were imaged through a circular variable filter scanned through the 3.08 μm water ice band or through a linear polarizer with the K filter. These images are used to separate the scattered light from the line-of-sight radiation which together make up the published single-beam SEDs. While resolved, anisotropic scattering accounts for the NIR excesses in some objects, the general scenario is somewhat more complex. For instance, scattering from circumstellar material is seldom significant at wavelengths greater than 3 μm and thus will not explain excesses in the 3 – 5 μm region. Some objects appear completely point-like, yet have significant NIR excesses, implying that either scattering is significant on very small scales or that other processes are involved. The implications of these findings concerning models of YSOs and their SEDs are discussed. In addition, we find that approximately 40% of these objects (and of a larger sample) appear to be multiple, in rough agreement with the

apparent frequency for Main Sequence stars. Finally, five of the fourteen objects appear to have varied significantly in intensity over periods ranging from months to years. We suggest several possible mechanisms for variations on these time scales.

Table of Contents

List of Tables

List of Figures

Chapter 1: Introduction

1.1) Star Formation Summary

The evolution of stars after they reach the main sequence is well understood. The progression from main sequence star to giant to the product (white dwarf, neutron star, or black hole) is a natural consequence of thermonuclear reactions. However, the evolution of a star from molecular cloud to main sequence is not yet well understood, and therefore remains one of the fundamental problems of astronomy.

Our current understanding of the formation of stars less massive than a few solar masses is as follows (from Adams, Lada, and Shu 1987, hereafter ALS). A region of a giant molecular cloud begins to collapse, perhaps gravitationally due to Jeans instability. This initial collapse is probably roughly spherically symmetric, although the "poles" will tend to become less dense than the "equator" of the system since there is no centripetal acceleration to help support the material against collapse at the poles. An embedded core begins to form at the center of the collapsing region along with a disk of material in the equatorial plane. This core heats up due to the release of the gravitational potential energy of the infalling material – this object will ultimately become the new star. As the core continues to heat up, it starts to drive an extremely violent stellar wind (the mechanism for producing it is not yet known), although this wind may not be initially observable because it may be suppressed by the dense infalling material.

As the material originally at the poles falls onto the disk, the density above the poles decreases faster than along the equator. At some critical density, the stellar wind will be able to break through the infalling material at the poles and form a bipolar outflow. In this phase, large quantities of material are ejected along the poles. These flows may be focussed by the large density gradients that exist between the poles and the equator (Boss 1987). As the density continues to decrease, these flows become less collimated until the wind is essentially isotropic. At some point when there is little obscuring material left around the star except for the disk itself, these objects become optically visible; the classical T Tauri stars are examples of this type of object. During this phase, the disks start to dissipate (possibly losing some material to planet formation) and the stellar wind begins to die down as the object becomes a main sequence star.

Lada & Wilking (1984) and Strom *et al.* (1988) proposed related classification schemes to divide up YSO's. Both place them in one of three categories: deeply embedded infrared sources which lie in or near dense cores in molecular cloud complexes (Class I), optically visible sources with infrared excesses which are located in or near star forming regions and whose Hα equivalent width is greater than 5 Å (Class II), and optically visible sources without infrared excesses whose Hα equivalent widths are less than 5 Å (Class III). Class I objects usually correspond to the embedded cores and outflow sources of the ALS scenario, Class II objects correspond to the classical T Tauri stars, while Class III objects include the "naked" T Tauri stars. These last objects are

usually found by their X–ray or Ca II H and K line emission; they represent YSOs which are probably in the last stages of disk clearing before entering the main sequence.

Although the above scenario seems plausible as a likely star formation sequence, it is far from being complete. There is presently controversy concerning the origin of the stellar wind, the mechanism for the collimation of bipolar outflows, and the mechanism for dissipating the magnetic fields presumed to exist in the original giant molecular cloud. In fact, it was realized only a few years ago that bipolar outflows were part of the stellar evolutionary sequence (Lada & Harvey 1981). A further problem, the one I wish to address in this dissertation, is the nature of the infrared radiation emitted by these objects, in particular, the radiation emitted by the youngest, Class I objects.

1.2) Spectral Energy Distributions

The standard diagnostic for YSOs is the spectral energy distribution, which is the plot of the energy emitted by an object as a function of wavelength (λF_λ vs λ where λ is the wavelength and F_λ is the energy flux per unit wavelength interval). From the theoretical side, they are constructed by combining a photospheric (blackbody) spectrum from the central object with a power law infrared spectrum ($\lambda F_\lambda \propto \lambda^\alpha$ where α is the spectral energy index; $\alpha = -3$ for a blackbody in the Rayleigh–Jeans limit) in which the radiation originates in an optically thick disk. For younger objects (Class I), it is

presumed that the stellar surface temperature and luminosity are derived from accretion. These youngest sources have additional sources of radiation: thermal reradiation from a dense dust shell and radiatively released gravitational potential energy from the infalling material. The 1 – 5 μm wavelength region of the spectrum is extremely sensitive to this last energy source since the geometry of the infalling material (a disk-shaped structure produced by rotation) will determine how much of the near-infrared radiation from the photosphere escapes to the observer; thus the near-infrared should serve as a valuable indicator of the rotational characteristics of the YSO. The near- and mid-infrared power law spectrum due to the disk is computed by assuming that the disk can be treated as a series of concentric annuli, each having its own unique temperature which is usually assumed to be a power law function of the distance from the central object. Thus the spectral energy distribution can also be a valuable indicator of the temperature structure of the disks in YSOs.

Observationally, the distributions are constructed by measuring the flux from the object as a function of wavelength, which in the past has been in a relatively large beam from the optical to the far-infrared wavelength regimes. The spectral energy index can then be defined as

$$\alpha = \frac{d\log(\lambda F_\lambda)}{d\log(\lambda)} . \qquad (1.1)$$

The spectral energy index is typically measured by finding the slope between two wavelengths; Myers *et al.* (1987) use the slope between 2 and 25 μm to compute their indices.

The fact that the spectral energy distribution contains information about temperatures is exceedingly important in light of the fact that the distribution should change as a function of the YSO's evolution. We would expect Class I objects to have infrared spectra which rise toward longer wavelengths because of the heavy local extinction, the thermal reradiation by a dusty disk and/or circumstellar shell, and the fact that these objects (their photospheres) tend to be cooler. Class II objects should have a spectrum that is based almost solely on the stellar-blackbody-plus-disk spectrum, therefore it should decrease with increasing wavelength but not as steeply as a blackbody. Since Class III objects are thought to have very little disk material, their infrared spectra should almost be identical to a blackbody spectrum. Therefore, as the YSOs evolve, their spectra evolve from a flat or even rising spectrum to that of a "normal" stellar blackbody. The spectral energy distribution may therefore serve as an indicator of the evolutionary state of the YSO.

1.3) PHYSICAL CONDITIONS IN YSOs.

Though the following discussion is in most cases model dependent, it should serve as an outline of our present knowledge of such systems. ALS model several protostars in the Taurus cloud with mass ~ 0.5 $M_\odot$, isothermal sound speed ~ 0.2 km s^{-1}, rotational speed of the parent molecular cloud ~ 3×10^{-14} rad s^{-1}, luminosity ~ 6 $L_\odot$, core radius ~ 10 AU, and line-of-sight column density ~ 0.3 g cm^{-2}. The sources modeled in the Ophiuchus cloud tend to be somewhat more massive and luminous as well as having a slightly higher initial rotational speed. They also model several T Tauri stars with infrared excesses (presumably caused by the presence of disks) and find that stars with a few solar luminosities and passive disks (optically thick) fit several cases very well. In other objects the presence of an infalling dust shell is also required in order to reproduce the observed far infrared flux. They assume a disk radius of 10^{15} cm and that the outer disk temperature is the same as the parent molecular cloud temperature; thus they find an inner disk temperature of ~ 1500 K (Adams & Shu 1986). If the infall rate is of order 10^{-6} $M_\odot$ yr^{-1} (necessary to explain the observed excess infrared luminosity), then the disk must contain 0.1 – 1 $M_\odot$ of material.

Myers *et al.* (1987) report that visual extinctions of 30 – 90 magnitudes (based on radio observations of CO column densities) are common for embedded cores, which implies that the core density must rise sharply with decreasing radius. They also derive

a volume averaged density for the cores of 10^4 cm^{-3}; this density is required to explain the observed excitation of NH_3. In their models, they find a photospheric temperature of 3000 – 6000 K, consistent with low-mass stars, a minimum grain albedo of ~ 0.4 in the V band, and they conclude that the density distribution can be fit by a power law with an exponent between –1 and –2. An interesting result from their data is that *for their sample*, the only objects optically visible were those which had spectral energy indices less than 0.5. This fact can be explained as a consequence of the clearing of the circumstellar material from the poles as well as the object's motion carrying it away from the center of the cloud toward less obscured regions. Both of these phenomena depend on the object's age, thus lending support to ALS's contention that the spectral energy index may be used as a crude age indicator.

1.4) Confusion from Scattered Light.

Although the above models seem to work well in the mid-infrared, they tend to fail by an order of magnitude or more in the near-infrared, with the discrepancy becoming worse at shorter wavelengths. An additional source of radiation seems to be required in order to adequately explain the observed NIR flux. Based on the high polarizations (~ 20% in an 8 arcsecond beam) observed in some of these objects (Hodapp, 1984), the extra flux is probably due to photospheric light scattered by material in the less dense polar regions. Because the contribution to the flux by scattered light apparently tends to

dominate the NIR portion of the spectrum, scattered light must be eliminated (or at least appropriately taken into account) if the spectral energy distribution in this wavelength regime is to be of any use in constraining the physical properties of YSOs.

Nowhere is the problem of scattered radiation more clearly illustrated than in the case of LDN 1551–IRS5. This young star is the central object of an extensive bipolar molecular outflow in Lynds Dark Cloud 1551 as well as the source for an optical jet (Strom *et al.* 1985, Campbell *et al.* 1988, Moneti *et al.* 1988). It also has an intricate pattern of extended emission within a few arcseconds of the source at near-infrared wavelengths. However, the nature of this circumstellar material is uncertain. Strom *et al.* (1985) interpret their extended images as light scattered from the inner surface of a thick flared disk. In their scenario, the inner accretion disk is coaxial with a larger molecular disk and the outflow itself. The model of Campbell *et al.* (1988) is similar except that the inner accretion disk is tilted an angle of 20° with respect to the outflow axis. They also point out that the position of "IRS–5" changes as a function of wavelength, making it plausible that the "source" is actually the last scattering surface ($\equiv \tau_\lambda=1$) for that wavelength.

Moneti *et al.* (1988) propose a somewhat different model to explain the observed object shifts: they postulate an ellipsoidal geometry with a major to minor axis ratio of four. The observed light is then due to photons which are scattered from the geometrically thinner poles. This model explains the observations well phenomenologically; however,

it is difficult to explain physically how this geometry can be produced in preference to the flared disk geometry. Flared disks seem to be a natural consequence of molecular cloud collapse if the models of Boss (1987) are physically realistic.

Campbell *et al.* (1988) point out that the failure of the ALS models of LDN 1551–IRS5 in the near-infrared is probably caused by the inability to model the geometry-dependent scattered light. Hodapp *et al.* (1988) conclude that all of the NIR flux (at least in the J, H, and K bands) is scattered light based upon their images of the extended (~ 4 arcsec) source and previous polarimetric work. Indeed, ALS themselves give a heuristic correction factor in an appendix to partially account for the scattering in YSOs in general. ALS point out that in true scattering, although the photons are scattered out of their original direction of propagation, on average the unabsorbed photons will still emerge within the observing beam if the source is unresolved and isotropic. However, by resolving the source, it may be possible to reconstruct the near-infrared spectral energy distribution without resorting to such corrections.

1.5) Dissertation Goals and Layout.

The primary scientific goal of this dissertation was to obtain the first near-infrared spectral energy distributions of YSOs which are uncontaminated by spatially resolvable scattered light. To this end, I have imaged 14 YSOs in the 6 near-infrared broadband

filters (J, H, K, L, L', and M) available in ProtoCAM at the NASA Infrared Telescope Facility. Some of these objects were imaged through a narrow passband circular variable filter to obtain information about the 3.08 μm water ice absorption band while some were imaged at K (2.2 μm) with a polarizer mounted in front of the camera so that the significance of scattering could be assessed directly. The flux from an object in a given passband was found by fitting a model stellar profile to the apparent central source in each image; the spectral energy distributions were constructed by plotting these results vs. the wavelength. These SEDs are then compared with the ALS models or with other discussions of the spectral slope in order to gauge the importance of scattering in these models.

During the course of examining the images, it became apparent that a significant number of the objects had companions or were otherwise multiple. I discuss the fraction of objects which are binary and compare this with the frequency of binaries on the Main Sequence and I comment on the large color differences between the members seen in some systems. In addition, a large fraction of objects displayed variability both during the course of this study and in comparison to previously published results. Various possible causes of these variations are discussed.

This dissertation is divided into two sections: the first (Chapters 2 and 3) will describe the theory of operation and the performance of ProtoCAM, the instrument with which all original data presented here were collected; the second section (Chapters 4, 5

and the Appendices) will describe the observation and interpretation of a selected list of protostars. Chapter 4 is a large paper which will be submitted to a refereed journal, thus it is formatted in such a way as to able to stand alone. Chapter 5 is a summary of the results and a discussion of potential future directions. Appendix A is a slightly modified paper which was published in the Astronomical Journal in 1991 (Vol. 102, p. 1398). It is closely related to this study, but is of a somewhat different nature than the work presented in Chapters 4 and 5. Appendix B is a table which lists all the photometry obtained during the course of this work. It is hoped that such a division will allow the unique nature of these observations to be clearly delineated without cluttering the discussion of the more fundamental questions of star formation.

Chapter 2: ProtoCAM - Theory of Operation

2.1) PROTOCAM

ProtoCAM is a 58 × 62 element InSb photodiode array camera which has been designed to match the NASA Infrared Telescope Facility's excellent seeing and background characteristics. Its useful wavelength sensitivity extends from roughly 1.0 to 5.6 μm; it contains a full complement of broadband filters within this range - J, H, K, L, L' and M (1.2, 1.65, 2.2, 3.5, 3.8, and 4.8 μm effective central wavelengths, respectively). To allow crude spectroscopic imaging over the complete sensitivity range, three circular variable filters (CVFs) are also included: one spanning 1.3 to 2.5 μm with a 0.9% passband, one spanning 2.7 to 4.3 μm with a 1.4% passband, and one spanning 4.3 to 5.8 μm with a 1.8% passband (because the earth's atmosphere is opaque between 2.5 and 2.7 μm, CVF overlap was not required here).

ProtoCAM's platescale is continuously variable in realtime - at the IRTF the platescale varies from 0.135 arcseconds per pixel (8.4 × 7.8 arcsecond field of view) to 0.35 arcseconds per pixel (21.7 × 20.3 arcsecond field of view). Available on-chip integrations are limited in length by support electronics. Fast integrations are currently limited by the array addressing electronics to be no shorter than 20 milliseconds (16.2 ms to read out the array plus approximately 3 ms of software overhead); slow integrations are limited by a counter in the integration control circuitry to be no longer than 3276

seconds. The long integration length limit is generally not a concern as the infrared sky background tends to be highly unstable over long time scales. It is true, however, that the array cannot be saturated with "dark" current in this amount of time - the ability to do so is desirable for some engineering applications. (Dark current here refers to the small current generated in the photodiode itself due to diffusion, generation-recombination, and perhaps tunneling phenomena. However, it is also true that the array cannot be saturated in this amount of time even with the current 5 ADU/s heat leak inside the dewar.) The short integration length limit allows imaging through all of the broadband filters at all platescales except for the M filter during nights of high sky emissivity (e.g. thin cirrus clouds); during good observing conditions, the M background will fill the wells only 20% full in a 20 ms integration at 0.35 arcsec/pix. Moving to a smaller platescale during high emissivity nights will usually allow broadband M measurements assuming the sacrifice of the large platescale is permissible. The CVFs may also be used in their entirety - while looking at a room temperature paper-covered aluminum plate (assumed to be a blackbody, i.e. it should produce much more flux than the telescope + sky background) during engineering tests to determine the thickness profile of the array, measurements were made every 0.05 μm over the wavelength interval 4.30 - 5.65 μm.

The ProtoCAM project was begun in November, 1988, to fill a recognized need at the IRTF to have near-infrared wavelength imaging capabilities. A prototype camera was desired both to provide experience with infrared arrays for the IRTF staff and to provide temporary imaging capabilities at the IRTF itself. A goal was thus set to have an

imaging array camera operational and on the telescope within six months, with the camera available for visiting scientist use six months after that. ProtoCAM saw first light at the IRTF with an engineering grade array during June, 1989, and became available for visitor use at the beginning of the first semester of 1990. Three groups were responsible for allowing such an aggressive time schedule to be met. The array and the clocking electronics were designed and constructed by the Hughes/Santa Barbara Research Center (SBRC); the preamplifier, the analog-to-digital converter board, and a high speed digital frame buffer board were designed by staff electrical engineers at the Institute for Astronomy; and the cryogenic dewar, all optics, and the controller computer system and software were designed by IRTF personnel. Each of these components and their performance will be discussed in greater detail in the following sections.

2.2) Array Characteristics and Operation

The detector itself is a 58 × 62 array of InSb photodiodes, with centers 76 μm apart. The intensity of light incident on the detector is measured by first charging the intrinsic capacitance of each photodiode with some reset bias voltage, then allowing the induced photoelectrons to bleed off this charge. The capacitance of an individual pixel is measured to be approximately 0.4 pF, which when combined with a bias voltage of approximately 400 mV (200 mV set by computer plus 200 mV from unidentified

additional biases) produces well depth of approximately 10^6 e^-. The experiments performed to derive these values will be discussed below.

The readout operation of the array can best be understood in light of the simplified unit cell diagram presented in Figure 2.1 (refer to the Santa Barbara Research Center's documentation for a complete unit cell diagram). Decoding circuitry on the array die turns on the row and column switches at the appropriate intervals to select a given pixel. When the row and column are first powered on, the signal from the detector is free to pass through an amplifier (FET 1 - which is biased by the current source FET 2), through the column enable switch (SW 5), then through another FET amplifier which is biased by an external resistor. The combined gain of these two amplifiers is measured to be approximately 0.85. To reset the pixel, the CΦRESET signal must be enabled while both the row and column are enabled; the clock signal is blocked if the column is not enabled at SW 4, and the 2 V reset level is not available if the row is not enabled at SW 2. The length of time an individual pixel is enabled is divided into three sections - the "signal" level, the voltage on the detector at the end of an integration before it is reset; the "reset" level, the time when CΦRESET is active and the voltage on the detector is forced to be that of the detector bias voltage; and the "reset pedestal", the voltage at which the pixel settles to when the reset voltage is removed. Sections 2.5 and 2.8 discuss the timing the array output waveform in further detail.

The various bias voltages indicated in parentheses in Figure 2.1 are observed to have the following effects on the output voltage waveform and/or the image:

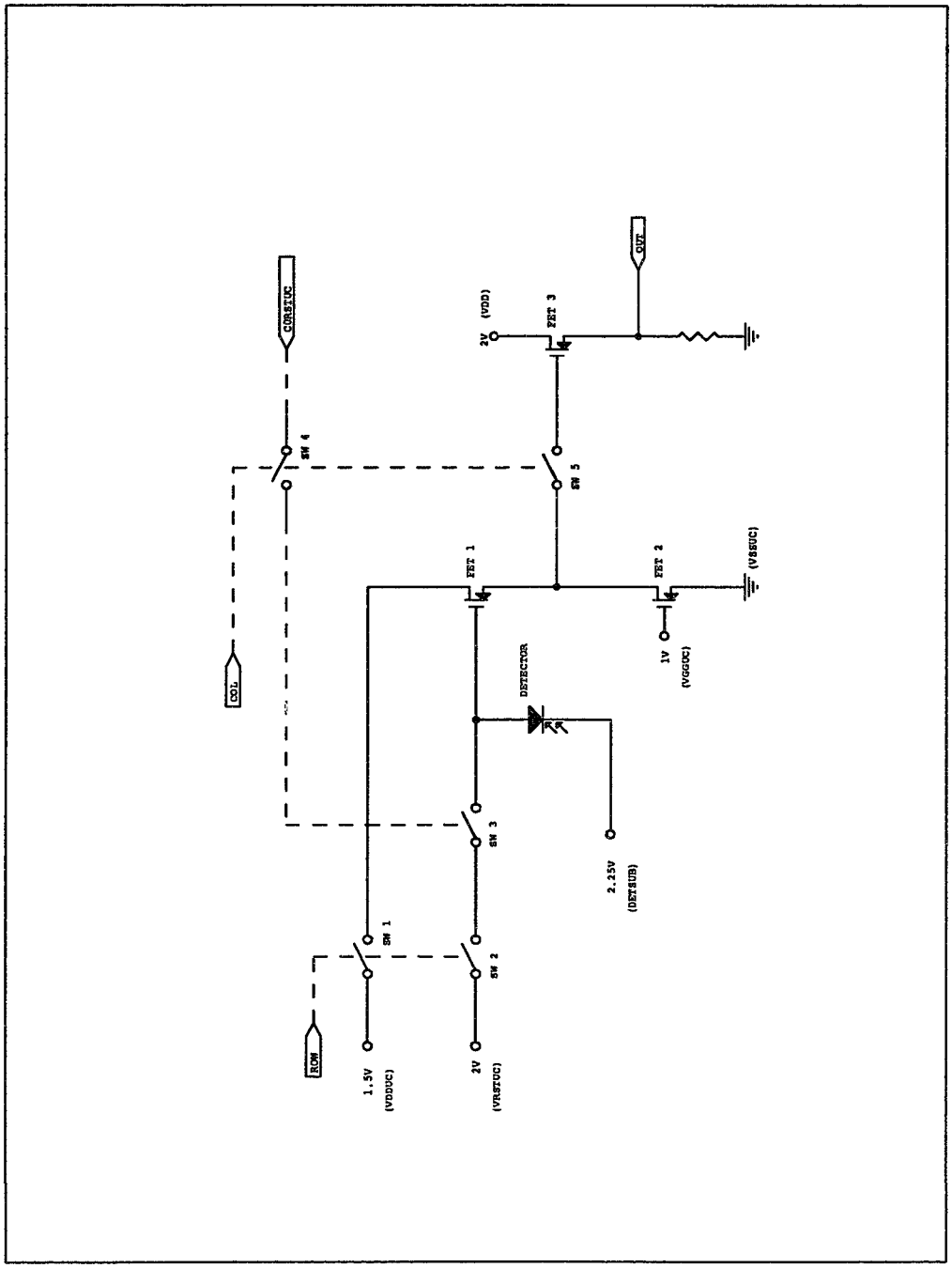

Figure 2.1: Simplified unit cell schematic of the array. In the real unit cell, a second pixel shares the same control lines, but has different output circuitry.

VDDUC: controls gain in signal part of readout. Does not affect reset level until absurdly low values are used. The gain increases linearly with voltage until a plateau is reached near 1.9 V. Set at 2.0 V.

VSSUC: effectively the unit cell ground. Positive voltages greater than a few mV introduce negative-going spikes into the output waveform at the signal/reset boundary. Above 50 mV the array becomes inoperable. Negative voltages less than -40 mV reduce gain. Set to 0 mV.

VGGUC: reduces gain for voltages greater than 1.75 V. Introduces spikes and other oddities at voltages less than 0.9 V. Between these limits the DC level of the readout pattern shifts linearly. Set to 1.0 V.

VDD: no effect on the output signal until it drops below 1.2 V, where it begins to reduce the gain. Set to 2.0 V.

VRSTUC: causes linear shifts in the DC level of the output signal . Adds some visible streaks to the image for voltages less than 1.8 V. Set to 1.95 V.

AVRST (one of the clock reset voltages not shown in this diagram): introduces "blotchiness and streakiness" into the observed images - becoming worse at more positive voltages. Set to -80 mV.

The row and column control voltage levels have all been set to toggle between 0 and 4 V. At voltages higher than 4 V, glow from the switching FETs becomes apparent in images.

Two quantities which will figure importantly in later discussions are the effective capacitance of the photodiode junction and the gain of the on-chip MOSFET output amplifiers. I first derive the output gain by measuring the array saturation voltage as a function of the initial bias voltage. As the bias voltage is increased (toward more negative voltages), the apparent "well depth" should also increase in an approximately linear fashion, so that the gain between the photodiode and the "outside world" should be easily measurable. Doing a linear least squares fit to the number of ADU at saturation vs. the reverse bias voltage, I find a slope of 1.04×10^5 ADU/V and an offset of 22,900 ADU. Because there are 306 μV/ADU at the input of the A/D converter (derived later), this yields a gain of 31.8 from the photodiode to the output of the preamplifier. The preamplifier has a gain of 37.6 (also derived later), so that the gain from the photodiode to the output of the on-chip MOSFET amplifiers is ~ 0.85. The offset of 22,900 ADU in the fit similarly implies that there is an approximately 210 mV offset present in the bias voltage setting, so that setting a bias of "200 mV" actually places 410 mV reverse bias on the photodiodes. It is not clear where this offset originates; most of it is due to the photodiode's reset level "snapping" to a more negative voltage after the reset signal is released. Measurements on an oscilloscope show that this contributes approximately 160 mV to the offset, leaving 50 mV of unknown origin.

With the MOSFET gain in hand, the photodiode junction capacitance can now be estimated. In this situation, the capacitance can be found from

$$C = K q G_{FET} G_{PREAMP} G_{A/D} \tag{2.1}$$

where K is the electron-to-ADU ratio (~25, derived in Chapter 3), q is the electronic charge, G_{FET} is the MOSFET gain (0.85), G_{PREAMP} is the preamplifier gain (37.6), and $G_{A/D}$ is the A/D "gain" (3273 ADU/V). This yields an *effective* junction capacitance of roughly 0.42 pF. It should be kept in mind that the junction capacitance is a function of the applied voltage on the junction (Sze, 1981), thus the value obtained here should be treated only as a estimated operating point.

2.3) SBRC Control Electronics

The control electronics provided by SBRC (affectionately known as "the blue boxes") provide the clocking and bias voltage generation circuitry necessary for the operation of the array. The interface to the computer is rather simple: a 16-bit data bus (3 bits for opcode, 12 for data, and one spare) with a strobe signal to load the data - this bus allows loading the detector gate and bias voltages as well as determining the readout rate - and a 4-bit bus which controls the type of sampling to be performed. I will not describe these electronics further, except to highlight a few things which I changed and/or

measured. See the SBRC manual for further details and definitions of terms used in this section.

An important clock waveform which needs to be discussed further is the CTC signal - the command-to-convert. This signal is generated by the blue boxes to tell the analog-to-digital converter when a new pixel is ready to be sampled. The blue boxes are capable of generating two CTCs per pixel, and this has been exploited to enable correlated sampling (discussed later in this chapter). The generation of these pulses is quite simple: several counters are clocked with a continuous input clock and the output count is compared with timing values selected by DIP switches. When the values are equal, the counter is reset, a pulse edge is generated (either rising or falling), and the process is repeated. There is a set of counters to generate the leading (rising) edge of each pulse, and a counter to generate the width (and thus falling edge) of each pulse. There is sufficient latitude in the DIP switch settings so that any part of the pixel signal (signal, reset, or pedestal), or any part of the output of the SBRC analog processing electronics can be sampled. The current setting generates two CTCs per pixel; one during the signal part of the output waveform, and one during the reset pedestal part.

The SBRC boxes also generate two bias voltages of significant individual importance: the detector bias voltage and the gate voltage. Both of these biases are generated in a similar manner: 12-bit D/A converters which have a ±5 V range are loaded with data presented by the 16-bit data bus mentioned earlier. In the case of V_{gate}, it is

passed directly (after buffering) to the array. The expected voltage range is thus -5.000 V to 4.998 (from the manufacturer's data sheet); I have measured -4.999 to 4.997 V at the output. V_{bias} is generated in a similar manner, except that it is divided by approximately 21 and offset. From the circuit diagram, one would expect the output voltage to range from -238.6 mV to 0.0 mV; however, measurements at the output of the blue boxes indicate that there is a 10.4 mV offset generated somewhere in the circuit so that the measured voltage range is -229.0 mV to 10.4 mV. This offset has been taken into account in the engineering software used to set the bias; however, it is relatively insignificant compared with the unidentified source of -200 mV offset observed by other tests.

2.4) PREAMPLIFIER

The preamplifier's principal functions are to provide the necessary gain, offset, and buffering to make the array's output signal readable by an external device. A secondary function is to provide appropriate filtering in order to prevent high frequency noise from being aliased into the signal frequencies. Because it was anticipated that the full well depth of the array would be 0.25 V and that a 10 V signal would be required for the analog to digital conversion, the original design specifications called for an amplifier with a gain of 40 and an output voltage slew rate of at least 10 V/μs. To allow the output to settle to the resolution of the A/D converter (1 part in 65536) at the fastest readout rates

(3 μs per pixel segment), the time constant of the circuit could be no longer than 300 ns, meaning that the gain-bandwidth product of the circuit had to be greater than 120 Mhz. Finally, the overall noise of the preamplifier had to be less than 1 ADU (306 μV). The above constraints place a considerable burden on modern operational amplifier technology. The solution was to build a two-stage preamplifier: the first stage provides only a gain of eight using a moderate speed, but very low noise op-amp, while the second stage provides a gain of five using a very high speed, very high slew rate, but somewhat noisy device. The circuit diagram for the preamplifier is given in Figure 2.2 and a detailed analysis of it follows.

As the signal enters the preamplifier box, the first circuit element it encounters it a simple voltage divider with gain 2/3. This divider supplies the requisite 30 KΩ drain impedance to properly bias the array's output MOSFETs, while at the same time providing a measure of static protection for the pre-amp. The signal is then passed through a non-inverting, gain of 12 (for a net gain of 8) active low pass filter. This filter's time constant is 165 ns, thus allowing 18 time constants for the signal to settle - more than enough for 16 bit accuracy but still able to eliminate some of the higher frequency noise. The OP-37 which is driving the filter is a moderate speed device which has extremely low noise characteristics - in fact, the dominant noise source in the pre-amp is the Johnson noise due to the resistive voltage divider (see Figure 2.3).

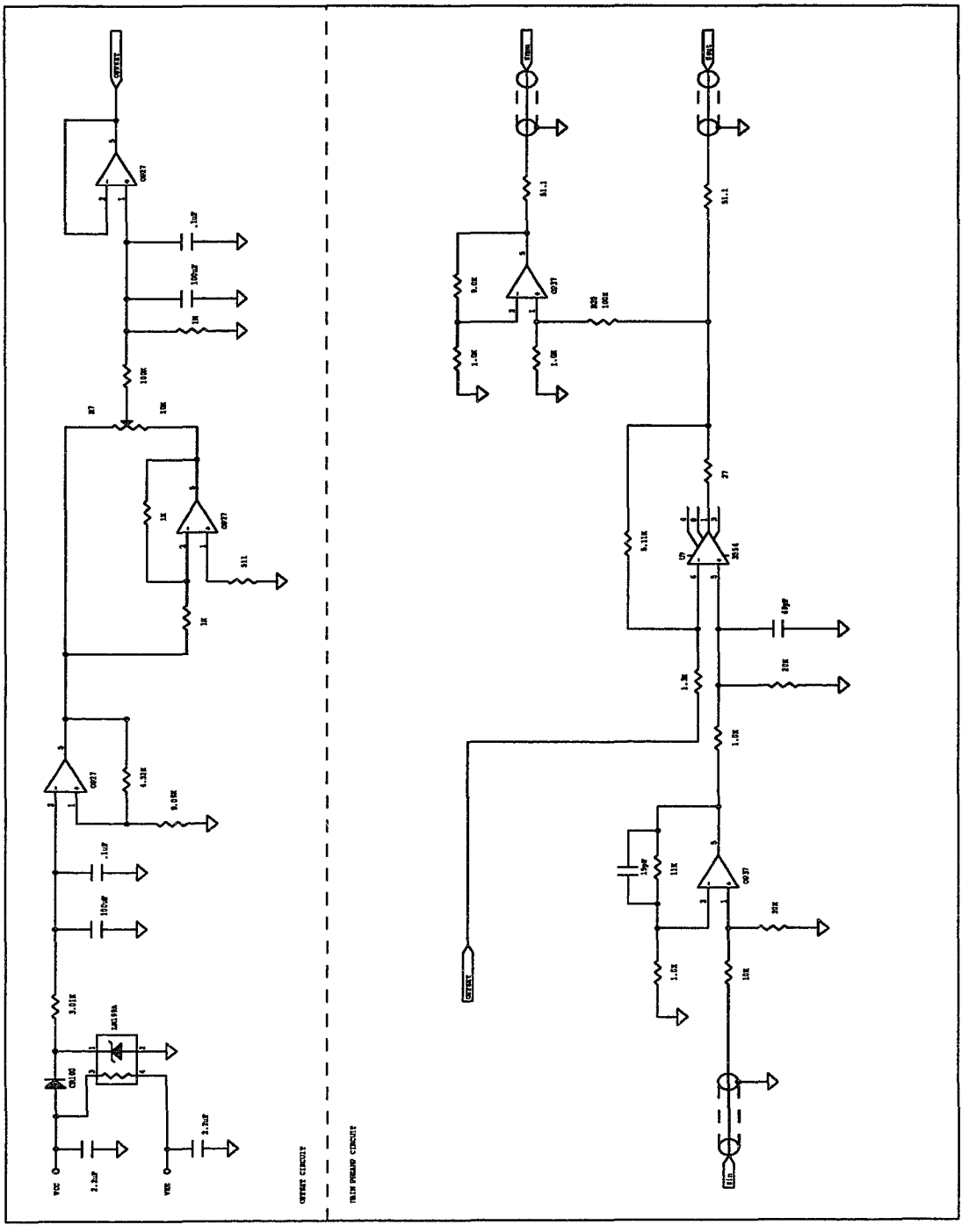

Figure 2.2: A simplified circuit schematic for the preamplifier. All circuitry directly affecting the signal has been retained. Power supply circuitry, etc. has been omitted.

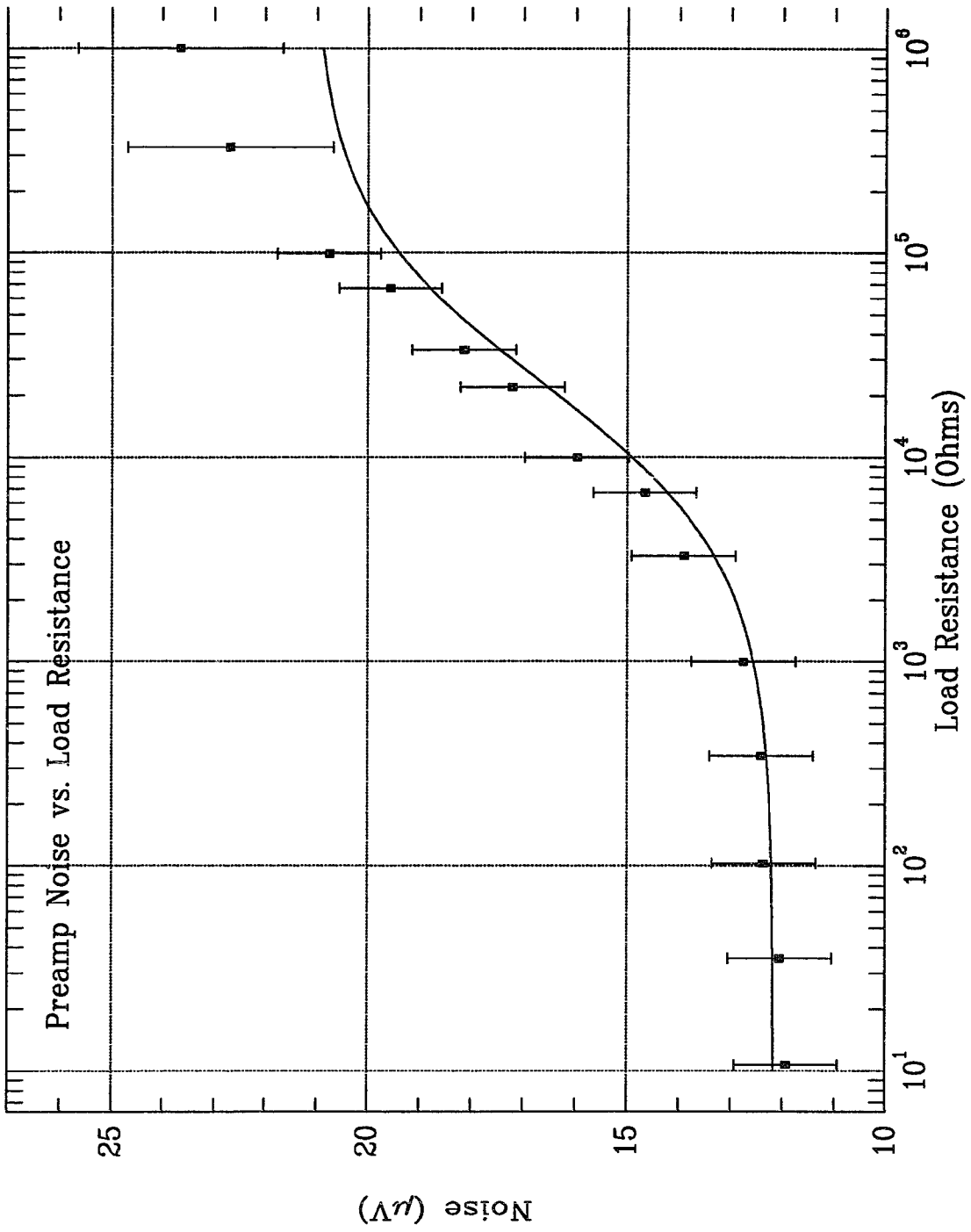

Figure 2.3: A plot of the preamp noise vs. input load resistance. The larger discrepancies seen at the higher impedances are due to pickup.

While this amplification and filtering are taking place, a subcircuit is generating an offset voltage which is used to eliminate the bias voltage on the MOSFET outputs. A stable reference voltage of 6.95 V is generated by an LM199A. This level is passed through an OP-27 non-inverting amplifier circuit with a gain of 1.475 to produce a reference voltage of 10.25 V. This reference is tapped and inverted by a second OP-27 inverting buffer to provide an additional reference of -10.25 V. An adjustable offset voltage is now available by using a buffered potentiometer resistor divider network. Through a judicious choice of component values, the offset voltage is quite linear as a function of the potentiometer wiper position. If we let x represent the fractional wiper position (0 being one end, 1 the other), analysis of the equivalent resistor network shows that the offset voltage at the output of the buffer amplifier is given by Voffset = (10.25 V) $\times$ (100 - 200x) / (110 + x - x^2); it can be seen from this equation that the maximum deviation from linearity ((real - ideal) / ideal) is only 0.23%. Linearity to that precision is mostly of aesthetic value, but reasonable linearity (no more than a few percent) is important for ease of human adjustment and to insure good stability in the case of thermally induced wiper drifts. This offset voltage is also heavily filtered to eliminate any noise or transients which may have been picked up during the offset generation process.

In the second stage of the preamplifier, this offset voltage and the amplified signal are combined by the use of a summing amplifier. The signal is injected into the non-inverting node of the amplifier; it sees a net gain of 4.70 (for a total signal gain of 37.6). This amplifier has somewhat higher input noise characteristics than the first stage

amplifier, but the fact that the signal has already been magnified by a factor of eight makes this increased noise negligible. The offset voltage is injected into the inverting node; it sees a net gain of -3.93. Because of this, and because the output op-amp will saturate at approximately 15 V, the trimpot will only provide a usable level change over 40% of it's range; however, which 40% of its range is determined by the operating voltages of the array's output amplifier mosfets.

After the second stage amplifier, the signal is sent to the outside world via 50 ohm BNC cable. This cable can be terminated or unterminated depending on its length. The signal is also split off into a divide-by-ten monitor circuit. The output signal can thus be monitored on an oscilloscope or dynamic signal analyzer while the camera is in operation. It is important to note, however, that connecting the monitor outputs tends to inject 60 Hz line noise back into the preamp, and the effects can be quite obvious in the images (a single wave at the fastest readout rate, 16.2 ms, or a series of waves at the longer rates). Thus the monitor circuits should be used only during engineering tests.

2.5) SBRC Analog Signal Processing Electronics

After the preamplifier, the signal can be directed either straight into the A/D conversion electronics (which will be described later) or into SBRC's analog signal processing electronics. Although the analog electronics are no longer being used, because

the camera was operated with them for one and a half years and because much of my data was taken using it, I will describe it here briefly. The simplified circuit schematic is shown as Figure 2.4.

The SBRC control electronics allow several software-selectable signal processing modes. Common to all these modes is the ability to select anti-aliasing filter cutoff frequencies and signal gain. The first stage of the signal processing chain is, in fact, the anti-aliasing filter whose cutoff frequency is chosen by the current readout rate. The time constants and sample times chosen by SBRC are compromises so that four selectable filters match eight readout rates. Thus the signal has typically 7 to 22 time constants to settle before it is sampled. For reference, the signal requires approximately 11 time constants to settle to 1 ADU accuracy (1 part in 65,536) for a full-scale swing. Analysis of the individual filter circuits in combination with the different readout rates shows that the worst case is the 64.8 ms readout rate, where it is theoretically possible to have errors of up to 45 ADU. Because the voltage swings are almost always relatively small, the typical settling error even at this readout rate will still be negligible. For the default readout rate in this observing mode (129.6 ms) the maximum settling error will be only 0.03 ADU.

The next stage of the signal processing electronics is a programmable gain stage, with gains of 0.5, 1.0, and 2.0 being normally allowed (as an amusing exercise, gains of 1/3, 2/3, 2/5, and 2/7 can also be chosen due to the fact that SBRC does not check to see

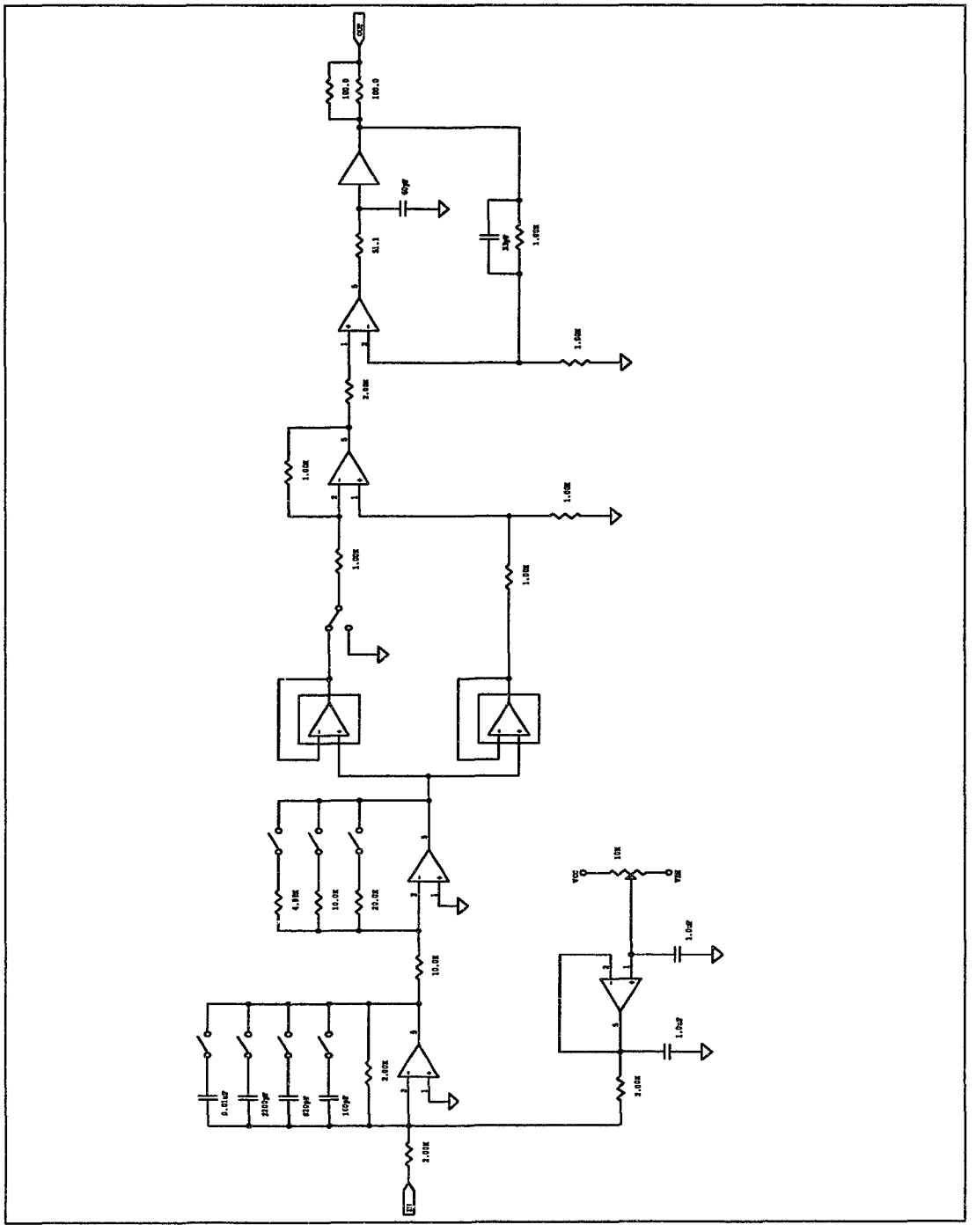

Figure 2.4: A simplified circuit schematic of the SBRC analog signal processing electronics.

if a "valid" gain op-code was chosen). In actuality, neither the gain nor the filter circuits are well-designed from a circuit theory point of view. Both are inverting designs rather than non-inverting; inverting amplifiers have inherently greater noise and frequency response problems. Since both circuits are very simple, it would have cost nothing to design and build their non-inverting equivalent. In addition, the filter is only a single-pole design (20 dB/decade attenuation) which is generally not adequate in an anti-aliasing application.

After the signal is conditioned, it is fed into a pair of sample and hold circuits (S/Hs). The outputs of the S/Hs are differenced in a unity gain summing amplifier, then buffered and presented to the outside world. The use of two S/Hs allows the use of several simple readout schemes through both hardware and software control.

These readout modes are selectable via the SBRC control buss. In the simplest modes, the input of the summing amplifier is tied to ground rather than S/H 2 and only one CTC pulse per pixel is generated. This allows the signal to be read (or reset or pedestal if those are desired instead). After reading this level, the pixel can either be reset, thus yielding signal-ground data, or it can be left to continue integrating if some more complex multiple readout scheme is desired. While signal-ground is the simplest useful readout scheme, it suffers the worst noise performance as it does not eliminate variations in the reset level or drifts in the DC bias voltages.

An improved readout method is to tie the input of the summing amplifier to S/H 2 and let S/H 2 sample the reset level. This produces signal-reset data and improves performance by eliminating some of the DC bias voltage drifts. This was ProtoCAM's normal mode of operation prior to January 26, 1991. The timing for this scheme is shown in Figure 2.5.

More advanced readout methods are available with the SBRC electronics; for instance, two CTC pulses can be enabled. This can allow a (signal - reset) - (pedestal - reset) for the best DC bias drift cancellation. If two such readouts are stored, the (pedestal - reset) from the first integration may be subtracted from the (signal - reset) from the

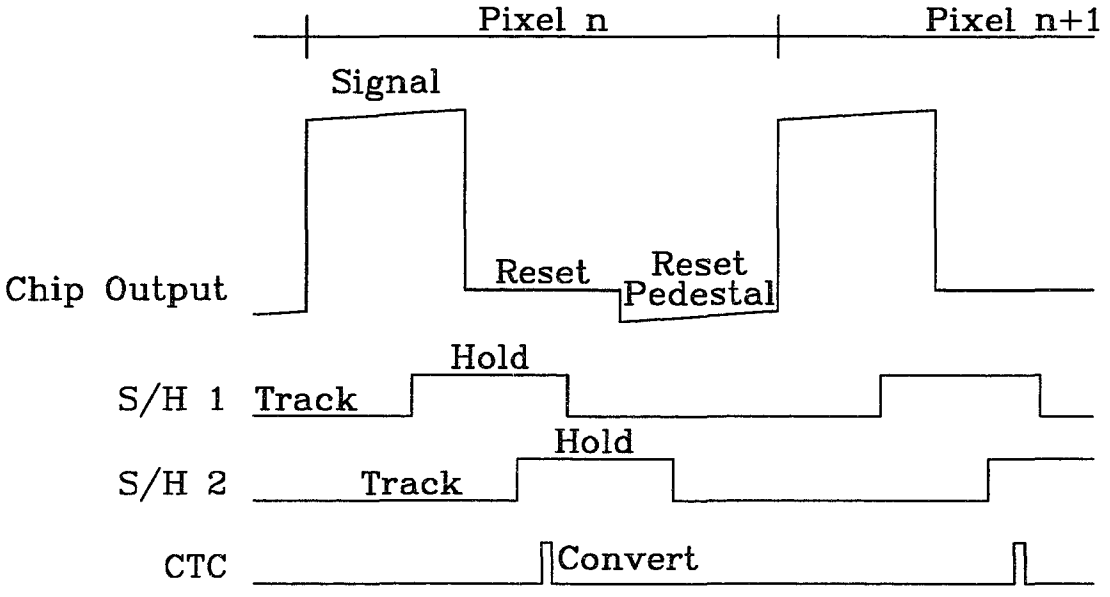

Figure 2.5: Timing diagram for "old mode" pixel readouts.

second to yield a true correlated double sample - this also eliminates the uncertainty associated with the reset level, known as "kTC noise" as it is the noise produced by recharging the capacitance of each photodiode. These more complex schemes were never implemented with ProtoCAM due to their excess overhead and the desire to ultimately do away with the entire SBRC analog signal processing chain in favor of some cleaner processing scheme. The end result will be discussed later.

2.6) A/D Converters

The analog-to-digital converter circuits were specifically designed to sample and convert any piece of the analog output signal with time to spare. As the fastest readout is 9 μs/pixel (for a 16.2 ms frame rate), or 3 μs per segment, an A/D conversion time of 2 μs per sample is easily sufficient. The Analog Microdevices AM40116 A/D converter was chosen as the heart of the circuit (Figure 2.6) because of its 2 μs conversion time, its 16 bit precision capabilities, its linearity and its stability. Tests of the converter show that it is linear and accurate to the accuracy of the measuring instruments (Figure 2.7). From the slope of the fit, we find that the "gain" of the A/D circuit is 3273 ADU/V, not really significantly different from the theoretical value of 3276.8 (65,536 levels divided over a 20 V input range). Both this value and the offset value could be trimmed to their theoretical values by adjusting trimpots on the A/D converter packages if higher accuracy were desired.

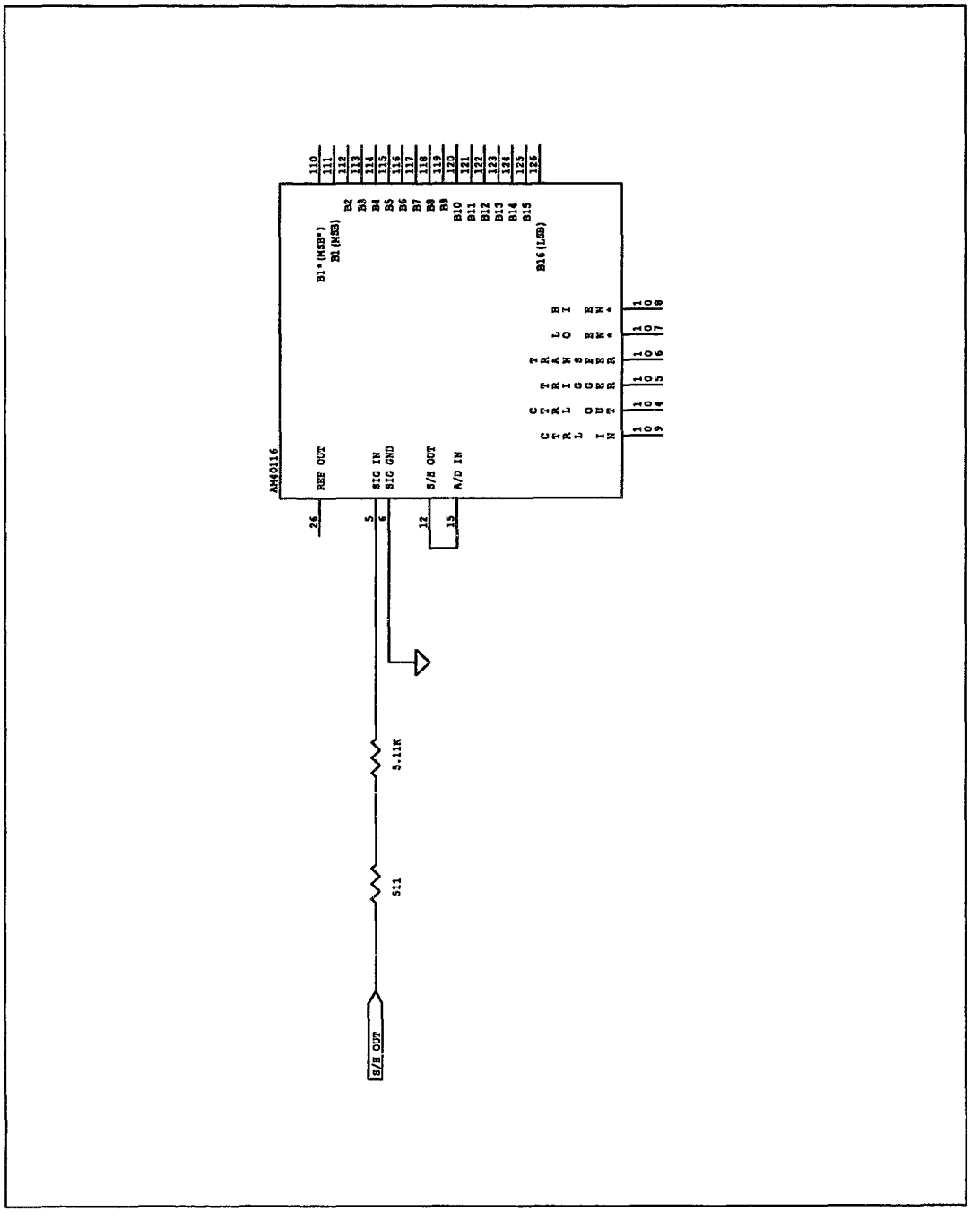

Figure 2.6: A simplified circuit schematic of the analog-to-digital converters. All digital wave-shaping circuitry has been omitted.

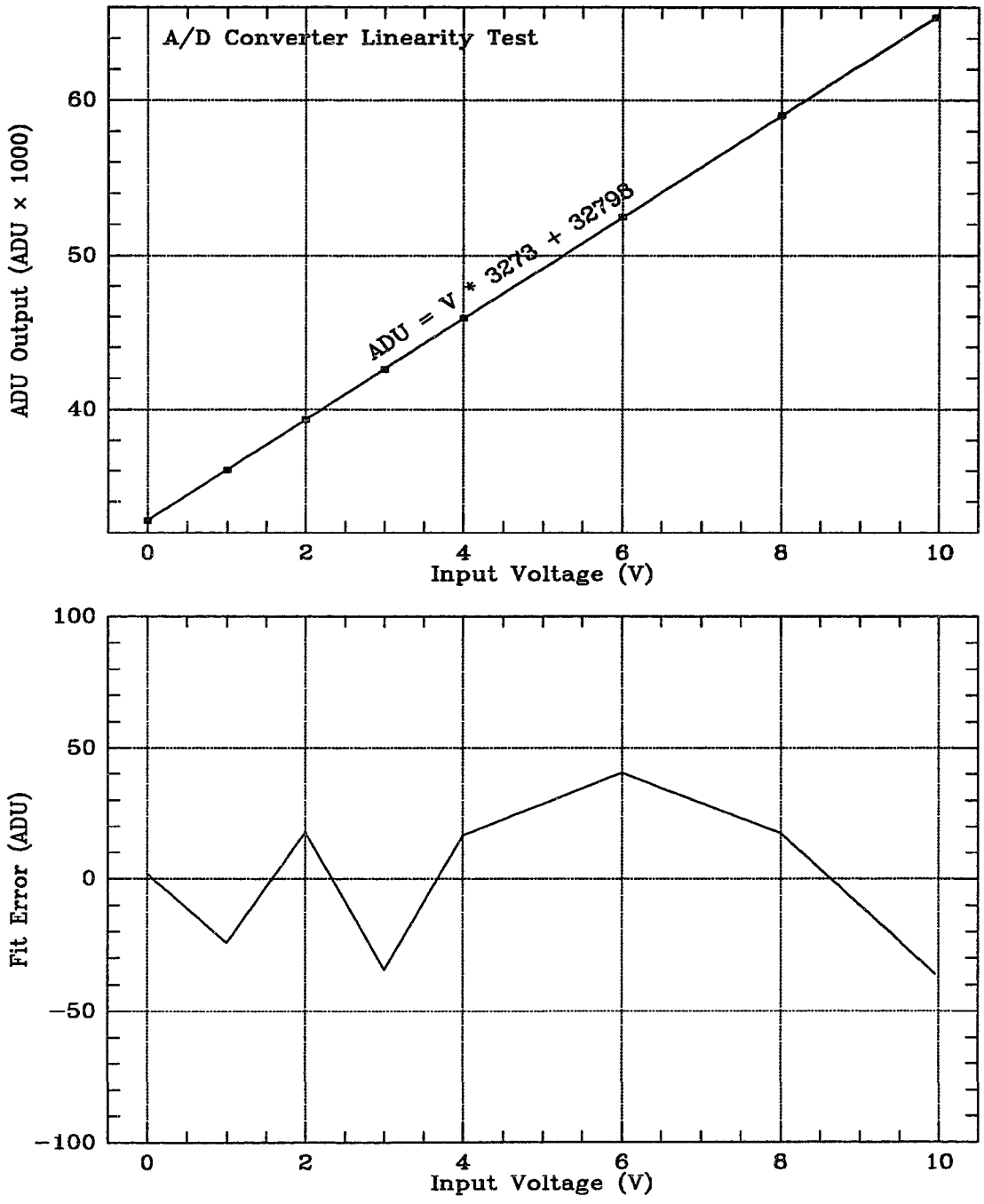

Figure 2.7: A test of the A/D's linearity. The top figure shows the data along with the fit. The bottom shows the residual differences between the data and the fit.

2.7) DIGITAL BUFFER BOARDS

Figures 2.8 and 2.9 show the circuit schematics for the digital buffer boards which are housed in a 80386-based microcomputer. The boards are responsible for several actions: sending information to the SBRC control electronics, controlling the starts of readouts (and thus the integration length), loading the digital data from the A/D converters, and coadding multiple frames in real time.

The PC Interface Board (PPCI Board, Figure 2.8) is responsible for most of the control and interface functions. A series of control registers indicated in the upper right of the diagram allow the computer to control various operational modes of the buffer boards, such as what type of math operation to perform (overwrite or coadd), single readout vs. continuous readout, etc. At the upper left is the primary memory and address counter for the data. The data is read in starting at the high memory address, counting down to zero. This address may be manipulated during the integration to store several subframes; this technique allows correlated sampling and will be discussed in the next section.

Central to the timing control is the 8254 timer located left of center of the diagram. This chip has three internal counters; in our application, one counter is used to divide down a 1 MHz input clock to a 1 kHz or 20 Hz clock (user-selectable), the second counter counts the output of the first to indicate the end of the integration, and the third

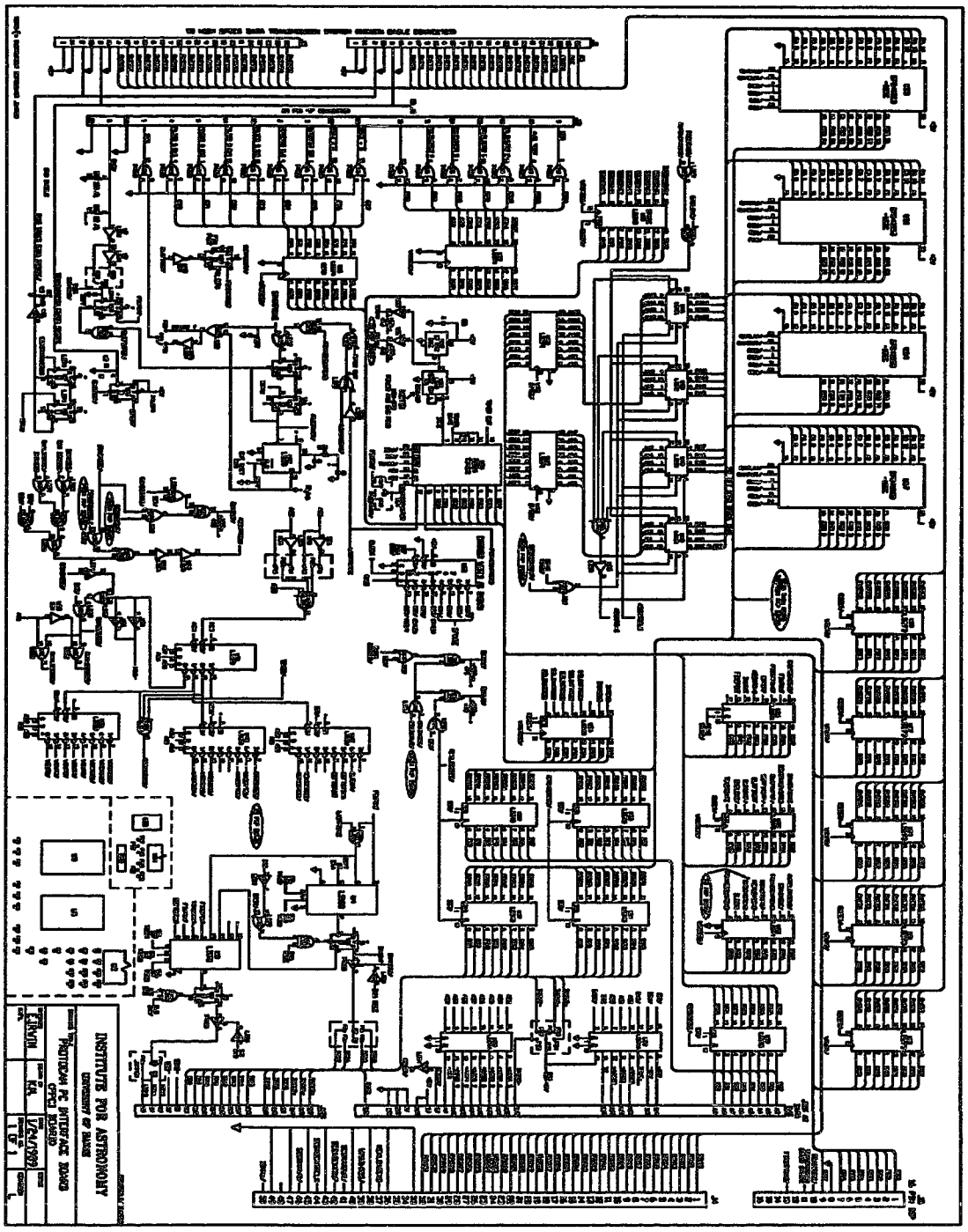

Figure 2.8: The circuit schematic for the PPCI board. This figure is intended only to be a road map. For details, refer to the original schematics at the Institute for Astronomy.

counts the number of integrations. Below this in the diagram is the logic circuitry necessary for the timer command the board to read in data from the A/Ds and prepare the board for the next mode of operation. The logic sequence necessary for this is described in pseudocode in Section 2.8.

Finally, there are some buffered control lines indicated at the left edge of the diagram; these control the motions of the filter wheels and array position in the dewar, sending switching information to the chopping secondary mirror, as well as telling the SBRC electronics when to begin a readout. The lower right portion of the diagram shows circuitry involved in memory control (including an untested and unused DMA controller) and transferring data between the two buffer boards.

The Math Processor Board (PMP Board) has two primary functions (Figure 2.9). The first, indicated in the left half of the diagram, is to receive the incoming 16-bit data and either overwrite the data in memory or add the incoming data to it. The sum is stored as a 32-bit integer and written back to the PPCI board. The right half of the diagram shows circuitry needed for generating the memory address control signals for both boards.

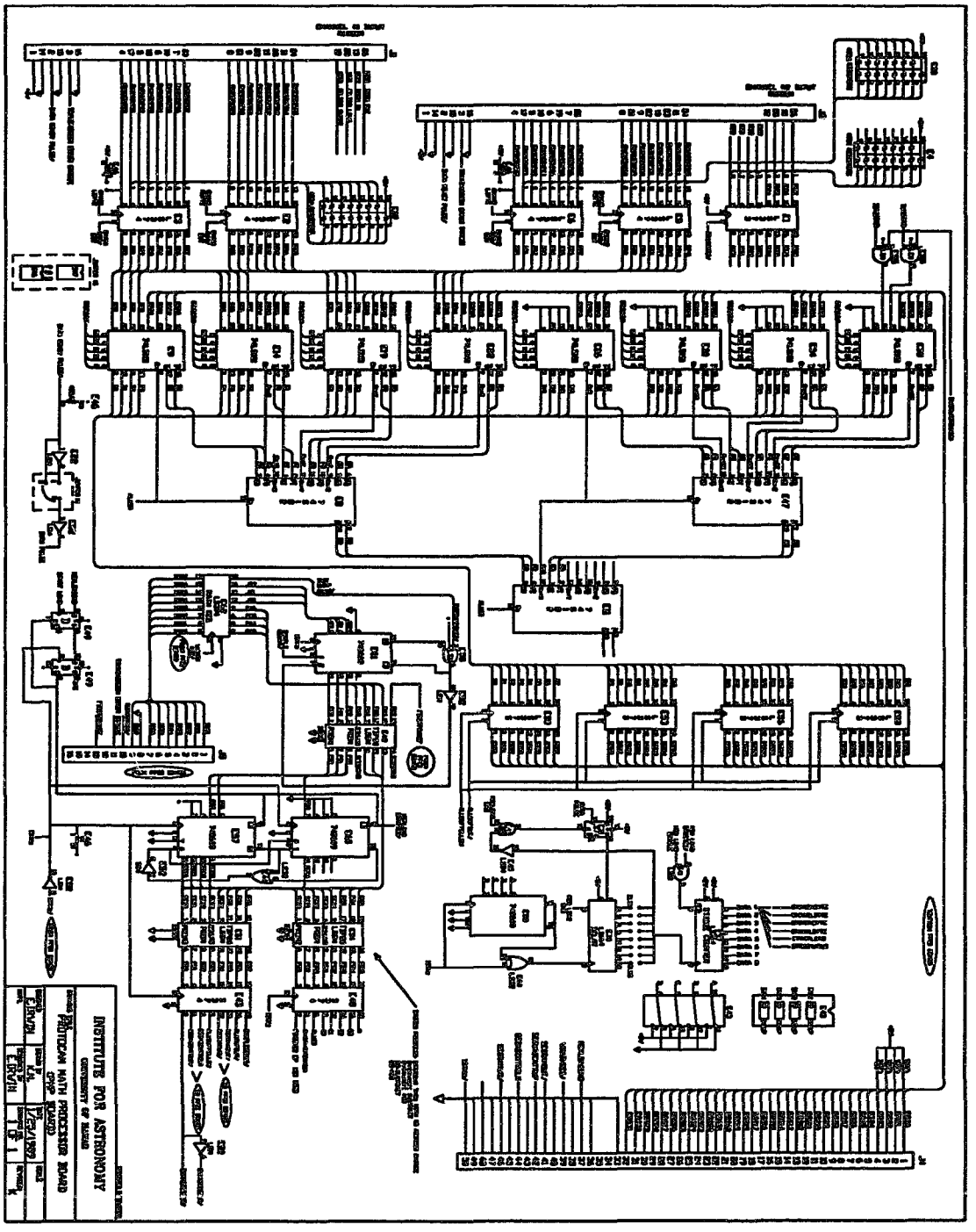

Figure 2.9: The circuit schematic for the PMP board. Again, this figure is only intended as a road map. For details, see the original.

2.8) New Mode Operation

As mentioned earlier, the more complicated readout schemes involving the SBRC analog signal processing chain were never implemented. This is due in equal parts to the desire to read out the array faster than the SBRC analog electronics are capable of running in order to be able to observe with the broadband M filter, to reduce the observed read noise, and to simplify the overall signal path. This was accomplished through a rare burst of insight which occurred late one night at 14,000 feet while particularly oxygen starved: feed the output of the preamplifier directly into the A/D converter, generate two CTC pulses per pixel with the SBRC electronics timed to sample the signal and reset pedestal levels, store both levels on the buffer boards in their interlaced format, then combine them appropriately in software after the actual integration is finished. These modifications did indeed lead to the simplification of the signal chain and the ability to read out the array at the fastest rate - 16 ms per frame, adequate for broadband M observations. However, the read noise was not significantly reduced. More speculation on this topic will appear in Chapter 3. I will now describe the changes I made to the system in greater detail as this mode has now become the standard operating mode of ProtoCAM (as of January 26, 1991).

Correlated sampling is a popular readout technique because it eliminates the noise inherent in the process of resetting a pixel to some predefined bias value ("kTC noise"). This uncertainty appears to be a constant DC offset until the pixel is again reset. Since

this process occurs only at the beginning of an integration, sampling the pixel immediately after it is reset (the "reset pedestal"), then again at the end of the integration (the "signal"), allows us to do a difference which removes the kTC noise since the offset is the same for both reads. This is a single correlated sample. Double correlated sampling reads the reset level as well, allowing determination of the quantity ($signal_1$ - $reset_1$) - ($pedestal_0$ - $reset_0$), where the subscript 0 refers to the readout at the start of the integration and 1 refers to the readout at the end of the integration. This technique allows the removal of any DC drifts in the bias electronics as well as the kTC noise. For ProtoCAM we chose to use the single correlated sample because we believe the bias drifts are small and it did not require any modifications to existing hardware.

Implementing this in ProtoCAM required only a few cabling and DIP switch changes. First, the output signals from the preamplifier were fed directly into the A/D converters rather than going through the SBRC signal processing electronics. Next, some jumpers which allowed 50 ohm termination on the input of the A/D converters were removed because of the very short cables which were now present. Finally, the SBRC digital electronics were told to generate two A/D convert commands (CTCs) per pixel and the timing of these pulses were adjusted via DIP switch settings; the first pulse was timed to sample the signal portion of the pixel output after it had settled for 10 time constants (to allow the signal to settle to the A/D resolution), the second pulse sampled the pedestal level after 10 time constants. These timing changes are summarized in Figure 2.10.

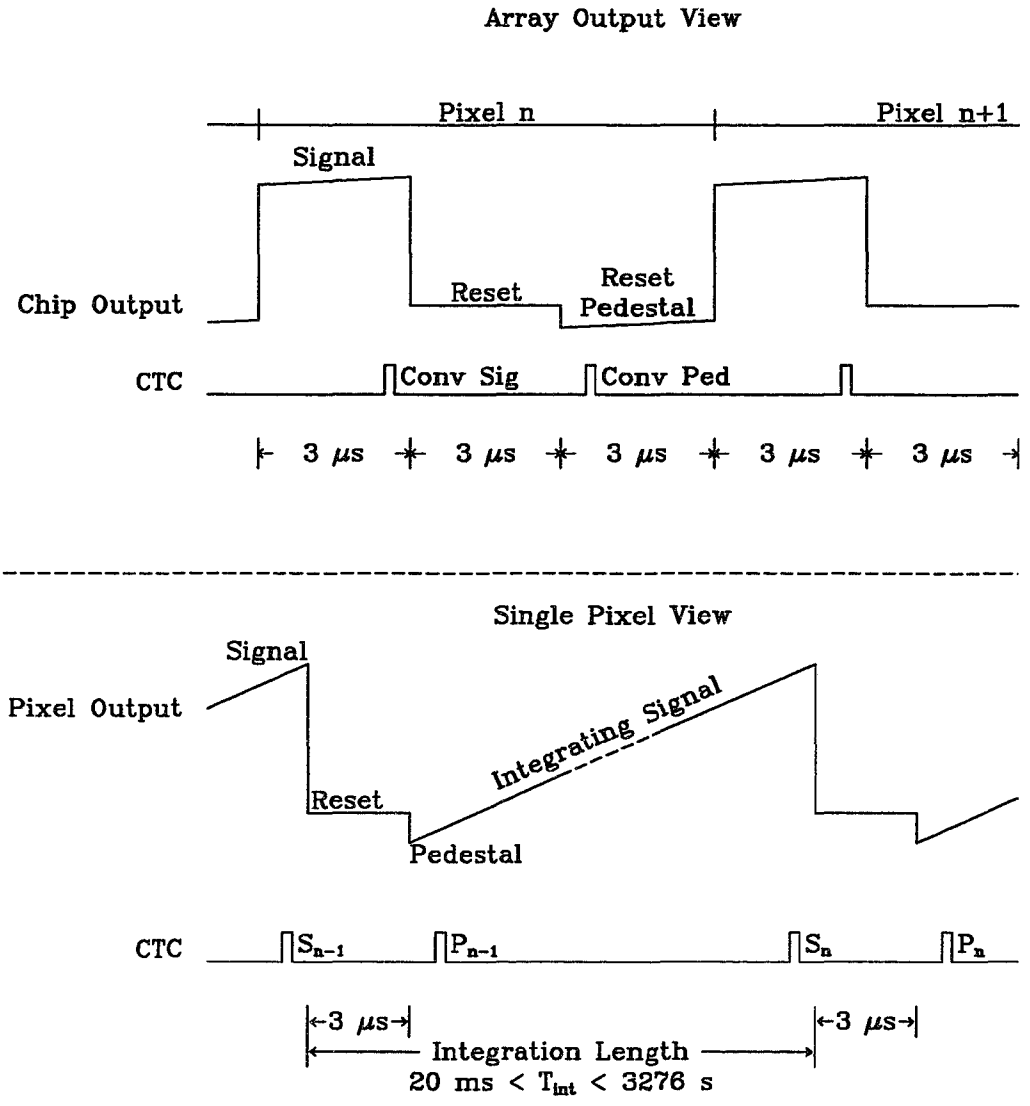

Figure 2.10: Timing diagram for the "new mode" pixel readouts.

The changes required by the software were much more extensive, and the end results are discussed in the next section; here I will discuss the tangled format of the data as it is read into the buffer boards. Because there are two output channels from the A/Ds and because there are two quantities read per pixel, the data becomes interlaced in a complicated fashion. The buffer boards always load the odd A/D channel first, then the even; there will be one of these odd/even pairs for the signal level of the read, and one for the pedestal level. Thus the format as the entire array is read looks like (s=signal, p=pedestal) $s^1, s^2, p^1, p^2, s^3, s^4, p^3, p^4, \ldots, s^{3595}, s^{3596}, p^{3595}, p^{3596}$. If the observation desired is only a single integration, then two such readout frames are required, one at the beginning of the integration ("initial" and subscript 0) and one at the end ("final" and subscript 1). The s's from the initial frame are thrown away, as are the p's from the final frame; the reduced pixels are then $s^1_1 - p^1_0$, $s^2_1 - p^2_0$, etc.

If more than one integration is desired, three readout frames are required; the initial and final as before, plus a coadded intermediate frame. The coadd frame can be any number of intermediate frames; a unique data frame for each integration is not required. Consider the following N-coadd example. The correlated sample equation dictates that for each pixel we want to obtain the quantity $(s_N - p_{N-1}) + (s_{N-1} - p_{N-2}) + \ldots + (s_1 - p_0)$ where the subscripts refer to the readout number. This is obviously equivalent to $s_N + (s_{N-1} - p_{N-1}) + \ldots + (s_1 - p_1) - p_0$ and thus to

$$s_N - p_0 + \sum_{i=1}^{N-1} (s - p)_i \qquad (2.2)$$

Because both the pedestal and signal levels are coadded in each frame, this final summation shows that only the single coadded intermediate frame is necessary, not the individual intermediate frames.

To actually perform this technique, three memory areas on the buffer board are required; each memory area is 3596×2 32-bit values (the factor of 2 is due to saving the signal and pedestal). The initial readout is written into memory area 0; if there is more than one coadd, the intermediate frames are coadded in memory area 1; the final readout is written into memory area 2. At the end of the observation, all 3596×6 values are read into the computer, which then does the pixel sorting and final arithmetic.

A final addition to the new mode is the ability to chop the telescope's secondary mirror in synchronization with ProtoCAM's readouts. I discuss it here because it involves several related memory switching games and is intimately related to the readout process. The mechanics of synchronizing the secondary to ProtoCAM are trivial; it merely involves generating a waveform which tells the secondary mirror to move just before each integration is performed. Maximizing the rate at which this can be done requires more skill. Because of the overhead involved in reading the data from the buffer boards into the computer, it was desired to store (and coadd) all necessary information on the buffer boards during the chopping sequence, then post-process all that data into a sensible image at the end. Fortunately, this is not too difficult; the memory on the buffer board is divided into two banks (0 and 1) each of which can contain the three memory areas mentioned

earlier. Thus for chop beam A, the data are written into memory area 0, 1 (if more than 1 coadd per beam), and 2 in memory bank 0; beam B is written into bank 1. After the observation sequence, 3596 × 12 values are read into the computer, processed into an "object" and a "sky" frame, and stored as two unique images. This process works quite well; the secondary can be chopped at 5.7 Hz when doing a 20 ms integration with 1 coadd per beam. Of course, the observing efficiency at this rate is pretty bad (77% devoted to purging, reading, and other non-photon-collecting activities). This can be improved by increasing the integration length or number of coadds at the expense of speed. However, problems which will be discussed in Chapter 3 make chopped observations non-ideal under most conditions, so that chopping is rarely used at present.

2.9) PROTOCAM SOFTWARE

The software which drives ProtoCAM is integral to the lowest level of operation of the camera. While independent hardware takes care of many of the details, the 80386 computer software orchestrates most of the hardware tasks. In this section I will describe the low level operation of the camera interface of the software, some of which was originally written by Ev Erwin, but which was rewritten, augmented, and optimized by me. Tony Denault was responsible for the remainder of the software, including incorporating the low level code into a very usable human interface.

The software has several different types of procedures it must take care of while operating the camera. It must set various parameters in the SBRC interface electronics such as the detector bias voltage, gate voltage, readout rate, and type of readout. In addition, the software must control a variety of logic and strobe bits on the digital buffer boards designed by Ev Erwin. Setting the SBRC parameters is a relatively simple task. The computer communicates with the SBRC electronics via two busses - one with 16 bits, one with 4 bits - and two strobe signals. To set the bias and gate voltages, a twelve bit number representing the desired voltage is placed on the lower twelve bits of the 16 bit buss; a three bit op-code indicating which voltage is to be set is placed on the highest 3 bits of the 16 bit buss. The remaining bit is a spare. After this data is placed on the buss, a strobe signal is sent to the SBRC electronics which commands them to load the appropriate value. The readout rate is set in a similar manner, along with several other parameters which are no longer used (the SBRC analog signal processing electronics gain and a bit controlling whether the address clocking is generated internally or externally): the "parameter" op-code is loaded into the top three bits, while a three bit number representing the readout rate is loaded into the bottom three bits; this is then strobed.

The 4 bit buss controls the type of readout the SBRC electronics thinks it is doing. Because ProtoCAM no longer uses the SBRC analog signal processing electronics, the setting of this buss it not significant beyond the fact that two CTC pulses per pixel must be generated. To facilitate this, all four bits of this buss are set high. These values are strobed into the SBRC electronics whenever the buffer boards generate an RFD signal.

This will be covered in detail below. Because all of the mentioned parameters change infrequently, they are typically loaded with their default values when the program is initialized; only the gate voltage is commonly adjusted after startup, and even then it is generally changed only at the beginning of the night.

The control of the logic on the buffer boards is more intricate and is quite active during every readout. Perhaps the simplest way to describe it is through the use of pseudocode to illustrate the flow of logic. Pseudocode representing a full staring integration (valid on September 25, 1991) is presented below. It represents one of the simplest possible ProtoCAM observations: *n* on-chip integrations, but no cycles of any kind. Notes indicated by superscripts follow the code. Discreet procedure names are italicized to make them distinct; bit names are indicated by bold type.

go_stare_mode {

    go_start_integration {

        set timer variables

            time_left contains number of seconds or milliseconds

            time_flag indicates whether time_left unit is seconds or milliseconds

        initialize address frame pointer (not necessary)

        do_frames {

            zap array if enabled[1]

            initialize buffer board math registers

            set control registers for startup:

c1: lo - **AUTO_LOAD_ENABLE_LOW, GRAB_MODE_LOW,**

FRAME_COUNTER_ENABLE, MEMORY_LOAD_ENABLE,

ONE_SHOT_ENABLE, FRAME_COUNT_ENABLE

hi - **NO_AUTO_STOP**

c2: lo - **START_FRAME, CLEAR_FINISHED_FRAME_F_F_LOW,**

SET_FIRST_FRAME_F_F_LOW, CLEAR_FIRST_FRAME_F_F,

TIMER_GATE_ENABLE

inttime0 {

load timer 0 with ms cts (1000) or s cts (50000)

load timer 1 with number of timer 0 units to count for the complete integration

load timer 2 with the number of coadds

}

set address counter to frame 0[2]

start purge (continuous) reads (**START_FRAME** high)[3]

check if SBRC alive (must wait [readout rate]/2 seconds for SBRC to sync)[4]

release **CLEAR_FINISHED_FRAME_F_F_LOW** in order to count purges[5]

count n purges

during last purge, turn off **START_FRAME**, wait for purge to end

clear **CLEAR_FINISHED_FRAME_F_F_LOW**

reset address frame to 0 in case it moved

reset SBRC electronics

can put an indefinite pause at this point

set **SET_FIRST_FRAME_F_F_LOW** high

set **MEMORY_LOAD_ENABLE** high

set **TIMER_GATE_ENABLE** high

toggle START_FRAME high, making sure pulse width is wide enough, this is the pedestal readout[6]

wait until readout finishes

if more than 1 coadd, correct timer 1 and set to address frame 1[7]

prepare buffer boards to read first integration:

set lo - AUTO_LOAD_ENABLE_LOW, NO_AUTO_STOP

hi - FRAME_COUNTER_ENABLE, FRAME_COUNT_ENABLE, MEMORY_LOAD_ENABLE

enable ONE_SHOT_ENABLE (set high)

set COMMAND_LOAD_ADCNTR_LOW high

toggle CLEAR_FINISHED_FRAME_F_F_LOW, SET_FIRST_FRAME_F_F_LOW low

if more than one coadd set address frame to 1, else 2

}

}

go_timer_wait {

chk_frame {

wait for integration to finish, reporting status

toggle CLEAR_FINISHED_FRAME_F_F_LOW low

repeat until coadds-1 are finished

tog CLEAR_FINISHED_FRAME_F_F_LOW and SET_FIRST_FRAME_F_F_LOW low[8]

set to address frame 2

wait until integration finished

run grab_off (gets run twice - redundant)

}

grab_off {

disable memory area so data will not be overwritten, turn off timed readouts:

```
                    set AUTO_LOAD_ENB_LOW and GRAB_MODE_LOW high
                    set ONE_SHOT_ENABLE and MEMORY_LOAD_ENABLE low
                put START_FRAME high to start continuous readout
            }
        }
        go_read_data {
            write FITS header information
                (TIME_OBS appears to be time at end of integration)
                (FITS keywords: SIMPLE, BITPIX, NAXIS, NAXIS1, NAXIS2, ORIGIN,
                TELESCOP, INSTRUME, OBSERVER, DATE_OBS, TIME_OBS, ITIME,
                CO_ADDS, OBS_CYC, POLAR, FILTER, WAVE_LEN, PLATE_SC, RA,
                DEC,EPOCH, AIRMASS, OBJECT, COMMENT, DATAMAX, DATAMIN,
                VGATE,DIVISOR (?), ASEC_PIX (?), END)
            read signal data from FRAME_ADDRESS_02
            add signal data and subtract pedestal data from FRAME_ADDRESS_01
            subtract pedestal data from FRAME_ADDRESS_00
                full equation is s2-p1+s1-p0
            update stats
        }
        display frame and info
}
```

1) "Zapping" refers to toggling the gate voltage of the array between two levels: typically between -2.2 V (the nominal operating point) and -1.0 V. This procedure arose when it

was discovered that the engineering-grade array which was originally in ProtoCAM needed "rough" treatment to clear out residual charge left on the pixels when they were reset after an integration. In January 1991, it was discovered that this zapping was not required for normal operation of the science-grade array; indeed, it was determined that zapping was responsible for a "bowl-" or "dome-shaped" pattern seen in many (object-sky) images, particularly those taken through thermal wavelength filters. As of January 26, 1991, zapping is no longer done, although it can be reenabled through a password-protected engineering menu in the software.

2) Double-correlated-sampling images which are obtained without the use of the SBRC analog signal processing electronics are only possible by exploiting the extra memory placed on the buffer boards. When the array is read out, the pixels are read sequentially and stored in the buffer board memory automatically in descending order. Since the starting memory address can be changed, different pieces of the integration can be stored in different areas of the memory; these can be processed later by the CPU in order to obtain the desired correlated frame. This procedure was described in greater detail earlier. For now, suffice it say that the pedestal part of the integration is stored in memory area 0, the final signal level is stored in memory area 2, and the intermediate coadd information (if any) is stored in area 1.

3) "Purging" refers to reading out the array a few times before the official beginning of the integration in order to remove small amounts of residual charge. Testing shows that

two are typically required, more than this (up to 10) have a small but generally negligible effect. Also, whenever START_FRAME is high, RFD is forced high. A jumper on the SBRC boards is set so that the electronics continuously read out as long as RFD is held high.

4) The SBRC electronics are synchronously controlled. Because the signal must be active on one of the SBRC's clock edges, it must be active at least this length of time to ensure that the SBRC electronics will initiate the readout.

5) The "finished frame flip flop" is the device the computer actively reads to determine if a readout is finished. The ability to manipulate the state of this flip flop, as well as the "first frame flip flop", is central to the ability to do correlated reads as well as to synchronize the integrations with the chopping secondary mirror.

6) While this readout is similar to the purge readouts, it is not considered a purge since the pedestal information contained in this frame will be used for the final image. The signal information will be discarded.

7) The hardware timers used on the buffer boards have a "bug" in that the data loaded into the counters does not become valid until the next clock pulse. The end result is that the first on-chip integration will be too long by one timer 0 unit (either 1 msec or 50 msec) for the first on-chip integration only, as the data would already be valid for

subsequent integrations. Thus the counter must have n-1 units loaded in it before the first integration, but then have n units loaded *during* the first integration. This trick has been shown to be accurate by examining the resultant RFD pulses on an oscilloscope; the worst integration length error is less than 100 microseconds (the resolution of the scope while being able to display two RFD pulses 20 milliseconds apart).

8) The final signal readout is treated as a first frame because it is stored in frame address 2, separate from the other coadd reads (if any).

Chapter 3: ProtoCAM - Camera Characterization

3.1) Introduction and Definitions

In Chapter 2, the basic operation of various components of ProtoCAM was discussed from a "theory of operation" point of view. In this chapter, the performance of the camera as a whole will be analyzed. Particular attention will be paid to the camera's photometric performance; its optical and spectrographic performances are important and will be touched on; however, my personal responsibilities have mostly dealt with its photometric capabilities.

A few definitions will be helpful before proceeding further. First is the use of the term "analog to digital unit" (ADU) rather than the more general "data number" (DN) for our basic unit of light intensity. ADU describes more accurately what the numbers recorded by the computer really are, so I use it throughout. A "readout" is the physical act of reading the intensity data on the array, whether or not the array has been integrating for any length of time. A "destructive" read is one in which each pixel is reset after being read; a "non-destructive" read is one where the pixel is only read - the pixel can be read again at a later time, yielding more information on the current integration (this mode in its simplest form is not used in ProtoCAM - the pedestal read described in Chapter 2 is related since there is no reset between the pedestal data and the subsequent signal data, but this does not fit the usual definition of "non-destructive" since the pixel

is reset at some time during each readout). "Integration" shall always refer to a single exposure of the array to light, from the time it is reset until it is destructively read out. "Coadd" refers to the number of integrations that are added together on the buffer boards - individual coadds are not saved, only their sum. A "cycle" is one complete coadd set (or pair of sets if the telescope has been switched or chopped to a secondary beam after the first set) which is read into the computer and is available for further processing, usually the coaddition of more cycles. The final processed set is an "image" or an "observation". As an example, if an observation is five beamswitched cycles of ten coadds, each with a one second integration length, the telescope is moved to beam A, ten one second integrations are performed, the telescope is moved to beam B, ten one second integrations are performed, the telescope is returned to beam A, ten integrations are performed, etc. until five pairs are completed. A common variation of this alternating pattern which reduces the amount of overhead (and is currently standard practice with ProtoCAM) is to switch only after odd numbered coadd sets, resulting in an ABBAABBAAB pattern for the sequence described above. "Beamswitching" refers to moving the whole telescope a small distance to obtain a blank sky image to use for background subtraction; "chopping" is tilting only the secondary mirror so that a blank sky may be obtained.

3.2) ELECTRONS/ADU

A number of great importance in ultimately determining the ability of the camera to turn incoming photons into readable data is the electron-to-ADU conversion ratio. This ratio indicates how many *detected* photons (electron-hole pair generated in the photodiode) are contained in each ADU. Theoretically, if the junction capacitance of each photodiode is approximately 0.4 pF, each detected electron would add q/C or 0.4 μV to the signal. Since the ratio of the voltage on the detector to the voltage measured by the A/D converter is the gain of the array's output mosfets (0.8) times the pre-amp gain (37.6) or 30, each electron will generate approximately 12 μV at the A/D. Since one ADU is 306 μV at the A/D input, each electron generates 0.04 ADU, or, in the more usual form, there should be approximately 25 electrons per ADU.

This ratio can be measured by a rather easy experiment, although it is often difficult to get reliable results. Let us assume a linear device which integrates a constant current I for an integration length t. The number of integrated electrons is thus $e_{signal} = It/q$. The noise in such a current is determined by the arrival times of the electrons, which is a Poisson process; thus the noise is given by $e_{noise} = \sqrt{(It/q)}$. Now let $K = e^-/ADU$. Substituting this into both equations and squaring the noise equation, we find that $K = ADU_{signal} / (ADU_{noise})^2$. Thus the slope of the line relating the signal contained in a frame with the noise squared of that frame will yield the electron to ADU ratio directly.

One wrinkle in this scheme is, of course, that the array is not a linear integrator. More about this non-linearity will be discussed later; for purposes of this experiment, correcting the data with an appropriate linearization algorithm should restore the statistics required to give a reasonable estimate of the e^-/ADU ratio. I have done this and the results are presented in Figure 3.1.

3.3) Quantum Efficiency

With the electron/ADU ratio in hand, a typical quantum efficiency (QE) of the array can be obtained. Estimates of the QE of the total system (camera + telescope + sky) can be obtained by dividing the number of electrons integrated by the array (ADU × e^-/ADU) by the number of photons anticipated to be emitted by a standard star. The number of photons can be estimated by converting the standard star's magnitude to a flux, then multiplying that flux by the telescope aperture and filter bandwidth. The value of the array's QE can be obtained by estimating the sky transmission (derived from extinction coefficients), telescope transmission, and ProtoCAM's transfer optics' efficiency. Estimates of the system QE, array QE, and the values of associated sources of light absorption are given in Table 3.1. The mean QE (averaged over all filters) for the array is 26%.

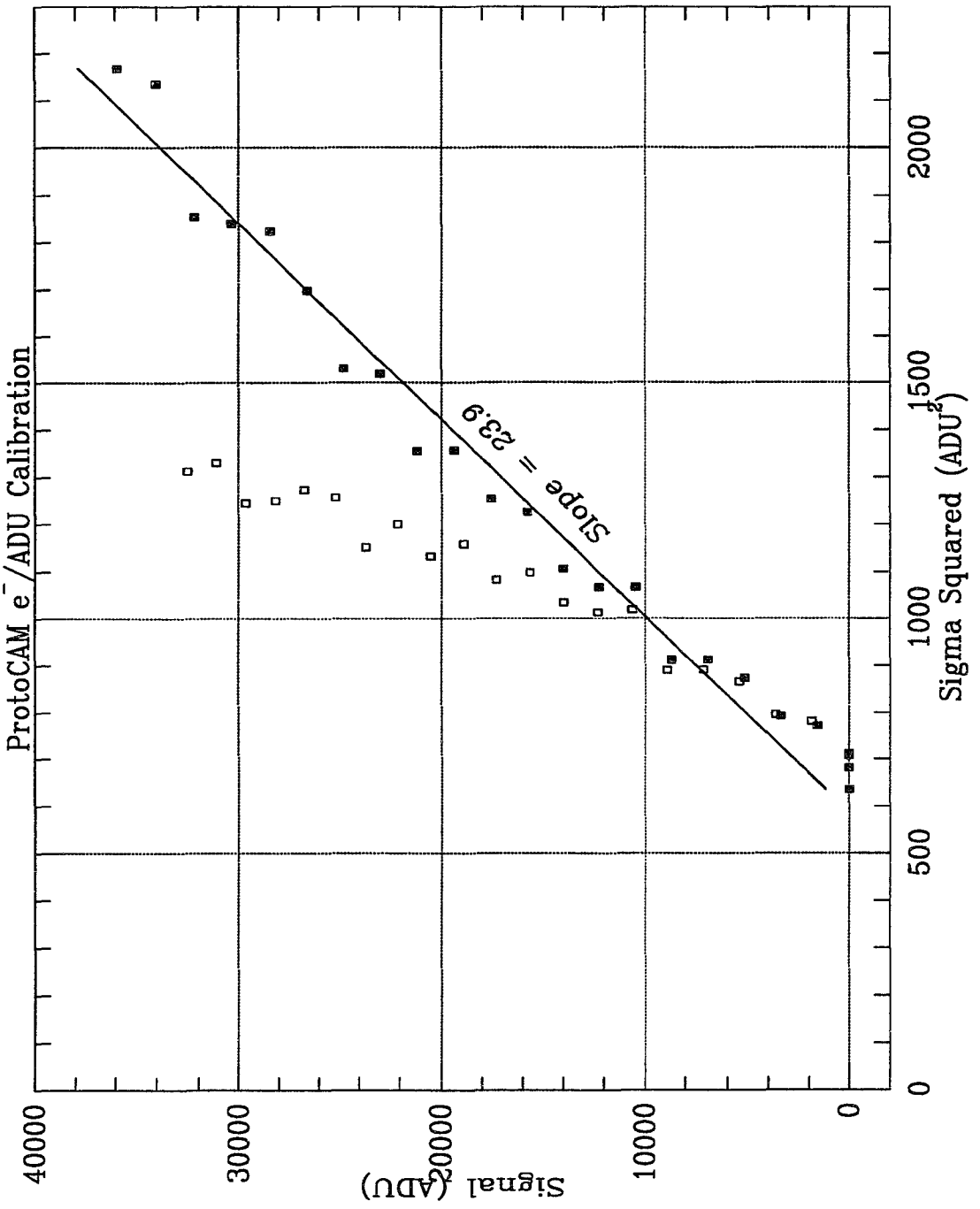

Figure 3.1: A plot of well depth vs. noise squared. The open points represent the raw data, the filled points are the data after they have been linearized.

Table 3.1: Quantum Efficiency Estimation

Filter	Predicted Phots/sec	Meas'd e^-/sec	Total System QE	Mean Filter Trans.	Other Trans.[+]	Estim'd Array QE
J	1.8×10^{10}	5.8×10^{9}	0.16	0.70	0.79	0.29
H	9.0×10^{9}	3.2×10^{9}	0.19	0.85	0.79	0.28
K	4.4×10^{9}	1.5×10^{9}	0.12	0.72	0.79	0.21
L	1.2×10^{9}	9.0×10^{8}	0.18	0.91	0.73	0.27
L'	9.8×10^{8}	7.8×10^{8}	0.19	0.88	0.73	0.29
M	5.2×10^{8}	3.2×10^{8}	0.13	0.89	0.69	0.22

[+] Assumes telescope = 90%, dewar optics = 90%, and typical atmospheric extinction values for 1 airmass from the IRTF Photometry Manual.

3.4) Read Noise

"Read noise" is a catch-all term referring to the quadratic sum of all noise sources associated with the array readout process. Typically this noise is dominated by the voltage noise generated in the output MOSFET amplifiers on the array. The usual method used to estimate the read noise in ProtoCAM is to start by assuming all pixels in the array have the same noise statistics with a normal distribution. If this is true, then the difference of two short integrations (negligible integrated photocurrent) will also have a normal distribution with a standard deviation which is $\sqrt{2}$ times that of an individual frame; using difference frames rather than an individual frame eliminates pattern noise due to changes in the bias level from pixel to pixel. The standard deviation (σ) of this difference frame

can be obtained either by fitting a gaussian distribution to its histogram or from an estimation of the full width at half maximum of its histogram: $FWHM = \sigma \sqrt{(16ln2)}$. A histogram of a typical difference frame with a gaussian fit and its parameters are shown in Figure 3.2. The FWHM of the curve is about 90 ADU which yields a standard deviation for an individual frame of 27 or about 650 e^-. It is not understood why the noise level is this great given that the manufacturer's specifications indicate that it should be in the 400 neighborhood. The excess noise appears to be generated by some external source; the array noise is generally a function of the rate at which the array is readout, but in ProtoCAM we see no change in the noise level when tested at rates of 16.2 ms/frame and 520 ms/frame. However, both the preamp and the A/Ds have been measured to be near their theoretical noise floors (for instance, a shorted input to the preamp yields less than 1 ADU noise at the output of the A/Ds), thus it is not immediately obvious where the noise originates.

3.5) Detector Thickness

The thickness and gradients in thickness of the array play an integral role in the QE of the array, and thus its flat field properties. The thickness of the array can be estimated by virtue of the fact that the array becomes transparent at long wavelengths. The front and back surfaces of the array now act like Fabry-Perot etalons and interference fringe patterns can be seen in the images. Examples of this are shown in Figure 3.3. The

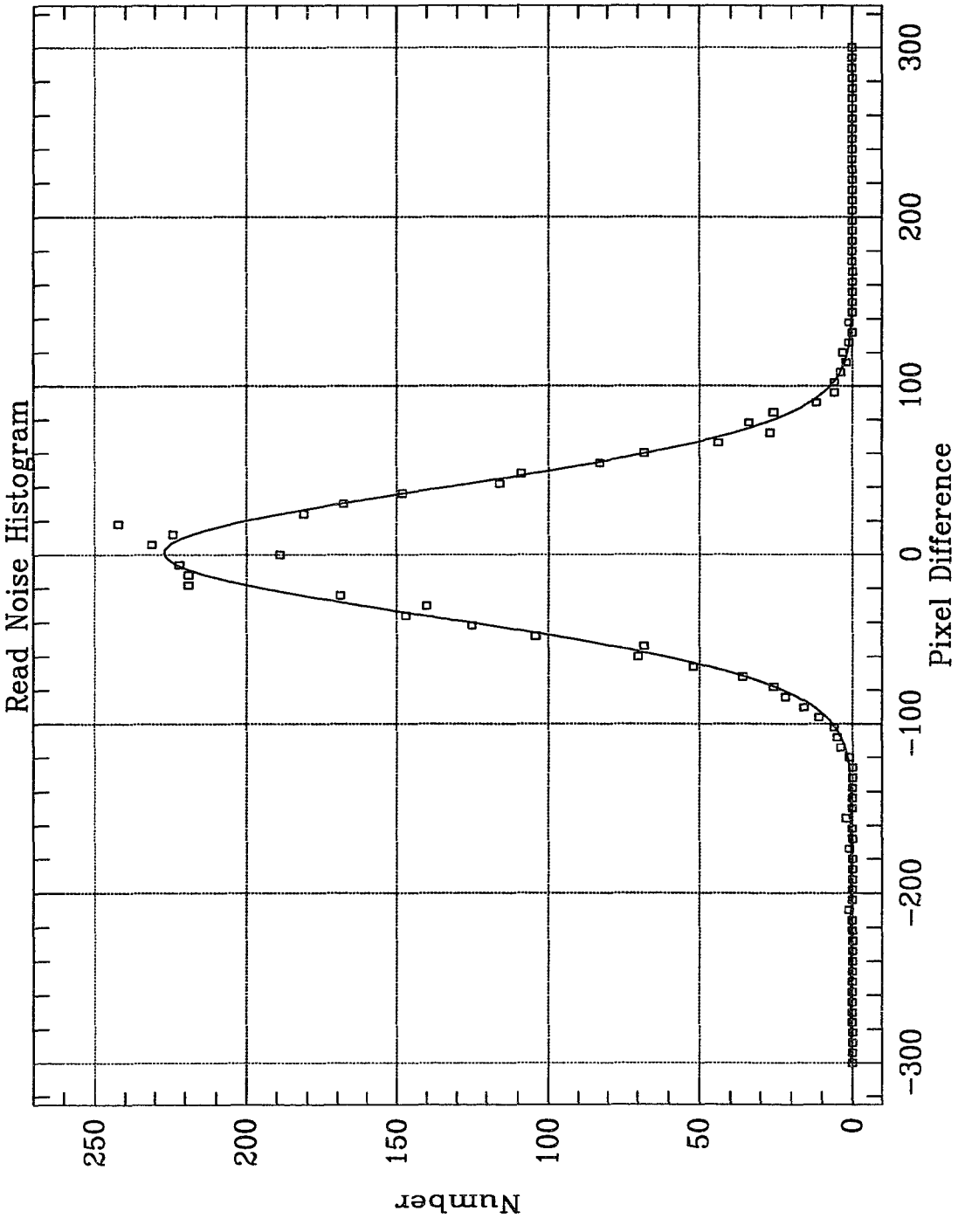

Figure 3.2: A histogram of the difference between two dark frames. The width of the fitted normal curve is proportional to the read noise.

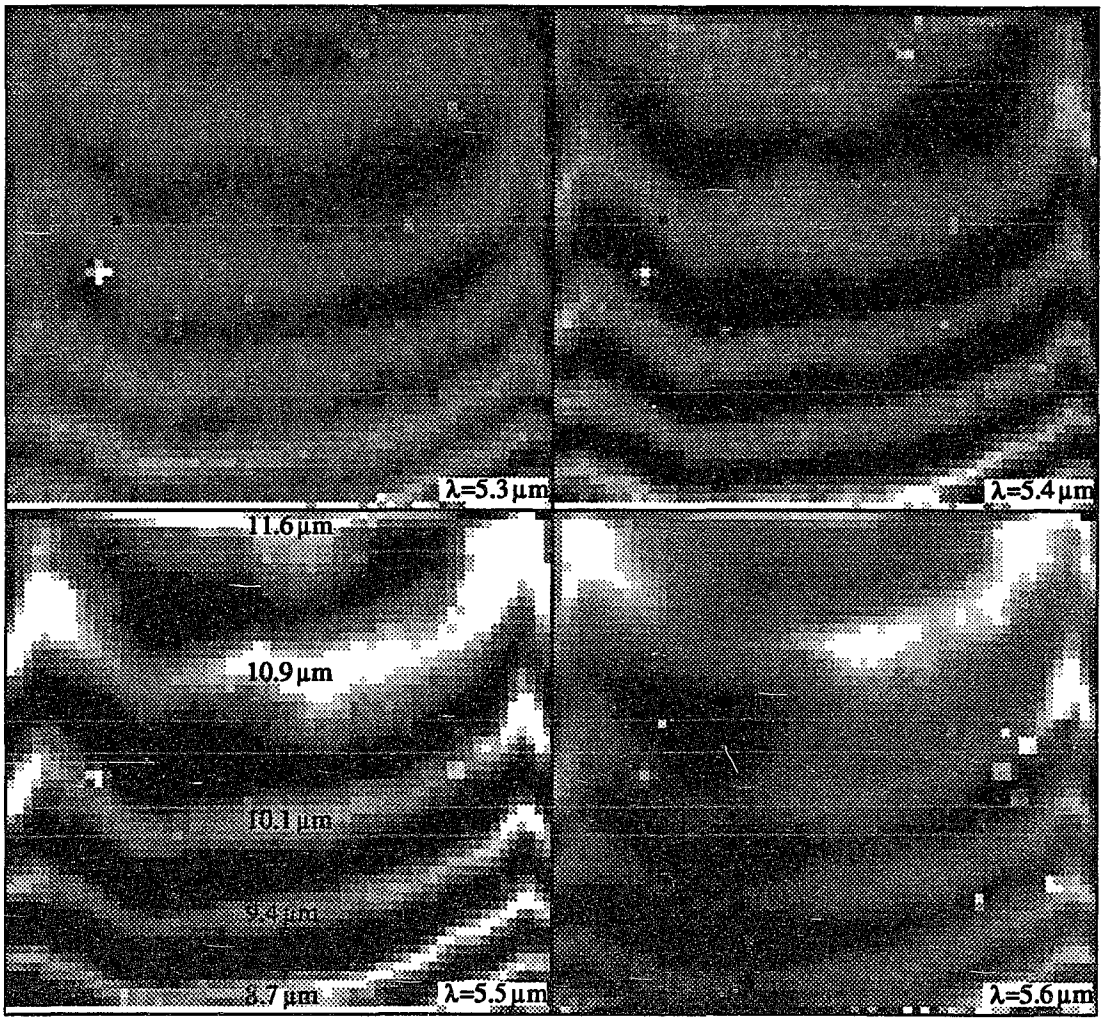

Figure 3.3: Four frames showing the fringe effects at long monochromatic wavelengths. The wavelength is indicated in the lower right corner. Thicknesses are indicated along the middle of the 5.5 μm image.

strongest effect is seen at 5.5 μm due to a good combination of transparency and quantum efficiency. The pattern amplitude decreases at 5.6 μm due a rapid fall-off of quantum efficiency at longer wavelengths, while the pattern amplitude diminishes at 5.3 μm and shorter because the opacity of the detector material rises sharply.

To estimate the array thickness, we obtained images of a flat plate using circular variable filters scanned from 4.3 to 5.65 μm in 0.05 μm increments. For constructive interference

$$t = \frac{m\lambda}{2n} \tag{3.1}$$

where t is the thickness, m is the interference order, λ is the wavelength, n is the index of refraction of the detector material (InSb = 3.8, Forrest *et al.*, 1989), and the factor of two arises because the light must travel two path lengths through the detector before interfering. We find m first by examining the images and finding two wavelengths which have overlapping maxima near the center of the array. For instance, maxima occur near row 16 (counted from the top) at both 5.25 and 5.6 μm. Since $(m+1)(\lambda-\Delta\lambda) = m\lambda$ under this condition, we find that the 5.6 μm light is interfering in the 15th order. To determine whether the interference order is increasing or decreasing from the top to the bottom of the array, we solve for m at the bottom of the array; since 5.15 and 5.6 μm overlap, the interference is 12th order, thus the array is thinner at the bottom edge than at the center.

We now apply equation 3.1 and summarize the results by labeling the intensity maxima on the 5.5 μm image presented in the lower left corner of Figure 3.3.

3.6) Timing Accuracy

A common concern when measuring the photometric properties of a system is the accuracy with which the integration length is measured. In ProtoCAM, the duration of an integration is defined as the time from the start of the last purge readout to the start of the signal readout. Because each readout is begun by an RFD (request for data) trigger, the accuracy of an integration length is as good as the RFD trigger timing. While this timing is accurate in principle to the microsecond level, I could measure it on a digital oscilloscope to a timing error of no more than 100 microseconds; thus the maximum possible integration length error is less than 0.5% for the shortest integration lengths (20 msec).

3.7) Temperature Effects

For imaging in wavelength regimes in which the sky background is small, reduction of the intrinsic dark current in the array is desired. Because dark current is highly temperature sensitive, generally this means reducing the operating temperature of the array to the lowest possible value. The coldest temperature normally achievable by

ProtoCAM's array is approximately 17.4 K, due to a balance of radiation loading and conduction by a copper strap between the array and the liquid helium bath. The camera was run at this temperature until it was discovered completely by accident (thanks to a temperature monitor short circuit) that the array's overall performance was improved by operating it at a slightly higher temperature.

Figure 3.4 shows a sequence of dark frames taken at 17.4, 19.6, 22.4, 25.7, 30.6, and 36.2 K. The readout rate is 16.2 ms and the camera was operated in the "new" mode. Immediately visible is the very strong odd/even effect in the 17.4 and 19.6 K frames, a

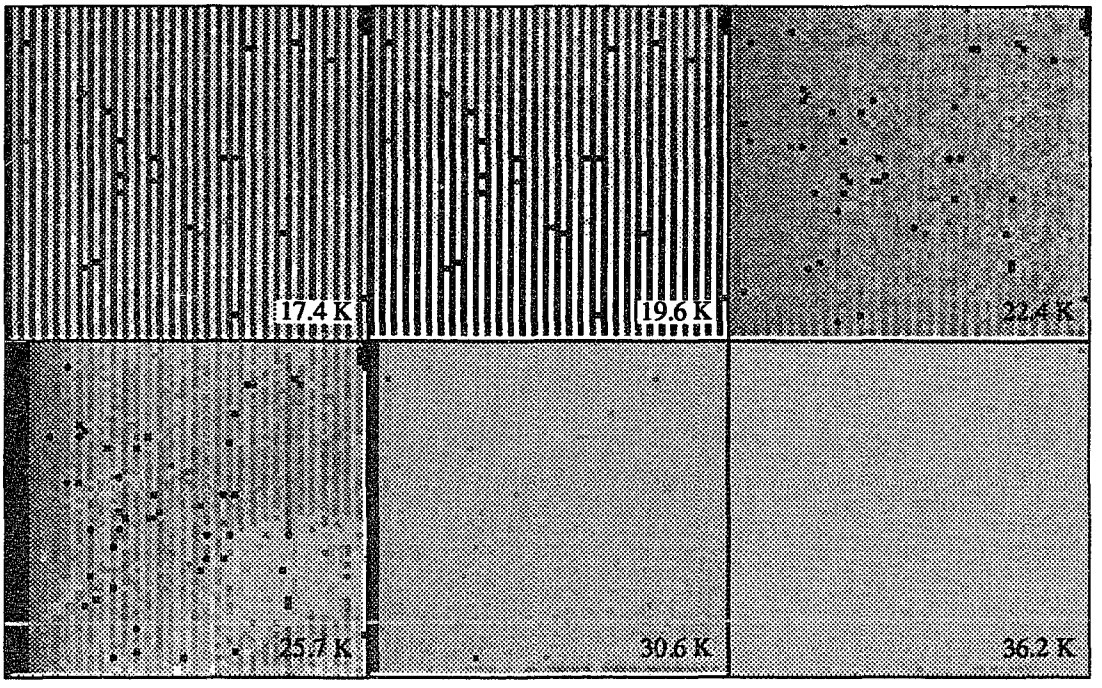

Figure 3.4: Appearance of a 1 s dark frame as a function of array temperature.

relatively uniform frame at 22.4 K, the beginnings of inoperability at 25.7 K, and the virtual lack of any features, including bad pixels, in the 30.6 and 36.2 K frames. The illuminated frames shown in Figure 3.5 confirm the breakdown in operation at temperatures above 25 K due to the freezing of charge carriers in the array multiplexer. The breakdown has noticeably begun at 25.7 K, and by 30 K, the array is almost completely insensitive to light. This is very puzzling because many other groups (UKIRT, for example) run their chip at ~35 K, where ProtoCAM is completely inoperable. This discrepancy has not yet been resolved.

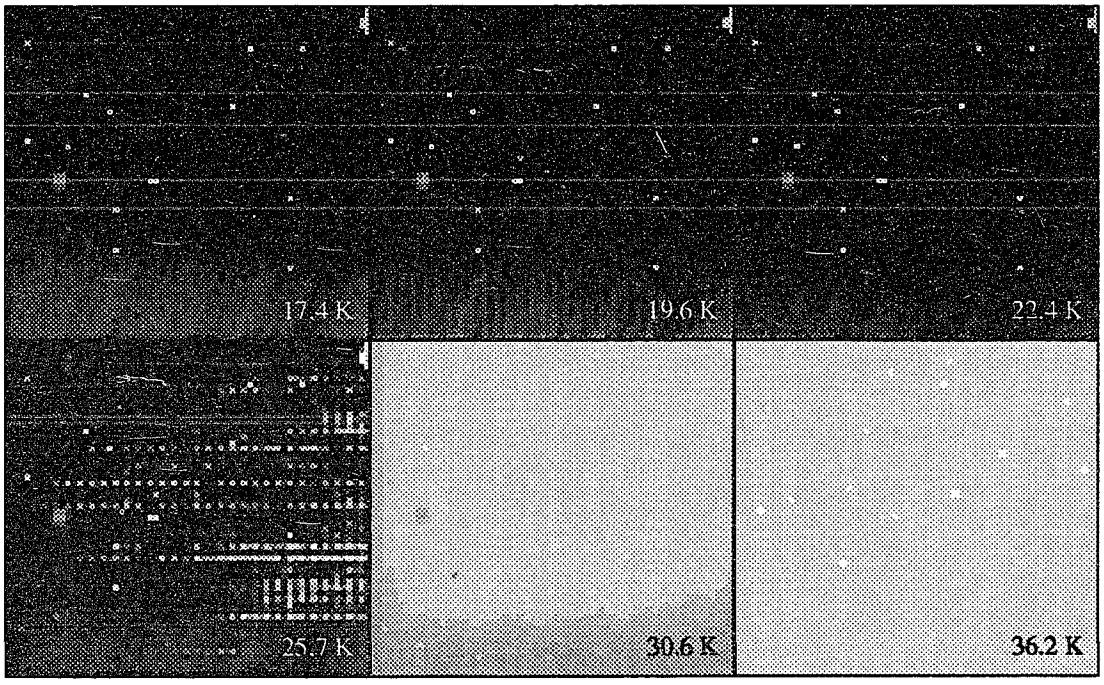

Figure 3.5: Appearance of illuminated images as a function of array temperature.

At temperatures below 20 K, the dominant effect in the raw frames is the odd/even pattern. However, this pattern subtracts out very well, but not perfectly (problems are much more visible in real object minus sky frames), as shown by the difference frames (illuminated minus dark) shown in Figure 3.6 (the spot near the middle of the left side of the array is due to a piece of dust on the array cover glass). The odd/even pattern seems to be due to some time dependent characteristic of reading out the array. The dark frames in Figure 3.4 were 16.2 ms readout rates; Figure 3.7 shows the dark frames at various readout rates at an array temperature of 17.4 K, and it is apparent that whatever produces the odd/even effect, it equilibrates with a time constant of ~0.3 s. Thus the fast

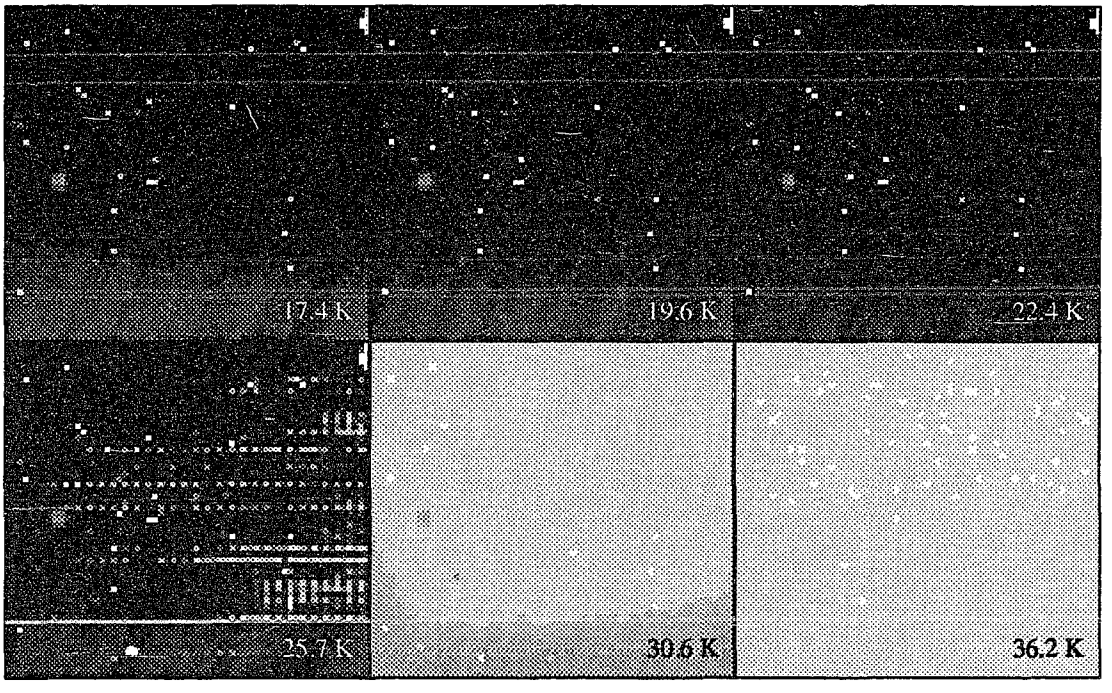

Figure 3.6: Appearance of illuminated – dark frames as a function of array temperature.

readout rates seem to have a constant odd/even mismatch, because they are so much shorter than the equilibration time, while the longer readout show a decreasing odd/even pattern from the bottom to the top of the array (the array is read out starting at the bottom). It's possible that this is some sort of freeze-out effect in the multiplexer, but this has not been investigated further.

Because it lies in a valley between the heavy odd/even effects and complete inoperability, the operating temperature of 22.4 K has been chosen. Linearity and bad pixel problems are no worse than at the cooler temperatures, although a slight adjustment in optimum gate voltage is necessary, and the increased liquid helium boil-off rate was not a major penalty; thus, it has been the standard operating temperature since Jan. 1991.

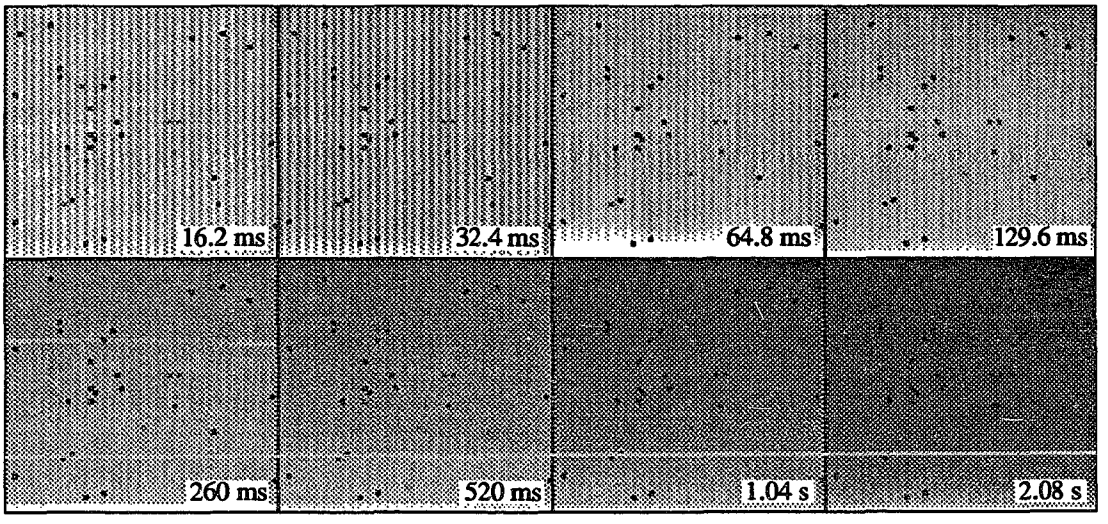

Figure 3.7: Appearance of a 3 second dark frame as a function of the readout rate.

3.8) LINEARITY

The following figures demonstrate various properties of the ProtoCAM linearity curve as measured at various times from Dec. 1989 until Aug. 1991. Five properties become immediately apparent: Linearity is not a function of instantaneous flux, temperature (for ΔT's on the order of a few degrees), V_{gate} (for ΔV's of order 0.2 volts), or the number of coadds, but the linearity does vary in some unknown way with time. This may be an electronics problem. An additional property learned from these measurements is that the linearity properties vary smoothly across the array; that is, local averaging may be used to improve the noise statistics without a significant loss of information when computing calibration frames.

Figure 3.8 is a plot of the linearity over the period December, 1989 to January 1991. The left column shows all "old mode" data (uncorrelated signal minus reset) while the right column is "new mode" (correlated signal minus reset pedestal). Two things are apparent: The slope of the flat portion in the old mode changes and the saturation level in both modes changes. Such changes are possible if the bias voltage applied to the detectors is not constant. An alternative explanation is that perhaps the "zapping" has something to do with the slope changes; zapping is certainly responsible for the jagged appearance in some of the older linearity curves.

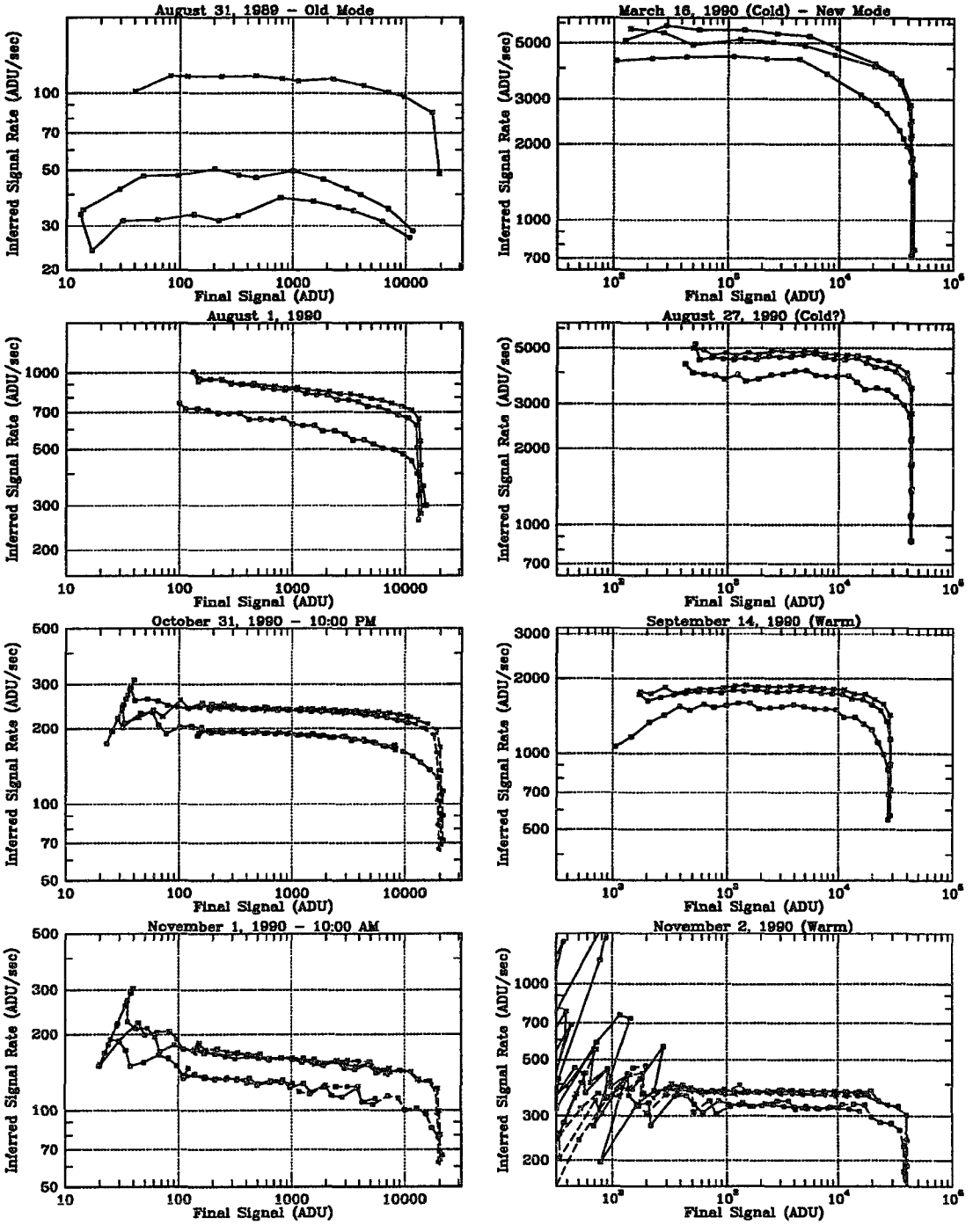

Figure 3.8: A collection of linearity curves over the period from December, 1989 to January,1991.

Figure 3.9 shows that the linearity is not a function of instantaneous flux. Data was taken using the same integration lengths at seven different CVF positions plus a dark position; dark (open squares), 2.1 (x's), 2.3 (x-like stars), 2.5 (filled squares), 2.7 (open diamonds), 2.9 (pluses), 3.1 (plus-like stars), and 3.3 μm (filled diamonds). This represents a ratio of approximately 1000 in flux. The fact that there is no significant scatter in the points above the read noise implies that the linearity curves are indeed the same.

The next plot (Figure 3.10) shows curves at different temperatures and gate voltages while operating the camera in the old mode. The unusually high scatter is due to a 60 Hz pattern noise that was picked up during these tests - the tests were performed on a bench in the instrument prep room. The negligible differences between curves imply that the linearity is at most a weak function of temperature and gate voltage in these regimes. It should be noted, however, that the sensitivity may be somewhat better at 22.4 K, given the observed ~20% increase in ADU rate.

Finally, Figure 3.11 shows the effects of changing the gate voltage and the number of coadds in the new mode (at 22.4 K). Again, the linearity is at best a weak function of the gate voltage and the number of coadds. The slight flux shift seen in the coadded data is not understood - it may be caused by a slight temperature change in the aluminum plate covering the window (this run was performed some non-negligible time after the gate voltage runs).

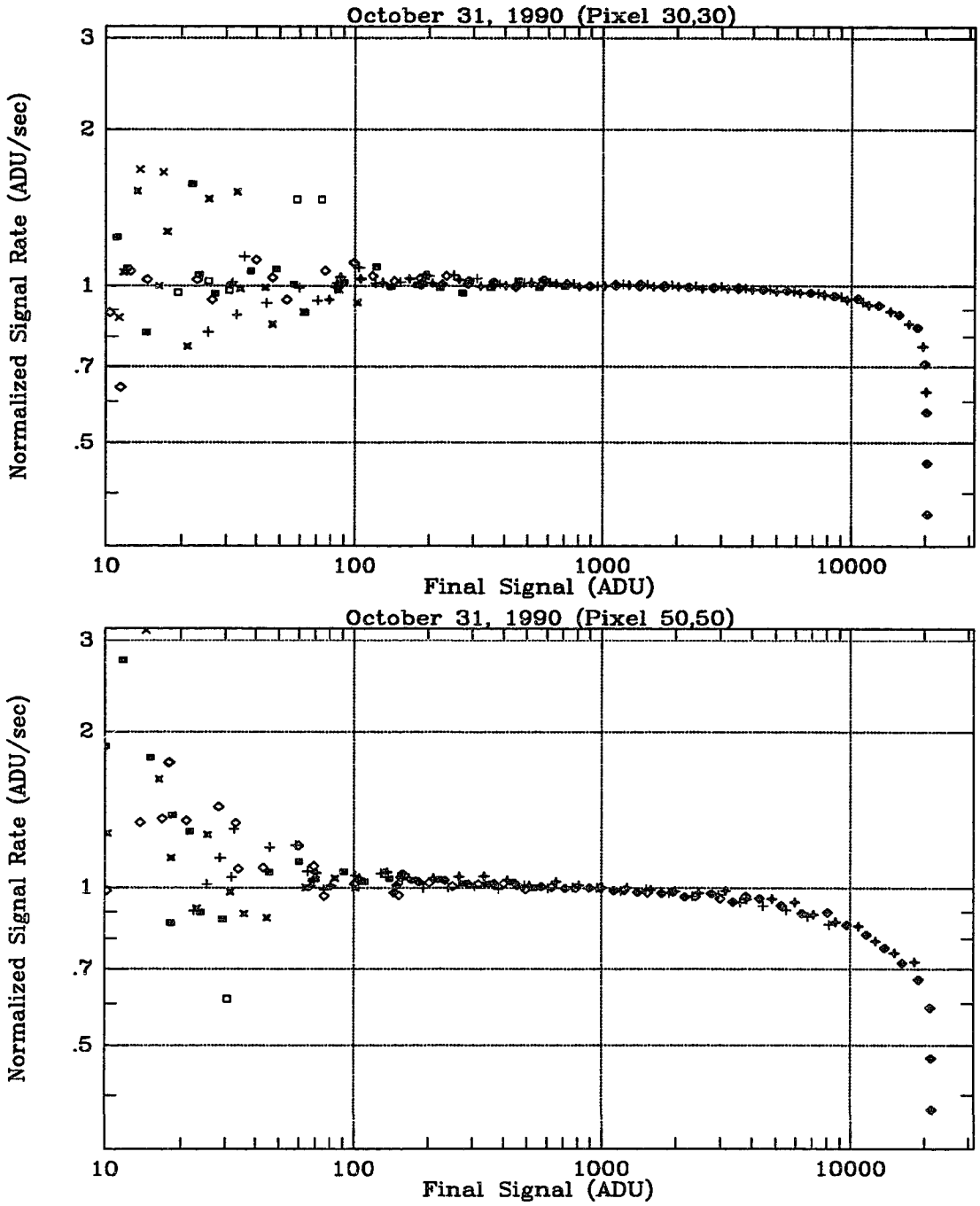

Figure 3.9: Normalized flux as a function of final well depth. If the linearity were dependent on the magnitude of the flux, the seven data sets plotted here would not be coincident.

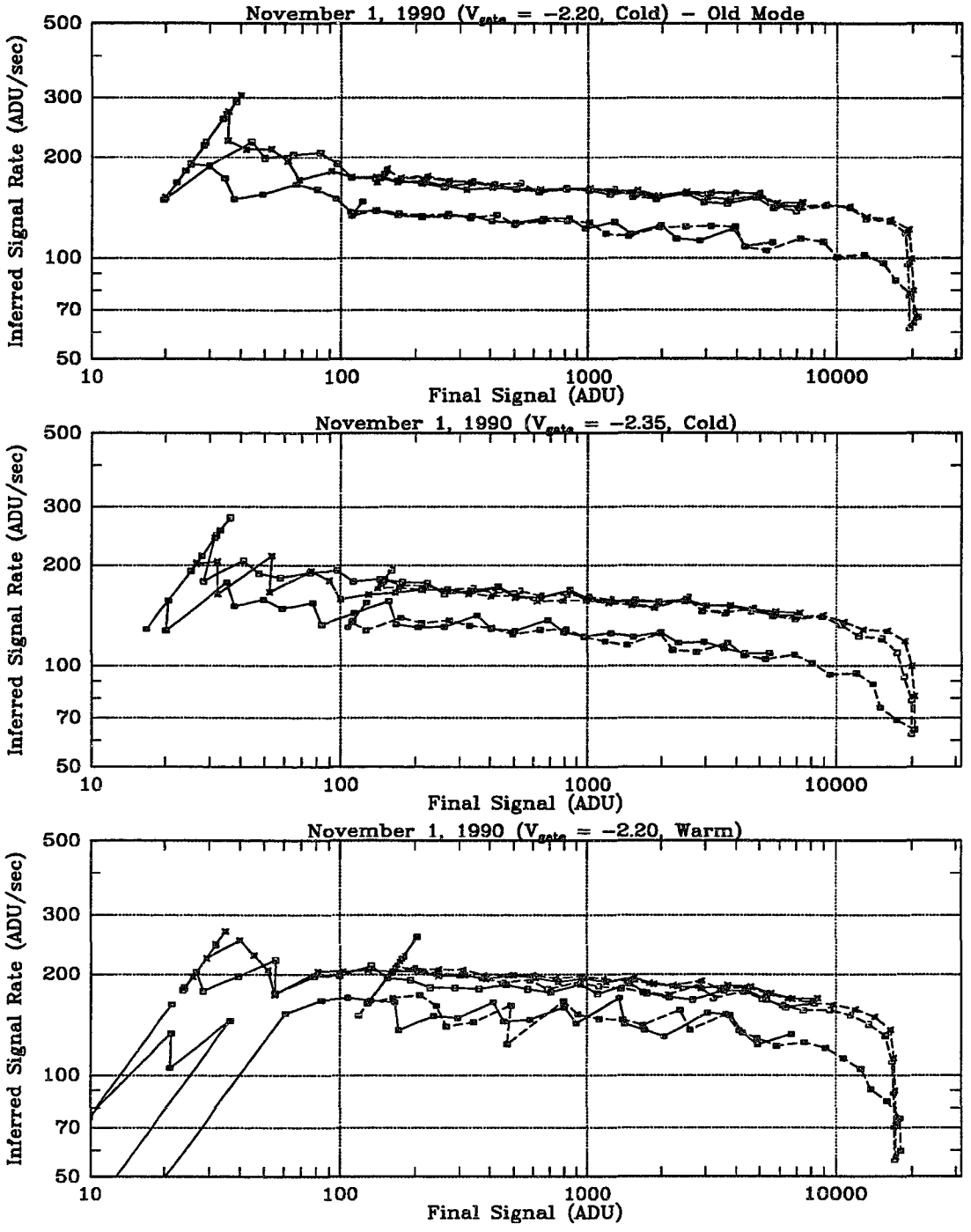

Figure 3.10: Linearity as a function of detector temperature (top frame) and V_{gate} (bottom) in the old mode.

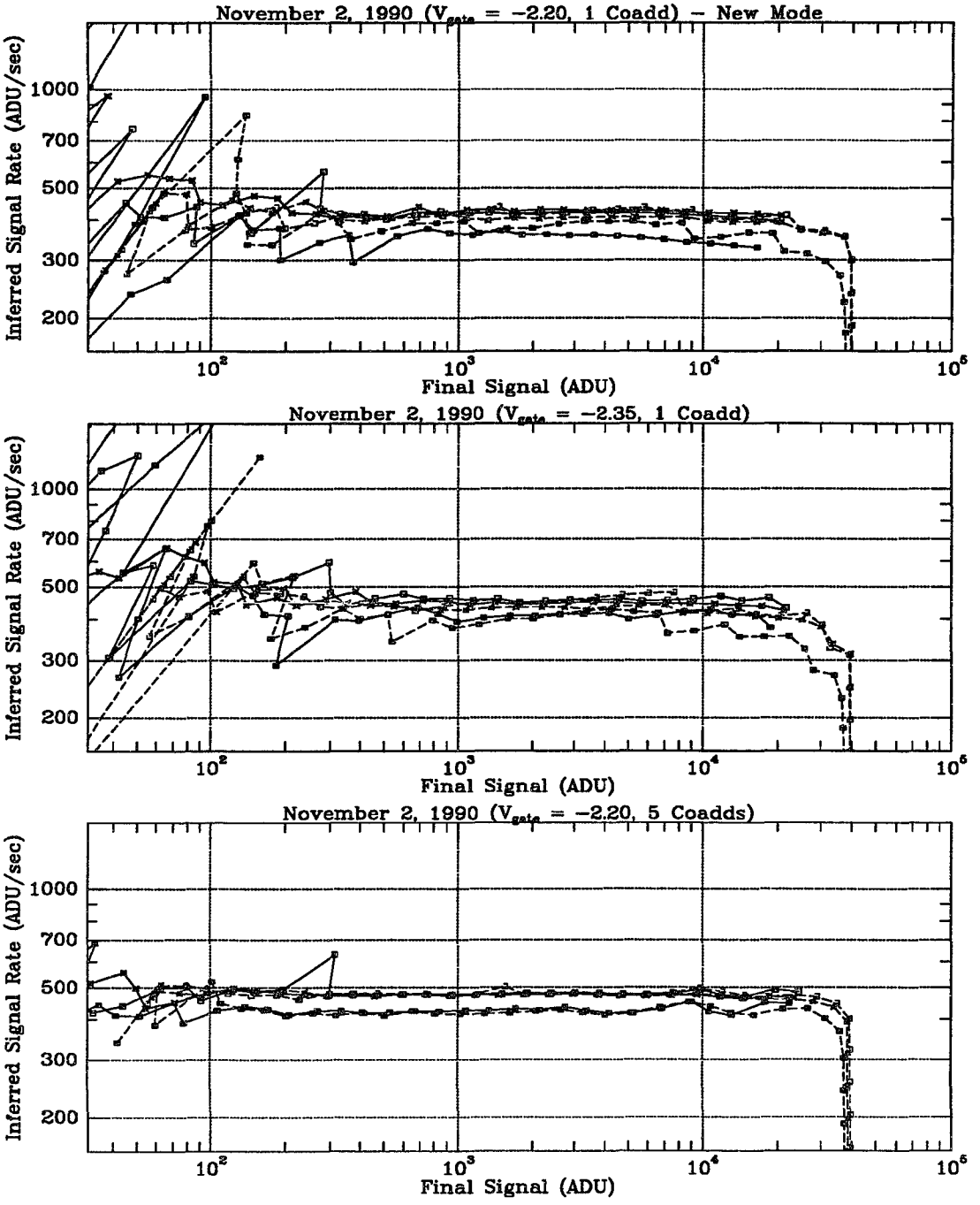

Figure 3.11: Linearity as a function of V_{gate} (top frame) and the number of coadds (bottom) in the new mode.

3.9) LINEARIZATION ALGORITHM

It was discovered purely by accident that the shape of the linearity curve is a very simple function over most of the signal range. In fact, the plot of the measured flux (the number of ADU on a pixel at the end of the integration divided by the integration length) versus the number of ADU squared is a straight line over most of the range. Figure 3.12 shows the curves for three widely spaced pixels, including one near the bottom, "bad" edge of the array. Pixels near the center of the array follow a straight line to 0.5% accuracy for over 90% of the total well depth. This is a pleasant property to have because it allows integrations to proceed well into the non-linear zone, thus allowing the greatest dynamic range without sacrificing photometric accuracy.

Because the linearity function is so simple, it is also simple to construct a computer algorithm to correct raw image frames for non-linearity effects. The correction procedure requires two steps: first, generate a set of coefficients from calibrations images which describe the linearity properties of each pixel, then apply these coefficients to the program images. I have written two small C programs to take care of the above steps, and these programs are now in wide use for correcting ProtoCAM data. The source code is given is Appendix A, but I will outline it here.

Lincoeffs is the routine used to generate the calibration coefficients. For input, it requires one or more bias frames (to give an accurate zero well-depth measure) and a

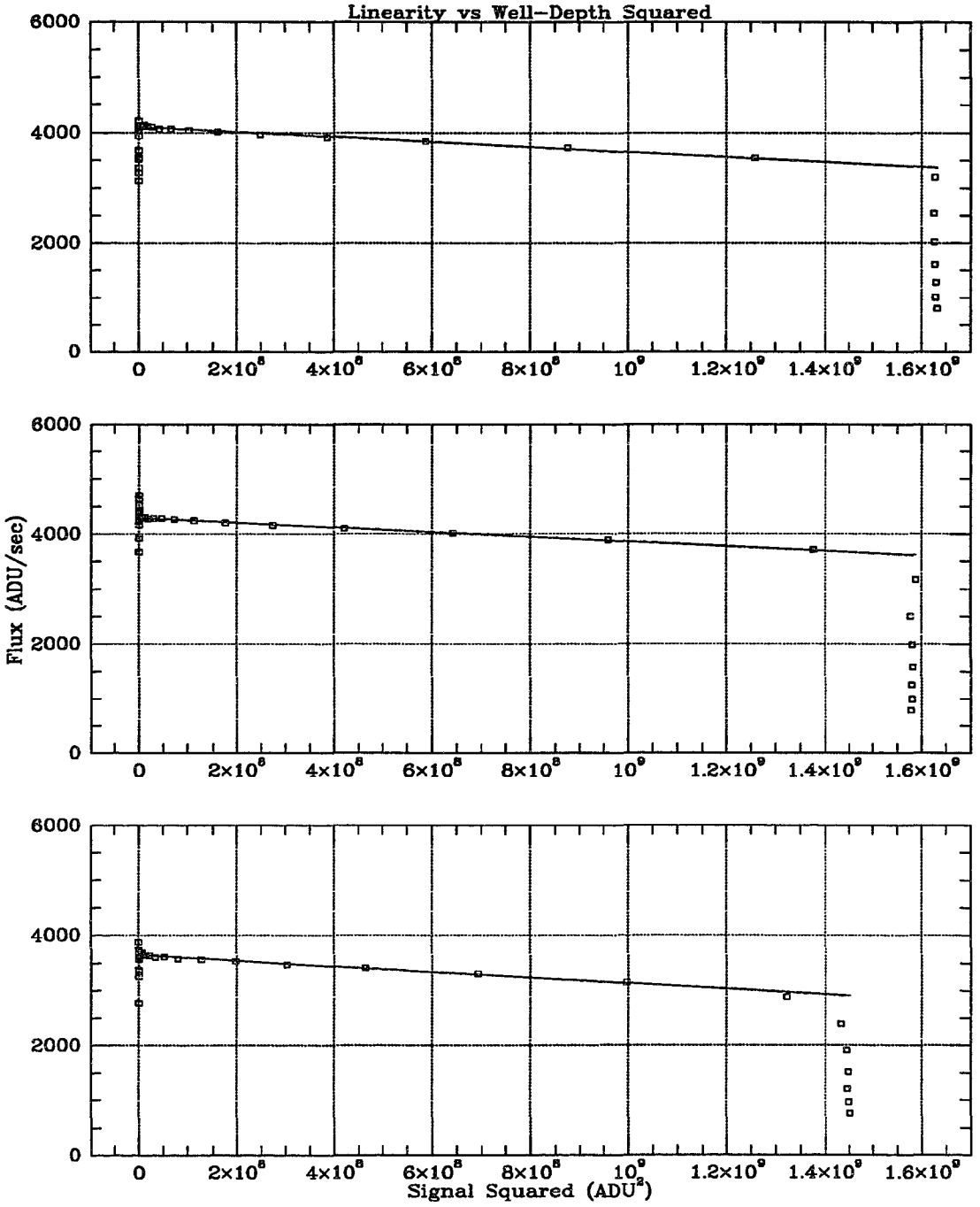

Figure 3.12: A plot of the derived flux (final counts divided by integration length) vs. the final counts squared.

series of frames of incrementally increasing illuminated well-depth. Traditionally, this is done by placing a flat object (paper-coated aluminum was the original choice) over the dewar entrance window, selecting a CVF wavelength near 3 μm, and varying the integration length to obtain the series. It is important to note that the image field the array sees does not need to be uniformly illuminated; it only needs to be constant. Each pixel is calibrated individually and the flux is effectively normalized during the calculations, thus it does not matter how bright or smooth the flux source is; the only requirements are that each pixel has a good range of well depths over the integration series and that the flux on each pixel is unvarying. For input, *lincoeffs* requires a single file with the following format: the first one or more lines is a comment which can be used to identify which data this file applies to, one blank line, one or more lines each with the name of a single bias frame (the entire path name of the file can be given: /gscr0/ressler/data/10nov000.img is a legal specification), one blank line, then the names of the illuminated calibration frames at one per line.

Lincoeffs parses this file, reads in the bias frames (it will issue a warning message if the indicated frame is longer than 1 s integration length), divides them by the number of coadds and cycles, then averages them, so that the result is a single, short integration length bias frame. Now the program reads in the calibration frames, again dividing by the number of coadds and cycles, subtracts the bias level, then checks to see if the resulting pixel level is between 2,000 (5% of full well - 40,000) and 32,000 ADU (80% full). Values below 2,000 are considered to be too contaminated by read noise to be of use,

while values above 32,000 are considered to be too close to saturation. Note that this check is done on a pixel-by-pixel basis, not frame-by-frame. Thus is a possible to have a given frame useful for some but not all pixels on the array. This is one of the reasons a uniform illumination source is not necessary.

As the images are read in, the flux is computed (ADU divided by integration length) as well as well depth squared; additionally, intermediate frames necessary for a linear least-squares fit are generated. After all data is read, a fit is performed for each pixel, and the slopes are written to an ASCII file to be used later to calibrate the program images. The intercept from the fit is thrown away as it is only a measure of the flux on the pixel during the calibration.

The second phase of the linearization process is covered by *linearize*, which uses an input file similar input to *lincoeffs*. The first one are more lines are comments, one blank line, one line with the name and path (if any) of the coefficient file, one blank line, one or more names and paths of bias frames, one blank line, and the names and paths of the images to be linearized. *Linearize* then reads in the coefficient file, followed by the bias frames (which are divided by the number of coadds and cycles). Next, the program images are read in, converted to double precision floating point, divided by the number of coadds and cycles, bias-subtracted, then passed into the actual linearization algorithm. Here the pixel value is squared and multiplied by the linearization coefficient; this yields a correction factor to be applied to the original pixel value; this value is the fraction by

which the measured value deviates from the expected value. The pixel value is divided by this correction factor, multiplied by the number of coadds and cycles, rounded to the nearest integer value, then written to the new image file. It should be noted that the output file has all the same characteristics as the input files (32 bit integers, same number of coadds and cycles, etc.), except that it has been bias-subtracted and linearized. This was done to hopefully avoid confusion and potential loss of precision during the various data format conversions.

Examples of the result of this process are shown in Figure 3.13, where the before and after results are shown for the same three pixels described earlier. The ability to linearize pixels even in the "bad" part of the array to better than 2% over much of the well-depth is particularly satisfying.

3.10) FLAT-FIELDS

The issue of what constitutes a flat field for ProtoCAM has not yet been adequately resolved. This issue arises from the fact that the response of various parts of the array to stars does not match the apparent response from things which supposedly illuminate the array uniformly, such as the sky or the dome. The array does have one property which can be exploited to minimize this effect, however. The flat fields are "locally smooth", meaning that the pixel-to-neighboring-pixel variations are very small.

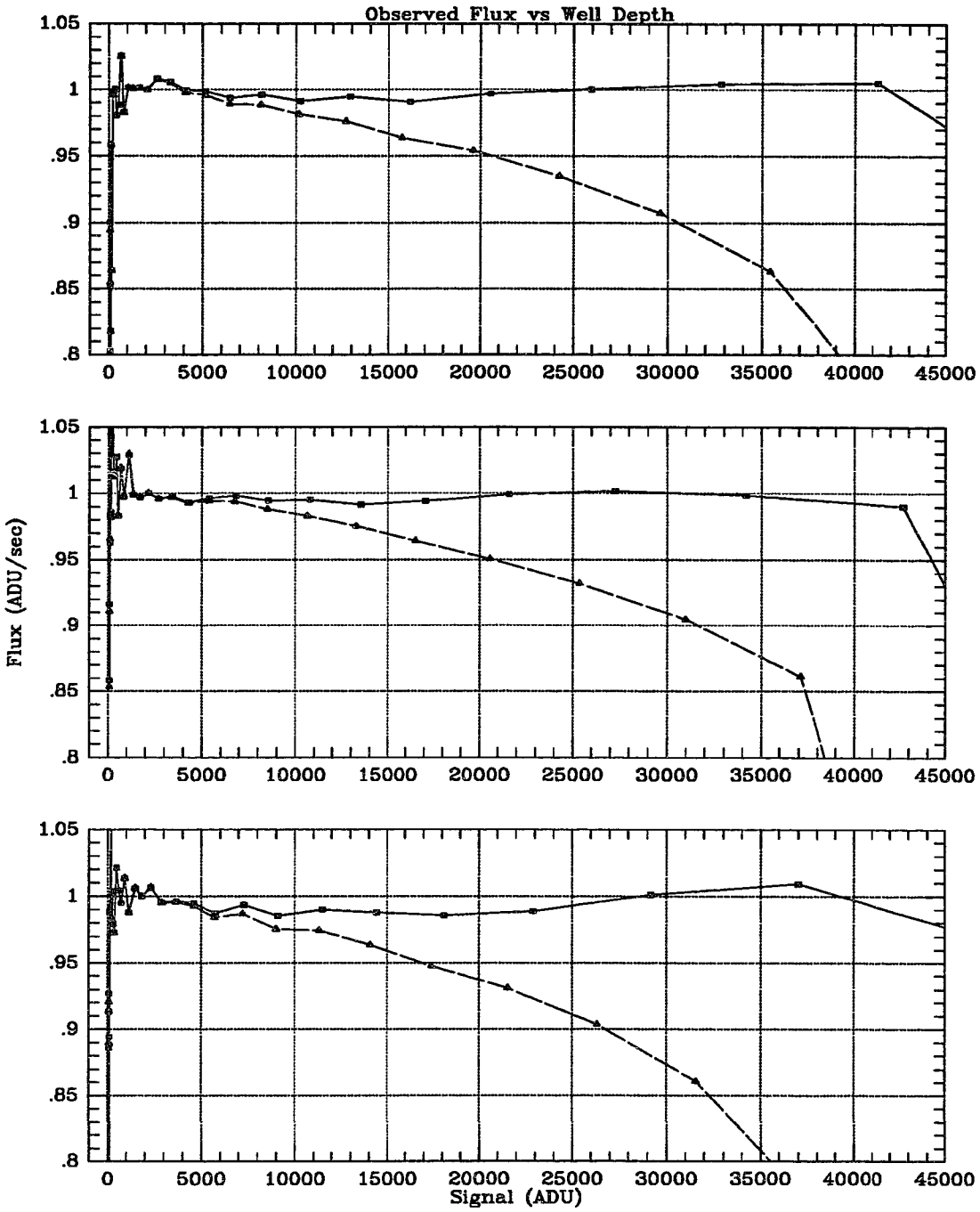

Figure 3.13: A plot showing the effectiveness of the linearity algorithm for the same pixels as in Figure 3.12. The raw data are indicated by the dashed lines, the linearized data by the solid lines.

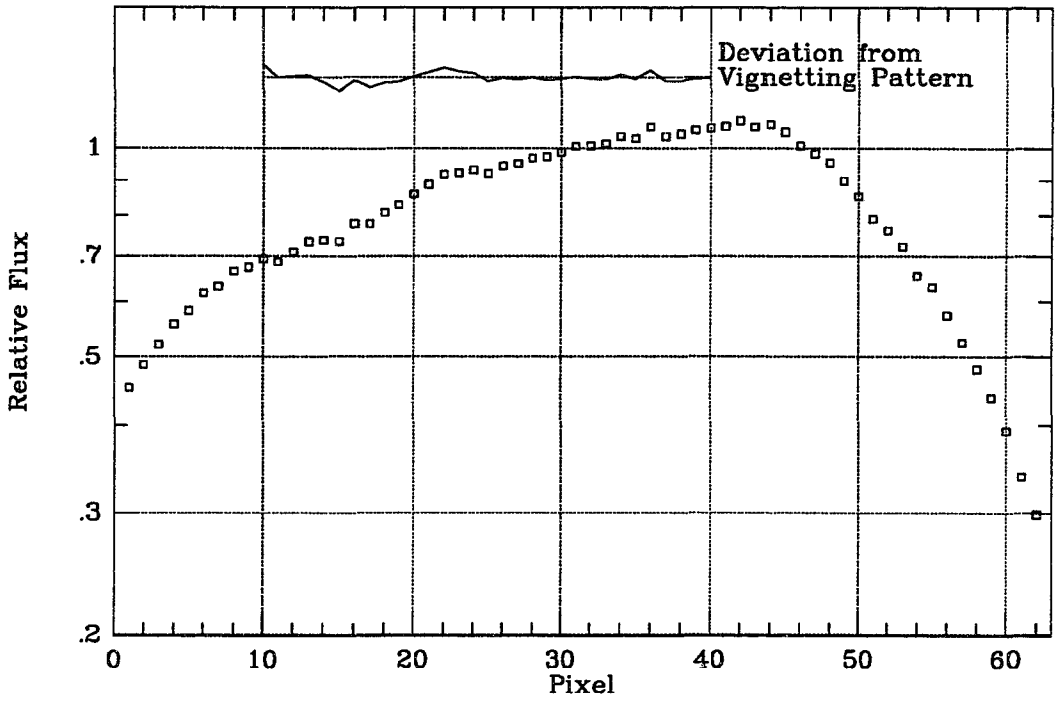

Figure 3.14: Line cut through a heavily vignetted flat field. The short line shows the deviation from the large scale pattern and has been shifted up for clarity.

Figure 3.14 shows a line cut from a uniformly illuminated frame when the 0.9 arcsec/pix temporary reimaging optics were in the dewar. The field is heavily vignetted, but we take advantage of this fact to argue that the observed gross structure is due primarily to the vignetting, while the small-scale structure is due to variations only in the photodiodes themselves. The observed deviation from the vignetting pattern is quite small - pixel-to-pixel sensitivity variations are only 2 – 3%. It is thus the case that if the object of interest (as long as it is relatively point-like) and the subsequent standard stars can be imaged on the same part of the array to a half dozen pixels or so, the photometry will be completely unaffected if flat-fielding is not done. Extended objects require more careful consideration and will be discussed below.

To examine the nature of the large scale structure of the flat fields, a standard star was observed in 16 or 25 positions around the array, roughly a 4 × 4 or 5 × 5 grid, but individual positions were displaced enough to avoid any obviously bad pixels. For comparison, the brightness of the flat frames was measured in a small aperture centered on each of the star positions. The K flat was produced by pointing the telescope at a uniformly illuminated portion of the dome, obtaining images with the domes lights on and off, then subtracting them. The L' flat was constructed by subtracting a sky frame from a dome frame. The results are presented in Table 3.2. Each entry represents the sensitivity variation normalized to position (3,3) converted to magnitudes.

Table 3.2: Flat-field Performance

K Star Scan				K Dome Flat (Lights on - lights off)				K Ratio			
-0.005	-0.004	-0.015	0.070	0.003	0.005	-0.058	-0.105	-0.008	-0.009	0.043	0.175
-0.041	-0.037	-0.020	0.037	0.037	0.014	-0.040	-0.096	-0.078	-0.052	0.021	0.132
-0.023	-0.003	0.000	0.021	0.029	0.102	0.000	-0.126	-0.051	-0.105	0.000	0.146
0.109	0.176	0.243	0.246	0.182	0.171	0.148	0.052	-0.073	0.004	0.095	0.194

L' Star Scan				L' Flat (Dome - sky)				L' Ratio			
-0.053	-0.113	-0.209	-0.172	0.022	0.019	-0.022	-0.017	-0.075	-0.132	-0.187	-0.155
-0.071	-0.131	-0.138	-0.220	0.012	-0.003	-0.087	-0.052	-0.083	-0.129	-0.050	-0.167
0.007	-0.044	0.000	-0.172	0.070	0.035	0.000	-0.071	-0.063	-0.078	0.000	-0.101
0.245	0.115	0.164	0.212	0.200	0.130	0.126	0.030	0.045	-0.015	0.037	0.181

In principle, the methods of obtaining flat fields mentioned above should be correct assuming a that there is a truly uniform illumination source and that the light follows an optical path similar to those of astronomical sources. At short wavelengths, where the dome lights will be significantly brighter than the telescope and dome thermal emission, subtracting an image of the dark dome from an illuminated dome will produce a good signal-to-noise image while simultaneously subtracting background thermal radiation which might enter the optical system. At longer wavelengths, the dome lights are not significant; by subtracting a sky image from a dome image, we exploit the fact that the sky has an emissivity of 0.1 – 0.2, while the dome has an emissivity of 1.0.

The cause of the failure of the flat fields to match the point source sensitivity pattern has not yet been adequately identified, but the most likely explanation is that the pupil plane may not be properly focussed on the cold stop. This would allow some photons from the sky and the mirror support structures to strike the array resulting in a complex, non-uniform illumination pattern.

3.11) Plate Scales

ProtoCAM was designed to take advantage of the excellent seeing and imaging capabilities of the IRTF. This led to the ability to vary the platescale in realtime, with a desired range of 0.15 to 0.4 arcsec/pix. The 0.15 end was chosen so that the images

would still be Nyquist-sampled on nights when the seeing allowed diffraction limited images at thermal wavelengths (e.g. the diffraction limit at L, 3.45 μm, is 0.29 arcsec). The 0.4 end was chosen to allow Nyquist-sampled imaging, but not grossly oversampled imaging, on nights of typical seeing on the order of 0.7 - 1.0 arcseconds.

The platescale was calibrated by measuring the separation of double stars. The platescale range at K was measured by observing γ Ari (separation 8.8 [?] arcsec) on Dec 23, 1989. The platescale was found to have an actual range of 0.14 to 0.35 arcsec, and the intermediate platescales were found to follow the equation $ps\ (arcsec) = 0.351 - 1.091\times10^{-3}\ (step) + 2.345\times10^{-6}\ (step)^2 - 2.143\times10^{-9}\ (step)^3$, where the step number is the stepper motor travel, ranging from 0 to 459.

Variations of the platescale at different broadband wavelengths at the large platescale end were investigated by observing γ Del on July 14-16, 1991. Such variations are most likely due to differences in the thickness of the filters involved, as there is no obvious trend in the shifts. The platescale as a function of CVF wavelength has not yet been measured. The separation of γ Del was extrapolated from two previous reports; 9.50 ± 0.05 arcsec (1984.7), and 9.45 ± 0.05 arcsec (1988.7). Assuming a linear extrapolation, I determined a separation of 9.41 ± 0.05 arcsec. The uncertainties in my measurements were estimated by assuming 0.1 pixel accuracy with the centroiding algorithm used to measure the separations; each reported separation is the sum of four individual measurements. The results are presented in Table 3.3.

Table 3.3: The platescale for each broadband filter

Filter	Separation (pixels) ± 0.05	Platescale (arcsec/pix) ± 0.002	Platescale relative to K ± 0.003
J	28.09	0.335	0.978
H	27.95	0.337	0.983
K	28.48	0.343	1.000
L	28.14	0.335	0.977
L'	26.47	0.356	1.038
M	26.52	0.355	1.037

3.12) PHOTOMETRIC ACCURACY

Having discussed the complications involved in determining the brightnesses of objects observed with ProtoCAM, it is now appropriate to ask, "So how reliable is the real photometry?" In Table 3.4, a summary of standard star measurements performed from Sep. 1, 1989 to Jan. 10, 1991, is presented. For each date, the standard stars observed are listed (these stars are all from the Elias "faint" standards list except for ξ^2 Cet, π^4 Ori, and 4 Lac, which are from the IRTF "bolo" standards list), as well as the maximum deviation in the computed zeroeth magnitude flux derived from each measurement. Maximum deviation was chosen over standard deviation because of the extremely small numbers of measurements for a given night, often no more than two.

Table 3.4: Summary of standard star photometry

Date[1]	Stars[2]	ΔJ[3]	ΔH	ΔK	ΔL	ΔL'	ΔM
09/01/89	161903 197406		0.18	0.18			
11/07/89	203856 40335	0.03	0.05	0.11	0.11		
11/08/89	1160 40335	0.003	0.06	0.05	0.014		
12/23/89	203856 40335			0.10			
03/21/90	40335 161903		0.08	0.08	0.19	0.18	0.22
08/02/90	147889[4]	0.005	0.05	0.06	0.03	0.009	
11/24/90	π^4 Ori 4 Lac	0.07	0.11	0.11	0.06	0.08	0.08
01/07/91	ξ^2 Cet 22686 40335	0.008 (0.002)[5]	0.03 (0.006)	0.01 (0.009)	0.15 (0.014)	0.13 (0.020)	0.21 (0.214)
01/09/91	ξ^2 Cet 22686 40335	0.11	0.07	0.04	0.14	0.20	0.12

Notes:
(1) Date is given in month/day/year format (UT dates).
(2) Standard stars are from the HD catalog unless otherwise named.
(3) Δmag is the absolute magnitude of the maximum deviation (as opposed to standard deviation) of the computed zeroeth magnitude fluxes derived from each standard.
(4) Δmags are from different airmass measurements of this one star.
(5) Δmags given in parentheses are those obtained if ξ^2 Cet data are ignored. The large discrepancy at M is due to the low S/N in the faint standard (22686 and 40335) frames.

One thing is immediately apparent from this table: the observer would be hard pressed to claim better than 5% accuracy in the photometry. In fact, 10% appears to be the norm, except perhaps at the shorter wavelengths. A case can be made that the cause of some of the deviation is because the standard star magnitudes are incorrect; perhaps they have varied since the original magnitudes were published. For example, the magnitude and sign of the discrepancy at K on 11/07/89 and 12/23/89 are the same. Similarly, ξ^2 Cet is consistently brighter with respect to HD 22686 and HD 40335 except at M (which should be interpreted with caution anyway since the M magnitude of the two HD stars was extrapolated from shorter wavelength magnitudes) on both 01/07/91 and 01/09/91. This data base is much too small, and the known ProtoCAM calibration problems are too significant, however, to take this suggestion too seriously. Indeed, the lack of reported discrepancies noted with the InSb photometers makes incorrect standard calibrations unlikely. However, this idea should not be dismissed if upcoming instruments have similar difficulties.

3.13) Filter Transformations

In order to produce accurate broad-band spectra and to report brightnesses which are directly comparable to those obtained with other instruments, accurate determinations of the filter transmission profiles and color transformation equations are required. Unfortunately, ProtoCAM was in full operation before filter transmission issues were

discussed, so that it has not been possible to work with the instrument directly. However, the factory transmission curves for the filters are available, plus the filters from another instrument (the Echelle spectrometer) which were cut from the same batch as ProtoCAM have been scanned by IRTF personnel. While these scans do not match the absolute transmission values of the factory very well (this is a known problem with the scanning equipment at the IRTF), the gross shape of the transmission curves does match, so I assume the factory curves are essentially correct.

I have digitized the factory transmission curves and computed several characteristic quantities for each filter. The curves are presented in the top half of Figure 3.15 and the data are summarized in Table 3.5. Column 1 of the table is the filter name. Column 2 is the weighted mean wavelength; this was computed by dividing the integral of the transmission times the wavelength by the integral of the transmission. The bandpass in column 3 is simply the distance between the points at which the transmission is 50% of the maximum transmission. It should be pointed out that the mean wavelength in column 2 is never more than 0.03 μm different from the point midway between the half maximum transmission points. Column 4 lists the mean transmission of the filter which was computed by dividing the integral of the transmission curve by the bandpass. This quantity is simply the effective transmission of an ideal, square bandpass filter with the same area and half transmission points as the real filter. Column 5 gives the magnitude-to-flux coefficient for each filter. These values were obtained by interpolating the data given in the IRTF photometry manual to the ProtoCAM mean wavelengths in log-log

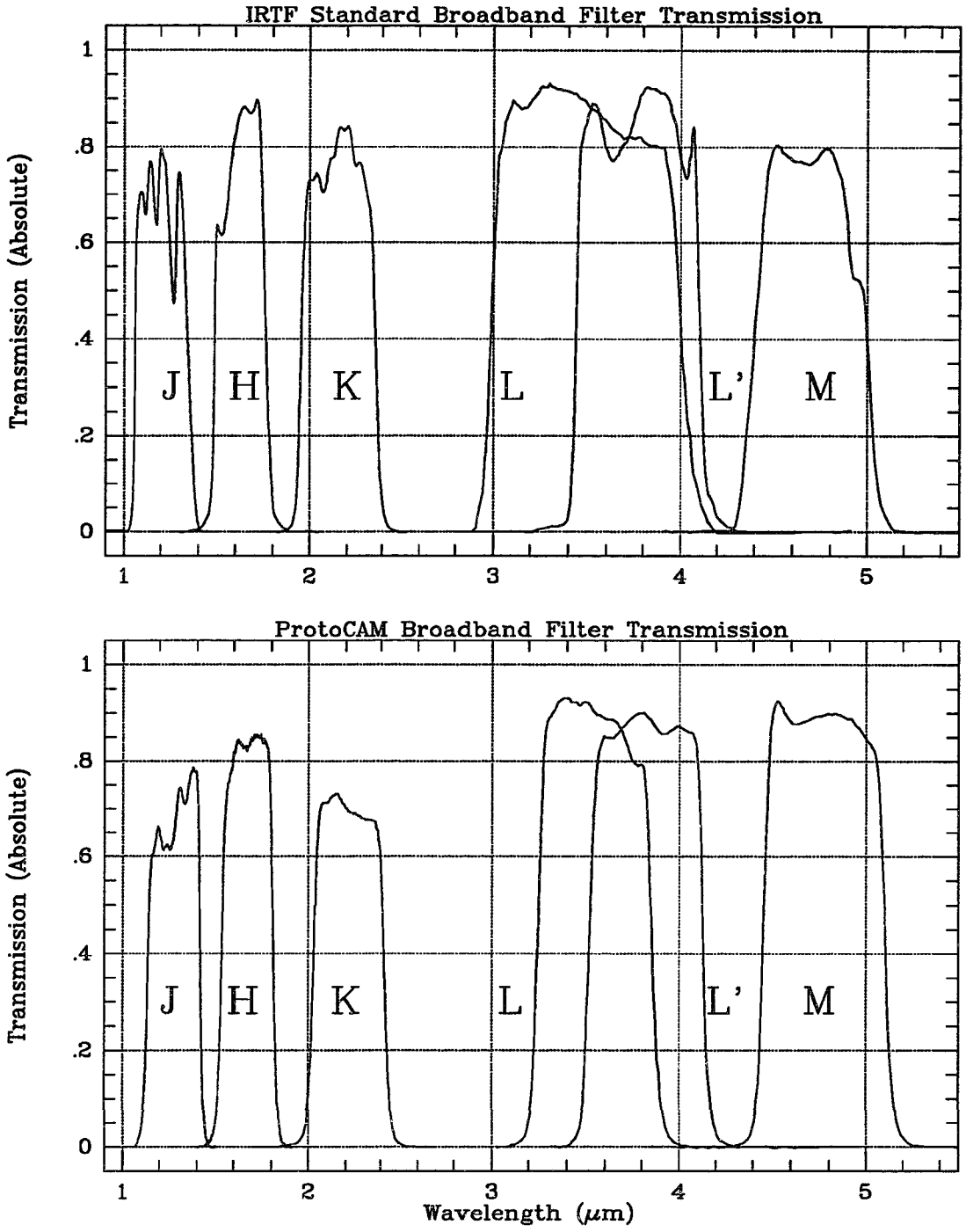

Figure 3.15: A plot of the absolute transmission of both the IRTF InSb photometer and ProtoCAM broadband filters.

Table 3.5: A summary of the filter profile data

Filter	Central Wavelength	Bandpass	Mean Transmission	Flux for 0 Mag Star
ProtoCAM	(μm)	(μm)	(%)	(Jy)
J	1.29	0.28	0.70	1530
H	1.67	0.27	0.85	1000
K	2.23	0.39	0.71	644
L	3.55	0.60	0.90	279
L'	3.82	0.61	0.88	250
M	4.78	0.65	0.89	164
IRTF				
J	1.21 [1.25]	0.28	0.71	1700 [1600]
H	1.63 [1.65]	0.27	0.83	1040 [1020]
K	2.16 [2.20]	0.41	0.78	674 [657]
L	3.48 [3.45]	1.00	0.86	287 [290]
L'	3.78 [3.80]	0.66	0.87	254 [252]
M	4.69 [4.80]	0.60	0.76	170 [163]

space. The similar quantities I found by examining the IRTF InSb photometer filters are presented in the bottom half of the table, with the IRTF photometry manual values in square brackets. The IRTF filter curves are presented in the bottom half of Figure 3.15.

While it is possible to produce good broadband spectra based on Table 3.6 which have characteristics consistent with previously published results, transforming the brightnesses from ProtoCAM magnitudes into those of other systems is more problematic. Obviously, observing many standard objects of known, widely varying colors would allow the derivation of ProtoCAM's filter transformation equations; since this is not presently possible given the current demand for the instrument, a model-based approach must be taken. Since the filters in the IRTF's InSb photometers are well known and a photometric system of standard stars is based on them, I have chosen those as the reference system. The following method is used to then derive the transformations: 1) assume that the only wavelength dependence is in the filters themselves; *e.g.* the wavelength dependent variations of the detector's quantum efficiency are small compared to the filter variations. 2) Assume an A0 type star is well-modeled by a 9600 K blackbody. 3) Integrate a blackbody curve times the filter transmission for each filter in both photometric systems over a large range of blackbody temperatures. 4) Compute the "magnitude" of each computation in step three using the 9600 K blackbody as a zeroeth magnitude reference. 5) Fit a parabolic curve to the difference of magnitudes between the two systems vs. some suitable color difference in the ProtoCAM system (e.g. $K_{IRTF} - K_{PCAM}$ vs. $[H - K]_{PCAM}$).

The resulting transformation equations are as follows (where the unsubscripted letters indicate ProtoCAM filters):

$$J_{IRTF} - J = 0.298\ [J-H] - 0.007\ [J-H]^2$$

$$H_{IRTF} - H = 0.109\ [H-K] - 0.003\ [H-K]^2$$

$$K_{IRTF} - K = 0.086\ [H-K] - 0.001\ [H-K]^2$$

$$L_{IRTF} - L = 0.067\ [K-L] - 0.005\ [K-L]^2$$

$$L'_{IRTF} - L' = 0.021\ [K-L'] - 0.0003\ [K-L']^2$$

$$M_{IRTF} - M = 0.069\ [L'-M] + 0.002\ [L'-M]^2$$

The difficulty with these equations, in addition to the fact that they are only model-based, is that they do not take into account extinction by circumstellar or interstellar material. In principle, one can add an extinction curve, such as Draine & Lee's (1984), and compute fluxes which vary with both blackbody temperature and optical depth. I have done this, and Figure 3.16 illustrates the spread of the points when extinction is added. The solid line in the figure represents the parabolic fit to the pure blackbody points; extinction causes the locus of point to move up and to the right of the curve. Because real astronomical objects, at least those which I am primarily interested in, will have some combination of temperature and extinction effects, it is not obvious how to define the appropriate set of transformation equations. Because these transformations are already so far removed from observational tests, the extinction characterization will be omitted from the model until some observational data is obtained. As a side note, some standard star observations conducted by other researchers are consistent with the above equations at H

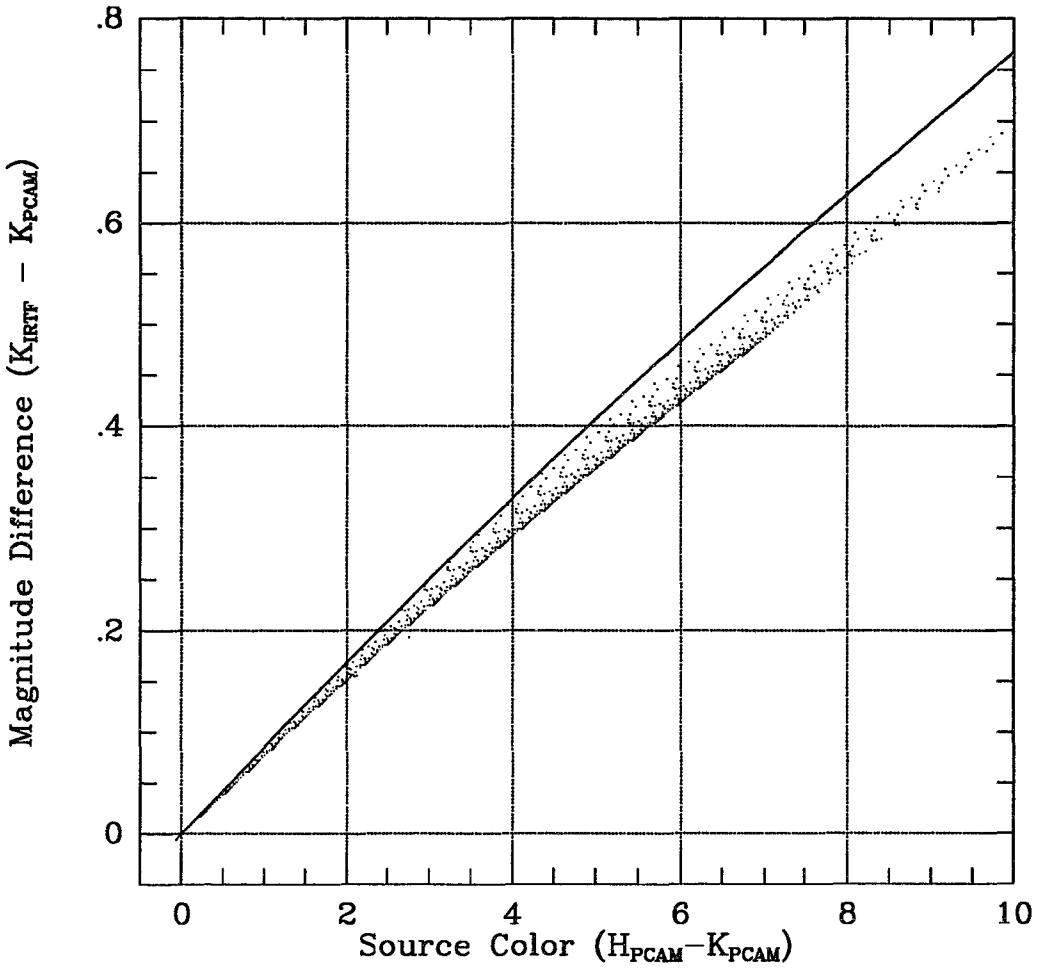

Figure 3.16: A plot of the difference in observed K magnitude between the IRTF and ProtoCAM systems as a function of apparent ProtoCAM color.

and K, so I take this as evidence that the models are at least moving in the correct direction.

3.14) Polarimetric Calibrations

ProtoCAM has proven to be quite adept at polarimetric imaging. To perform polarimetry, a rotating, wire-grid linear polarizer is mounted atop the dewar, and the polarizer is rotated 45° between each image. Images are recorded at 0, 45, 90, and 135° position angle at the minimum, with the complimentary set (180, 225, 270, and 315°) being useful for canceling small asymmetries in the instrumental beam. The instrumental polarization of ProtoCAM is quite small, always less than 1%, and the magnitude as well as the pattern of the polarization derived for the well-known source BN agree quite well with values published in the literature. A summary of the ProtoCAM data is given in Table 3.6.

Table 3.6: A summary of polarization standards

Date	Telescope	Filter	Unpolar. Standard	BN[a] (Meas.)	BN[b] (Publ.)
11/09/89	UH 2.2m	K	0.27%	19.8%	17.1% @ 113°
03/14/90	IRTF	H	0.89%	33.2% @ 111.5°	38% @ 117°
"	"	K	0.97%	17.8%	17.1% @ 113°
"	"	L	1.92%	7.2% @ 104.2°	~9% @ 102°
01/08/91	IRTF	K	0.74%	Lost	17.1% @ 113°
01/10/91	IRTF	K	0.51%	17.4%	17.1% @ 113°

a) Assumes that the polarization angle at K is 115°.
b) Data are from ApJ, 226, 863. L point is estimated from their polarization vs. wavelength figure.

Chapter 4: 1 – 5 Micron Imaging of Deeply Embedded Young Stellar Objects

4.1) INTRODUCTION

Great strides have been made in recent years in our understanding of how stars form. Theoretical studies have concluded that the general star formation sequence tends to follow four broad phases (Shu *et al.* 1987): 1) the formation of a molecular core due to the molecular cloud losing internal support; 2) the collapse of the core into a protostar and disk; 3) the breakout of a stellar wind along the rotational poles which forms a bipolar outflow; and 4) the end of infall, which reveals a new star with a circumstellar disk. At the same time, observations of young stellar objects (YSOs) have allowed them to be classified into three morphological groups based on the shape of their spectral energy distributions and of the value of their spectral index, given by α = d(log λF_λ)/d(log λ). Class I objects have an index which is positive, and these objects are believed to correspond to "infrared protostars", or phases 2 and 3 of the formation sequence outlined above. Class II objects, which correspond to phase 4 above, have indices which are slightly negative but not as negative as a pure blackbody ($\alpha = -3$). These objects are generally T Tauri stars; the shape of the SED arises from the blackbody flux of a stellar photosphere plus an infrared excess from a multi-temperature circumstellar disk. Class III objects, which have SEDs which show no or very small excesses ($\alpha \sim -3$), which imply little or no circumstellar material, correspond to the Weak Line or Naked T Tauri stars.

Because of this convergence of theory and observation, it has become practical to compare SEDs predicted from theory with those observed at the telescope. One of the more successful models of the SEDs of YSOs is that given by Adams & Shu (1986, hereafter AS86), and Adams *et al.* (1987, hereafter ALS). AS86 describes the model and the calculations involved, while ALS fits the model to seven YSOs of Class I. While the fits are generally quite acceptable given the "by eye" fitting technique and the use of "round" numbers while exploring the parameter space, ALS noted that there was a significant departure of the model SED from what is observed for many objects at wavelengths less than 3 μm. They attribute this to the neglect of scattering by circumstellar material in their models and develop a heuristic approach to account for it in one object.

In this paper, we present the results of a series of imaging experiments designed to provide information about the nature of these near-infrared "excesses". We have observed six of the seven Class I sources modeled by ALS (WL-22, at a brightness of K=14.55, was deemed to be too faint to study completely in a reasonable amount of time), plus another nine objects of varying fame and complexity. We present images of these objects taken at near-infrared (NIR) wavelengths (J, H, K, L, L', M, and for many objects, three CVF positions in and around the water ice absorption band, 2.85, 3.08, and 3.40 μm) and describe the SEDs of the point sources seen in these images. In addition, we will describe the results of imaging polarimetry observations for nine of these objects. These observations indicate that for those objects which have extended structure, the

emission is predominantly due to scattered light (as opposed to line emission, for example).

4.2) Observations and Data Reduction

All observations described here, unless explicitly stated otherwise, were performed with ProtoCAM, a 58×62 InSb array camera which is now a facility instrument at the NASA Infrared Telescope Facility (IRTF) on Mauna Kea, Hawaii (Toomey *et al.*, 1990). One observing run in 1989 November was performed with ProtoCAM attached to the University of Hawaii 2.2-m Telescope on Mauna Kea (nominal plate scale was 0.43 "/pix); the remainder of the runs were a combination of engineering and observing runs at the IRTF over the period from 1989 September to 1991 January (plate scales usually 0.14 or 0.35 "/pix). The observations of each object are summarized in Table 4.1.

Because a substantial fraction of the data presented here was taken during engineering runs, or during observing runs before some significant upgrades were made to the camera's performance, an in-depth discussion of the data reduction techniques is in order. Because many of these issues have been resolved since this data was taken, current users of ProtoCAM should be able to obtain cleaner results with less processing.

Table 4.1 - Summary of YSO Observations

Object	RA (1950.0)	DEC (1950.0)	Broad-Band Photometry	H_2O Ice Phot.	K Filter Polar.
SVS 12	03 25 55.7	+31 10 03	89/09/01(H-K), 89/09/02(J-K), 89/11/07(J-L), 91/01/07(J-M)	89/11/07	91/01/08
LDN 1489-IRS	04 01 40.6	+26 10 49	89/11/08(J-L), 90/03/20(K-L), 90/03/21(H-M), 91/01/07(L'-M)	89/11/08	89/11/89
HARO 6-10	04 26 22.0	+24 26 30	90/11/24(J-M), 91/01/07(J-M)	91/01/07	91/01/08
LDN 1551-IRS5	04 28 40.2	+18 01 42	89/12/22(K-L), 91/01/09(J-M)	91/01/09	no
04365+2535	04 36 31.0	+25 35 52	91/01/09(J-M)	no	91/01/10
HH 43-IRS1	05 35 42.1	–07 10 09	91/01/07(J-M)	no	91/01/08
SSV 63	05 43 34.7	–00 11 08	89/11/07(H-K), 90/03/20(L), 91/01/09(J-M)	91/01/09	91/01/10
S255-IRS1	06 09 58.4	+18 00 12	89/12/21(H-L), 90/03/13(J-M), 91/01/09(J-M)	90/03/13 91/01/09	90/03/14
AFGL 961	06 31 59.1	+04 15 10	89/12/22(K), 91/01/07 (J-M)	91/01/07	91/01/08
EL 21	16 23 19.9	–24 16 18	90/03/21(J-M), 90/08/02(J-M)	no	no
WL 16	16 24 00.3	–24 30 44	89/09/02(K), 90/08/02(J-L')	no	no
EL 29	16 24 07.8	–24 30 33	89/09/02(J-L)	no	no
22272+6358A	22 27 11.5	+63 58 20	89/09/02(J-K), 89/09/03(J-K), 89/11/08(K-L), 89/11/09(K-L), 89/12/24(K-L), 90/08/02(K-L'), 90/08/03(L'), 90/09/14(K-M), 91/07/31(K,L'), 91/08/01(L.M)	no	89/11/09
22272+6358B	22 27 17.6	+63 58 17	89/09/02(J-L), 89/11/08(K), 89/12/24(K), 90/08/03(K-M), 90/09/14(L-M)	no	89/11/09

The first issue to be faced is that of obtaining useful background (sky) frames. Three common options are available: 1) construct a sky frame from the median of a large number of on-source images; 2) chop - tilt the secondary mirror from an on-source position to an off-source position; or 3) beamswitch (or nod) - move the entire telescope from the source position to a suitably blank area of sky nearby. Median filtering a large

number of images is the method of choice if the sky emission is stable, the array subtends a large field of view, and/or the observer is concentrating on one particular filter. Because the observations presented here are multi-wavelength, with long delays between observations with the same filter, this technique could not be employed. Traditional infrared observing would call for chopping; indeed, this is still the lowest sky noise technique, even with arrays. However, (at least in ProtoCAM's case) the spatial pattern noise introduced by altering the optical configuration (moving the secondary) overwhelms any improvement in sky noise reduction. This pattern noise is most pronounced when there is dust on an optical surface which is not in the focal plane. The apparent location of the out-of-focus dust speck shifts slightly with the beam position. Because of this misalignment, when the two images are subtracted, the ring-shaped residual has the appearance of a "tilted doughnut". These effects are readily apparent in most of the images taken at wavelengths greater than 3 μm presented here. Other, more subtle, effects of chopping not directly attributable to dust specks (e.g. slopes in the background) are also apparent. These considerations point to beamswitching as the preferred technique for background removal in this type of experiment.

Another effect caused by the array itself disguised this advantage, however. In 1989 June, when an engineering-grade array was placed in the dewar to test the hardware and driver software, it was found that "zapping" the array was necessary in order to produce a usable image. Zapping was the act of pulsing the array gate voltage +1 V from it's operating level for a duration of 1 msec. This eliminated residual charge in the array

and improved pixel bleeding characteristics. Unfortunately, the necessity of zapping was not reevaluated when the science-grade array was installed two months later, and the camera was used in this mode through 1991 January. The effect of zapping on the data is sometimes manifested as a bowl- or dome-shaped background, and the effect is most pronounced when there are significant changes in the background levels (e.g. immediately after changing from the K to the L filter). Because the problem appeared mostly in thermal wavelength images and early observations were done by beamswitching (with 2 s deadtime per switch), we initially assumed (wrongly) that the effect was due to a variable sky background; thus the ability to chop was implemented. Initially, this seemed to reduce the problem, but after some time it became apparent that it had not. This finally led to a reanalysis of zapping, and the technique was eliminated at the end of 1991 January - after the last observing run detailed here; beamswitching has again become the sky-subtraction technique of choice for this type of observation. The original problem of residual charge has been eliminated by slightly increasing the detector gate voltage.

The sum of all these effects with regard to the data presented here is that many of the images at the longer wavelengths (> 3 μm) are contaminated by significant amounts of pattern noise (both bowl-/dome-shaped background and doughnuts) and care must be exercised in interpreting any extended structure visible in these images. Point sources are relatively unaffected by these problems; the data is still relevant for the SED information desired, as described below.

The second major issue in the data reduction is linearity corrections. It was found that a plot of the signal rate (ADU/T_{int}) vs. the final signal squared (ADU^2), where T_{int} is the integration length, follows a straight line to good accuracy at signals up to 90% of the full well depth. In fact, near the center of the array, the deviations are less than 0.5% up to 95% of full well. The south edge of the array, where the response of the array falls off sharply, is the worst position. Even here, deviations are less than 1% up to 85% of full well. In light of this behavior, a linearization algorithm was developed by one of us (Ressler) and it has become a standard part of the ProtoCAM data reduction process. To linearize the data, a set of frames are taken of a reasonably flat illumination source, typically a paper-covered aluminum plate, as well as a few short dark frames to be used as bias frames. The illuminated frames are taken through a circular variable filter positioned at a wavelength of ~ 3 μm and the integration length is linearly increased from one frame to the next. (Neither the wavelength chosen nor the flatness of the illumination source is critical - the only requirement is that a good range of fluxes for each pixel is obtained. Choosing a long wavelength ensures that the data set can be obtained quickly; a uniform illumination source means all pixels can be corrected to approximately the same accuracy.) These frames, after bias subtraction, are then used to fit a unique left-facing parabola (derived from the plot mentioned above) to each pixel in the array. These coefficients, along with the bias frames, are then used to apply a multiplicative correction factor to each pixel in the data frame of interest. The result of the linearization process is a linearized, bias-subtracted image. This linearization process is applied to the raw object and sky frames individually before any other processing is done (i.e. before sky

subtraction and flat-fielding); it should always be the first step in the ProtoCAM data reduction process.

Flat fields for ProtoCAM are not well understood. Sky- and dome-flats do not repeat the variations in response indicated by imaging a standard star at various positions across the array in a raster pattern. The star scans show that the response across the array without flat-fielding is uniform to approximately 5% except at the extreme east and west edges of the array (increases to 10%) and the southern fifth of the array (rapidly increases to 20%). The sky and dome flats appear much more nonuniform than this. We tentatively attribute this to having the pupil plane incorrectly focussed on the cold stop inside the dewar. This would cause point sources to be imaged in a different way than extended sources, such as the sky or dome surface.

Fortunately, the array is "locally smooth" - neighbor-to-neighbor pixel variations are very small. This fact, plus observing so that the standard stars and the program objects were kept in the same part of the array to a half dozen pixels or so, led us to not flat field the data whatsoever. This decision will have significant implications only for extended structure which fills most of the field of view; point sources will not be affected above the few percent level.

Photometry of the point sources was performed either by false aperture photometry in the cases where no extended emission was visible, or by fitting an empirically

determined stellar profile. It was found that the sum of a two-dimensional gaussian profile plus another gaussian with twice the width but half the volume provided a suitable fit to most of the data, as shown in Figure 4.1. The validity of the fits was checked by comparing the fluxes obtained from profile fits with the fluxes obtained by false aperture photometry on standard stars observed each night. Discrepancies between the methods are randomly distributed with a range of 3 - 5%.

The final stage of data reduction is the conversion of the measured magnitudes into monochromatic fluxes. Examination of the manufacturer's filter transmission curves (Barr Associates Inc.) taken at temperatures similar to ProtoCAM's operating temperature show that all six broadband filters have significantly longer wavelength half-power points than most other photometric systems. In addition, the L filter's passband is roughly one-half that of the standard IRTF filter. The central wavelengths (defined as the integral of wavelength times transmission, divided by the integral of transmission), passbands (FWHM), and magnitude to flux conversions derived from these curves (and interpolated from the magnitude/flux tables given in the IRTF Photometry Manual) are presented in Table 4.2. The SEDs presented here use these values; we have not tried to convert the fluxes to those of more familiar photometric systems.

The filter transformation equations of ProtoCAM to other systems as determined from measurements of standard stars are not yet known. We have estimated them by integrating the product of the filter transmission curves, from both ProtoCAM and the

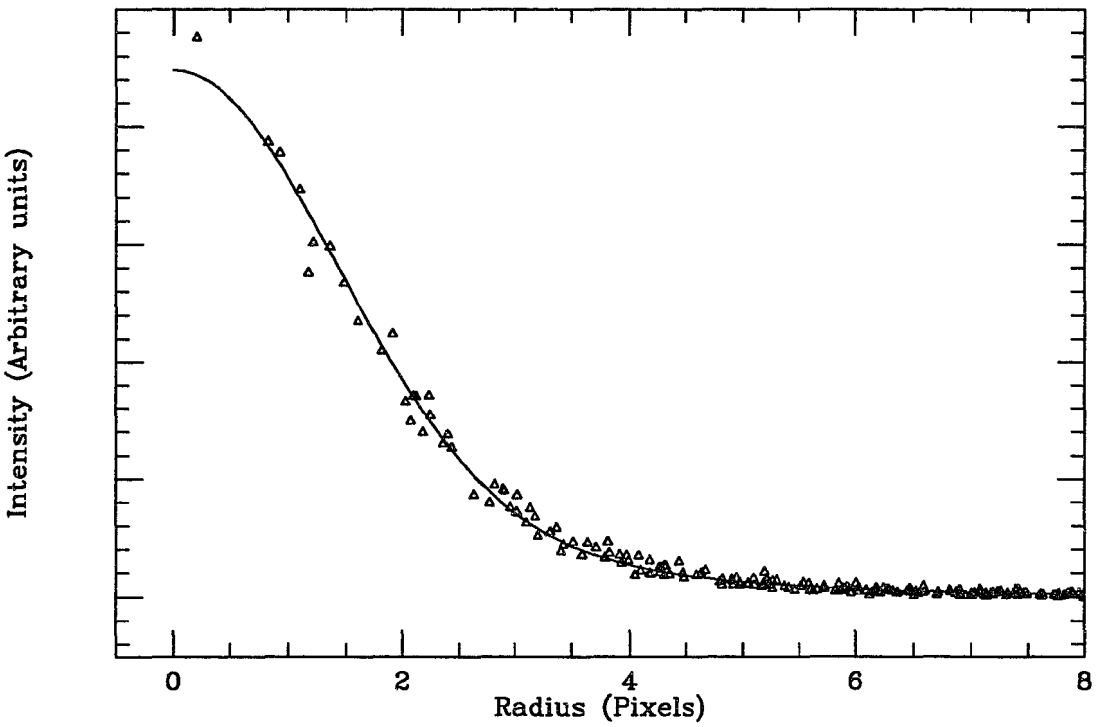

Figure 4.1: Test of the profile fitting function. The small triangles show a radial profile for a standard star (HD 22686 at 1.05 airmasses) and the solid line illustrates the fit of the two-component profile model.

Table 4.2 - ProtoCAM Filter Properties

Filter	Central Wavelength (μm)	Bandpass (μm)	Flux for 0 Mag Star (Jy)
J	1.29	0.28	1530
H	1.67	0.27	1000
K	2.23	0.39	644
L	3.55	0.60	279
L'	3.82	0.61	250
M	4.78	0.65	164

IRTF "standard" filter set, convolved with various temperature blackbodies and fitting these integrated results with polynomials. The raw ProtoCAM magnitudes can thus be converted to the filter characteristics of the IRTF photometry system, for which the central wavelengths and fluxes are known (given in the IRTF Photometry Manual). However, because these transformations are not yet verified experimentally, we have avoided comparing colors (e.g. J–H and H–K) found in other systems to those obtained here.

The polarization data were obtained by mounting a warm rotating wire-grid polarizer on top of the dewar entrance window and taking images at either 4 or 8 positions of the polarizer, stepped in 45° increments. For each polarizer angle, object images were interspersed with nearby blank sky images. These sky frames were subtracted from the object frames, and any residual offsets were removed by subtracting the statistical mode of the resulting image. Because polarimetry involves only image ratios, and because the spatial offsets between frames was never larger than two pixels, the data have not been divided by flat field images. The 4 or 8 reduced frames were then combined using standard formulas to derive the linear polarization and the position angle for each pixel in the array. BN was used to calibrate the instrumental rotation angle (P = 17.1% @ 113°, Capps *et al.*, 1978), as well as to check the consistency of the linear polarization magnitude determined from our polarization maps. Statistical errors for the following figures range from a few percent and a few degrees at the highest contour levels to ~ 10% and 10° at the lower contour levels.

The plate scales of the images were determined by observing binary stars with known separations and position angles. ProtoCAM has an adjustable plate scale: the range of scales was determined by observing γ Ari and found to be 0.14 to 0.35 "/pix at the IRTF. The reproducibility of the plate scale was examined at this time by imaging the binary, then varying the plate scale between opposite extremes several times, then returning to the nominal position and taking another image. The value of the platescale was found to be consistent to less than 0.5%, so we do not consider reproducibility to be a problem. The plate scale is also a function of the broadband filter used due to variations in filter thickness. This dependence was calibrated by observing γ Del; the maximum deviations in platescale are $< 4\%$ from the K filter value (the L and L' filters are at opposite extremes), but all images presented here were rebinned to have the same platescale as the K filter images.

4.3) RESULTS

We begin the discussion of our results by examining each object in detail, starting with the six objects modeled by ALS. For each, we discuss the SED of the central source or sources, the overall morphology with respect to other multi-wavelength observations, and the nature of the polarization map (if obtained for that object). General properties for each object found in the literature are presented in Table 4.3. A summary of results found by this work are given in Table 4.4 and three-color images of the sources with resolved

Table 4.3 - YSO Properties Available in the Literature

Object	RA (1950.0)	DEC (1950.0)	IRAS PSC Designation	Dist. (pc)	Lum. ($L_\odot$)	CO outflow? (P. A. °)	Optical Jet? (P. A. °)	IRAS variability?	Modeled by ALS?	References
SVS 12	03 25 55.7	+31 10 03	03260+3111?	350			307	0.6	no	l
LDN 1489-IRS	04 01 40.6	+26 10 49	04016+2610	140	4.2	yes		0.2	yes	f
HARO 6-10	04 26 22.0	+24 26 30	04263+2426	140	12	no	65	0.5	yes	e,f,m
LDN 1551-IRS5	04 28 40.2	+18 01 42	04287+1801	140	32	256b	246	0.0	yes	m
04365+2535	04 36 31.0	+25 35 52	04365+2535	140	2.4	no		0.2	yes	f
HH 43-IRS1	05 35 42.1	–07 10 09	05357–0710	460	5		143	0.0	no	l,m
SSV 63	05 43 34.7	–00 11 08	05435–0011	460	25		335, 150	0.3	no	i, j
S255-IRS1	06 09 58.4	+18 00 12	06099+1800	2500	900	no		0.0	no	h,n
AFGL 961	06 31 59.1	+04 15 10	06319+0415	1400	6800	150?		0.3	no	a,b,m
EL 21	16 23 19.9	–24 16 18	16235–2416?	160	120	200b		0.0	no	n
WL 16	16 24 00.3	–24 30 44	16240–2430[+]	160	22			0.9	yes	d
EL 29	16 24 07.8	–24 30 33	16240–2430[+]	160	48			0.9	yes	d
22272+6358A	22 27 11.5	+63 58 20	22272+6358A	1000	1100	yes	no	——	no	g
22272+6358B	22 27 17.6	+63 58 17	22272+6358B	1000	43	no?	no	——	no	g

[+] EL-29 and WL-16 are unresolved by the IRAS PSC and thus have the same designation.

References: a) Castelaz *et al.* (1985b), b) Henning *et al.* (1990), c) Castelaz *et al.* (1985a), d) Wilking *et al.* (1989), e) Strom *et al.* (1988), f) Myers *et al.* (1987), g) Ressler & Shure (1991), h) Mezger *et al.* (1988), i) [Cohen *et al.* 1984] ApJ 278, 671, j) Mundt *et al.* (1991), k) Campbell *et al.* (1988), l) Cohen & Schwartz (1983), m) Strom *et al.* (1986), n) Tamura *et al.* (1991a)

structure are given in Figure 4.2. It must be emphasized that comparisons of the colors between the different images should not be made; the same three colors were not chosen for every object, and even if two objects are presented with the same three filters, different intensity stretches may have been used. These images have been processed to maximize color contrast and to serve as a visual reference for later discussion - they are not colorimetrically accurate.

Nomenclature is difficult given the number of multiple sources we have observed; we thus follow the 1988 IAU recommendations for subcomponent/multiplicity nomenclature as closely as possible, with the letter sequence following the K filter brightness. For example, we will name the infrared companion in Haro 6-10 as Haro 6-10:B and the "primary" as Haro 6-10:A. In cases where other identifications exist, we will continue to follow the IAU recommendations, but will note the existing names in the literature.

Sources Modeled by ALS

1) *LDN 1489-IRS*

LDN 1489-IRS (listed as *IRAS* 04016+2610 in ALS) is a source which exhibits extended emission at many wavelengths. Myers *et al.* (1988) report that there is a very weak, bipolar CO outflow associated with the source, and Tamura *et al.* (1991b) interpret the structure seen in K filter images as a concave emission structure opening to the south.

Table 4.4 - YSO Properties Determined in this Work

Object	Nebulous?	Multiple?[a]	NIR Color Temp[b] (K)	$\tau(H_20)$[c]	Variable?[d]
SVS 12	mono jet	no	610	1.64	no?[e]
LDN 1489-IRS	3 lobes	no	590	2.83	no
HARO 6-10	none	yes	A:1600?, B:490[f]	A:0.38, B:0.69[g]	both components
LDN 1551-IRS5	2 lobes	no	1080[h]	1.67[h]	yes
04365+2535	faint diffuse	no	690	N/A[i]	no
HH 43-IRS1	asymm diffuse	yes	A:520, B:790	N/A	yes?
SSV 63	asymm diffuse	yes	A:610, B:1240, C:1270, D:320	A:1.51, D:>0.5	components A and D
S255-IRS1	bipolar jet	yes	A:600, B:380	A:0.21, B:1.22	neither component
AFGL 961	asymm diffuse	yes	A:610, B:1020	A:2.33, B:0.96	one or both components
EL 21	mono jet	no	650	N/A	no
WL 16	none	no	820	N/A	no
EL 29	none	no	500	N/A	yes
22272+6358A	bipolar jet	no	N/A	N/A	N/A
22272+6358B	asymm diffuse	no	860	N/A	N/A

Notes: a) See Table 4.6 for more detail. b) Derived by blackbody fits to broadband points. c) Depth measured as difference between 3.08 μm flux and that calculated from blackbody fit in (b). d) See Table 4.7 for more detail. e) Question marks indicate answer is tentative. f) Capital letter indicates which binary member. g) Continuum of the northern source determined by linear interpolation between the K and M points. h) Determined from aperture photometry. i) Indicates either not observed or no data available in the literature.

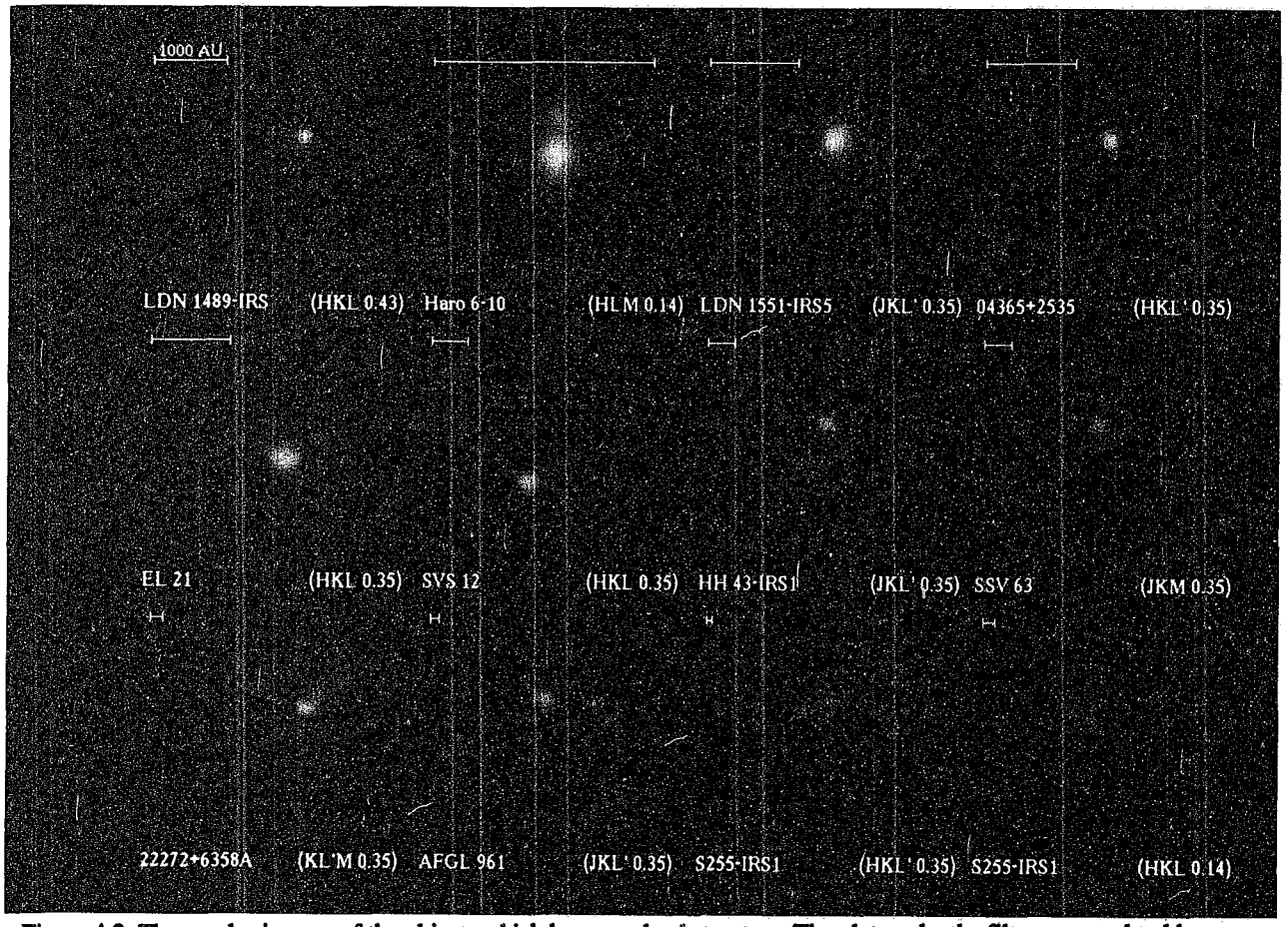

Figure 4.2: Three-color images of the objects which have resolved structure. The platescale, the filters mapped to blue, green, and red, respectively, and a 1000 AU scale bar are indicated on each frame. Comparisons of colors between frames should not be made as different filters and different intensity stretches were used to enhance the color detail for each object. The noise and chopping artifacts in the SSV 63 M image (red) overwhelmed the true structure; thus, point source profiles were fit to the known sources and a synthetic image was constructed from these fits; all other images are actual data.

ALS found that a source of 0.4 $M_{\odot}$ provided the best fit to the SED. While they note that the discrepancy between their model and the observational data available to them is probably due to scattering, they argue that additional departures at mid-infrared wavelengths prevent them from stating the case strongly. In fact, we find that this is perhaps the only object in which the NIR excess can be easily explained by scattering.

Our images of this source at H and K (Figure 4.3) show a three lobed structure with the southeastern lobe being most prominent. This confirms the general morphology reported by Heyer *et al.* (1990) and Tamura *et al.* (1991b) in their somewhat lower resolution images, but we note that the lobes are more jet-like and prominent in our higher resolution images. Heyer *et al.* suggest that the structure formed by the southeastern and southwestern lobes may be similar to that observed in LDN 1551-IRS5 since (they claim) the CO outflow is also directed to the south. Our interpretation of the Myers *et al.* (1988) CO map is that the blue-shifted portion of the outflow is possibly directed at a position angle of ~ 120°, roughly parallel to the southeastern lobe. Under this interpretation, this southeastern lobe (or jet) marks the less dense polar region of a YSO which is angled slightly toward the observer, while the redshifted NIR jet is extinguished by a thick circumstellar disk. There is a third, fainter lobe projecting to the north-northeast near the apparent point source, parallel to the southwestern lobe. We are uncertain of the nature of these lobes; perhaps the southwestern lobe is associated with the redshifted CO knot which lies to the southwest of the IRAS source, but higher resolution CO maps are required to shed more light on these correlations. At longer

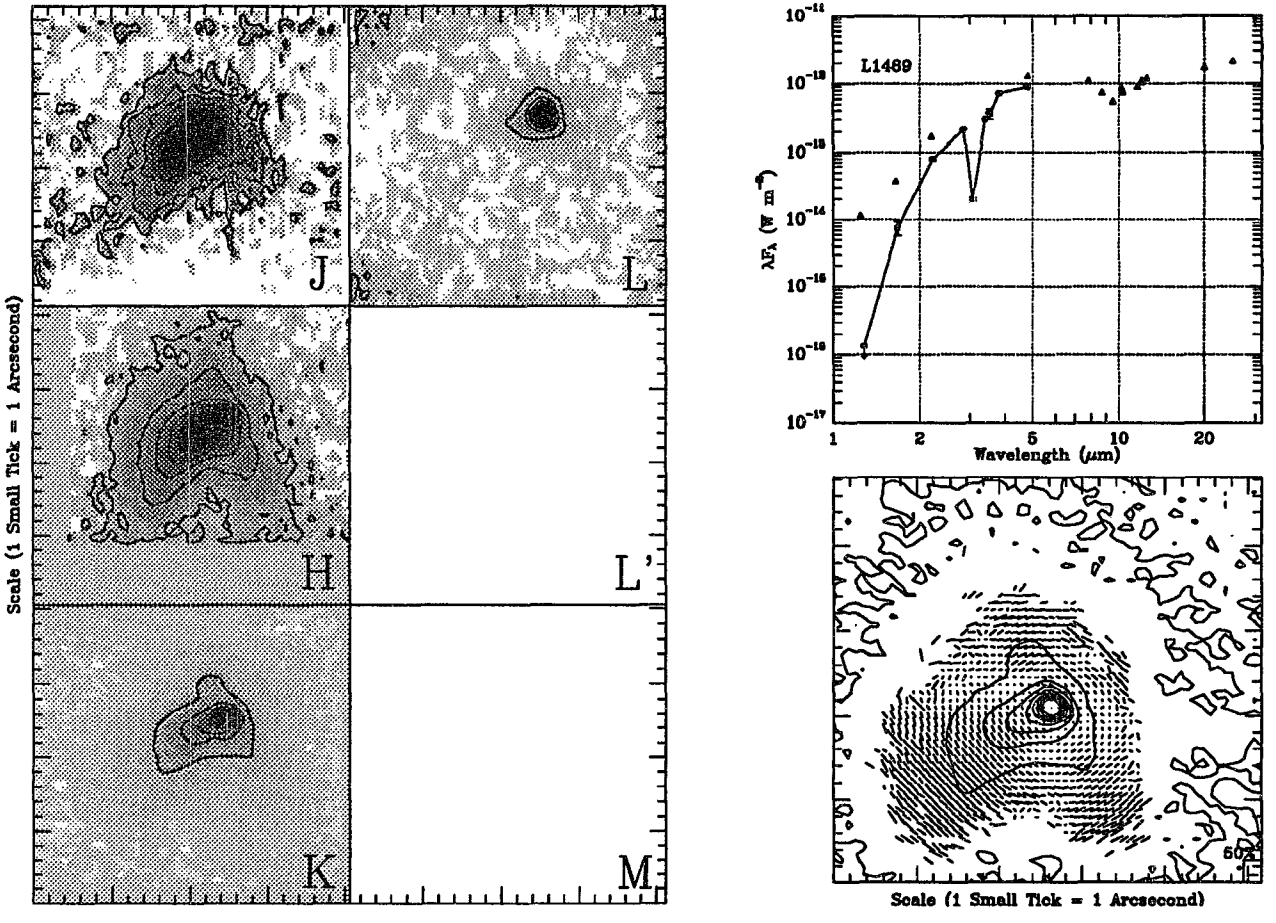

Figure 4.3: The data set for LDN 1489-IRS. The left side of the figure presents broadband images obtained with ProtoCAM. Contours (square root spacing - 0, 0.01, 0.04, 0.09 ... 1.0 times the maximum intensity) are plotted to highlight the intensity levels. The upper right panel shows the spectral energy distribution for this object. The small triangles are data obtained from the literature (Beichman *et al.*, 1986, Meyers *et al.*, 1987 and Clark, 1992) while the solid squares (connected by solid lines) are data obtained by profile fitting the illuminating source. The bottom right panel shows the K filter polarization map. A 50% polarization vector is located in the lower right hand corner for reference.

wavelengths, the nebulosity rapidly fades, leaving only the point source, while at J, only the lobe to the southeast is visible.

Our K filter polarization map of LDN 1489-IRS is also presented in Figure 4.3. The pattern is very clearly centrosymmetric about the apparent point source and we identify it as the illuminating source. This result contrasts with that of Heyer *et al.* (1990) whose maps were not sufficiently centrosymmetric to accurately locate the illuminating source. We attribute this to the combination of source complexity and the low spatial resolution available to them. The large magnitude and centrosymmetric pattern of polarization argue for scattering being the dominant mechanism in the extended structure.

The SED we derive for this source by profile fits to the apparent point source agrees remarkably well with the ALS model, particularly if the luminosity is scaled downward by a factor of ~ 2 (Figure 4.4). (Such a reduction can be achieved without significantly changing the shape of the SED by either reducing η_D, the fraction of the material accreted onto the disk which is transferred to the star, or by lowering the mass in the fit by 10 – 20%. See AS86 for plots detailing these effects.) This rescaling eliminates the argument against scattering raised by ALS. In fact, this is the one source out of the six observed in which we can confidently reconcile the NIR data with the ALS model by attributing the excess to scattering.

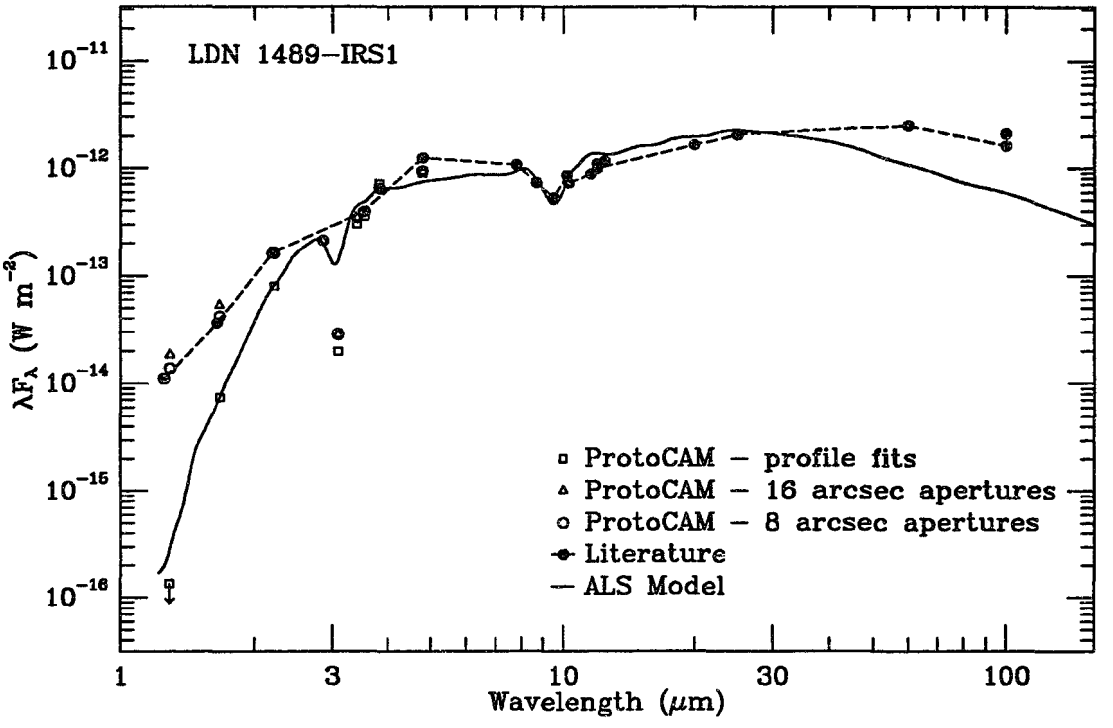

Figure 4.4: The SED of LDN 1489-IRS comparing the observed fluxes to the ALS model. The solid circles are data taken from the literature (see Figure 4.2), while the solid line is the ALS model. The open triangles and circles represent false aperture photometry obtained from the ProtoCAM images. Note the excellent agreement between the 8" false apertures and the data obtained by Myers *et al.* (1987) who used an instrument aperture of 8". The open squares are the data obtained by fitting profiles to the ProtoCAM images; this technique eliminates resolvable scattered light from the SED.

2) *Haro 6-10*

Haro 6-10 was discovered to be a double source by Leinert & Haas (1989) using speckle techniques; we confirm this with direct imaging as shown in Figure 4.5. They also reported extended emission along an east-west scan; we find no compelling evidence for this in our data, but we cannot rule it out. Leinert & Haas assume a spectral type of K3 III - K5 V for the southern source based on the prior observations of Goodrich (1986); they conclude that the southern source is a Class II object, while the northern source is still in the Class I phase.

Unfortunately, Haro 6-10 was not known to be double by ALS at the time of their modeling. They found a reasonable fit with a 0.5 $M_{\odot}$ object, and they attribute the NIR excess to scattering, but in light of the observations by Leinert & Haas (1989) and those presented in this paper, this model is incorrect.

Our broad band images of this object show that at wavelengths less than 3 μm, the northern source (B) is completely invisible, but it is very conspicuous at the longer wavelengths. We find a separation of 1".32 ± 0.02 at a position angle of 355°.6 ± 0.7. Leinert & Haas (1989) reported a separation of 1".21 ± 0.04 at the same position angle; the difference is marginally significant, but is more likely to be due to systematic errors in platescale calibration rather than physical motion of the objects.

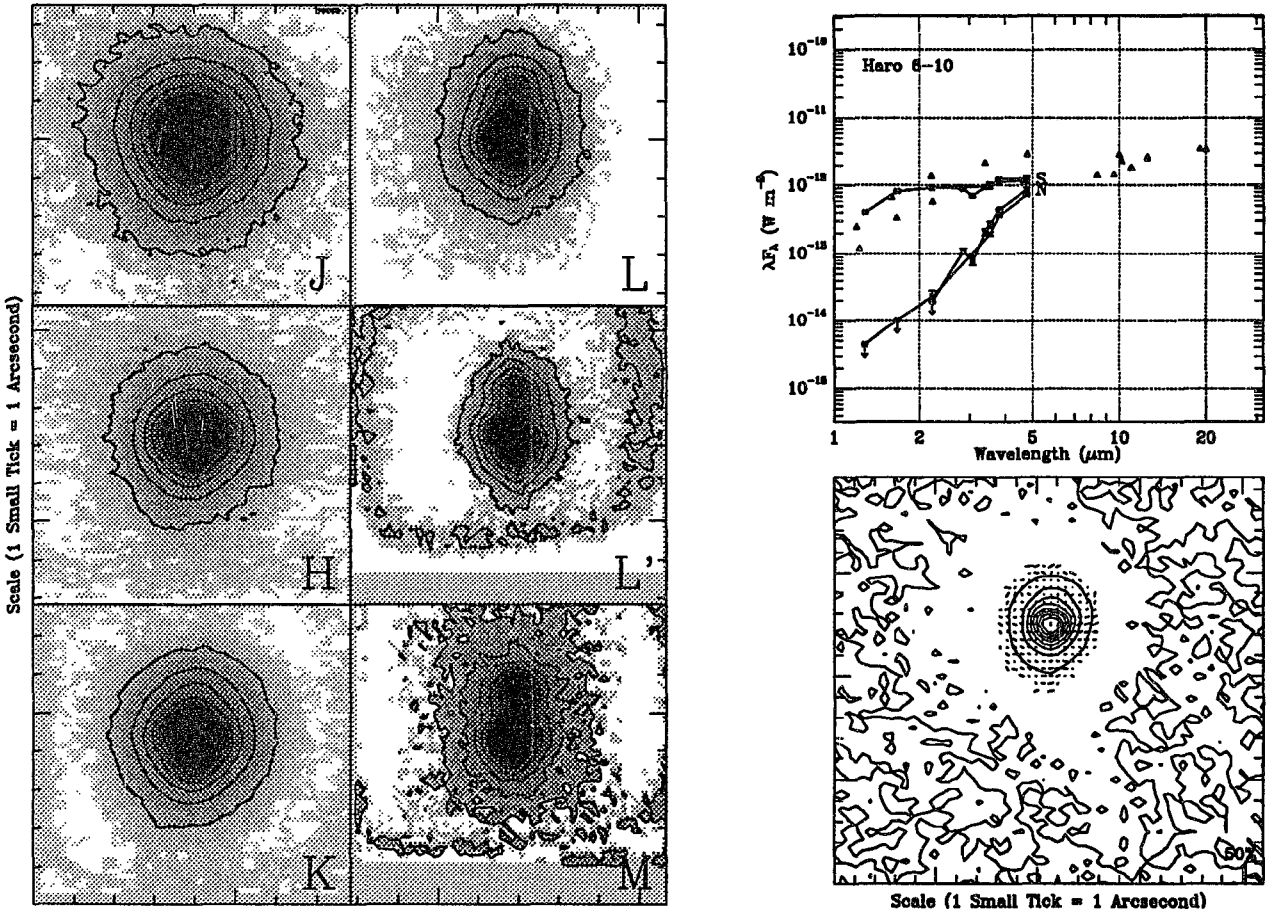

Figure 4.5: The data set for Haro 6-10. Layout is the same as for Figure 4.2. The open triangles are from Elias (1978b), Cohen & Schwartz (1983), Cohen *et al.* (1984), and Myers *et al.* (1987).

The SED of the two sources is presented in Figure 4.5. It is apparent that the previously observed breadth of the SED is due to the sum of the fluxes of two very different sources. Most of the longer wavelength flux (> 5 μm) is emitted by the northern source, while the flux shortward of 3 μm is primarily due to the southern, optically visible source. Previous observations have indicated that the southern source was variable while the northern source was constant. "Haro 6-10" faded by approximately 1 magnitude at NIR wavelengths between the observations of Elias (1978b) and Cohen & Schwartz (1983), then brightened by 0.5 magnitude by the time of the observations of Myers *et al.* (1987).

We observed Haro 6-10 twice, in 1990 November and 1991 January. Over that time interval, the red northern source brightened by ~ 0.25 magnitudes at L, L', and M, while the southern source remained constant within our photometric errors. Our NIR measurements for the southern source are consistent with Myers *et al.* (1987). Because the previously reported variations were at short wavelengths where the northern source is not a significant contributor to the combined flux, we assume (as did Leinert & Haas, 1989) that the southern source is variable over long timescales, although it appears that either the southern source has not varied in the last few years or that we were fortunate to observe it while it was at the same brightness as Myers *et al.* (1987). The new results we report here indicate that the northern source is variable as well, with a brightening rate which is much faster than for the southern source. We conclude that both sources are variable, although there is not yet enough information to determine if the variations are

periodic and or if the rates of change are indicative of the timescales over which the variations typically occur.

Because both sources seem to be in approximately the same state as during the observations of Myers *et al.* (1987), we use their optical data to supplement our observations of the southern source, and their 10μm silicate feature and 20 μm data to supplement our data for the northern source so that we may attempt to fit extinguished blackbodies to the individual SEDs (solid lines, Figure 4.6). Because a spectral type for the southern source exists (K3 - K5), we choose a photospheric temperature of 4500 K and vary only the extinction. Because it is apparent that the SED is broader than a blackbody, we fit only the V through K points since we are likely to see emission from circumstellar dust at longer wavelengths. We derive an extinction of 7.4 magnitudes - consistent with the H_2O ice band depth if the A_V-τ relationship for EL 16 (a K star which lies behind the Taurus Dark Cloud) holds: $A_V \approx 17 \tau_{3.08\mu m}$ (Smith *et al.*, 1989, Hough *et al.*, 1988). This visual extinction estimate also agrees well with the extinction derived from BVRI photometry by Meyers *et al.* (1987), but it is greater than the estimates of 2.5 to 6 magnitudes determined from spectral line ratios (Elias, 1978b, Cohen & Fuller, 1985). From the flattened NIR shape of the SED, we conclude that the southern source is a flat-spectrum K3 - K5 T Tauri star, in agreement with the color and luminosity arguments of Leinert & Haas (1989).

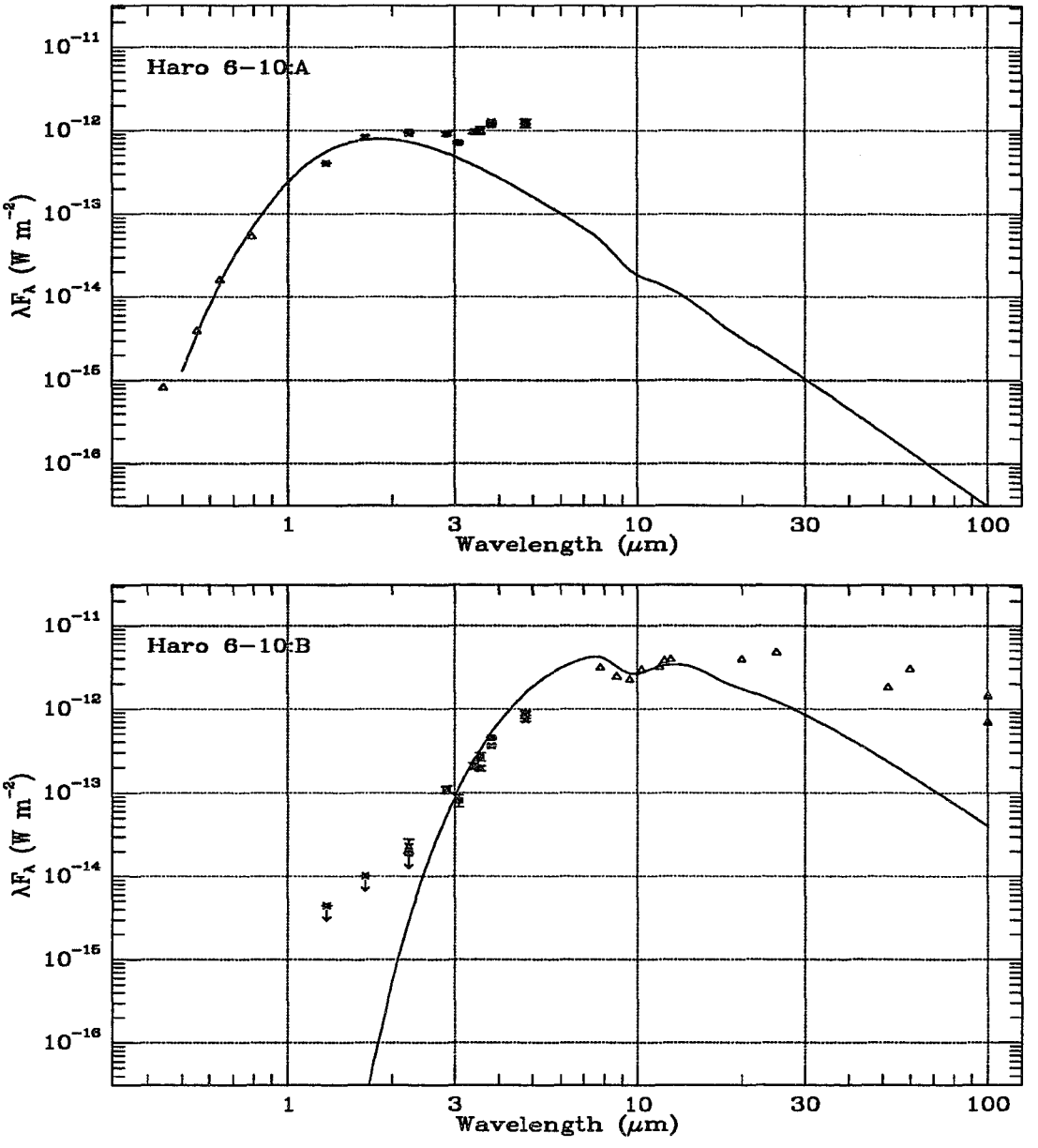

Figure 4.6: Extinguished blackbody fits to the Haro 6-10 SEDs. The upper panel shows the fit of a 4500 K blackbody with 7.4 magnitudes of visual extinction to our data in conjunction with data from Myers *et al.* (1987) for the southern, bluer source (A). The lower panel shows a fit of a 400 K blackbody with 13.5 magnitudes of visual extinction to the northern, red source.

We fit the northern source in a similar manner, this time varying the temperature but holding the extinction at $A_V = 13.5$, consistent with its water ice band depth. By fitting the L through Q points, we find a temperature of 400 K; however, the SED is much broader than this extinguished blackbody, so we conclude that it is a Class I YSO, confirming the conjectures of Leinert & Haas.

Both Leinert & Haas (1989) and Moneti *et al.* (1984, for example) report that Haro 6-10 is either unpolarized or very slightly polarized (< 2%) at K, consistent with having two sources of radiation with an insignificant amount of scattering from circumstellar material. Our direct images and the polarization map shown in Figure 4.5 agree with this result. The polarization vectors which are indicated in our map result from a combination of very low signal to noise on the outskirts and slight changes in the recorded point spread function and are thus not significant. We can also determine the polarization of the "visible" point source through the use of false apertures (summing the flux in a circle centered on the source in each of the polarized images); we derive a value of 1.9% at 120° in an 8" aperture. This is close to the value found by Moneti *et al.* (1.4% at 111°); however, the observed general photometric errors of ProtoCAM could also produce a polarization of this magnitude, so we regard this result as insignificant. In fact, if only the first 4 of the 8 polarizer positions are used to determine the polarization, a value of 0.5% is found. We conclude that the polarization of Haro 6-10 is $\leq$ 1.9% and consequently that scattered light is not a significant contributor to the near-infrared SEDs of these sources.

3) *LDN 1551-IRS5*

The primary result which can be obtained from our data on LDN 1551-IRS5 is that there is no clear point source visible at any of the near-infrared wavelengths (Figure 4.7). Even at 5 μm, the "point source" is significantly larger than the seeing disk. Because of this, the profile fitting technique we employ here breaks down, and no clear insights into the nature of the illuminating source SED can be obtained by this method.

We confirm the morphological results reported previously (*e.g.* Campbell *et al.* 1988). We observe the same cusp-shaped structure, with one lobe pointing south and a second extending to the northwest at an opening angle of ~ 140°; we report for the first time that this general structure is observed even at 5 μm though it is smaller in extent. This is consistent with assertions by Campbell *et al.* and Davidson & Jaffe (1984) that the extinction to the actual source should be quite large (> 150 A_V and > 100 A_V, respectively), corresponding to at least 2 or 3 magnitudes of extinction at 5 μm (Draine & Lee, 1984). Thus, it is possible that the material around the star is optically thick, even at 5 μm, so that we still see only scattered radiation in the near-infrared. However, the water ice band depth we observe (τ = 1.67) implies an extinction of ~ 30 A_V assuming a relation similar to Haro 6-10 and EL 16. This is not necessarily a contradiction as the ice band absorption depth measures the extinction to the last scattering surface, not to the source itself.

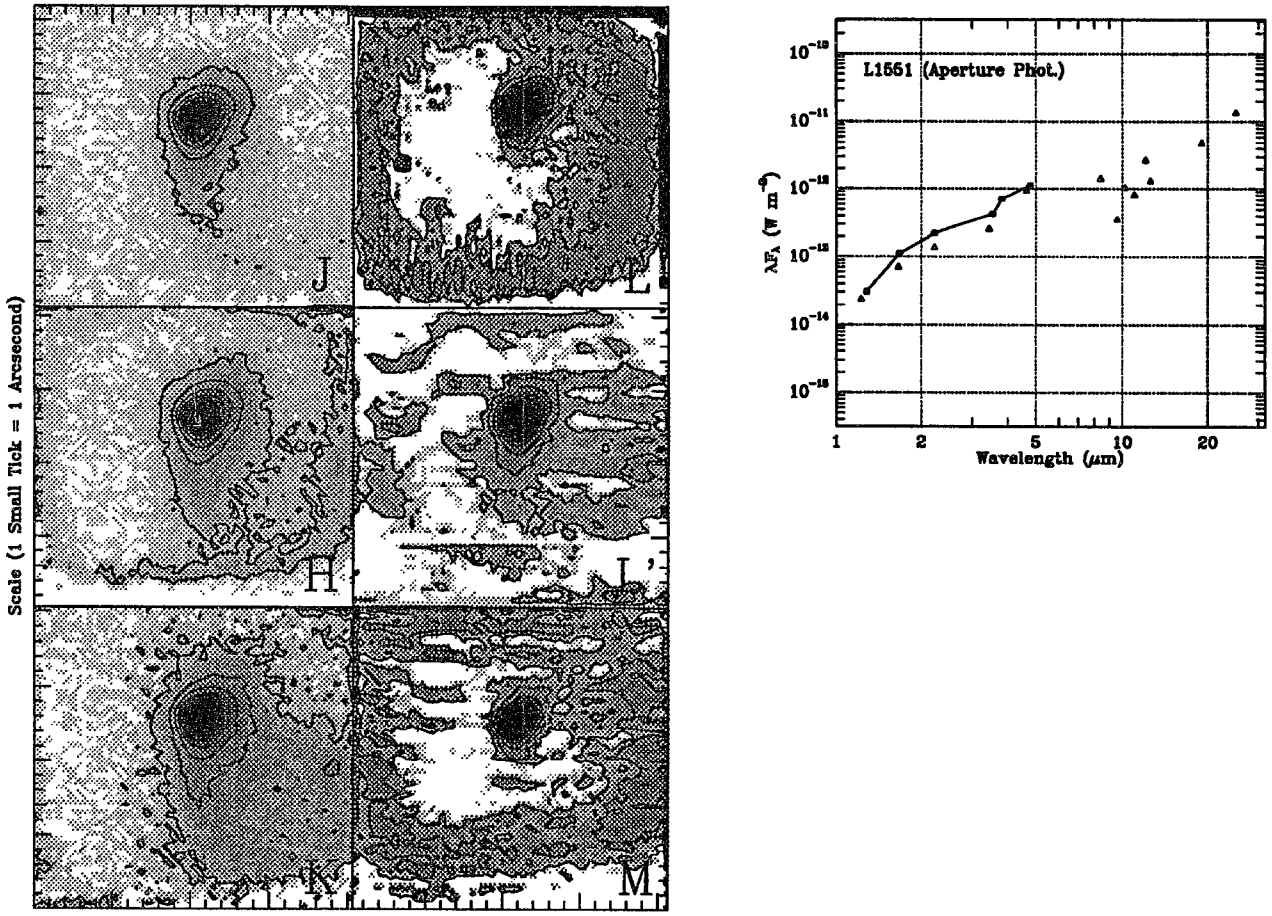

Figure 4.7: The data set for LDN 1551-IRS5. The ring filling the field in the L image and the ripples seen in the L' and M images are artifacts of chopping the telescope in conjuction with the gate voltage instability mentioned in section 4.2. No polarization data was obtained for this object. Literature data are from Cohen & Schwartz (1983), Cohen *et al.* (1984), Davidson & Jaffe (1984), Beichman *et al.* (1986), and Clark (1992).

By integrating the flux in circular software apertures (9" at J, H, and K; 7" for all other wavelengths - these are the smallest apertures which cover all observed nebulosity), we find that LDN 1551-IRS5 is roughly 0.4 magnitudes brighter at all NIR wavelengths during 1991 Jan. than during 1981 Dec. as reported by Cohen & Schwartz (1983) who used 16" apertures (Figure 4.8). A limited data set obtained in 1989 Dec. is consistent with our 1991 values. The H and K magnitudes obtained by Moneti *et al.* (1988) during 1984 Jan. are reasonably consistent with those of Cohen & Schwartz, though perhaps a little fainter (Moneti *et al.* note that this might be an aperture effect). Their L' point lies above the SED of Cohen & Schwartz, though not as far as ours. Although we are not as comfortable claiming variability when there is only one object in the image (the difference in magnitudes which can be obtained for Haro 6-10, for example, is a much more reliable test), the fact that several other objects observed on the same night are consistent with previously published photometry (e.g. 04365+2535) cause us to believe that the observed brightening is real and we conclude that LDN 1551-IRS5 has brightened over the last 10 years.

4) *IRAS 04365+2535*

IRAS 04365+2535 is assumed by ALS to be the youngest of the protostars they modeled since it apparently is not associated with a molecular outflow and it has the lowest luminosity. They find a best fit of 0.2 $M_{\odot}$ to this source, but it vastly underpredicts the NIR flux. While 04365+2535 appears mostly point-like in our images

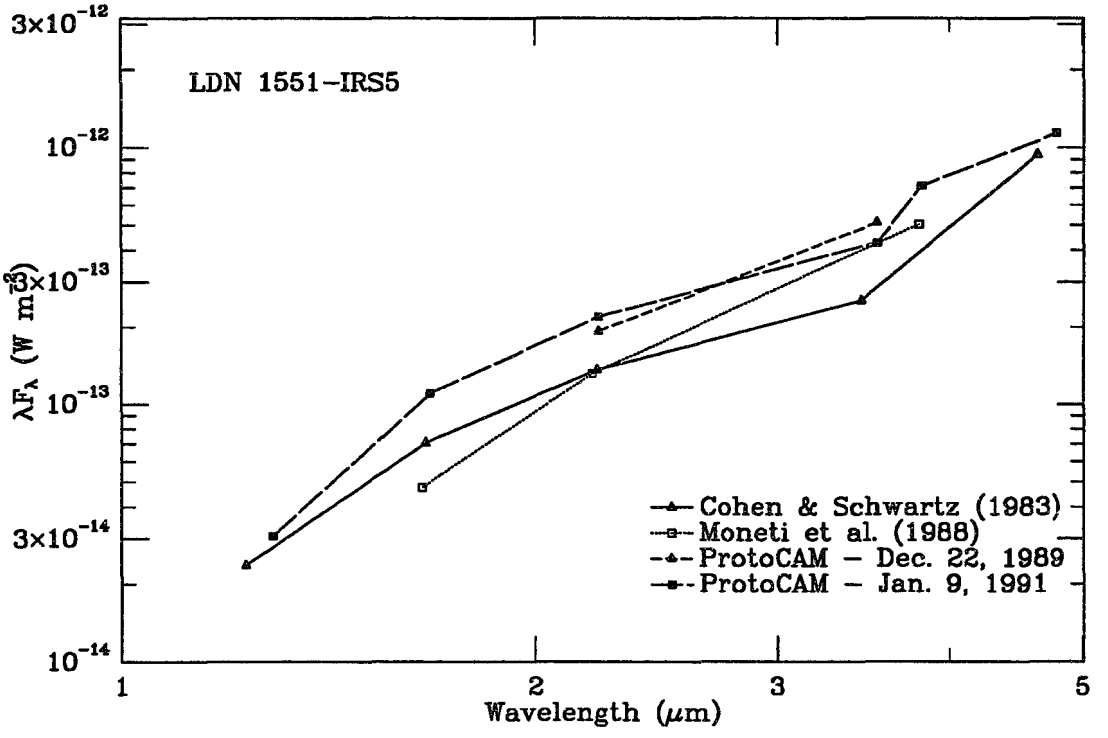

Figure 4.8: Detail of the 1 – 5 μm portion of LDN 1551-IRS5's SED. The ProtoCAM data were obtained by false aperture photometry (integrating over all observed emission) and the 3.08 μm water ice band data has been omitted for clarity. LDN 1551-IRS5 has brightened considerably over the last decade.

(Figure 4.9), we have discovered that there is definitely some very faint emission extending a few arcseconds to the south-southeast and there is perhaps a fainter halo which is more symmetrically distributed. Our polarization map in Figure 4.9 confirms that this south-southeast tail is highly polarized and that the pattern is centrosymmetric about the point source; we conclude that this is scattered radiation, but we would not expect it to seriously affect the observed SED since it is so faint relative to the illuminating source.

Our point source profile fitting agrees quite well with the SED derived from single beam photometers, as expected from the weakness of the extended emission. Thus resolved scattering cannot account for the order of magnitude discrepancy between the ALS model and the observations at J, H, and K as it does in LDN 1489-IRS. However, scattering could still be significant if the scattering material was of a very small scale so that it is still unresolved in our images. Indeed, the point source itself has an intrinsic polarization at K of 15% at a position angle of 167° as determined by profile fitting the point source. This is parallel to the vectors seen in the extended emission to the south and perpendicular to the extended emission itself. This value of polarization is too great to be caused by magnetically aligned circumstellar grains. Applying the empirical method presented by Minchin *et al.* (1991), where the (interstellar) dichroic polarization can be related to the optical depth by

$$P_K\ (\%) = 2.23\tau_K^{3/4} \qquad (6.6)$$

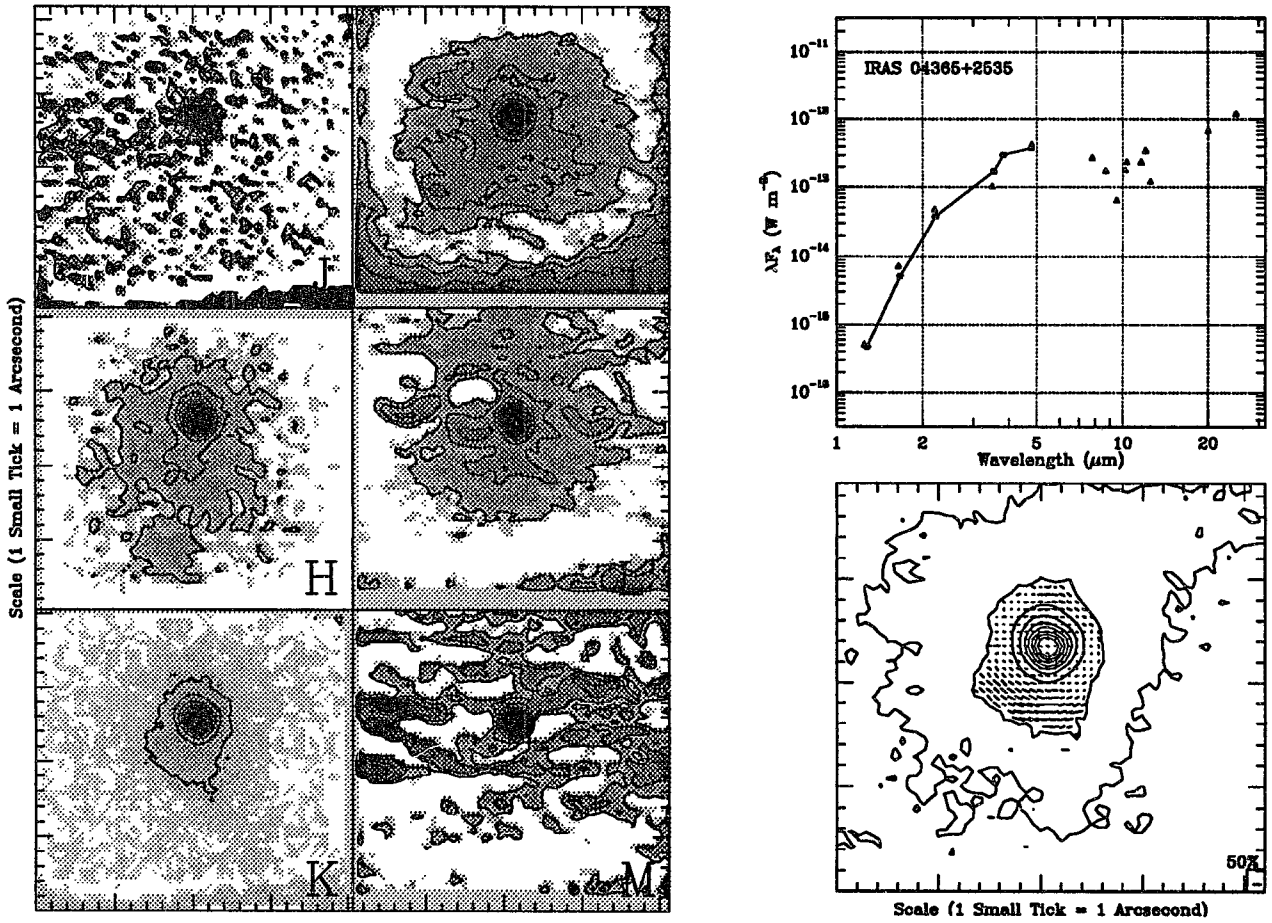

Figure 4.9: The data set for IRAS 04365+2535. The "objects" at the left edge of the M image are chopping artifacts. The literature data are from Beichman *et al.* (1986), Myers *et al.* (1987), and Clark (1992).

we find that an optical depth of 13 at K (A_K = 14 mag) would be required to produce the 15% polarization we observe; if the optical depth to 04365+2535 were truly this large, it would not be visible at K unless it were extremely luminous, in contradiction with the observed bolometric luminosity (2.4 $L_\odot$; Meyers *et al.*, 1987). Since aligned grains cannot explain the polarization, we conclude that scattering is a significant influence on the SED of 04365+2535. A likely model for this source would have a small, but thick, circumstellar disk enshrouding the illuminating source with a weakly illuminated polar outflow to the south-southeast. The fact that little resolved structure is seen implies that the scattering structures (i.e. the disk) must be quite small, of order 1 arcsecond (140 AU) or less.

5) *WL 16*

WL 16 is very similar in behavior to *IRAS* 04365+2535; its appearance in our images is nearly point-like (Figure 4.10), with perhaps a very faint extension to the northeast. Like 04365+2535, the SED we derive matches previously published SEDs well, thus the "excess" cannot be explained as previously unresolved scattering. Unfortunately we were not able to obtain polarization data for this object, so we cannot comment on whether scattering may exist on scales still unresolved by our images.

A recent paper by Hanner *et al.* (1992) sheds some light on this object, however. It seems that what was originally thought to be a deep 10 μm silicate absorption feature is in actuality strong emission by a series of the unidentified mid-infrared features thought

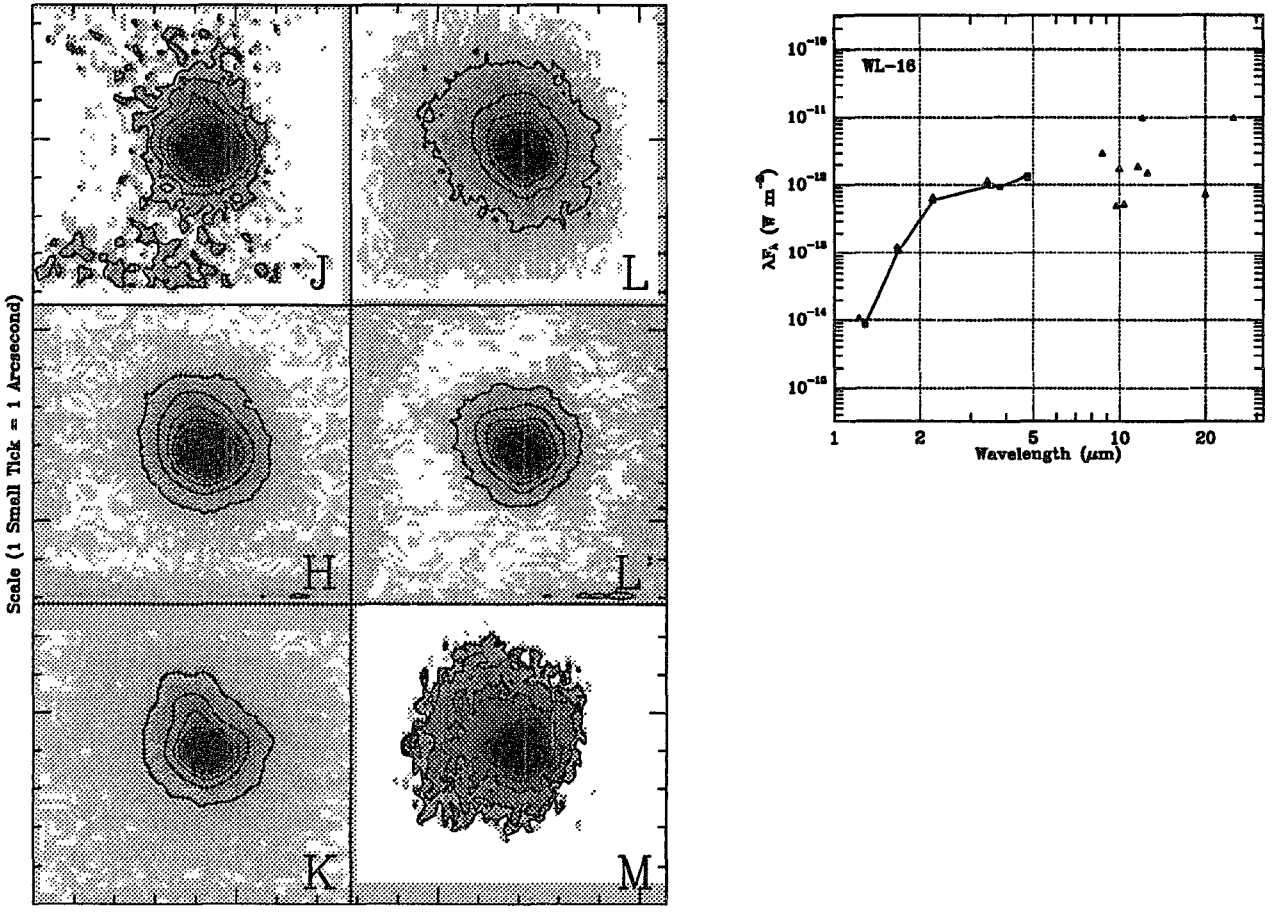

Figure 4.10: The data set for WL 16. The extended appearance of the M image is again an artifact. Literature data are from Wilking & Lada (1983), Lada & Wilking (1984), and Clark (1992).

to be produced by aromatic hydrocarbons superimposed upon a 900 K blackbody spectrum. We have recalculated this fit with our data and the 9.7 μm "continuum" point of Lada & Wilking (1984) since it corresponds well to the continuum level found by Hanner *et al.* and find a best fit blackbody of 820 K (Figure 4.11), in reasonable agreement with the estimate by Hanner *et al.* Adding extinction to the blackbody fit only slightly improves the fit: the values found are 890 K with 4 magnitudes of visual extinction. Since there is no direct spectroscopic evidence for silicate absorption, and our SED fit indicates only a small absorption, we conclude that the ALS model is not appropriate for WL 16 and that the NIR "excess" indicated by their model does not exist.

6) *EL 29*

Perhaps the most enigmatic of the six ALS sources we observed, EL 29 appears to be point-like in all our images (Figure 4.12); there is some evidence of a spherically symmetric scattering structure faintly visible at K, but deeper images are needed to confirm this. The most remarkable feature of EL 29 is that its SED is extremely steep in the NIR, and in fact, the SED we derive is even redder than that previously published by Elias (1978a). We find EL 29 to be possibly overluminous at L (and presumably at longer wavelengths as well), while becoming increasingly underluminous at shorter wavelengths. Lacking a better diagnostic, we fit a blackbody curve to the 1 - 5 μm broadband points to find the apparent NIR color temperature: Elias's data have a color temperature of 670 K while our data have a color temperature of only 500 K. Further discussion of the implications of such variations are left to the variability discussion of section 4.4.

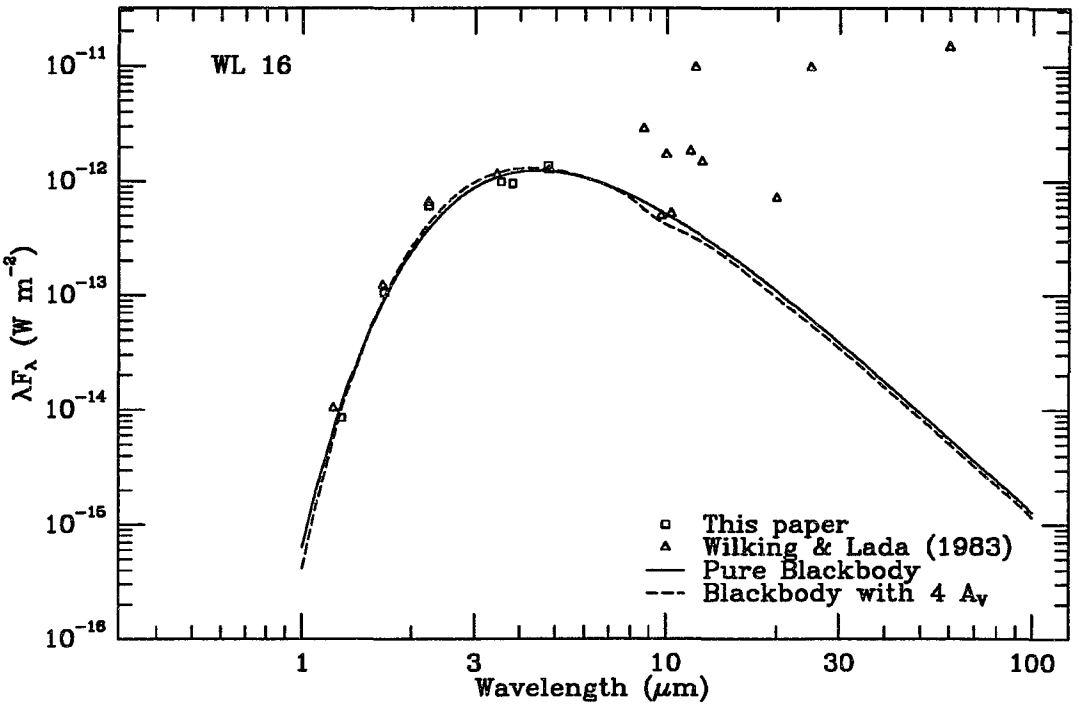

Figure 4.11: Fits of extinguished blackbodies to the observed "continuum" fluxes. The large scatter in the mid-infrared points near 10 μm is due to strong aromatic hydrocarbon emission. The blackbody temperatures found are 820 K if no extinction is included - 890 K if 4 magnitudes of visual extinction are allowed.

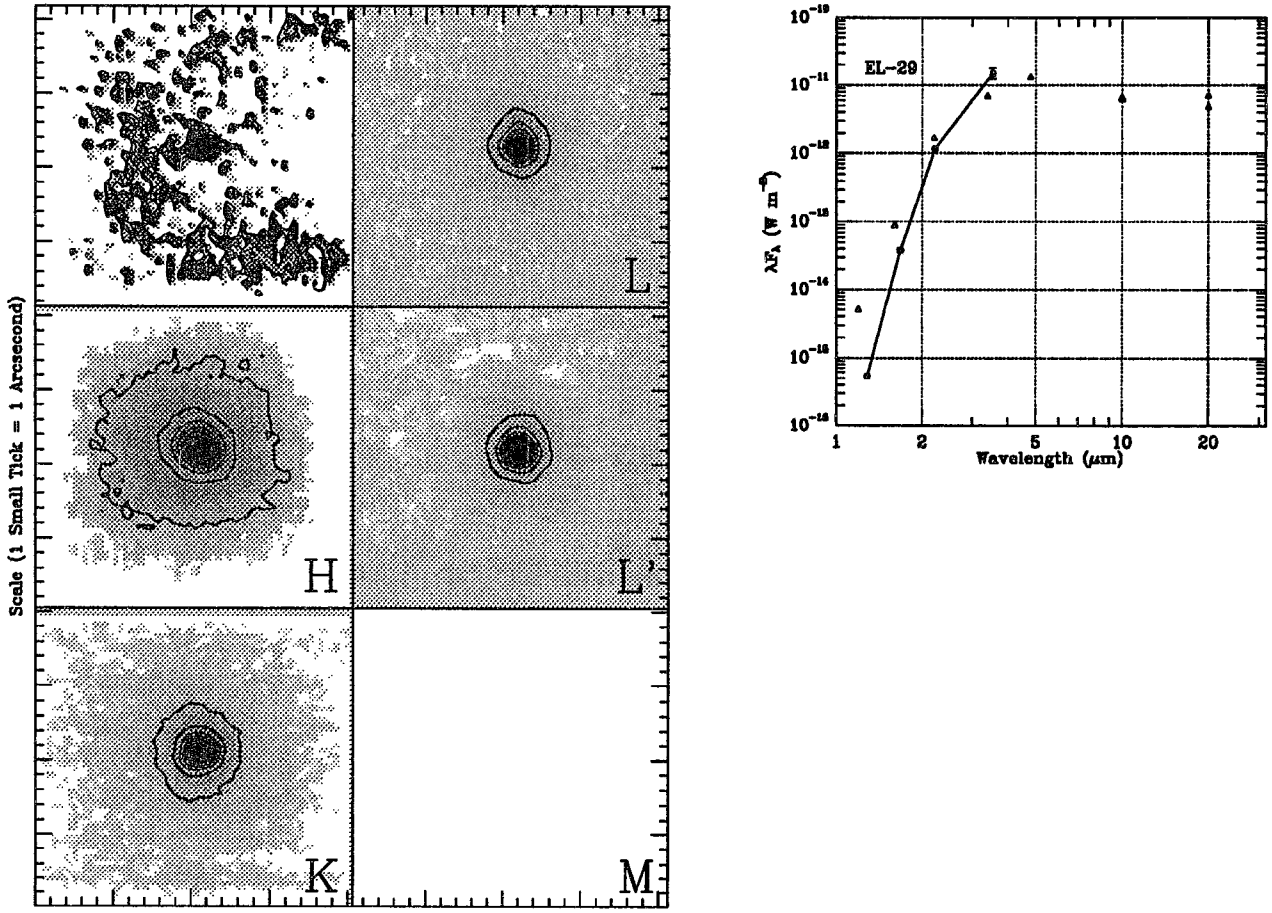

Figure 4.12: The data set for EL 29. The literature data are from Elias (1978a) and Lada & Wilking (1984).

Sources Not Modeled by ALS

1) *SVS 12*

Cohen & Jones (1987) took spectra of the optical jet associated with SVS 12. The optical jet lies at a position angle of 307° and extends 63". The infrared jet we observe agrees well in position angle with the optical jet, but it dims rapidly with increasing distance from SVS 12, so that the maximum extent is of order 20". In addition, they note that SVS 12 lies some 2".4 to the southeast of the tip of the optically visible emission so that the source itself and the first few arcseconds of the jet are not seen at visible wavelengths.

The SED of SVS 12 behaves as one might expect: at wavelengths > 3 μm, SVS 12 appears almost completely point-like, thus the SED matches work done previously reasonably well (Figure 4.13). At shorter wavelengths, the jet become more important, until at H (for example), the flux contributed by the jet is almost an order of magnitude greater than that contributed by the illuminating source. This result can have significant effects on the interpretation of the SED slopes. For instance, combining the K and 19 μm fluxes determined by Cohen & Schwartz (1983) yields a power law slope of approximately 0.9 for SVS-12 (following Myers *et al.*, 1987); using just the flux from the central source at K with the 19 μm flux, we find a slope of 1.4. While this may not produce radical reinterpretations of existing statistical databases, it does show that these

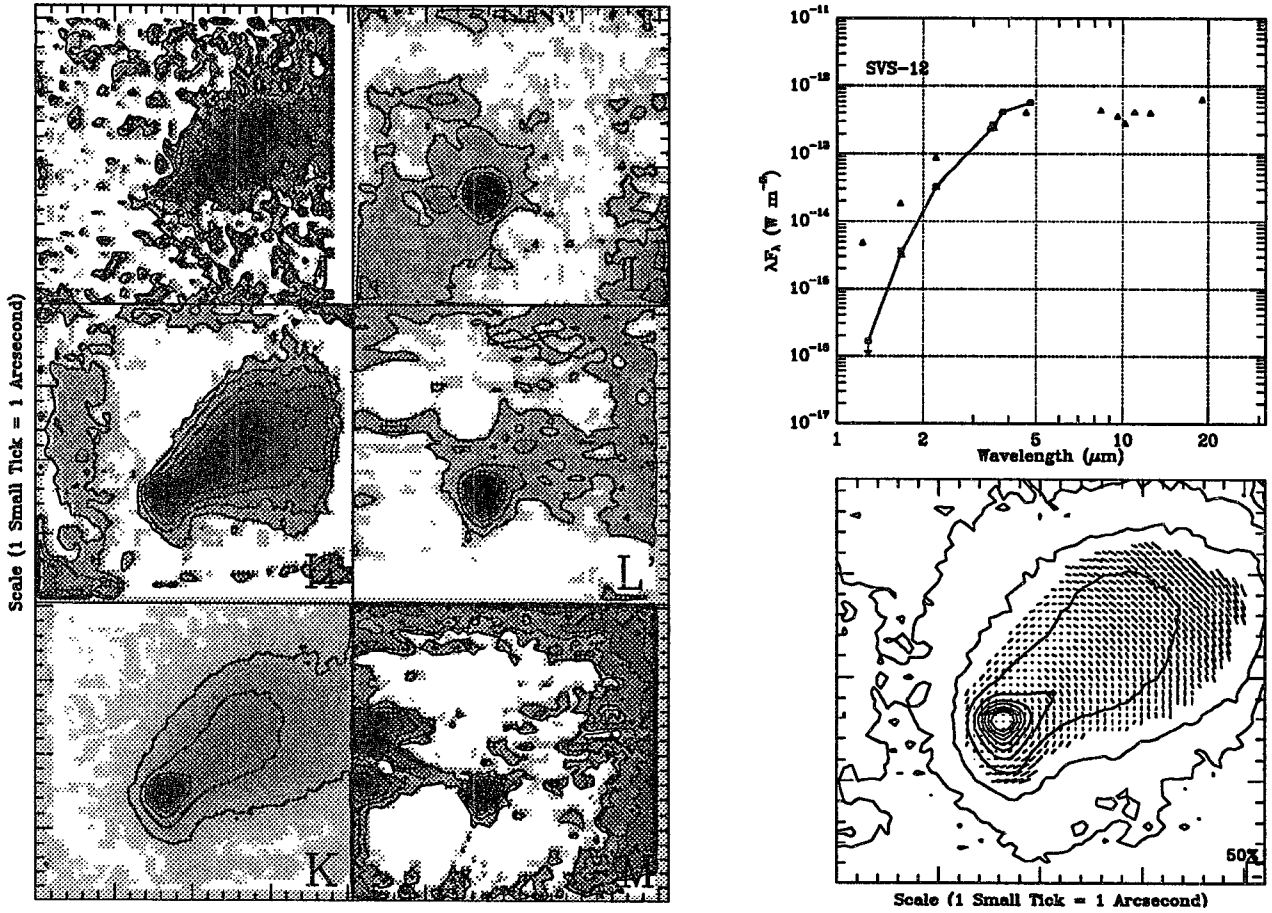

Figure 4.13: The data set for SVS 12. The point source is invisible at J. The objects at the left of the M image are again artifacts. The literature data are from Cohen & Schwartz (1983) and Cohen *et al.* (1984).

databases will be systematically skewed toward flatter SEDs and have an apparent underabundance of extremely steep-sloped sources.

From our polarization map of the vicinity of SVS 12, it is apparent that the jet is extremely polarized and that the polarization pattern is almost completely centrosymmetric. It is likely that we are observing an embedded protostar with a (perhaps bipolar) jet which lies close to, but not completely in, the plane of the sky. The opposing jet, if it exists, lies just behind a thick, dusty disk and is thus unobservable.

2) *HH 43-IRS1*

HH 43-IRS1 is the probable illuminating source for two Herbig-Haro objects, HH 38 and HH 43. HH 43 lies approximately 1.5 arcminutes to the southeast at a position angle of 138° with respect to IRS1, and both the proper motion and the polarization of HH 43 indicate that IRS1 is the driver of this object. HH 38 lies over 5 arcminutes to the southeast, but its proper motion implicates IRS1 as the driving source as well.

Our images reveal HH 43-IRS1 to be a double source with bright extended emission surrounding the two objects (Figure 4.14). At J, neither of the sources is easily visible; however, the nebulosity takes on a butterfly shape: the dark lane between the "wings" leads us to speculate that we are seeing the results of a nearly edge-on circumstellar disk which surrounds the southern source. The point sources are not

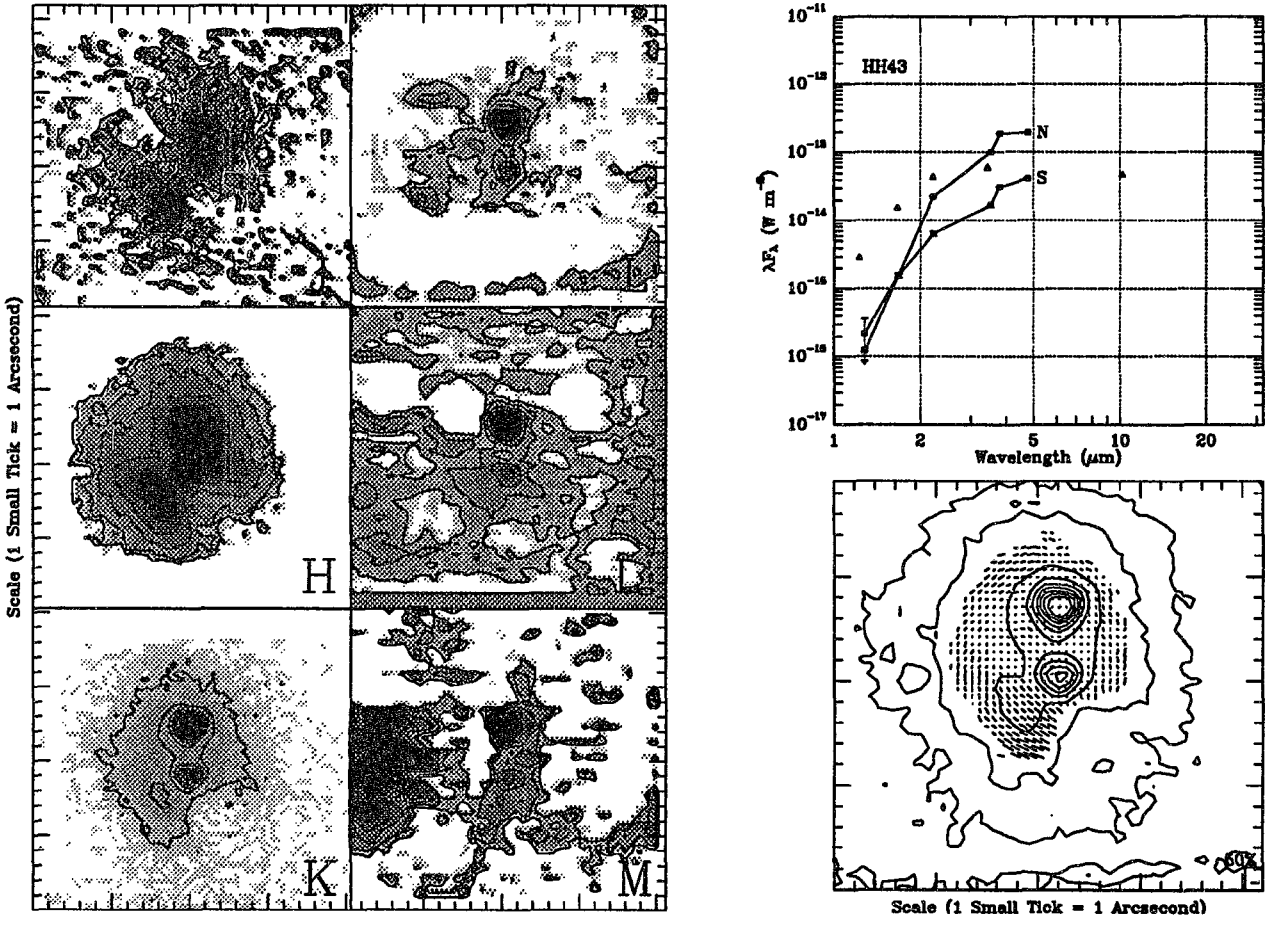

Figure 4.14: The data set for HH 43-IRS1. The objects at the left quarter of the L image and at the left of the M image are artifacts. The literature data are from Cohen & Schwartz (1983) and Cohen *et al.* (1984).

extremely different in color, but the northern source is somewhat redder than the southern source (K–L = 3.0 vs K–L = 2.5, respectively). The difference in colors plus the fact that the northern source is not located along a line of symmetry make it conceivable that the it lies behind the southern source in the cloud and we are viewing it through some of the latter's circumstellar material.

In our polarization map, we note that the extended emission to the southeast is highly polarized and lies in a direction consistent with the much more distant HH objects. It appears that the southern point source is dominant in illuminating the nebulosity; the polarization pattern seems to be more centrosymmetric around the southern source than the northern one. However, the northern source may contribute to the pattern given that the polarization vectors in the immediate vicinity (with 1 – 2 arcseconds) of the northern source tend to be centrosymmetric around it. We note the non-centrosymmetric patterns just to the northeast and southwest of the southern source; this may be nothing more that poor signal-to-noise in these areas, but the patterns do seem to be consistent with the "polarization disks" claimed to be present in some objects (e.g. Aspin *et al.* 1985). If a polarization disk is truly present, it adds additional evidence for a thick, circumstellar disk surrounding the southern source, with the major axis lying at a position angle of ~45°. The butterfly-shaped reflection nebulae and the HH objects would then be material ejected from the poles of this star.

3) *SSV 63*

SSV 63 appears to be the illuminating source of HH 24 (Strom *et al.* 1986 and references therein). Many of the knots in HH 24 are highly polarized and indicate SSV 63 as the illuminator. Strom *et al.* also note that there is a long arc of emission indicating an evacuated cavity illuminated by SSV 63, similar to the structure observed in LDN 1551-IRS5. Both Lane (1989) and Zealey *et al.* (1989) found that SSV 63 appears to be double with a ~ 10" separation. Zealey *et al.* labeled these sources SSV 63E and SSV 63W, and suggested that SSV 63E is the driving source of the associated jets; they suggest that the western component is due to scattered light while Lane proposes that both components are continuum sources.

Our broadband images (Figure 4.15) show that there are in fact four sources within 15" of "SSV 63". One of these (SSV 63:D) is so red that it is not visible at K, and thus does not appear in our polarization map. Examination of visible wavelength photographs (Jones *et al.*, 1987) suggest that the two sources (SSV 63:B and C which together comprise SSV 63W) at the right edge of our maps are probably coincident with two sources contained within the optical knot HH 24B (it appears that there is a declination error for the position of SSV 63 as indicated in Figure 1 of Solf, 1987, whose nomenclature for the emission knots we adopt; the position of SSV 63 is in reality due east of knot B rather than to the northeast); "SSV 63" is thus a combination of the two sources SSV 63:A and D, with SSV 63:A dominating at near-infrared wavelengths and SSV 63:D likely to dominate at mid- and far-infrared wavelengths; one of these objects

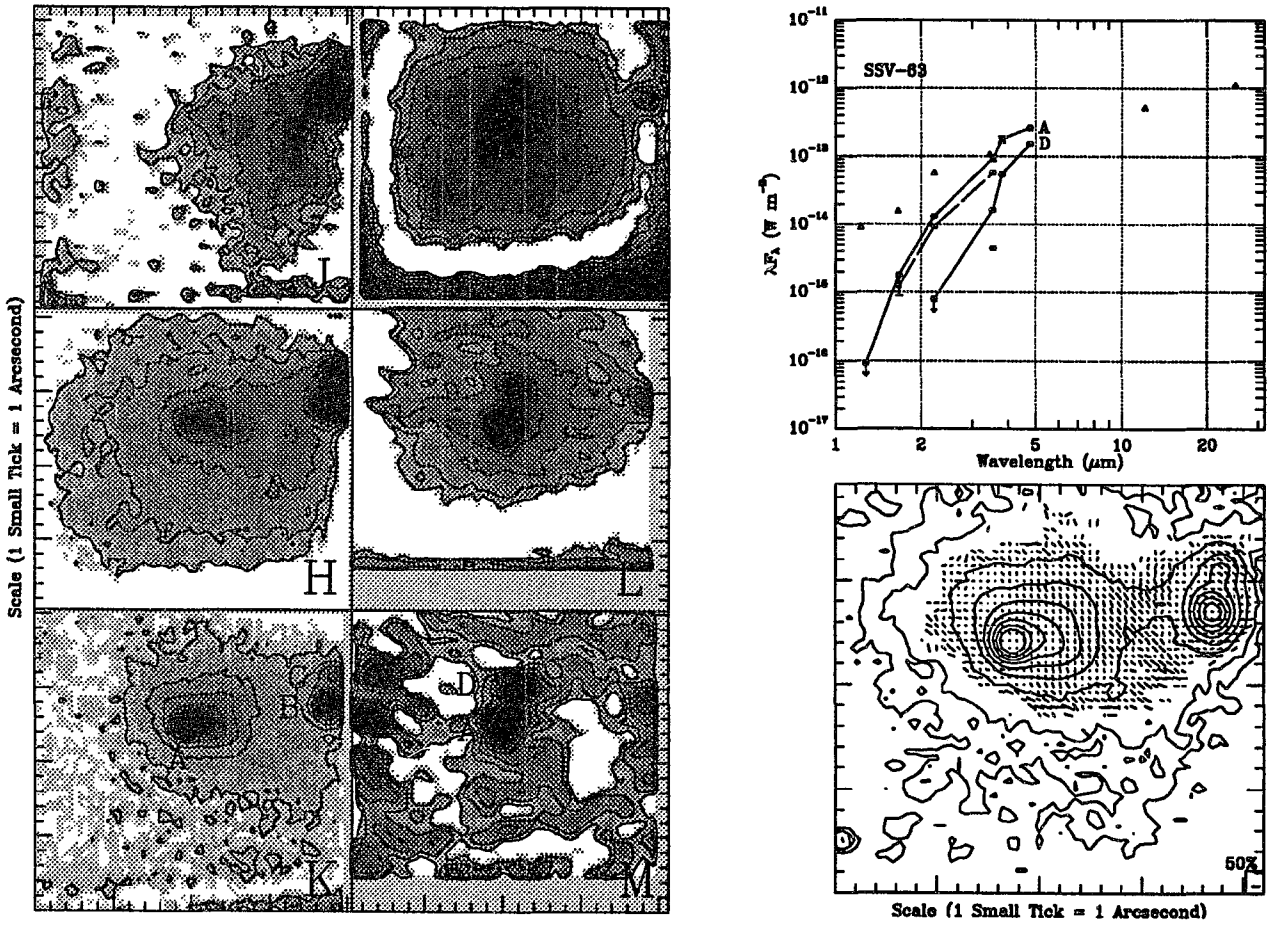

Figure 4.15: The data set for SSV 63, with the K and M images showing source labels. The L image is strongly affected by edge effects of the array and the objects at the left edge of the M image are artifacts. The literature data are from Cohen & Schwartz (1983), Cohen *et al.* (1984), and Clark (1992).

drives the bipolar jets consisting of knots HH24A, C, and F. Solf proposes that there is perhaps a different excitation source for knot B and SSV 63W was proposed by Mundt *et al.* (1991); we concur except to suggest that the source is one of the two components of SSV 63W. A K mosaic shown in Figure 4.16 shows that the infrared nebulosity is quite extensive. It is not clear if the two patches of nebulosity ~ 10" to the northeast of SSV 63 are directly related to the optical jets or if they are distinct structures.

The illuminating source of the material surrounding SSV 63 is not obvious from our polarization map. Common sense would suggest that either SSV 63:A or D illuminates the material immediately surrounding SSV 63:A, but the polarization pattern here does not allow an unambiguous determination. In fact, SSV 63:B appears to contribute as much or more than either A or D. The complex nature of the polarization pattern suggests that all four stars are contributing to the pattern, and in turn that the four are physically associated. It then appears possible that SSV 63 is a hierarchical system where each member of a double is itself a double. In fact, this system is strongly reminiscent of the fragmentation system described by Boss (1991), though its physical scale is more than an order of magnitude larger than that modeled by Boss. Deriving new polarized images of this object with higher signal to noise on a night of better seeing (seeing was a poor 1".4 in these polarization images) should help to clarify this entangled relationship.

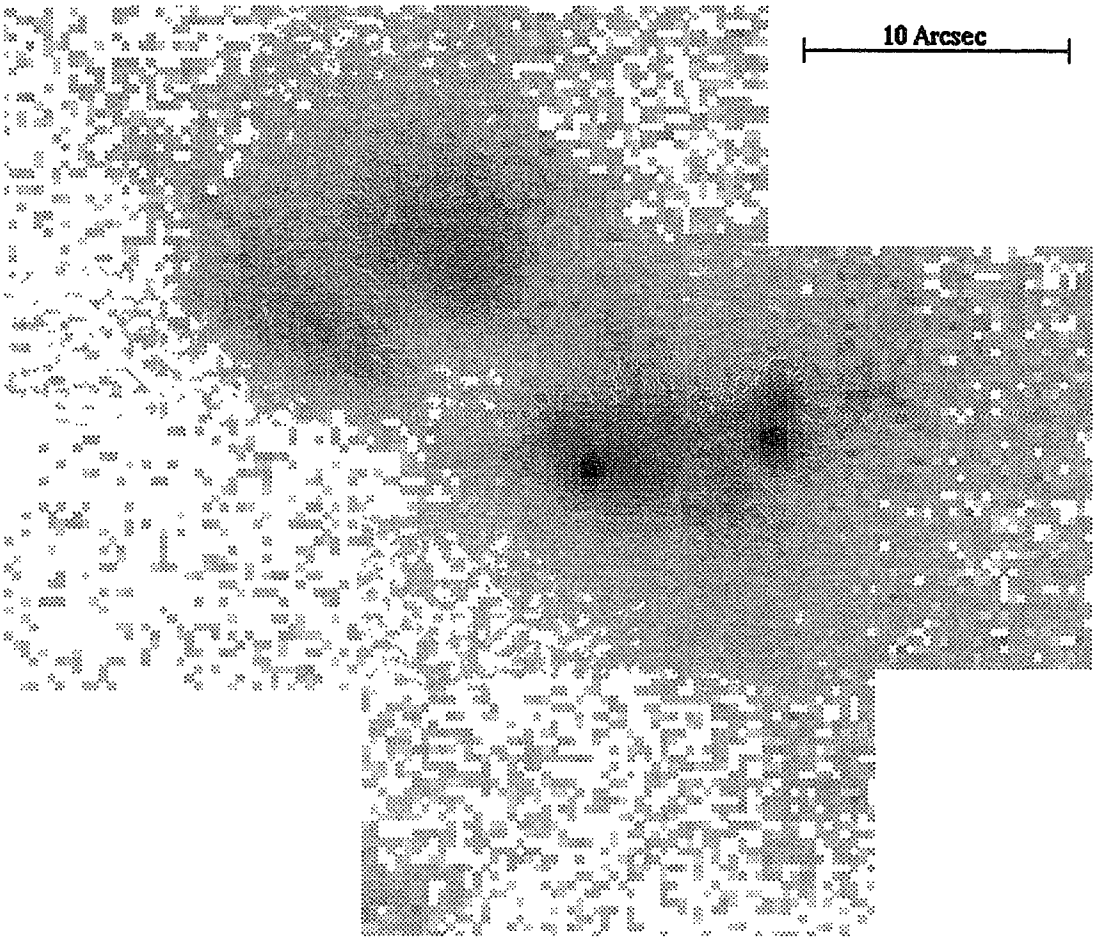

Figure 4.16: A K filter mosaic of SSV 63. The two point sources to the right of center coincide with the optical knot B, while the two nebulous patches to the northeast lie near knot G.

4) *S255-IRS1*

Although S255-IRS1 is a cluster of sources (more than 24 in a 25 × 25 arcsecond field centered on the brightest sources), it is dominated by two sources which are separated by ~ 2".5 (Figure 4.17), giving it the appearance of a binary system (though perhaps only an apparent binary, but the superposition of both objects on common nebulosity is evidence that they are physically associated). Earlier investigations did not detect this binary nature either because of insufficient wavelength coverage (typically cutting off at the K filter, e.g. Tamura *et al.*, 1991a) or because of low spatial resolution (e.g. Beichman *et al.*, 1979). The eastern source, which we will label S255-IRS1:B to emphasize the binary nature of the sources, corresponds to NIRS-3 in Tamura *et al.*, and the western source (S255-IRS1:A) to their NIRS-1.

Both sources appear stellar (unresolved point sources) in images taken at wavelengths longer than 3 μm (Figures 4.17 and 4.18), although some extended emission is visible even at L'; however, its point-like shape and its brightness at wavelengths longer than 3 μm argue that IRS1:A is a self-luminous source, not a reflection nebula as speculated by Tamura *et al.* (1991a). At shorter wavelengths, IRS1:A begins to fade slowly into the nebulosity, while the eastern source disappears almost completely at J and H. IRS1:B is one of the reddest objects we have observed, with an apparent NIR color temperature of 380 K (Table 4.4), while the western source has a color temperature of 600 K. Because the eastern source becomes brighter than the western source at wavelengths longer than 3 μm and because it has a more steeply rising spectrum which

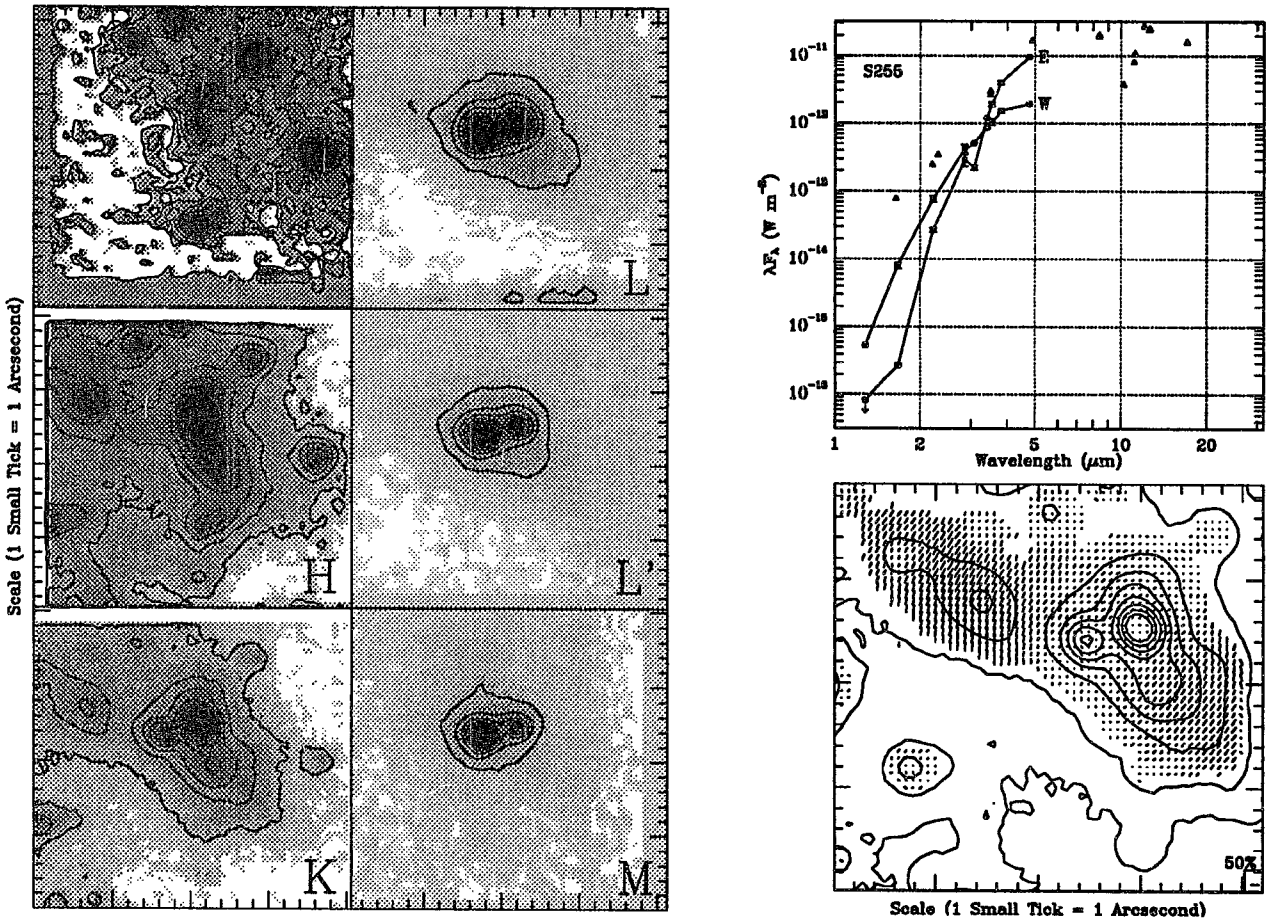

Figure 4.17: The data set for S255-IRS1. The J image is contaminated by non-uniform transmission through the filter. The literature data are from Pipher & Soifer (1976).

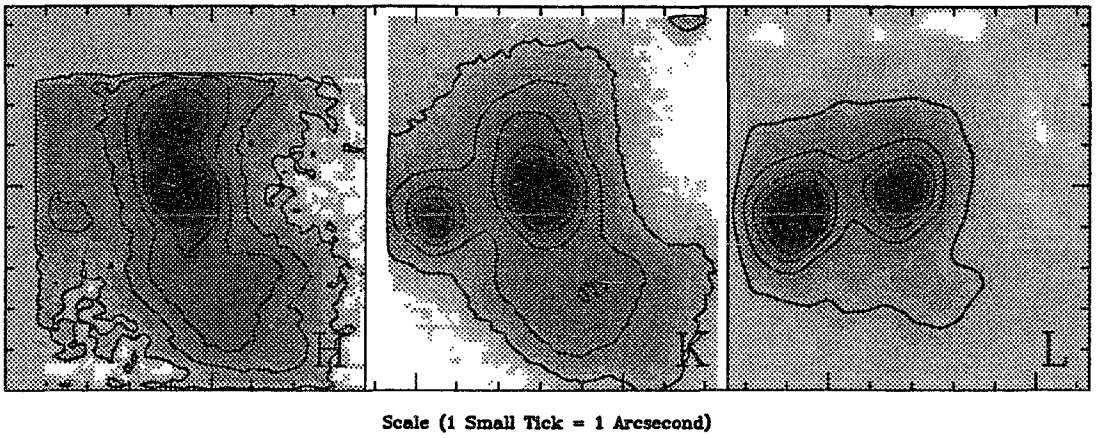

Figure 4.18: High resolution images of S255-IRS1 (0.14 "/pix in 0".5 or better seeing. These images, particularly at L, show the self-luminous nature of the sources.

smoothly joins the longer wavelength data, it is almost certainly responsible for the 20 μm flux observed by Beichman *et al.* (1979).

From the polarization map presented in Figure 4.17, we find that B is the primary illuminating source of the surrounding nebulosity, and we confirm the general bipolar structure found by Tamura *et al.* (1991a). However, we do note that the polarization pattern in the immediate vicinity of the two sources is quite complex. Polarization images at H and L, presented in Figure 4.19 along with the K map, show the same global pattern, but disagree in the details near the two sources. We further note that the polarization of the northeast lobe (~ 8" northeast of B) in the H map is smaller than that in the K map. The most likely explanation for this is that multiple scattering is becoming significant at

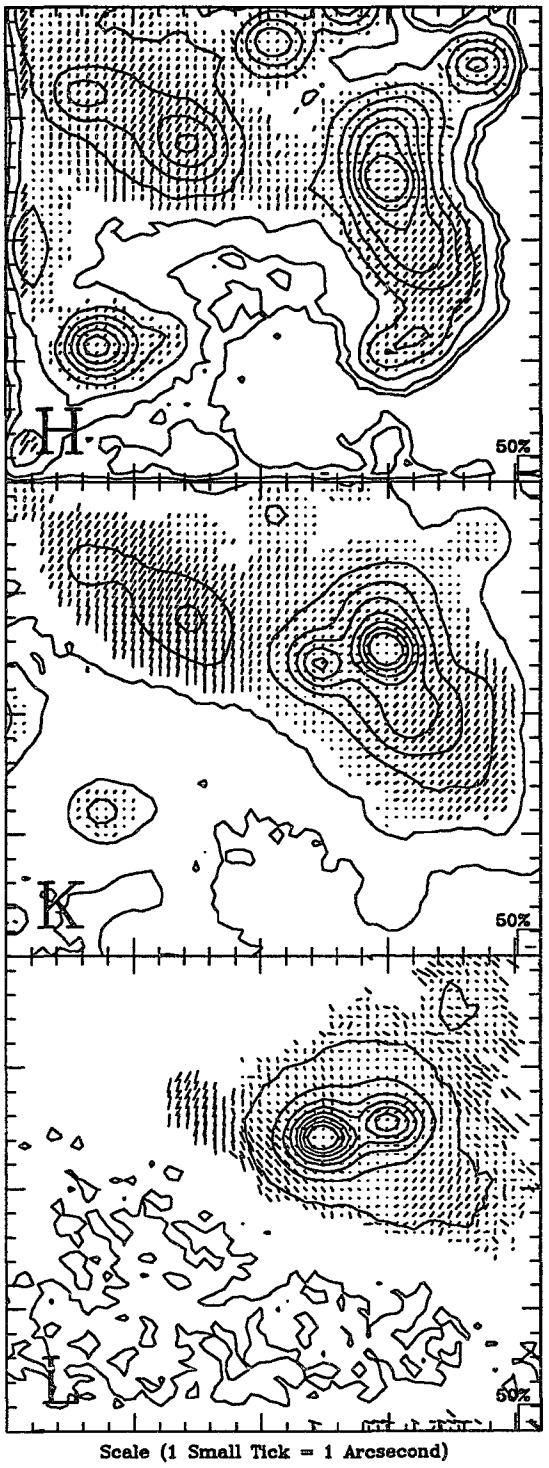

Figure 4.19: Polarization maps of S255-IRS1 at H, K, and L. 50% polarization bars are indicated at the lower righthand corner of each panel (all are the same size).

shorter wavelengths and is prevalent in the immediate vicinity of the sources. Tamura *et al.* reported seeing a polarization disk in S255-IRS1, implying that multiple scattering in a thick disk becomes important near the source; while our data do not convincingly show such a disk at all three wavelengths, multiple scattering does seem to be the most likely explanation of the polarization pattern.

5) *AFGL 961*

AFGL 961 is a double source with a separation of 5".4, in which the eastern source is significantly redder than the western source (Figure 4.20). Castelaz *et al.* (1985b) conclude that 961E is a compact HII region with a diameter of 0".6 illuminated by a B2-3 ZAMS star with a total luminosity of 1000 - 3000 $L_{\odot}$, while 961W appears to be a reddened, 6200 K pre-main sequence star with a luminosity of 4000 - 6000 $L_{\odot}$. Based on 10 μm silicate band depths and fitting interstellar extinction curves, they find that A_V ~ 17 for both sources, implying that the differences in color are directly due to differences in the sources themselves. However, our 3.08 μm water ice measurements indicate that while the extinction to 961W is about 17 magnitudes, the extinction to 961E is approximately 40 magnitudes, implying the colors are caused by extinction. More data on both sources in these two spectral features are needed in order to clarify this discrepancy.

In our images, both sources appear to be point-like. There is a tail of faint nebulosity extending to the north which is visible at all wavelengths less than 3 μm, and

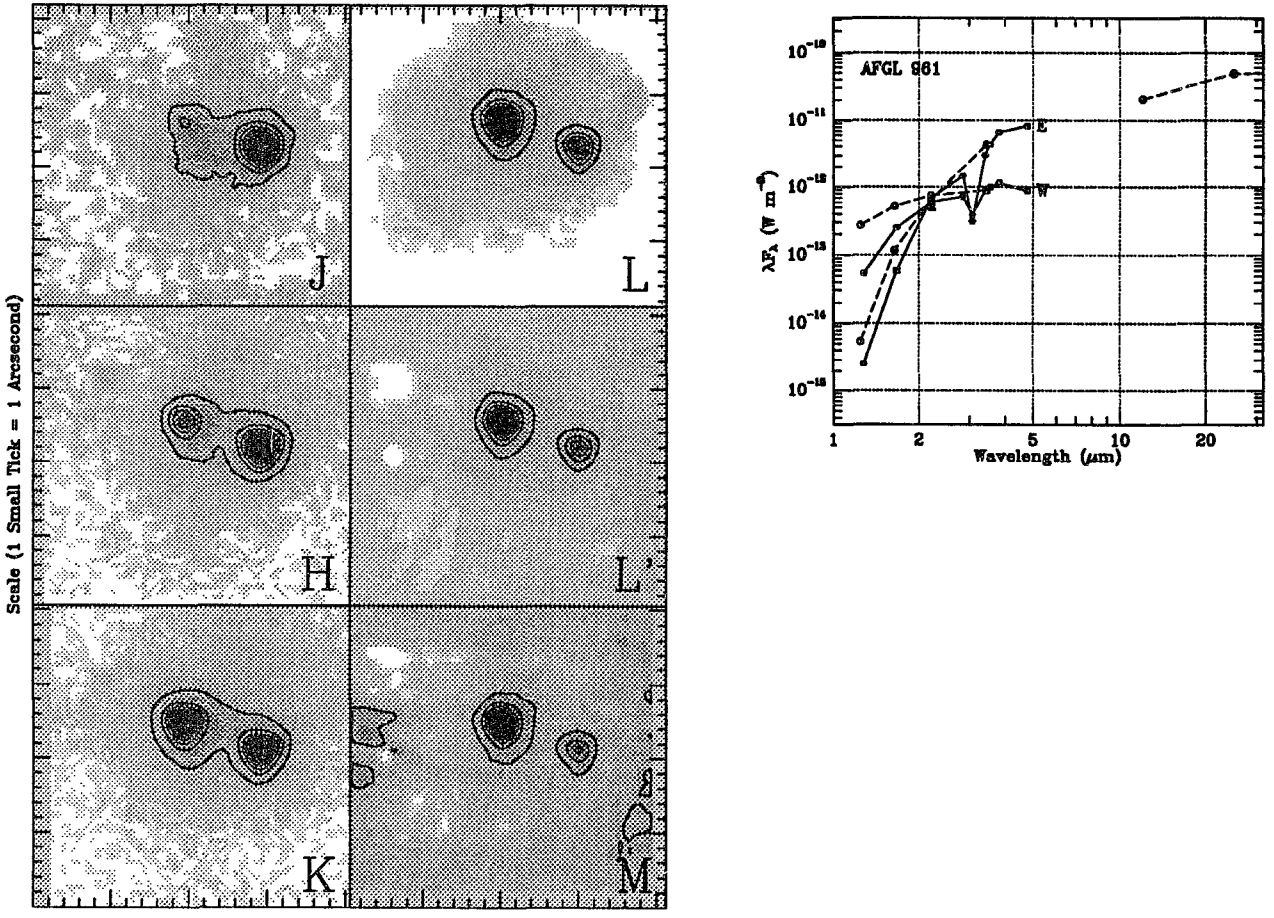

Figure 4.20: The data set for AFGL 961. The literature data are from Castelaz *et al.* (1985b).

there is a faint halo surrounding 961E with a brighter area a couple of arcseconds to the southwest visible at J. Our photometry convincingly demonstrates that at least one of the sources is variable. Castelaz *et al.* (1985) report a difference (E - W) in magnitude at K of 0.17. When we first observed AFGL 961 in 1989 December, the difference was –0.03 ± 0.04 magnitudes and in 1991 January the difference was –0.17 ± 0.02. The relative magnitudes we obtain are extremely reliable since they are derived from the same image; our absolute photometry, while not as good, suggests that both sources are varying. For instance, Castelaz *et al.* reported a K magnitude of 7.84 for 961E, while we measured it at 8.07 and 7.71 in 1989 and 1991, respectively. The brightness of 961W was reported by Castelaz *et al.* to be 7.67, while we measured 8.10 and 7.88.

6) *EL 21*

Castelaz *et al.* (1985a) observed EL 21 (also known as GSS 30) in detail at near-infrared wavelengths and found that the apparent point source IRS1 was the illuminating source for the associated nebulosity. Through several different means, they estimate the extinction to the central source to be approximately 35 mag (A_V), and by Hubble's relation they find that the star is probably type B2 V to A2 V (if it is on the main sequence).

Our images at 0.35 "/pix show EL 21 to be more complex than Castelaz *et al.* (1985a) envisioned (Figure 4.21). First, the "point source" does not really appear to be

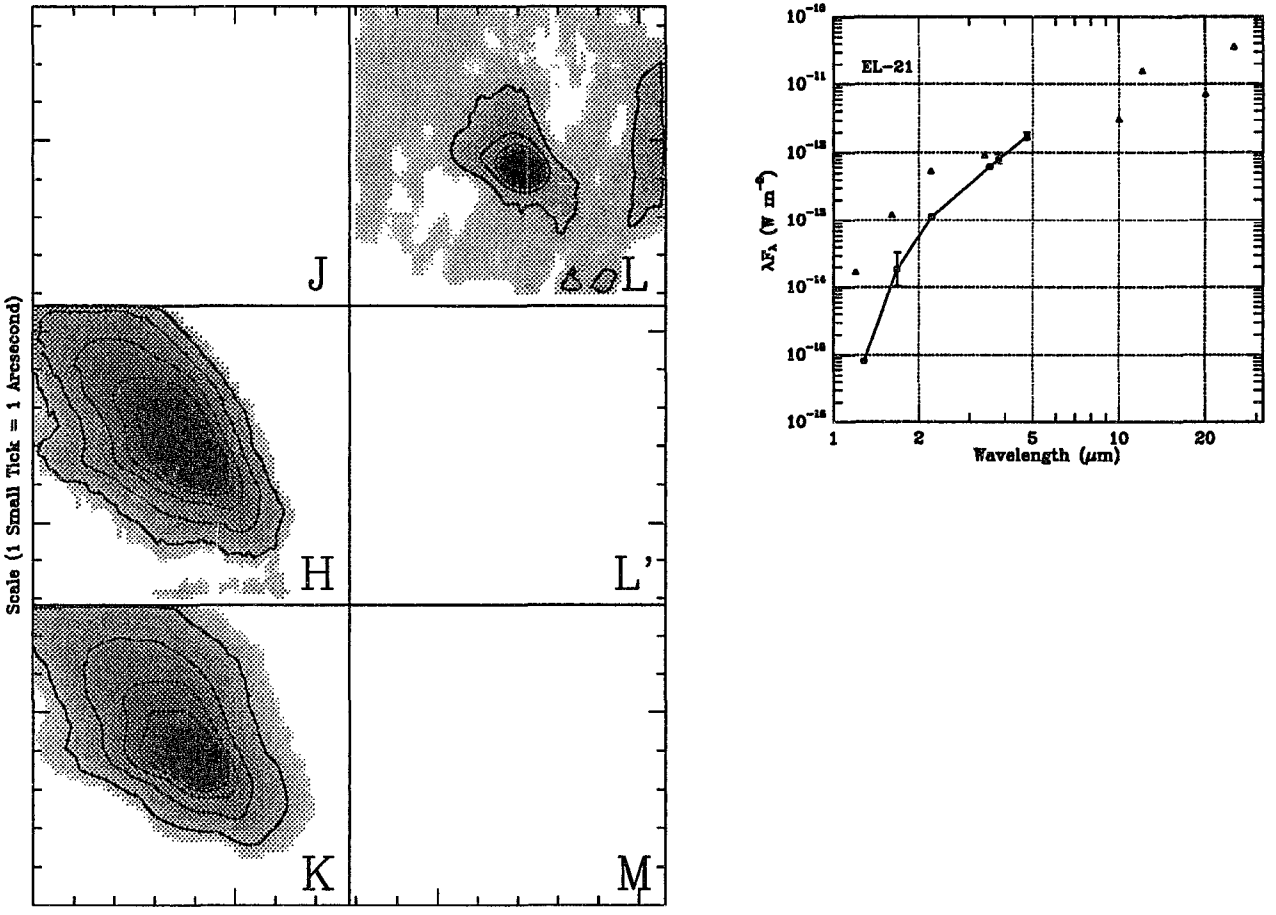

Figure 4.21: The data set for EL 21 (GSS 30). The ProtoCAM photometry is based on higher resolution images presented in Figure 4.21. The literature data are from Elias (1978a) and Clark (1992).

point-like at wavelengths shorter than 3 μm. In fact, the intensity contours, particularly to the northwest, are rather square. In addition, the nebulosity is jet-like, composed of at least five filaments (position angles at 12, 45, 79, 153, and 225°) with one of them (at 225°) appearing to be a "counter-jet". Higher resolution images (0.14 "/pix) reveal nothing new, but they do confirm the squarish nature of the intensity contours around the point source (Figure 4.22).

Because the presumed illuminating source is easily visible in our images, at wavelengths longer than 3 μm where no significant nebulosity is visible, the SED we derive is in relatively good agreement with those previously published. At shorter wavelengths, the departures become more significant and like SVS 12, the jet contributes most of the flux at J, H, and perhaps K. Also like SVS 12, the slope of the SED changes significantly when the flux from the jet is removed - from 1.7 to 2.4 (from K to the *IRAS* 25 μm point).

7) *IRAS 22272+6358A*

Both *IRAS* 22272+6358A and B have only been recently discovered to be protostellar candidates (Ressler & Shure, 1991, and references therein). While they are not as well known as the other objects discussed here, they nevertheless have similar properties and complement the sample well. *IRAS* 22272+6358A appears so be a young source which is seen nearly edge-on through a circumstellar disk and exhibits bipolar jets.

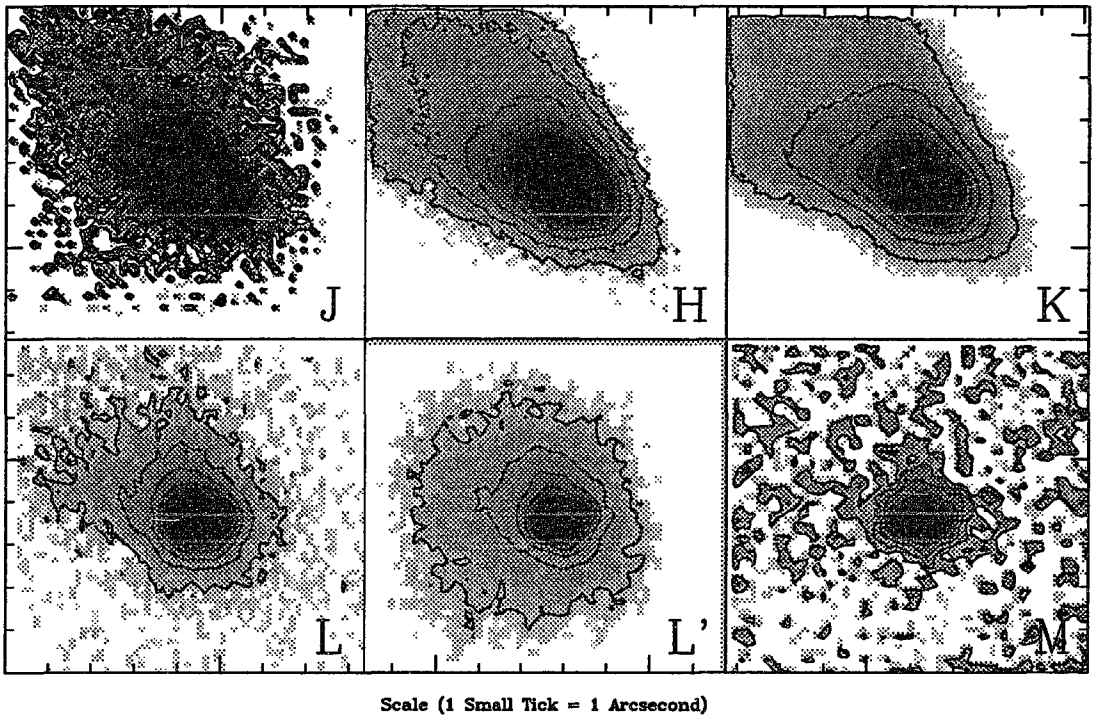

Figure 4.22: High resolution (0.14 "/pix) images of EL 21. Note the squarish contours to the northeast of the source at H and K; these are caused by the filamentary structure of the jet.

A blue-shifted CO outflow exists (Sugitani *et al.* 1989), but it has not yet been possible to establish a convincing outflow direction.

The location of the illuminating source was originally determined from examination of the K band polarization map by finding the point about which a majority of the electric vectors of the northwestern jet were centrosymmetric. Subsequent deep M images (Figure 4.23) show that there is indeed a point source visible at approximately this location. The polarization map in Figure 4.23 is a modified version of the original polarization map; several artifacts in the original data have been removed and the data are no longer binned to enhance the apparent signal-to-noise ratio. The match between the center of the polarization pattern in the northwest jet with the M source is outstanding; the match for the southeast jet, while not as good, is still quite convincing given the much lower signal-to-noise with which it is detected compared to the northwest jet.

In our first paper (Ressler & Shure, 1991), we speculated that the apparent shift in the intensity maximum of the northwest lobe was due to shifts in the last scattering surface similar to the phenomenon reported for LDN 1551-IRS5. Examination of a three-color image (Figure 4.2; made by assigning the K intensity to blue, L' to green, and M to red) and line cuts through these images (Figure 4.24) show that the peaks are in reality knots (at least two) in the nebulosity. The location of the knots observed is independent of the wavelength; only the relative brightness changes between filters. These changes are likely due to steep density gradients in the vicinity of the source.

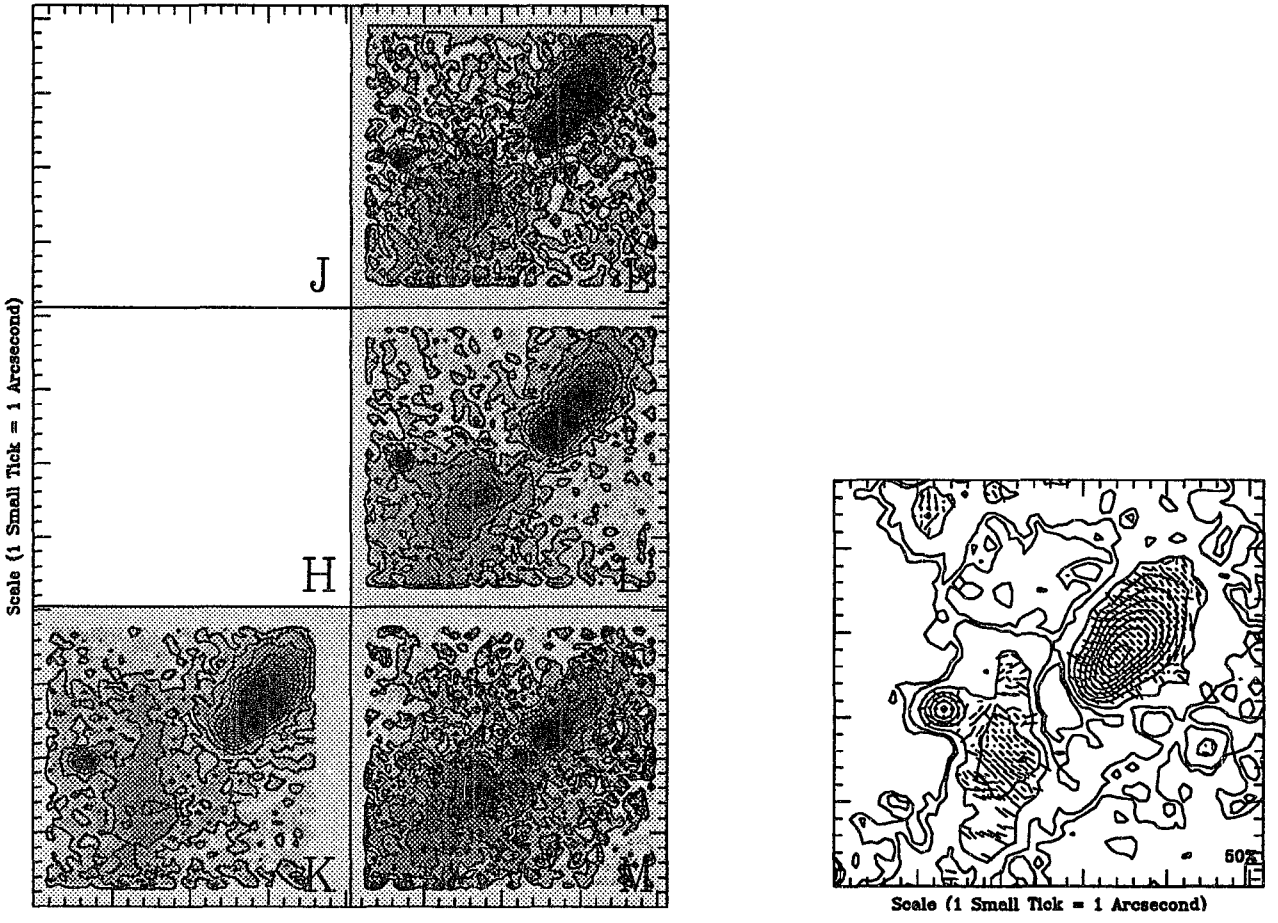

Figure 4.23: The data set for IRAS 22272+6358A. No independent, published photometric data are available, and the illuminating source is visible perhaps only at M.

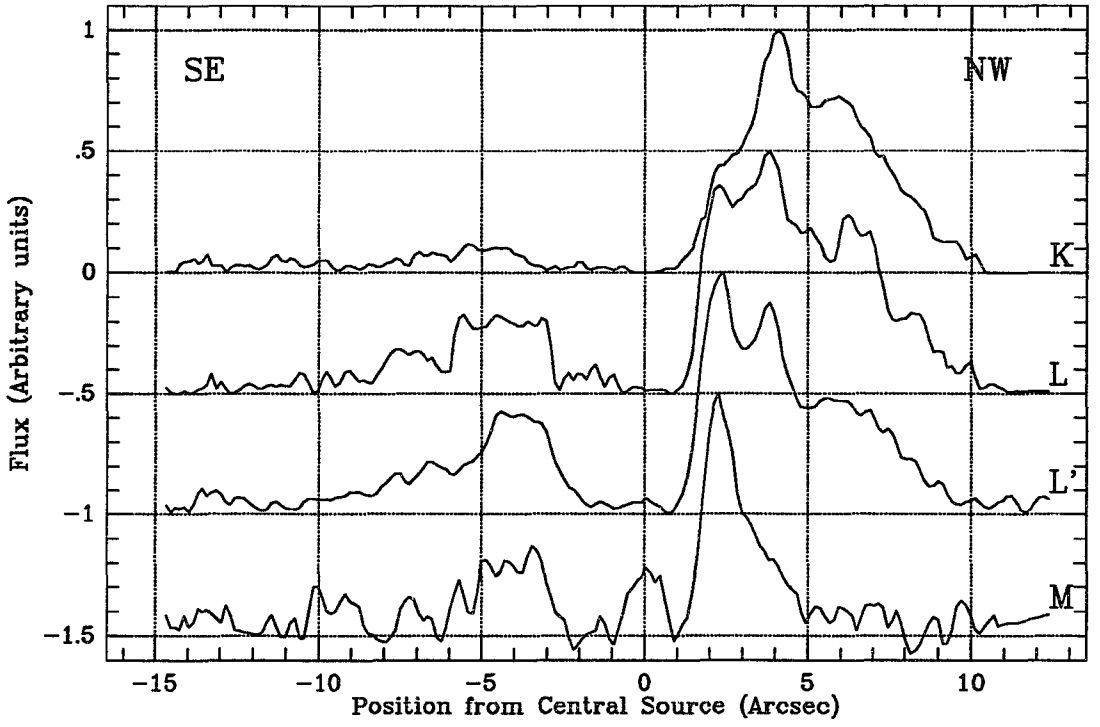

Figure 4.24: Intensity cuts through the nebulosity of IRAS 22272+6358A. The fact the the peaks do not shift, but rather only change intensity, argues that the peaks are knots of material which have differing column depths of material between the scattering surface and the observer.

8) *IRAS 22272+6358B*

IRAS 22272+6358B is a much less deeply embedded source than 22272+6358A, and it appears to illuminate a portion of the LDN 1206 cloud (Figure 4.25). Its SED indicates that it is probably a more mature Class I object since the SED is significantly broader than a blackbody, but it is not so steep as many of the other Class I SEDs reported here.

The polarization map for this source is shown in Figure 4.26. Unfortunately, the issue of whether 22272+6358B is illuminating the cloud is unresolved. The principal problem is that the nebulosity is significantly larger than the ProtoCAM field-of-view; thus most of it is removed during the data reduction process. It was hoped that the bright extension to the northeast would survive this process, but the signal-to-noise ratio has proven to be insufficient to establish if the cloud is illuminated by scattering. A polarization map produced by an instrument with a field of view of two to three arcminutes would be able to adequately resolve this issue.

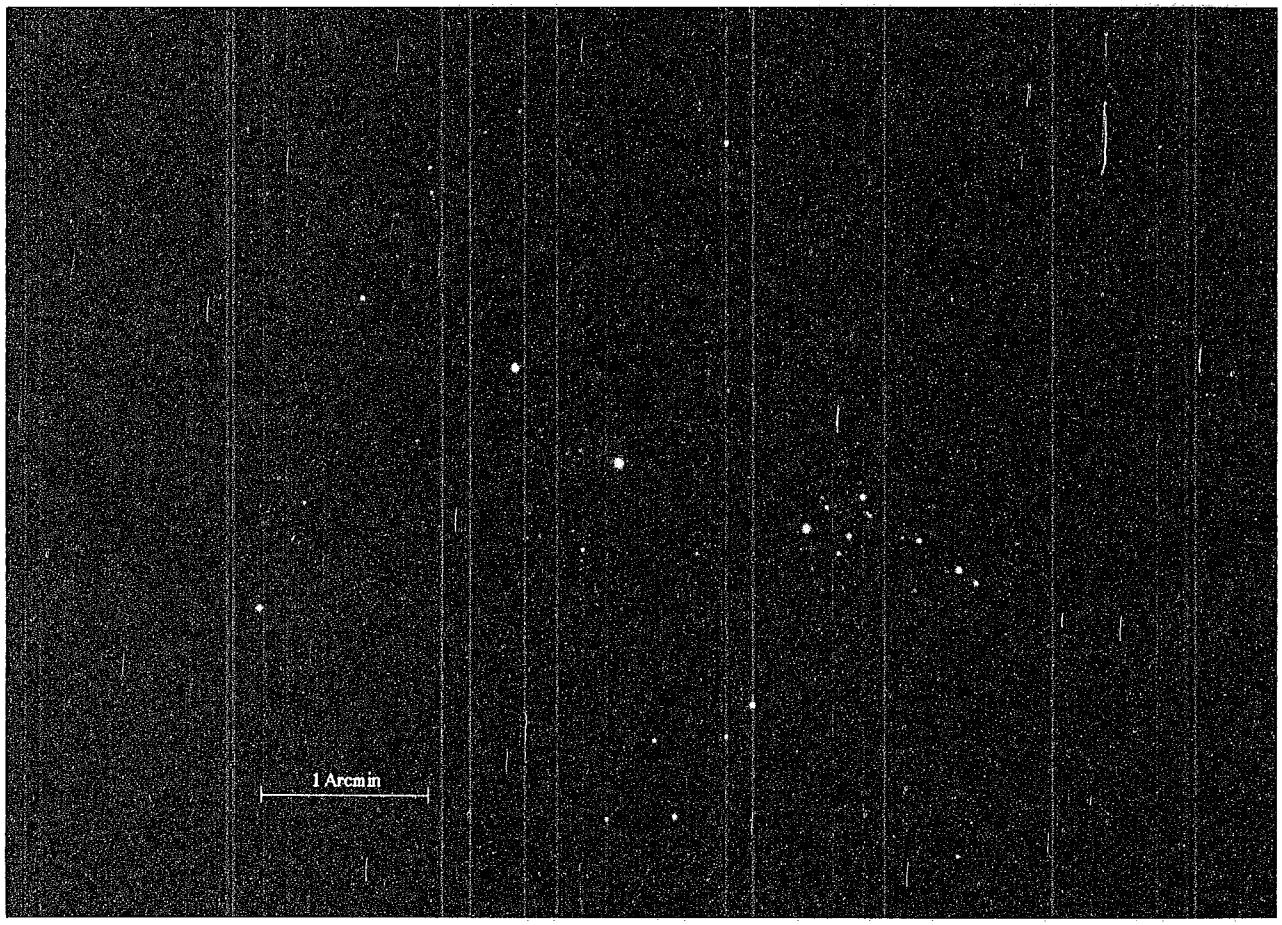

Figure 4.25: A three color composite image of the LDN 1206 dark cloud. The images were taken with the NICMOS 3 near-infrared camera at the University of Hawaii 2.2-m telescope through the J, H, and K filters. The brightest source near the center of the image is 22272+6358B. 22272+6358A is the jet-like nebulosity 40 arcseconds to the west.

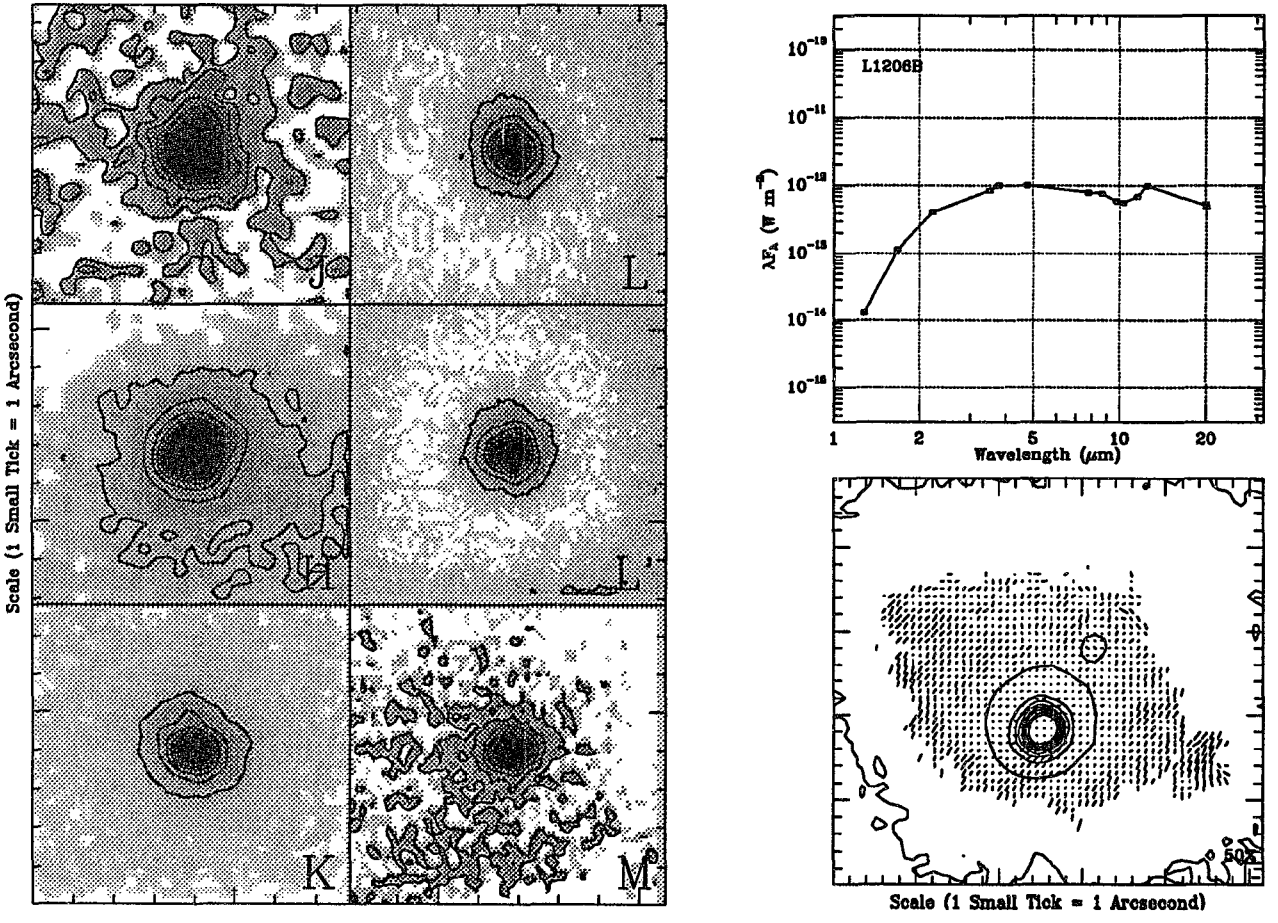

Figure 4.26: The data set for IRAS 22272+6358B. No independent, published photometric data are available.

4.4) DISCUSSION

Comparison to ALS Models

To establish a realistic comparison between our data and the models of ALS in an effort to judge the validity of those models, we must first determine what physical features ALS have included in their models and what those features correspond to in our images. Their basic model has three components: a radiating protostellar "surface", a circumstellar disk, and an infalling dust envelope (AS85, AS86). The protostellar surface is presumed to be at a constant temperature and to radiate energy accumulated through accretion, while the disk is assumed to have a gradient of temperatures and will reradiate intercepted stellar photons as well as radiate its own as a result of accretion. The star and disk will mutually heat and shadow each other and these effects are taken into account in the ALS models. The infalling envelope will absorb photons from both these sources, removing them from the visible and near-infrared parts of the SED and reradiating them in the far infrared.

To simplify the calculations, AS86 make two significant approximations: 1) the luminous energy from the star and disk comes from radii which are much smaller than the radius of the inner edge of the infalling shell; essentially, the star and disk constitute a point source as seen by the shell (with some projection factors modulating the combined

luminosity). 2) The extinction through the infalling envelope is calculated assuming an aspherical rotating envelope shaped like the isodensity contours found by Terebey, Shu, and Cassen (1984); the thermal reemission from this envelope is averaged over all angles, forming an "equivalent spherical envelope". As one of their assumptions, they ignore scattering completely - both into and out of the beam.

Several size scales arise during the course of their modeling. First is simply the stellar radius, R_*, which is given by

$$R_* = \frac{GM\dot{M}}{L} \tag{12.12}$$

where G is the gravitational constant, M is the mass, $\dot{M}$ is the mass accretion rate, and L is the luminosity, which can be rewritten as 3×10^{11} cm (a/0.35 km s^{-1}), where a is the isothermal sound speed (remembering that the luminosity is derived strictly from accretion whose rate is set by the properties of the surrounding isothermal core). Somewhat larger than the stellar radius is the radius at which dust is destroyed. This radius is defined as the radius at which the temperature in the vicinity of the star reaches 2300 K. Because dust cannot exist inside this radius, it forms a natural limit of integration when integrating over the contributions from a dusty disk. At a few times this radius is "r_1" which AS85 used as the inner limit for their infalling dust shell in the non-rotating case. It does not appear in their later models.

Next is the centrifugal radius, R_C, which is the equilibrium radius for a rotating system. If $R_C > R_*$, a circumstellar disk will form and its characteristic dimension will be given by

$$R_C = \frac{\Omega^2 G^3 M^3}{16 a^8} \tag{14}$$

where Ω is the rotational velocity of the cloud core and a is the isothermal sound speed. Thus, R_C is also the size of the region they assume is point-like in their calculations. The outer radius of the free-falling region, or the radius at which the free-falling region meets the ambient cloud, which they denote r_2 is given by

$$r_2 \approx \frac{0.4GM}{a^2} \tag{15}$$

This is the outer limit of integration for the infalling shell used by AS85 and AS86. Material inside this radius will have a density structure which follows an $r^{-3/2}$ power law, while material outside will follow an r^{-2} law appropriate for the isothermal case. Finally, there is the somewhat arbitrary radius r_3 introduced as a new limit of integration by ALS which has the value 2×10^{17} cm. This larger limit was introduced to produce a better match to the *IRAS* beamsize as well as to include possible material which interacts with the protostar but lies outside the infalling radius r_2. Table 4.5 summarizes the more important radii and gives the angular *diameter* of those structures as seen by an observer on Earth.

Table 4.5 - Characteristic Sizes for Observed ALS Objects

Object	R_* – AU (arcsec)[+]	R_C – AU (arcsec)[+]	R_2 – AU (arcsec)[+]	R_3 – AU (arcsec)[+]
04365+2535	1.1×10^{-2} (1.6×10^{-4})	7.7 (0.11)	1800 (25)	13000 (190)
EL 29	2.0×10^{-2} (2.5×10^{-4})	180 (2.2)	2900 (36)	13000 (160)
Haro 6-10	1.1×10^{-2} (1.6×10^{-4})	19 (0.28)	4400 (64)	13000 (190)
LDN 1489-IRS (04016+2610)	1.1×10^{-2} (1.6×10^{-4})	9.9 (0.14)	3600 (51)	13000 (190)
LDN 1551-IRS5	1.9×10^{-2} (2.7×10^{-4})	24 (0.35)	2300 (32)	13000 (190)
LDN 1551-IRS5 (alternate)	2.0×10^{-2} (2.9×10^{-4})	44 (0.63)	2900 (41)	13000 (190)
WL 16	2.0×10^{-2} (2.5×10^{-4})	140 (1.7)	1500 (18)	13000 (160)

[+] Numbers in parentheses are the apparent angular diameter, 2R/D, where D is the distance to the object.

The comparison of our profile fitting photometry to the ALS models is summarized in Figure 4.27. For each object, a digitized version of the ALS model, data obtained from the literature which ALS used to fit their model, and our imaging photometry data are shown. (For LDN 1551-IRS5, our brightnesses are obtained from false aperture photometry; brightnesses for the other objects were obtained by profile fitting). Only one object out of the five with a near-infrared "excess" (EL 29 is excluded) can be made to match the models by excluding resolved extended emission, if any exists. Explanations other than scattering geometries must be invoked to explain the failure of the ALS models in these four cases.

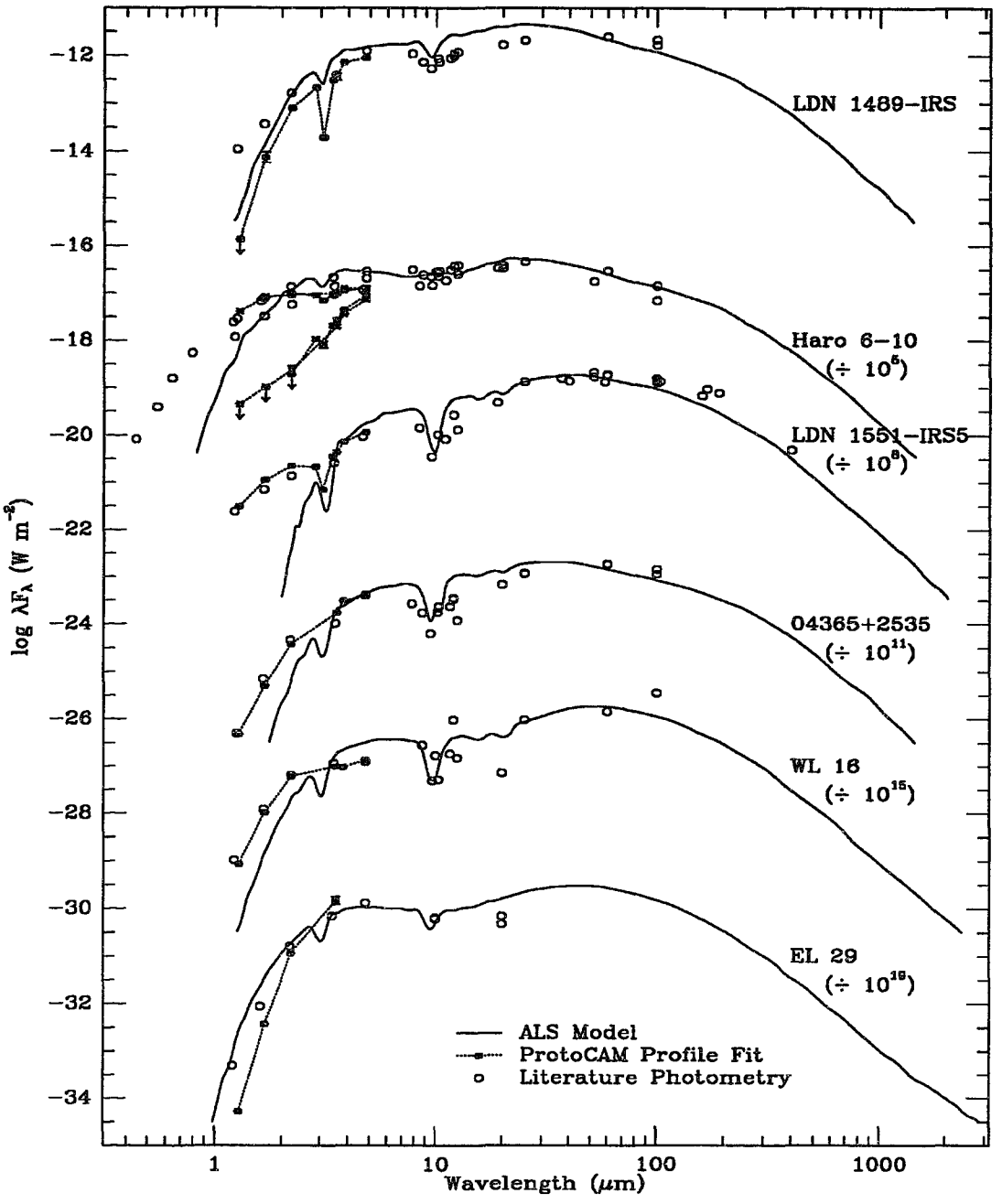

Figure 4.27: The SEDs of the six sources modeled by ALS which we observed. The SEDs have been shifted vertically for clarity (indicated beneath the object label). See the respective data set figures for the source of the literature data. The LDN 1551-IRS5 data were derived from false aperture photometry rather than profile fits.

A potential reason for our inability to reconcile the observations with the ALS models is that our beam size is much smaller than many of the scales in their models, and thus it is possible that we are observing only a part of the flux they predict. However, even though much of the structure modeled by ALS is in principle resolvable with a resolution like ProtoCAM's, perhaps even the circumstellar disks (R_C) predicted for the Ophiuchus cloud, most of it is not hot enough to be visible at near-infrared wavelengths. In fact, the only components of the model which should affect the NIR part of the SED are the emission from the stellar photosphere and from the innermost regions of the circumstellar disk (at radii where the temperature has not yet fallen below ~ 500 K - presumably less than ~ 1 AU and thus completely unresolved), and the extinction through the infalling shell. Except for scattering, we should be observing (both with single-beam photometry and imaging) exactly what is modeled at near-infrared wavelengths.

This is perhaps the case for LDN 1489-IRS and the excellent agreement between its SED and the model computed by ALS (after adjusting the luminosity downward as in Figure 4.3). At wavelengths less than 3 μm, the nebulosity (integrated over the entire surface) appears significantly brighter than the illuminating source; slightly brighter at K, one order of magnitude brighter at H, and more than two orders of magnitude at J. At H and K, the point source is very distinct, so that an accurate profile fit is possible; at J the source is not visible so that only an upper limit is possible. The fits should eliminate all light which has been scattered into the beam from regions ProtoCAM can resolve. Our profile fits will still differ from the models if the amount of light scattered *out* of the

beam by line-of-sight scatterers is significant, but this apparently does not affect the shape of the SED enough to be noticeable in LDN 1489-IRS.

Scattering which is not resolved can, of course, severely influence the number of photons reaching the observer if the scattering is anisotropic or if the distribution of scatterers is not spherically symmetric. Both Code (1973) and Jones (1973) derive the reduction of the apparent optical depth to a source if it is surrounded by a spherically symmetric dust cloud and Jones briefly extends the discussion to the asymmetric case. The essence of the argument is that scattering will put photons back into the beam to replace photons which have been scattered out. Two limiting cases are useful to bear in mind; in the limit of the albedo going to one (pure scattering) with a source of intensity I_0, an unresolved source will appear to be unaffected since as many photons will be scattered into the beam as scattered out, thus $I_{obs} = I_0$. In the limit of the albedo going to zero (pure absorption), photons will only be absorbed so that we will see just those photons which originated along the line-of-sight to the point source, thus the intensity will follow $I_{obs} = I_0 \, e^{-\tau_\nu}$. By similar mechanisms, the NIR excess (and importantly, the high polarization) can remain even if the source is unresolved as long as an asymmetrical scattering geometry is present. This may be the case in 04365+2535. The brightness of the nebulosity is insignificant with respect to that of the point source and will not account for the order of magnitude excess at J, H, and K. The fact that the point source has an intrinsic polarization of 15% in the same direction as the polarization of the nebulosity argues strongly for scattering structures with scales less than ~ 150 AU.

Haro 6-10 and WL 16 illustrate the danger of having only an incomplete understanding of an object before attempting to model it. While Haro 6-10 is composed of two types of objects which ALS modeled, the combination of the two produced an SED which was deceptively broad. Accordingly, the mass and angular velocity (Ω) would be overestimated (even though the fitted angular velocity is already lower than for any of the other objects). It would, of course, be interesting to see the ALS models reapplied to Haro 6-10 now that we have a better understanding of its nature. WL 16 showed that even though the depth of the silicate feature may be a reasonable diagnostic, one must make certain that it is in actuality the silicate feature being observed, not a collection of emission lines. Both types of problems (multiplicity and confusion) should be resolvable with the new generation of instruments. Both sub-arcsecond direct imaging at thermal infrared wavelengths and velocity-resolved spectroscopy at all infrared wavelengths will allow the detection of binary/multiple systems, while moderate and high resolution spectroscopy will allow the distinction between absorption bands and sets of emission features.

EL 29 is intriguing, not because of the fact that the ALS model fit it well in the NIR (the only one of the seven they modeled), but that the SED has changed so radically from those earlier observations. We will discuss this further below.

Binaries/Multiples

It is apparent from our images that many of these protostars are members of binary/multiple systems; in fact, five of the fourteen objects described in detail here may be double: AFGL 961, Haro 6-10, HH 43-IRS1, S255-IRS1, and SSV 63 (which is perhaps a "double double"). This sample can be enlarged somewhat by including objects which we surveyed but were not able to follow up in depth. The total number of objects in this list (including the 14 original objects) is 31, of which 12 may have "companions" (Table 4.6 and Figure 4.28). This fraction (39%) compares favorably with the 42% of Main Sequence stars found to be visual binaries by Heintz (1969, and quoted by Abt, 1983) given the small number statistics of the data presented here. Abt also gives data for the frequency of binaries as a function of their period for B, F, and G stars. While we do not have periods for our doubles, we make order of magnitude estimates by assuming the combined mass is 1 $M_{\odot}$, the eccentricity of the orbits is zero, and the stars are near their maximum separations. The stars presented here would thus have periods ranging from 10^3 to 10^6 years. The number of binaries we observe is roughly consistent with the total number of stars in these period bins presented by Abt (~ 30%).

Of course, the sample presented here is hardly unbiased. The most important bias is that there are a range of distances represented, thus objects which can be resolved at close distances (such as in the Taurus or Ophiuchus star formation regions) will appear unresolved at larger distances, while objects which appear double at large distances might

Table 4.6: Binary/Multiple Data

Object	Coords (1950.0)	ΔK (Mag)	Δ[H–K] (Mag)	Position
Haro 6-10	04 26 22.0 +24 26 30	> 4.24	1.08 (L–M)	1.32" @ 356°
HH 43-IRS1	05 35 42.1 –07 10 09	1.37	–1.38	3.25" @ 180°
SSV 63 (SSV 63W)	05 43 34.7 –00 11 08	> 3.06	1.31 (L–M)	2.48" @ 337° 1.98" @ 350°
S255-IRS1	06 09 58.4 +18 00 12	1.16	2.47	2.49" @ 104°
AFGL 961	06 31 59.1 +04 15 10	0.17	–1.74	5.41" @ 251°
BIP 11	06 41 12.5 –01 05 02	1.72	1.18	2.20" @ 304°
BIP 14	06 56 47.4 –03 55 24	1.14 1.40	--- ---	1.46" @ 167° 3.40" @ 103°
WL 1	16 24 02.4 –24 21 46	0.10	0.25	0.91" @ 140°
SR 21	16 24 08.9 –24 12 31	3.53	–0.21	6.37" @ 175°
WL 20	16 24 13.9 –24 31 59	0.45 3.22	–0.13 1.94	3.78" @ 278° 4.06" @ 229°
WL 4	16 24 16.8 –24 22 23	0.50 1.97	2.74 > 1.32	13.95" @ 341° 15.73" @ 308°
SR 24	16 27 56.4 –24 38 48	0.68	0.00	5.14" @ 348°

Single Sources

SVS 12	03 25 55.7 +31 10 03	Mon R2-IRS3	06 05 21.8 –06 22 26
SVS 13	03 25 58.3 +31 05 47	AFGL 989	06 38 25.3 +09 32 29
SVS 5	03 26 14.7 +31 08 17	EL 21	16 23 19.9 –24 16 18
LDN 1489-IRS	04 01 40.6 +26 10 49	WL 16	16 24 00.3 –24 30 44
LDN 1551-IRS5	04 28 40.2 +18 01 42	EL 29	16 24 07.8 –24 30 33
04365+2535	04 36 31.0 +25 35 52	W 33-IRS3	18 11 17.8 –17 56 34
BN	05 32 46.7 –05 24 17	NGC 7129-IRS1	21 42 51.2 +65 57 42
HH 34-SRC	05 33 03.7 –06 28 53	22272+6358A	22 27 11.5 +63 58 19
SSV 59	05 43 31.2 –00 15 22	22272+6358B	22 27 17.6 +63 58 17
Mon R2-IRS2	06 05 19.4 –06 22 24		

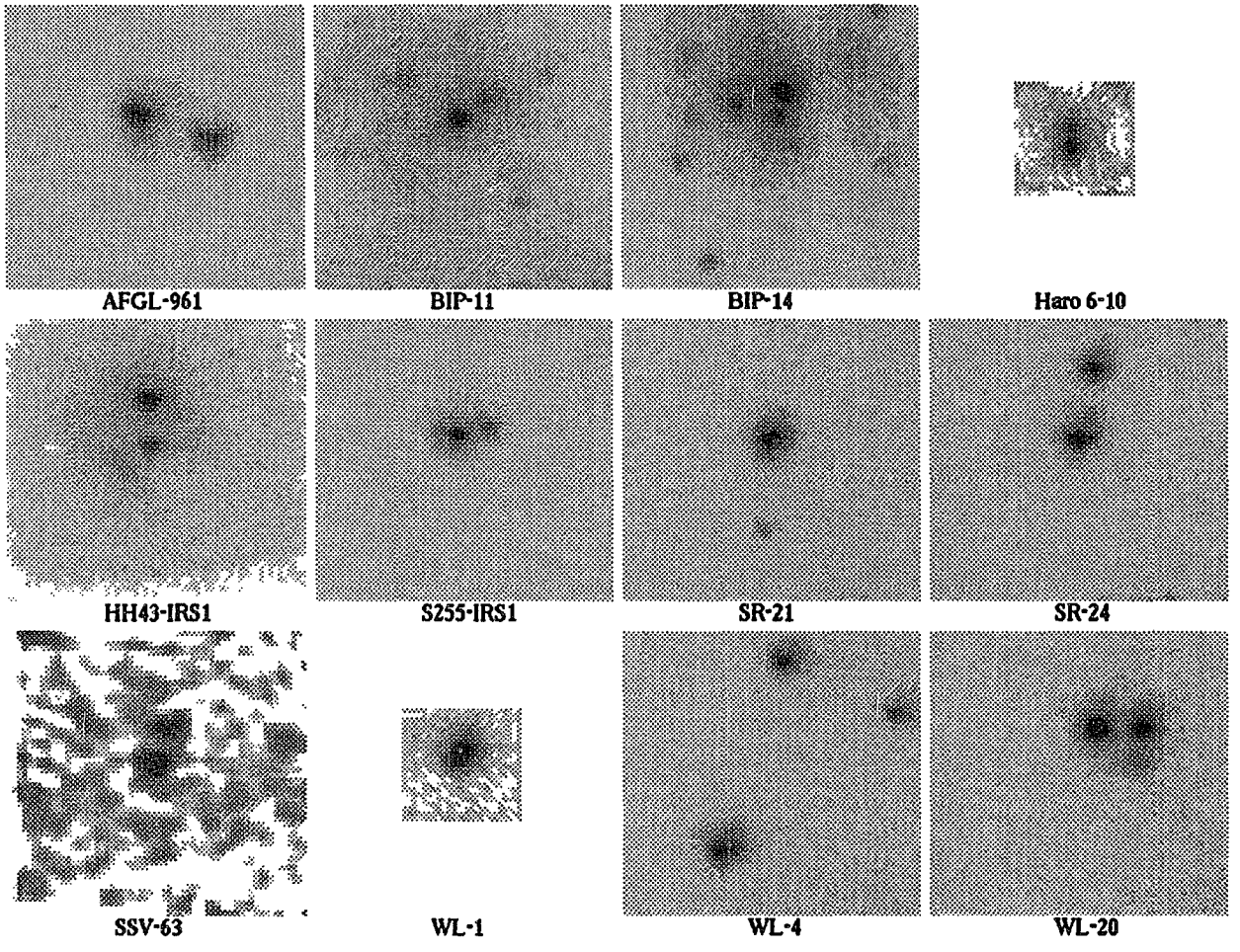

Figure 4.28: Images of the 12 multiple systems. All images were taken at a plate scale of 0.35 "/pix or were rebinned to this value; M images are shown for Haro 6-10, S255-IRS1, and SSV 63, while K images are shown for the remainder.

not both appear on an image if they were at the distance of the nearer regions. Both of these effects would decrease the number of multiples we find, although some chanceassociations might be added for systems at large distances.

We have no unambiguous way of knowing from our images whether the systems are truly physically associated, or whether they are chance alignments with foreground or background stars. In some cases we can argue that they are associated based on common nebulosity, particularly if polarization maps are available (e.g. HH 43-IRS1, SSV 63). A second argument is that the predicted density of field objects is too low to produce chance alignments. For instance, Simon *et al.* (1992) have computed the surface density of field stars brighter than K = 12 for the Taurus star forming region and found a value of 4×10^{-5} arcsec^{-2}. Since the field-of-view of ProtoCAM covers 420 arcsec^2, there is only a ~ 1.5% chance of finding a second star brighter than 12th magnitude in the image. Thus Haro 6-10 is almost certainly an associated pair. In other cases, we argue that the pairs are associated either by virtue of similar colors (implying similar extinctions, e.g., WL-1, SR-24) or because the extinctions to both sources are quite large (e.g., S255-IRS1, AFGL 961).

In spite of these two effects, the fact that we observe roughly the same number of multiples in our survey as exist under similar observing conditions for Main Sequence stars hints strongly that the Main Sequence distribution is established in its basic form at the earliest times in the star formation process (for at least the long period binaries).

Simon *et al.* (1992) concluded that the multiplicity of pre-Main Sequence stars in Taurus follow a Main Sequence distribution; the ages of these stars are of order 10^6 years. Since many of the sources in our sample are believed to be of order 10^5 years or less (cf. Zinnecker & Wilking 1992), it is likely that the distribution is established well before the end of the Class I YSO phase.

A final interesting feature of the data presented here is the association of a deeper H_2O ice band with the redder companion. Zinnecker & Wilking (1992) point out that the relative depth of the ice band is one of several important keys for trying to determine whether the formation of binaries is coeval or non-coeval and will also address the issue of whether or not circumstellar disks in binaries are misaligned. Haro 6-10 definitely follows the expectations of greater optical depth for the redder object (0.69 vs. 0.38) as do AFGL 961 and S255-IRS1, although these are not the low mass, infrared companion systems Zinnecker & Wilking are primarily addressing. SSV 63:A also displays a deep ice feature; unfortunately, we are able to derive only a lower limit to the companion's (D's) optical depth, but we expect it to be deeper as well. The correlation of deeper ice features to the redder object implies a greater column density to the companion. There are several formation scenarios that would predict this feature: 1) the companion itself is less massive so that it is evolving out of Class I slower than the more massive primary; 2) the companion formed at a slightly later time and is simply lagging behind the primary in its development; or 3) the circumstellar disks are misaligned and thus we are observing one member nearer to edge-on through the disk. Further observations are necessary to

distinguish between these possibilities: velocity-resolved spectra of photospheric features may allow determination of masses for the individual components or observations of outflows (either NIR or radio) from more than one component are necessary to distinguish between the possibilities.

Variability

An unexpected result of the observations presented here is the large number of variable sources. Five of the fourteen systems show evidence of variability: Haro 6-10, AFGL 961, SSV 63, EL 29, and LDN 1551-IRS5 (Table 4.7). The first three are multiple systems which varied significantly during the course of our observations. Since these sources have two or more objects per image, the relative brightnesses within a single image (which can be obtained with greater accuracy than absolute brightnesses) can be used as an indicator of variability; variations in sky quality or instrumental sensitivity are thus no longer an issue. We consider the variability of these three sources to be beyond doubt.

EL 29 and LDN 1551-IRS5 are single sources, thus we must rely on absolute photometry to determine variation. The internal consistency of our data coupled with the fact that systematic deviations are observed at four or more wavelengths with respect to

Table 4.7: Variability data

Object	Initial Date	Final Date	ΔJ	ΔH	ΔK	ΔL	ΔL'	ΔM
Haro 6-10:B	90/11/24	91/01/07	—	—	—	–0.34	–0.23	–0.19
AFGL 961	89/12/22	91/01/07	—	—	0.36(E)[a] 0.22(W)	—	—	—
SSV 63:A	89/11/07	91/01/09	—	–0.42	–0.38	–0.53	—	—
EL 29	77/05/21[b]	89/09/02	2.37	0.89	0.41	–0.89	—	—
LDN 1551	81/12/03[c]	91/01/09	–0.32	–0.43	–0.45	–0.56	—	–0.20
A_V = 10 Mag[d]	—	—	2.6	1.6	0.84	0.33	0.28	0.19

Notes: a) Although the variations listed here may be systematic rather than real, at least one definitely varied since the single-frame relative brightness changed. b) From Elias (1978a). The data have not been color corrected, thus the differences are only approximate. c) From Cohen & Schwartz (1983). The data have not been color corrected. d) Each entry in this row represents the change in magnitude if 10 mag A_V is added between the source and the observer (based on the extinction curve of Draine & Lee, 1984).

previously published observations lead us to conclude that they too have varied, but over longer timescales.

The color dependence of the variations of Haro 6-10, LDN 1551-IRS5, and SSV 63 are similar in the sense that the changes in the SED are relatively "gray" – all wavelengths change by roughly similar amounts, thus preserving the general shape of the SED, while the variation of EL 29 appears to have significantly altered the SED (we do not have enough wavelength coverage of AFGL 961 to determine if the SED has changed shape). The variation of Haro 6-10:B is the only one which is reasonably consistent with fluctuating foreground extinction which obeys an interstellar extinction law (e.g., Draine

& Lee, 1984; the wavelength dependence of this is indicated by the bottom row of Table 4.7). Given that we have reasonable estimates of the extinction to Haro 6-10:B (13.5 A_V, based on the 3.08 μm water ice band depth) a fluctuation of the required 10 A_V seems unreasonable, but we cannot rule it out without information on whether the depth of the ice band depth has also varied. Extinction could still play a role in the grayish variations if the obscuring particles were very much larger than the wavelengths discussed here (and thus very much larger than the grains in the interstellar medium), but we consider that unlikely without other evidence. Perhaps the grayish luminosity variations are caused by fluctuations in the mass accretion rate onto the star and disk. Such fluctuations should change the luminosity ($GM\dot{M}/R_*$ × geometrical factors) without radically changing the apparent temperature distribution (estimated from figures in AS86 and ALS). In addition to variable accretion rate, Liseau *et al.* (1992) explore the possibility of an "eclipsing" infrared companion producing the observed changes in SVS 13, an object similar to those investigated here. The change in SVS 13's SED appears to be due to the addition of a 1170 K blackbody source, so they propose the possibility that the sudden brightening of SVS 13 is caused by the reemergence of the companion from behind the primary's disk. While we regard companions as unlikely to explain variability in the cases presented here, the possibility of observing eclipsing, binary protostars is very intriguing.

The variations of EL 29 appear to be of a somewhat different nature. The changes in the shape of the SED of EL 29 are so large, data from a non-photometric night

(discrepancy between two standard stars is approximately 0.4 mag) confirm the results of photometric data presented in Figure 4.11 and extend the trend through L' (Figure 4.29). Elias (1978a) noted that EL 29 was variable over the year he observed it, but the variationhe saw was grayish, similar to what we observed in the previously mentioned sources. There are at least two possible mechanisms to alter the SED in this manner: 1) there has been a decrease in the temperature of the emitting surface with a corresponding increase in the surface area since the luminosity has apparently not decreased; perhaps the inner regions of an optically thick disk have cleared because of a sudden collapse of material onto the star or conversely, a stellar wind has pushed material out of the inner regions of the disk; this allows stellar photons to reach deeper into the disk, and moves the apparent radiant surface to larger radii where the equilibrium temperature is lower; or 2) there has been an increase in the circumstellar extinction to the source which has removed photons from the NIR: the circumstellar material could be clumpy and we are now looking through a denser volume of that material. The objection to extinction in the grayish variations does not apply as strictly here since the variations are strongly wavelength dependent, even if they do not obey the general interstellar extinction law. More observations over a longer time period and over a greater wavelength range are needed to distinguish between the possibilities. In particular, changes in brightness at 10 – 30 μm could allow the separation of the two effects; we might expect the mid-IR to undergo greater variations if the first scenario is correct since the effective temperature shift will move the radiant peak from NIR to longer wavelengths while the increased surface area will maintain the total luminosity; the second scenario should move the

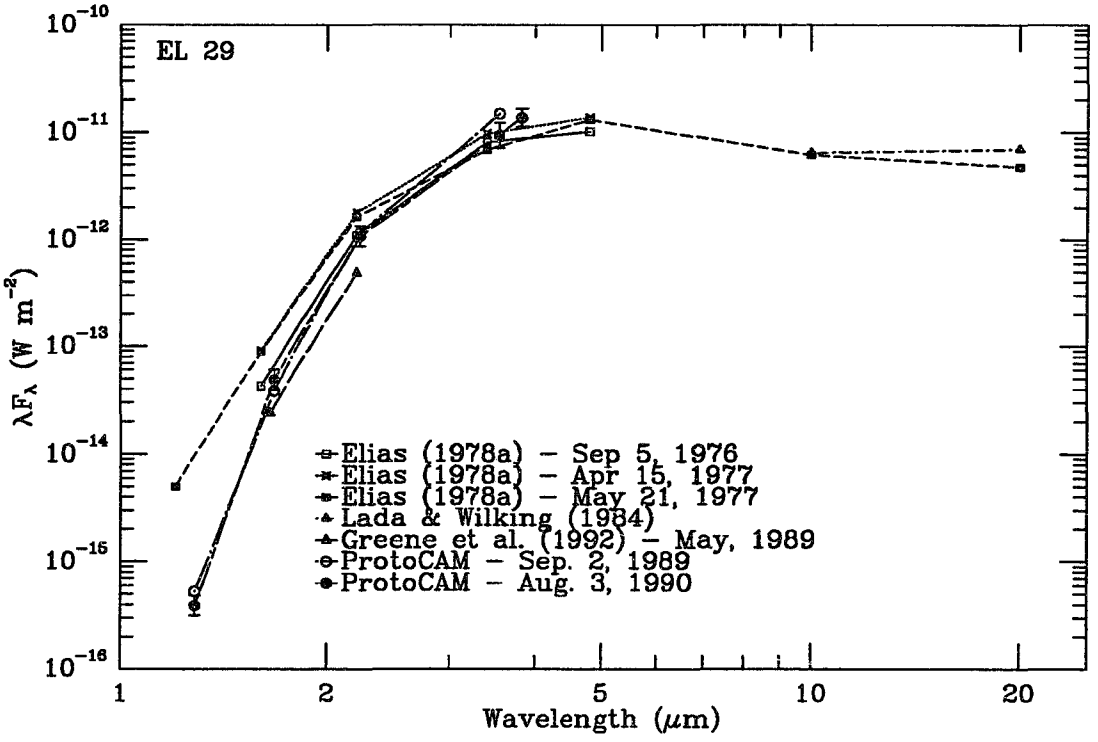

Figure 4.29: Detail of the 1 – 5 μm portion of EL 29's SED. The data taken on 1990 August 3 are not photometric, but they do confirm the change in the shape of the SED between the times of Elias' observations and ours.

optical and NIR photons into the far-IR without greatly altering the mid-IR flux. Monitoring the depth of the 3.08 μm water ice feature and the 10 μm silicate feature is also critical since this would either confirm or rule out changes in the column density of material and thus extinction to the star.

4.5) CONCLUSION

We have observed six of the seven Class I YSOs modeled by Adams *et al.* (1987) to gain a greater understanding of the individual objects in an effort to test the validity of their models as applied to the near-infrared portion of the spectral energy distributions. The ALS models appear to explain the basic components of observed protostellar SEDs and provide useful diagnostics for understanding the evolution of extremely young, deeply embedded objects. We conclude that the model's chief failure in the NIR is the inability to account for scattering in the immediate environment of the protostar (not too surprising given the unique morphologies of many protostars). In addition, we have seen that an incomplete understanding of a protostar's observable properties (multiplicity, line/band spectrum, etc.) can lead to inappropriate uses of the model.

An additional eight sources were observed in detail to establish a broader base of objects which have been imaged over the entire 1 – 5 μm wavelength range. We have found that scattered radiation is significant enough in many sources to affect the power

law index of the SED used by some authors to classify the objects. This simple fact points to the necessity of high resolution imaging as a tool in properly classifying YSOs.

Finally, we have found that a significant fraction of these objects are binary/multiple and many are variable. It is extremely important that follow-up observations be made of the variable sources in an effort to determine the driving phenomena of the variations. These variations can provide direct clues to the nature of the circumstellar environment. Observations of a much larger sample of Class I YSOs are necessary to convincingly prove that they follow the same multiplicity distribution that Main Sequence stars follow. The results presented here hint that they do, but a large, unbiased survey is needed to give this result a firm footing.

REFERENCES

Abt, H. A. 1983, ARAA, 21, 343

Adams, F. C., Lada, C. J., and Shu, F. H. 1987 (ALS), ApJ, 312, 788

Adams, F. C. and Shu, F. H. 1985 (AS85), ApJ, 296, 655

Adams, F. C. and Shu, F. H. 1986 (AS86), ApJ, 308, 836

Aspin, C., McLean, I. S., and Coyne, G. V. 1985, A&A, 149, 158

Beichman, C. A., Becklin, E. E., and Wynn-Williams, C. G. 1979, ApJL, 232, L47

Beichman, C. A., Myers, P. C., Emerson, J. P., Harris, S., Mathieu, R., Benson, P. J., and Jennings, R. E. 1986, ApJ, 307, 337

Boss, A. P. 1991, Nature, 351, 298

Campbell, B., Persson, S. E., Strom, S. E., and Grasdalen, G. L. 1988, AJ, 95, 1173

Capps, R. W., Gillett, F. C., and Knacke, R. F. 1978, ApJ, 226, 863

Castelaz, M. W., Hackwell, J. A., Grasdalen, G. L., Gehrz, R. D., and Gullixson, C. 1985a, ApJ, 290, 261

Castelaz, M. W., Grasdalen, G. L., Hackwell, J. A., Capps, R. W., and Thompson, D. 1985b, AJ, 90, 1113

Clark, F. O. 1992, ApJS, 75, 611

Code, A. D. 1973, in Interstellar Dust and Related Topics. IAU Symp. No. 52, Greenberg and Van de Hulst (eds.), Reidel, Dordrecht, p. 505

Cohen, M. & Fuller, G. A. 1985, ApJ, 296, 620

Cohen, M. & Jones, B. F. 1987, ApJ, 321, 846

Cohen, M. & Schwartz, R. D. 1983, ApJ, 265, 877

Cohen, M., Harvey, P. M., Schwartz, R. D., and Wilking, B. A. 1984, ApJ, 278, 671

Davidson, J. A., & Jaffe, D. T. 1984, ApJL, 277, 13

Draine, B. T. & Lee, H. M. 1984, ApJ, 285, 89

Elias, J. A. 1978a, ApJ, 224, 453

Elias, J. A. 1978b, ApJ, 224, 857

Goodrich, R. W. 1986, AJ, 92, 885

Hanner, M. S., Tokunaga, A. T., and Geballe, T. R. 1992, sub. to ApJL

Heintz, W. D. 1969, J. Royal Astron. Soc. Can., 63, 275

Henning, Th., Pfau, W., and Altenhoff, W. J. 1990, A&A, 227, 542

Heyer, M. H., Ladd, E. F., Myers, P. C., and Campbell, B. 1990, AJ, 99, 1585

Hough, J. H., Sato, S., Tamura, M., Yamashita, T., McFadzean, A. D., Rouse, M. F., Whittet, D. C. B., Kaifu, N., Suzuki, H., Nagata, T., Gatley, I., and Bailey, J. 1988, MNRAS, 230, 107

Jones, B. F., Cohen, M., Wehinger, P. A., and Gehren, T. 1987, AJ, 94, 1260

Jones, T. W. 1973, PASP, 85, 811

Lada, C. J. & Wilking, B. A 1984, ApJ, 287, 610

Lane, A. P. 1989, in ESO Workshop on Low Mass Star Formation and Pre-Main Sequence Objects, B. Reipurth (ed.), ESO, Garching, p. 331

Leinert, Ch. & Haas, M. 1989, ApJL, 342, L39

Liseau, R., Lorenzetti, D., and Molinari, S. 1992, A&A, 253, 119

Mezger, P. G., Chini, R., Kreysa, E., Wink, J. E., and Salter, C. J. 1988, A&A, 191, 44

Minchin, N. R., Hough, J. H., McCall, A., Burton, M. G., McCaughrean, M. J., Aspin, C., Bailey, J. A., Axon, D. J., and Sato, S. 1991, MNRAS, 248, 715

Moneti, A., Pipher, J. L., and Heefer, H. L. 1984, ApJ, 282, 508

Mundt, R., Ray, T. P., and Raga, A. C. 1991, A&A, 252, 740

Myers, P. C., Fuller, G. A., Mathieu, R. D., Beichman, C. A., Benson, P. J., Schild, R. E., and Emerson, J. P. 1987, ApJ, 319, 340

Myers, P. C., Heyer, M., Snell, R. L., and Goldsmith, P, F. 1988, ApJ, 324, 907

Pipher, J. L. & Soifer, B. T. 1976, A&A, 46, 153

Ressler, M. E. and Shure, M. 1991, AJ, 102, 1398

Shu, F. H., Adams, F. C., and Lizano, S. 1987, A. R. A. A., 25, 23

Simon, M., Chen, W. P., Howell, R. R., Benson, J. A., and Slowik, D. 1992, ApJ, 384, 212

Smith, R. G., Sellgren, K., and Tokunaga, A. T. 1989, ApJ, 344, 413

Solf, J. 1987, A&A, 184, 322

Strom, K. M., Strom, S. E., Wolff, S. C., Morgan, J., and Wenz, M. 1986, ApJS, 62, 39

Strom, K. M., Strom, S. E., Kenyon, S. J., and Hartmann, L. 1988, AJ, 95, 534

Sugitani, K., Fukui, Y., Mizuno, Y., and Ohashi, N. 1989, ApJL, 342, L87

Tamura, M., Gatley, I., Joyce, R. R., Ueno, M., Suto, H., and Sekiguchi, M. 1991a, ApJ, 378, 611

Tamura, M., Gatley, I., Waller, W., and Werner, M. W. 1991b, ApJL, 374, L25

Terebey, S., Shu, F. H., and Cassen, P. 1984, ApJ, 286, 529

Toomey, D. W., Shure, M. A., Irwin, E. M., and Ressler, M. E. 1990, Proc. SPIE, 1235, 69

Wilking, B. A. & Lada, C. J. 1983, ApJ, 274, 698

Wilking, B. A., Lada, C. J., and Young, E. T. 1989, ApJ, 340, 823

Zealey, W. J., Mundt, R., Ray, T. P., Sandell, G., Geballe, T., Taylor, K. N. R., Williams, P. M., and Zinnecker, H. 1989, Proc. Astr. Soc. Austr., 8, 62

Zinnecker, H. & Wilking, B. A. 1992, to appear in Binary Stars as Tracers of Stellar Formation, A. Duquennoy and M. Mayor (eds.), Cambridge

Chapter 5: Conclusion and Future Work

This dissertation has hinted at the advances in our understanding of young stellar objects which can be made by near-infrared imaging observations. The ability to image these objects over a broad wavelength range has allowed us to construct spectral energy distributions which should be more representative of the protostar, and less influenced by scattering from the circumstellar environment. Now that some of the instrumental problems which plagued the observations presented here have been eliminated, it should be possible to obtain information about the scattering material itself through the study of the nebular intensity profiles.

The most surprising aspect of this work has been the discovery/confirmation of a large number of binary and variable objects - something that should not be considered too unusual given the total number of binary and variable stars in the galaxy, but serious studies of multiplicity and variability in these very youngest stars have not yet been done. The ongoing study of binarity among T Tauri stars in the Taurus star forming region by lunar occultation techniques by Simon *et al.* (1992) will provide much useful data with regard to these somewhat older stars, and it is hoped that the Class I sources in Taurus can be studied this way as well. These data will address the 0.01 to 1 arcsecond separation range and will complement the results found here. A logical extension of all this work is to make unbiased surveys in several star forming regions (although lunar occultations are obviously limited in areal coverage of the sky!); with a large number of

observed systems it will be possible to address formally whether the frequency of multiplicity among the Class I sources matches that of Main Sequence stars. The ad hoc results presented here are encouraging, but a good statistical study will yield much information about how such systems are formed and may allow us to study the evolution of binary star orbits during these very early phases.

A long term study of variability among the sources is also desirable. If the variability is caused by the circumstellar material, properties of that material may be found from the wavelength dependence of the variations. In principle, such studies could yield information about the density profiles of the material and the effects of evolution on the circumstellar environment. Even before such information is found, it would simply be interesting to see what the shape and timescales of these variations are. Long term observations with good spatial resolution (to allow studies of variable objects in a binary system – a frequent occurrence) as well as a broad wavelength range, particularly with the next generation near- and mid-infrared wavelength cameras, should allow us to put the study of Class I variability on a strong footing.

A third area of followup is to search for objects even younger than most of those presented here. *IRAS* 22272+6358A may be one such object given its extreme properties morphologically and spectrally. Imaging a number of similar objects selected from the *IRAS* Point Source Catalog at mid-infrared wavelengths may perhaps identify objects which are truly protostars – stars which obtain most of their radiant energy by accreting

circumstellar material rather than though hydrogen fusion. Of course, objects like 22272+6358A may simply be older Class I sources that we are viewing directly edge-on through their circumstellar disks. In either case, the observations will provide much needed information on the mid-infrared properties of these systems.

Appendix A: Two Protostar Candidates in the Bright-Rimmed Dark Cloud LDN1206

ABSTRACT

We report the discovery of several near-infrared objects associated with two *IRAS* point sources in the LDN1206 region. *IRAS* 22272+6358A is probably a "protostar" which is seen only in scattered light at near-infrared wavelengths because of heavy obscuration by an almost edge-on circumstellar disk. In contrast, *IRAS* 22272+6358B is directly visible at these wavelengths and is perhaps an object which lies between protostars and T Tauri stars in its evolution. Both direct and polarimetric K band images of the region are presented, as well as spectral energy distributions constructed from our J, H, K, L, L', and M data and published far-infrared and millimeter data.

A.1) INTRODUCTION

The Infrared Astronomical Satellite (*IRAS*) has provided a wealth of data that can be used to search for extremely young stellar objects. Several surveys have been conducted in recent years to examine objects in the *IRAS Point Source Catalog* (PSC, Beichman *et al.* 1987) having far-infrared (FIR) colors which might be indicative of protostars (see, for example, Casoli *et al.* 1986). The primary search criterion in these surveys is that the 100 μm flux should be greater than the 60 μm flux, indicating a color temperature less than 50 K. Some secondary criteria, not necessarily common to all surveys, are flux limits on some of the bands, good correlation to a true point source, limits in declination or Galactic coordinates, and the correlation to an optical source (or lack thereof).

IRAS 22272+6358A (hereafter "*IRAS* A") is a source which has been examined in several such surveys because of its extremely low 60/100 μm color temperature (Casoli *et al.* 1986, Richards *et al.* 1987, Wilking *et al.* 1989, Wouterloot & Brand 1989). *IRAS* 22272+6358B (hereafter "*IRAS* B") is a bluer but less luminous object which lies approximately 40 arcseconds to the east of *IRAS* A. The relevant positions and continuum fluxes for both objects are given in Table A.1. *IRAS* A and B are distinguishable only at 12 and 25 μm; in fact, they are not truly resolved at any wavelength by *IRAS* - they are distinct only because of their extremely different spectra. Because the 60 and 100 μm points form a smooth spectrum with the 12 and 25 μm points from *IRAS* A, we assume

(as did the PSC) that the 60 and 100 μm measurements belong to *IRAS* A, and that the 60 and 100 μm fluxes of *IRAS* B are negligible compared with those of *IRAS* A.

LDN1206 is a relatively small (~ 10 arcmin), dense (> 10^5 cm^{-3}, Richards *et al.* 1987, Burov *et al.* 1987) dark cloud which lies at a distance of roughly 1 kpc with a center reported by Lynds (1962) to be at 22^h 27.0^m, 64° 10' (1950.0). We note that the densest part of the cloud lies some 12 arcminutes to the south of the published position. This discrepancy causes some confusion as to whether the very dense cloud we describe is in reality the "moderately" dense nebula 1206 that Lynds (1962) catalogued. However, we follow Sugitani *et al.* (1989) and identify this dense cloud as LDN1206. The Palomar Sky Survey E-plate shows that the southern rim of this cloud is bright; presumably it is being ionized by some nearby O star(s). Sugitani *et al.* (1989) propose the O9 V star SAO 020071 (HD 213023) as the ionization source. Actually a double, this pair lies

Table A.1: Far-Infrared and Radio Continuum Fluxes

Obj	RA (1950.0)	DEC (1950.0)	12 μm	25 μm	60 μm	100 μm	2.7 mm	2 cm	6 cm
	22^h 27^m	63° 58'	(Jy)	(Jy)	(Jy)	(Jy)	(mJy)	(mJy)	(mJy)
A	12.2ˢ	21"	< 0.25	18	380	730	67.	< 1.1	< 0.8
B	17.8ˢ	23"	2.6	< 1.9	< 380	< 730			

Note: The positions and FIR data are from the *IRAS* Point Source Catalog and the 2.7 mm, 2 cm, and 6 cm data are from Wilking *et al.* (1989).

approximately 33 arcminutes (a projected distance of 10 pc) to the south-southwest of LDN1206. An additional possibility is BD +62° 2078, an O7 star which lies at a projected distance of 15 pc from the ionization front, in roughly the same direction as SAO 020071. Though it is more distant than SAO 020071, it could contribute an equal number of ionizing photons because of its greater surface temperature. Both *IRAS* A and B lie in an optically blank area of the cloud immediately behind (north of) the ionization front.

A brief comment on the distance to LDN1206: at present the estimates range from a minimum of 0.8 kpc (Casoli *et al.* 1986) to a maximum of 1.17 kpc (Wouterloot & Brand 1989). Both these values were derived from the CO velocity at *IRAS* A. Crampton & Fisher (1974) and Georgelin & Georgelin (1976) found a value of 0.9 kpc based on studies of S145, the HII region in which LDN1206 is located. Several other authors have adopted this value based on similar CO velocities (Sugitani *et al.* 1989, Wilking *et al.* 1989). Throughout this paper we will adopt a value of 1.0 kpc, as it is midway between the values derived from CO velocities near *IRAS* A itself, and we will scale other authors' luminosities, etc. to this distance.

Most of the aforementioned surveys have examined LDN1206 by using the ^{12}CO molecule and its isotopic variants. While Richards *et al.* (1987), Wilking *et al.* (1989), and Wouterloot & Brand (1989) all note that the CO line profile of *IRAS* A is either "complex" or has a blue wing, Sugitani *et al.* (1989) were the first to map the region in the CO line wings. They find clear evidence of a blue-shifted outflow lobe, but the red-

shifted lobe, if it exists, is too faint to be mapped by the instrumentation available to them at the time. From the angular size and velocity of the outflow, they derive a dynamical time scale for the flow of 2×10^4 yr and conclude from this that the age of *IRAS* A itself is probably less than 10^5 yr. Because molecular outflows are indicative of star formation and because LDN1206 has a clearly delineated ionization front which is thought to be older than 10^6 yr, Sugitani *et al.* (1989) speculate that this may be an example of ionization front-induced star formation.

In an effort to better understand the interaction of LDN1206 with its ionization front, and to discover the nature of *IRAS* A in particular, we have obtained images of LDN1206 over the 1 - 5 micron wavelength range. In this work we present morphological, photometric, and polarimetric results for *IRAS* A and B in order to gain a broad overview of these objects. We argue that they are both very young stellar objects and that they are still interacting with their parent cloud.

A.2) Observations and Analysis

Observations

All observations presented in this paper were made with ProtoCAM at either the NASA Infrared Telescope Facility (IRTF) or the University of Hawaii (UH) 2.2-m

telescope. ProtoCAM is a near-infrared (NIR) camera based on the Santa Barbara Research Center 58 × 62 InSb photodiode array. It is sensitive from 1 to 5.6 μm and contains the J (1.28 μm), H (1.67 μm), K (2.22 μm), L (3.51 μm), L' (3.82 μm), and M (4.78 μm) broadband filters as well as circular variable filters (1 - 2% resolution) which span this wavelength range. The plate scale is continuously variable between 0.14 and 0.35 arcsec/pix. Before 1989 December, ProtoCAM had a temporary reimaging lens which provided plate scales of 0.30 - 0.89 arcsec/pix at the IRTF 3-m and approximately 0.43 - 1.2 arcsec/pix at the UH 2.2-m (with the f/35 secondary). A complete description of the instrument can be found in Toomey *et al.* (1990).

Observations of the two *IRAS* sources were first made through the J, H, K, and L filters at the IRTF on UT 1989 September 2 and 3 at 0.30 and 0.89 arcsec/pix and form the bulk of the direct imaging results presented in this work. Further direct and polarimetric imaging observations are summarized in Table A.2.

In all cases, data were obtained by first integrating on the object, then beamswitching north on the order of an arcminute. Beamswitched positions were displaced slightly east-west in order to avoid obvious stars in the sky frames. Flux standard stars for the direct imaging were BD +65° 1637, HD 1160, 22686, 40335, 147889, 161903, 197406, 201941, 203856, and 4 Lac. Polarimetry was obtained at the UH 2.2-m by mounting a rotating wire-grid polarizer in the optical path above the dewar. Images were obtained at four polarization angles in 45° increments for each object. The

Table A.2: Observing Log

UT Date	Telescope	Filters	Plate Scales (Arcsec pix^{-1})	Seeing at 2.2 μm (Arcsec FWHM)
1989 Sep 2	IRTF	J, H, K, L	0.30, 0.89	0.7
1989 Sep 3	IRTF	J, H, K	0.89	0.7
1989 Nov 8	UH 2.2-m	K, L	0.43	1.0
1989 Nov 9	UH 2.2-m	K, L	0.43	0.7
1989 Nov 10	UH 2.2-m	K Polarimetry	0.43	0.9
1989 Dec 24	IRTF	K, L	0.14	0.5
1990 Aug 02	IRTF	K, L, L'	0.35	0.7
1990 Aug 03	IRTF	K, L, L', 4.8 μm CVF	0.14	0.6
1990 Sep 14	IRTF	K, L, L', M	0.35	0.8

unpolarized standard stars were HD 22686 and HD 203856. BN was used as the polarized standard.

Data Reduction

Because almost all of the data presented here were taken during engineering runs to characterize the camera's imaging and photometric performance, our data reduction techniques (flat fields in particular) have evolved considerably during this project. However, we have found that the quantum efficiency varies slowly and smoothly enough over the array that as long as the object and the standard stars are positioned in the same

part of the array, to within a half dozen pixels or so, photometry derived from images which have not been divided by flat fields can be consistent to less than ±0.05 magnitudes. Thus, all of the photometric results given in Table A.3 are derived from images with a plate scale of 0.43 arcsec/pix or less (to avoid fill factor errors) and which have only been sky-subtracted. However, unidentified systematic errors limit the consistency of the current data set to only slightly better than ±0.1 magnitudes; thus all magnitudes are quoted only to the nearest tenth. Because we avoided placing objects on bad pixels in the array, the bad pixels were removed by simple interpolation.

Table A.3: Near-Infrared Magnitudes

Obj	RA (1950.0)	DEC (1950.0)	J	H	K	L	L'	M
	$22^h\ 27^m$	63° 58'			(Mags)			
A-1	11.12^s	22.5"	>17.0	15.3+	12.1+	9.5+		
A-2	12.11	16.7	>15.4*	>15.4*	13.4*	11.2*		
A-3	9.01	32.8	16.7	16.1	14.1			
A-4	12.70	19.9	>17.0	>17.0	14.9	12.4		
A-5	12.79	6.5	>17.0	>17.0	15.4			
A-6	12.82	31.4	>17.0	>17.0	15.6			
A-7	10.19	17.4	>17.0	>17.0	16.6			
B	17.55	16.7	13.6	10.5	8.3	6.1	5.7	5.0

+ Integrated magnitude over visible nebulosity
* Integrated magnitude in an 8 × 8 arcsecond box.

Notes: while the statistical uncertainties for the given magnitudes are often found to be ±0.02 magnitudes, we believe we are presently limited by systematic uncertainties to approximately ±0.1 magnitudes. All coordinate positions were determined using *IRAS* B as the origin and have an uncertainty of ±1.0 arcsecond.

Because the polarization data reduction involves only ratios, the polarization frames were not divided by flat fields in an effort to maintain the signal-to-noise ratio. The instrumental polarization was found to be less than 0.2% and we believe the efficiency of the polarizer to be approximately 95% based on the manufacturer's data sheet; therefore, we assume these effects are unimportant in the reduction. All frames for a given source were registered by matching the centroids of a point source visible somewhere on each frame and shifting to the nearest fifth of a pixel. No frame required a shift of more than 1.5 pixels. Our reference map of BN is in good agreement with similar maps obtained with IRCAM at the United Kingdom Infrared Telescope (Minchin *et al.* 1991) so we believe that, in spite of only obtaining four polarization angles rather than the more usual eight, our polarization data are reliable. Our estimated statistical uncertainties are ±5% for the magnitude of polarization and ±5° for the position angle at the intensity indicated by the heavy contour in Figure A.4, decreasing to about ±1% and ±1° for the intensity maximum inside that contour.

A.3) RESULTS

Figure A.1 shows an approximately 3.8 × 2.8 arcminute K filter mosaic of the LDN1206 dark cloud along with an R filter CCD image for reference. To establish the coordinates of the NIR sources, we first moved the telescope to a nearby SAO star (SAO 020088), then offset the telescope to the published position of *IRAS* B. Because the

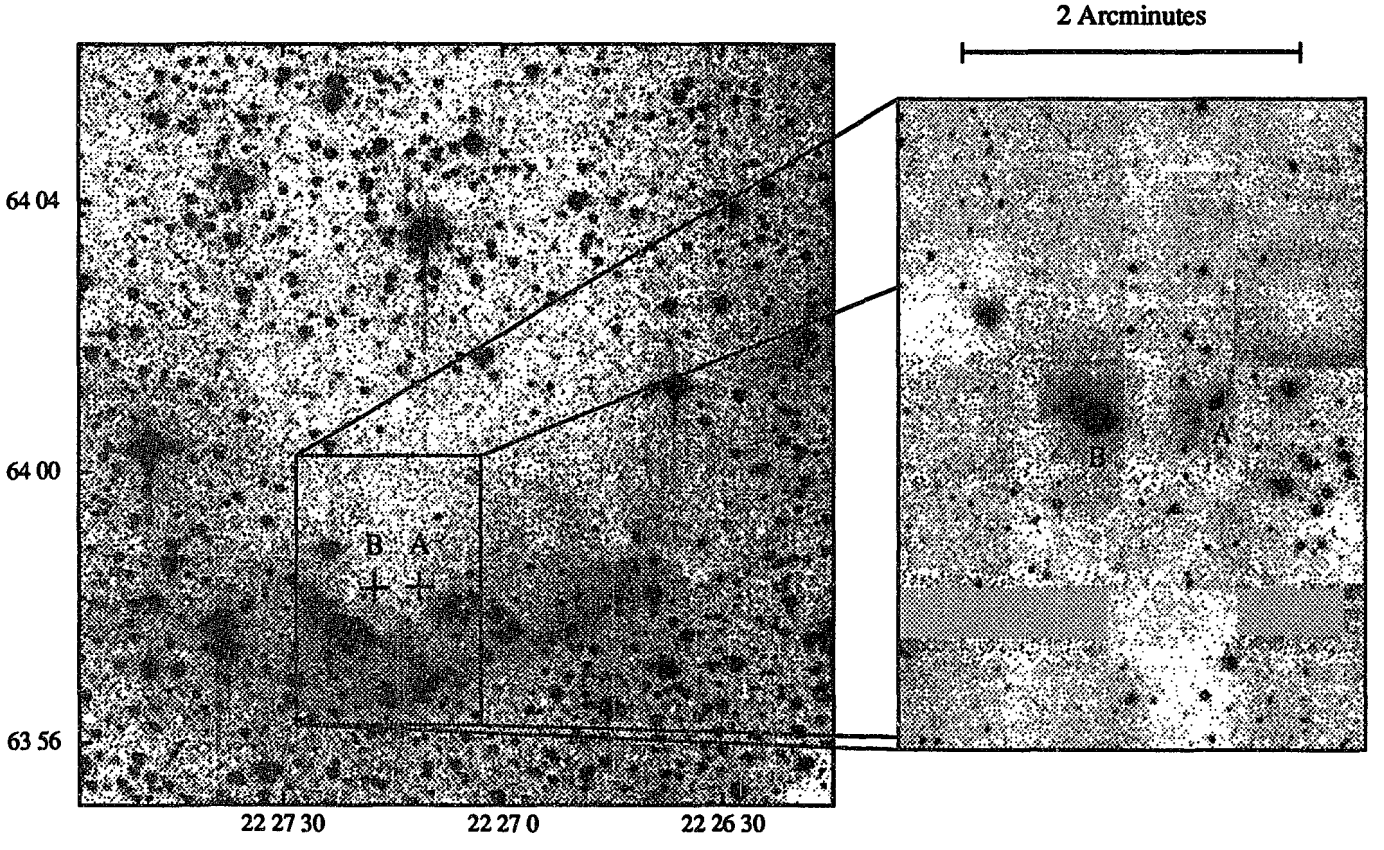

Figure A.1: A 12 × 12 arcminute R filter CCD image of LDN1206 along with a 3.8 × 2.8 arcminute K filter mosaic we obtained with ProtoCAM. The CCD image is a 400 × 400 pixel sub-array of an 800 × 800 pixel frame kindly taken for us by J. Annis (U. of Hawaii). The CCD plate scale is approximately 1.7 arcsec/pix and the exposure length was five minutes. The K filter mosaic is composed of 48 frames which have been cropped slightly to the present rectangle. The plate scale for each frame in the K mosaic is 0.89 arcsec/pix and the exposure length was one minute.

brightest object in our field falls neatly within the 95% confidence ellipse for the position of *IRAS* B, we identify it as such. The precise coordinates found for this object are 22^h 27^m 17.55^s, 63° 58' 16.7" (±1.0"). The plate scales of our images were then verified by matching objects visible in our images with objects visible in the Palomar Sky Survey and in a pair of K filter images kindly taken for us by Tom Herbst and Sylvain Veilleux with the NICMOS 3 256×256 HgCdTe camera on the UH 2.2-m telescope. We computed the coordinates of the other objects in our field using these derived plate scales and the position of *IRAS* B as the zero point. These coordinates are presented in Table A.3.

Although the NIR counterpart of *IRAS* B was easily identified, the counterpart of *IRAS* A is still undetermined. At first, we took the brightest nebulosity (A-1) to be *IRAS* A, but after careful placement of the *IRAS* 95% confidence ellipse, we ruled this out as it falls completely outside the ellipse (Figure A.2). It is possible that the fainter nebulosity to the southeast (A-2) is the *IRAS* source; it falls well within the ellipse. However, as a result of our longer wavelength images and polarimetry data, we do not believe that this is correct either.

In our K images, it appears that there is a point source contained within A-1. At a plate scale of 0.14 arcsec/pix and in seeing conditions of 0.5 arcsec FWHM (corresponding to 500 AU at the source), a significant amount of detail can be seen in it (Figure A.3). However, the position of this point source shifts more than two arcseconds to the southeast with respect to the K nebulosity in our L' images (the L' position is indicated by the heavy cross). Such a wavelength dependent position shift indicates that

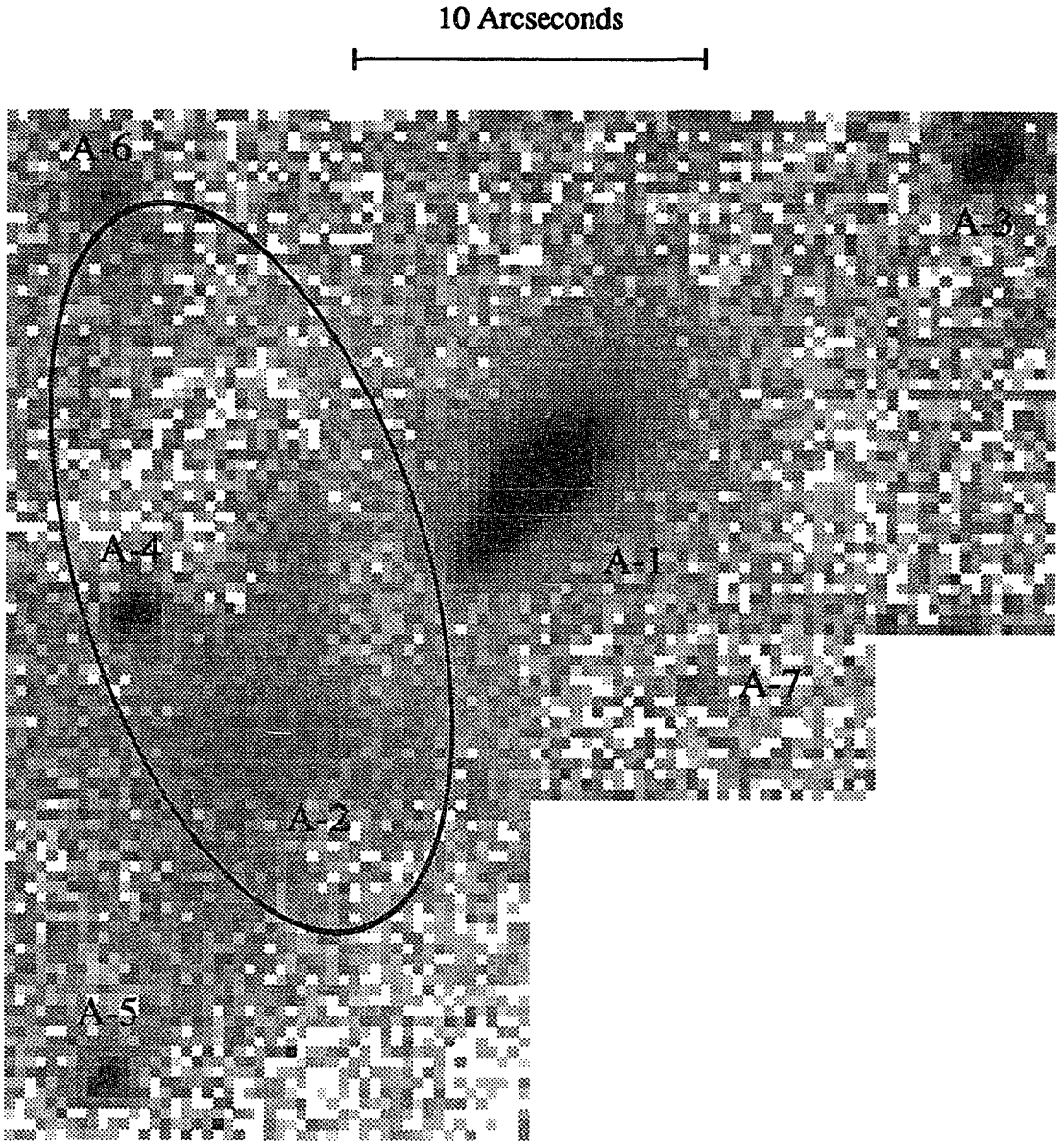

Figure A.2: A K filter mosaic of the region containing *IRAS* 22272+6358A at 0.30 arcsec/pix. All frames are 120 s exposures. The *IRAS* positional 95% confidence ellipse is shown.

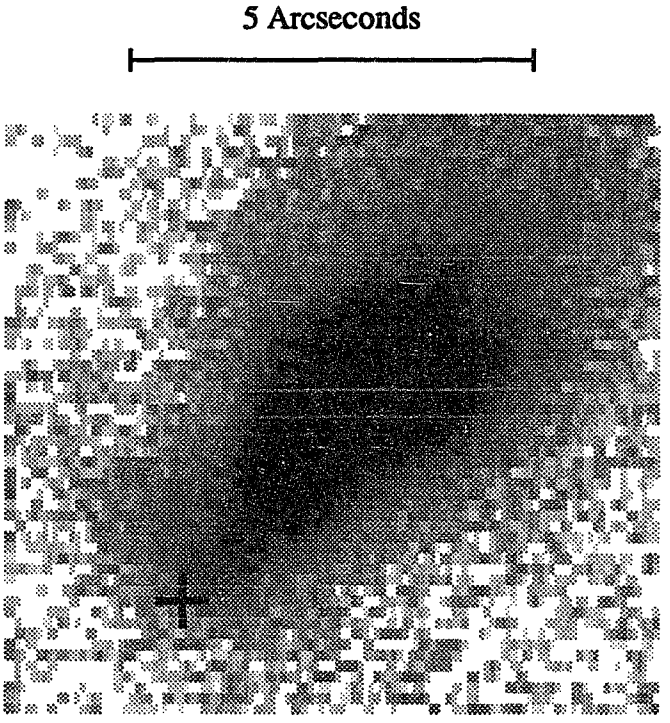

Figure A.3: A very high resolution image of source A-1 taken through the K filter. The plate scale was 0.14 arcsec/pix and seeing conditions were 0.5 arcseconds (FWHM). A 240 s and two 300 s exposures were coadded to form this image. The heavy cross indicates the position of the L' "point source" (see text).

this "source" may be some type of last scattering surface analogous to that in L1551-IRS5 (Campbell *et al.* 1988). We do note, however, that the angular distance between the K and L' positions of A-1 is several times larger than the distance between L1551-IRS5's K position and the position of the radio source (presumably the illuminating source) in spite of the fact that L1206 is some seven times more distant; this greater shift is likely due to a combination of inclination and density effects.

That A-1 is composed of scattered light is well demonstrated by our K filter polarization map of the region containing *IRAS* A (Figure A.4). The degree of polarization over the surface of A-1 is consistently 50% or more. Polarization this great can be produced only if the line of sight between the source and scatterer is nearly normal to our line of sight. We note that the polarization vectors are not aligned around the "point source" contained within A-1, lending additional support to our supposition that A-1 is a scattering surface. If lines perpendicular to the polarization vectors of A-1 are drawn, 27 of the 29 vectors contained within the heavy contour in Figure A.4 pass through a 1.5 arcsecond diameter circle located 5.5 arcseconds to the southeast of A-1. It appears, then, that the illuminating source is located here.

The polarization of A-2 supports this embedded source interpretation as well. The polarization magnitude of this source is even greater than that of A-1, and the directions of the vectors indicate the same illuminating source as for A-1, although the convergence

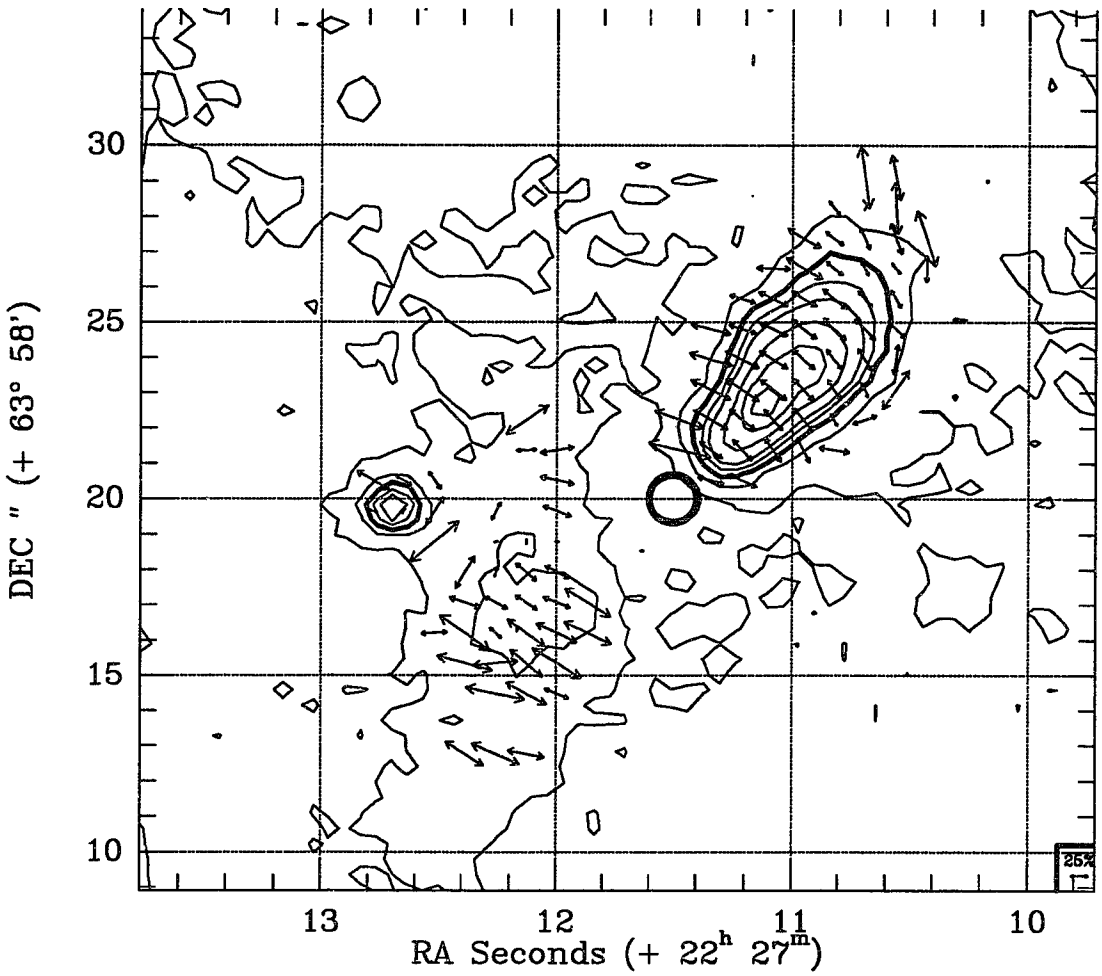

Figure A.4: A K band polarimetric map of *IRAS* 22272+6358A. The original 58 × 62 frames were binned to 29 × 31 for an effective 0.86 arcsecond beamsize. A vector with a magnitude of 25% is shown in the lower right-hand corner for reference. The underlying K filter contours are given for positional reference and are linearly scaled. If perpendiculars are drawn to the 29 vectors contained within the medium weight contour around A-1, 27 of them pass through the heavy circle; we take this point to be the location of the true illuminating source. The coordinates for this point are approximately $22^h\ 27^m\ 11.50^s$, 63° 58' 20.0" (1950.0). The position of the "point source" at L' marked in Figure A.3 falls between the position of the K filter peak and the position of our posited illuminating source.

is not as well defined. We thus conclude that the coordinates of the illuminating source are $22^h\ 27^m\ 11.50^s$, 63° 58' 20.0" (1950.0) - the center of the circle drawn in Figure A.4. This position falls within the *IRAS* confidence ellipse shown in Figure A.2.

Figure A.5a shows the spectral energy distribution for *IRAS* A and source A-1. The NIR portion of the spectrum is that obtained for the object A-1 in a false aperture which contains all of the extended emission. We recognize that this is not truly a valid spectrum of the underlying protostar since A-1 is almost certainly all scattered light and since *IRAS* A probably lies slightly southeast of A-1; however, it is useful as a reference point since we believe that A-1 is illuminated by *IRAS* A.

The *IRAS* data (color-corrected using the method described by Beichman *et al.* 1987 in the *Explanatory Supplement*) plus the 2.7 mm data of Wilking *et al.* (1989) can be fit with a single-temperature dust spectrum. Following Walker *et al.* (1990), if we assume that the dust is optically thick at mid-infrared and shorter wavelengths, we find that the dust has a temperature of approximately 50 K and that its optical depth follows a $\lambda^{-1.3}$ emissivity law. Both of these values are typical of the cloud cores investigated by Walker *et al.* (1990). The fit is presented in graphical form as the dashed curve in Figure A.5a. We also find that this fit yields a luminosity of 1100 $L_\odot$. This value falls between the estimates of Sugitani *et al.* (1989), who use the method of Cohen (1973) and report a value of 1450 $L_\odot$, and Wilking *et al.* (1989) who use the method of Emerson (1988) and find 990 $L_\odot$ but quote the luminosity only as an upper limit since the source was not

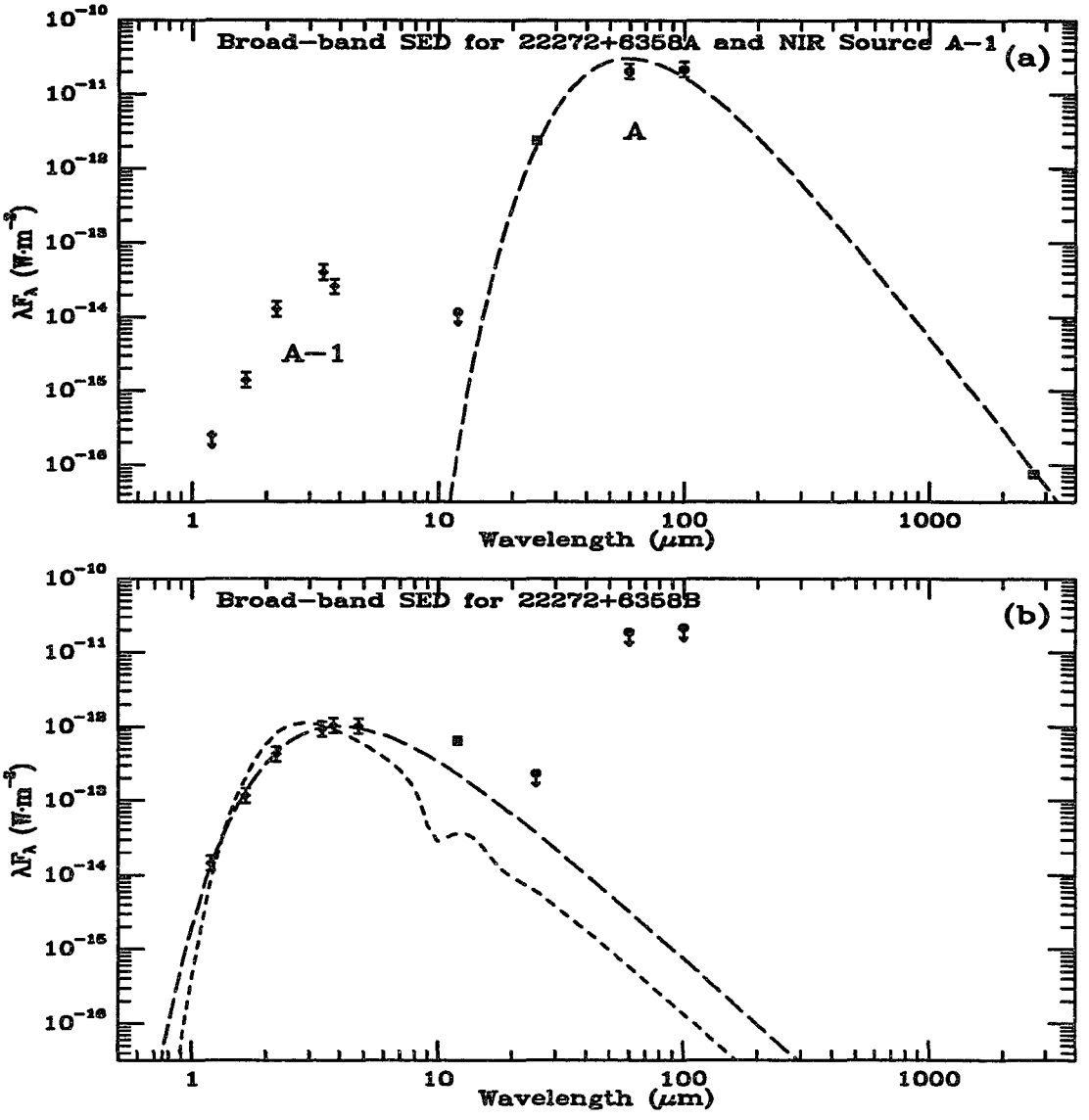

Figure A.5: The spectral energy distributions of *IRAS* 22272+6358A plus A-1 and *IRAS* 22272+6358B. The diamonds are our near-infrared measurements while the color-corrected *IRAS* point source data are shown as filled circles. The 2.7 mm point is from Wilking *et al.* (1989), which is shown as an open circle. *a)* Spectra of *IRAS* A and A-1. The dashed line shows a dust model with a temperature of 50 K and a $\lambda^{-1.3}$ optical depth scaling law. The NIR fluxes of A-1 are plotted only for reference, as they probably represent light scattered from the obscured outflow source. *b)* Spectrum of *IRAS* B. The long-dashed line represents a 920 K blackbody with no extinction, while the short-dashed line is a 8000 K blackbody with an A_V of 30.

detected at 12 μm. However, even if the 12 μm flux were zero, the change in the luminosity would be less than 1%. Casoli *et al.* (1986) also quote 990 $L_\odot$, while Wouterloot & Brand (1989) find 1240 $L_\odot$ based on extrapolations to cover the wavelength range 6 - 400 μm. We note, however, that all of these estimates use only the four *IRAS* fluxes to determine the luminosity. In light of the considerable uncertainties in the distance to LDN1206 and the variety of methods of determining luminosity, we consider 1100 $L_\odot$ to be a reasonable estimate of *IRAS* A's total luminosity.

As is the case for many young stellar objects, the 1.2 - 12 μm spectrum of *IRAS* B cannot be fit by an extinguished, single temperature photosphere (Figure A.5b). To illustrate this point, we present two limiting models. In the first we assume the [H-K] color is entirely intrinsic to the source. If we fit only our NIR data (1.2 - 4.8 μm), we find that a 43 $L_\odot$, 920 K blackbody provides a good fit to the spectrum, although it does underestimate the 12 μm flux by a factor of two. In the second model, we assume the [H-K] color is due solely to extinction. If we provide extinction which corresponds to *IRAS* B's [H-K] color ([H-K] = 2.2 $\rightarrow$ A_V = 30, Draine & Lee 1984), the fit yields a 8000 K photosphere. However, this fit seriously overestimates the 1.6 and 2.2 micron fluxes and underestimates the 1.2 and 4.8 μm fluxes, in addition to the 12 μm flux. These failures clearly demonstrate the need for a multi-temperature model which includes radiating material at a lower temperature than a stellar photosphere. We pursue this idea further in the discussion section.

We obtained polarization images of *IRAS* B as well. Because the extended emission visible in Figure A.1 is faint with respect to *IRAS* B, we did not detect it in our short integrations. *IRAS* B itself seems to have a small polarization - 5% at a position angle of 180°. Because this vector is orthogonal to the position angle between *IRAS* B and *IRAS* A, we cannot at this time determine if the polarization is caused by grain alignment in LDN1206 (although this is perhaps more likely) or if *IRAS* A is somehow playing a role in the polarization observed at *IRAS* B.

A.4) DISCUSSION

IRAS 22272+6358A

The extremely high polarizations and the fact that A-1 is brighter than A-2 lead us to propose the following model: *IRAS* A is a heavily extinguished (and thus invisible in the NIR) young stellar object of Class I (see Lada 1988) which has an optically thick disk lying almost edge-on to our line of sight; this object is currently in its outflow phase and has bipolar jets. A-1 is thus the lobe of the jet pointed slightly toward us (and blue-shifted), while A-2 is the lobe pointed away (red-shifted). The lower brightness of A-2 is thus explained by the added extinction through the disk. Such a model is in agreement with the conclusion of Wilking *et al.* (1989) that *IRAS* A should be optically thick even at mid-infrared wavelengths since they find that its 2.7 mm optical depth is greater than

2×10^{-3}. This model also agrees with their conclusion that the scale size of *IRAS* A is less than 10 arcsec.

One check of this model is the application of Hubble's relation to compute the extinction to the proposed illuminating source (see Castelaz *et al.* 1985 for a detailed discussion of the technique). The approximate limiting surface brightness of our K images is 17th magnitude per arcsec^2. At this level, the nebulosity of A-1 extends 13 arcseconds from the proposed source position. These facts imply a difference in extinction between the illuminating source and A-1 of at least 8.3 magnitudes at K, or an A_V difference of greater than 95. Because this is a lower limit and because there is quite a bit of reddening to A-1 itself, the actual extinction to the central source is likely to be quite a bit greater than this. One of the few plausible explanations of an extinction gradient this sharp (A_V=95 in ~ 10^4 AU) is the presence of an edge-on disk.

We note the similarity between *IRAS* A and the observations of NGC 6334-V by Harvey & Wilking (1984). In this object, they also observed a two-lobed structure with no visible central source at K, while the emission at 20 μm is dominated by one source located at the midpoint of the two NIR lobes. They conclude that this object is an edge-on disk system in which the disk becomes optically thin at mid-infrared wavelengths. Their contours are quite similar to those we present in Figure A.4, lending additional support for our model. *IRAS* A is also reminiscent of the theoretical models derived by Dent (1988). In particular, his standard model at 1 μm at an inclination angle of 5° compares

favorably with our observed K contours at *IRAS* A, both in relative intensity between the two lobes and in separation between the peak intensity and illuminating source (corresponding to a few arcseconds at a distance of 1 kpc). The good match in spite of the differing wavelengths can be explained as *IRAS* A simply having a higher density than assumed in his model.

At first glance our model of *IRAS* A appears to be discrepant with the outflow measurements of Sugitani *et al.* (1989) since the maximum intensity of the blue-shifted CO lobe is orthogonal to the direction of the outflow we propose, but we cannot at this time accurately deduce the orientation and position of the CO outflow with respect to our NIR maps for the following reasons: 1) their 17 arcsecond beamsize and 15 arcsecond spatial sampling does not resolve the complicated spatial structure we observe in the NIR, 2) they were able to map only the blue wing of the outflow, and 3) the outflow intensity maximum is coincident with the ionization front itself, leading to an ambiguity in what is producing the CO emission. Any of the following CO observations would aid in resolving these problems: obtaining higher spatial resolution maps, mapping the red wing with lower noise receivers, or producing several channel maps with higher velocity resolution.

IRAS 22272+6358B

In our images, *IRAS* B appears to be an isolated star with a reflection nebula to the northeast. However, if the light originates in a stellar photosphere with no extinction, it is too cool to be on the main sequence. On the other hand, its spectrum bears little resemblance to an extinguished, single temperature blackbody. However, young stellar objects with similarly broad spectra have been modeled as extinguished star-plus-disk systems by Adams *et al.* (1987). Because our simple model fits do not allow for temperature gradients, it is entirely possible that the spectrum may be explained by radiation from an extinguished photosphere along with a circumstellar disk which is contributing a significant infrared excess. Indeed, we find that the 1 to 12 μm portion of *IRAS* B's spectrum is very similar to Class I sources modeled by Adams *et al.* (1987), particularly *IRAS* 04016+2610 (see Figure A.6), *IRAS* 04365+2535, and Elias-29. However, the upper limit for *IRAS* B at 25 μm is seriously discrepant with these other sources. In the cited sources, the slope between 5 and 25 μm is relatively flat or rising slightly; *IRAS* B has a definite and significant decrease in this wavelength interval. In this regard, *IRAS* B's long-wavelength spectrum is reminiscent of Class II sources such as SR 9 (an embedded T Tau star). This leads us to conjecture that *IRAS* B is most likely a late Class I object or perhaps an early Class II object, an object which is still deeply embedded in its parent cloud (and thus the heavy visual extinction) but has already cleared a significant portion of its circumstellar disk and shell (and thus the decreasing spectrum at wavelengths longer than 5 μm).

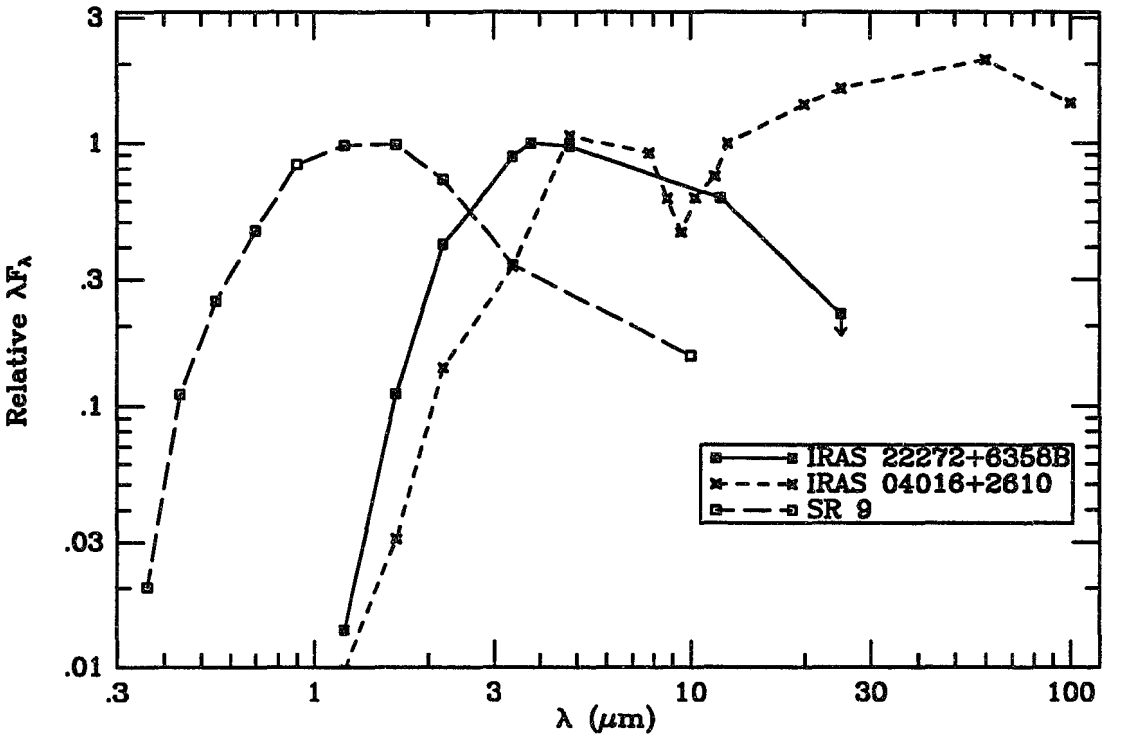

Figure A.6: The spectral energy distribution of *IRAS* 22272+6358B compared with that of the "protostar" *IRAS* 04016+2610 and that of the T Tauri star SR 9. The *IRAS* 22272+6358B data (solid line and filled squares) are from the *IRAS* point source catalog and this paper. The data for *IRAS* 04016+2610 (short-dashed line and open stars) are from the *IRAS* point source catalog and Myers *et al.* (1986). The data for SR 9 (long-dashed line and open squares) were taken from Chini (1981) and Rydgren *et al.* (1976).

Associated Objects

Because all the sources labeled in our images have an [H-K] color greater than 1.0, and they are all invisible on the Palomar Sky Survey, we assume that they are all embedded inside LDN1206 or possibly that they lie behind LDN1206. Object A-3 is less red than either A-1 or A-2 and therefore most likely to be a field star. A-7 may be a field star as well, but we could not detect it in any other filter, so its colors are not known.

The natures of objects A-4, A-5, and A-6 are less clear. They all appear to be point-like in the images (if they could be detected in a given filter). However, there appears to be a more or less complete arc of emission extending from A-6 to A-5 passing through A-2 (Figures A.1 and A.2). In addition, A-4 seems to lie on the inner edge of this arc. Because of this spatial superposition and because A-4 has a [K-L] color similar to A-1, they may be physically associated with *IRAS* A.

A.5) SUMMARY

We report the discovery of several near-infrared objects associated with two *IRAS* point sources in LDN1206. As a result of our near-infrared imaging, photometry, and polarimetry, we believe *IRAS* 22272+6358A is an extremely young stellar object which is seen only in scattered light because of heavy obscuration by an almost edge-on

circumstellar disk. We believe *IRAS* 22272+6358B is likely to be a less obscured young stellar object, perhaps midway between protostars and T Tauri stars in its evolution, whose photospheric spectrum is heavily extinguished by the parent cloud and is broadened by emission from a circumstellar disk.

ACKNOWLEDGEMENTS

We wish to thank Sylvain Veilleux and Tom Herbst (U. of Hawaii) for using some of their observing time to take several K band images of *IRAS* 22272+6358 for us with the NICMOS 3 camera on the UH 2.2-m telescope. These images were used to verify our coordinate system. We also thank Jim Annis (UH) for using some of his time on the UH 0.6-m telescope to obtain the R filter CCD image of LDN1206 we use in Figure A.1. We thank our anonymous referee who made several valuable suggestions which led to the improvement of the interpretations presented in this paper. Finally, we acknowledge the great time savings afforded by the SIMBAD online literature database, which is operated by the Centre de Données Astronomiques de Strasbourg.

MER acknowledges support through the NASA Infrared Telescope Facility graduate research assistantship under NASA contract NASW-4481.

NOTE ADDED IN PROOF

We have obtained new K, L, L', and M filter images of *IRAS* A with ProtoCAM at the IRTF on UT 1991 July 3. These are presented in the Figure A.7. The contours are linearly spaced and the dashed contours indicate levels which lie below the median background level. The origin of the coordinate grid indicates the location of the proposed illuminating source.

These images support the model proposed in section A.4. Specifically, we have now detected objects A-1 and A-2 at all four of these wavelengths and they are clearly lobes in a bipolar system. In addition, A-2 is confirmed to be the redder lobe: at M, the surface brightness of the two lobes is of the same order of magnitude, while the relative brightness of A-2 decreases monotonically at the shorter wavelengths. We also find that there are color gradients across both A-1 and A-2; the edges of the lobes near the proposed source are redder than the edges farthest away. Finally, there is a distinct 3 – 4 arcsecond gap between the two lobes at the three shorter wavelengths (the M image is of insufficient quality to establish the gap's presence at this wavelength unambiguously). Since the proposed illuminating source lies within this gap, it is likely that this gap is produced by the extreme extinction of a thick, circumstellar disk.

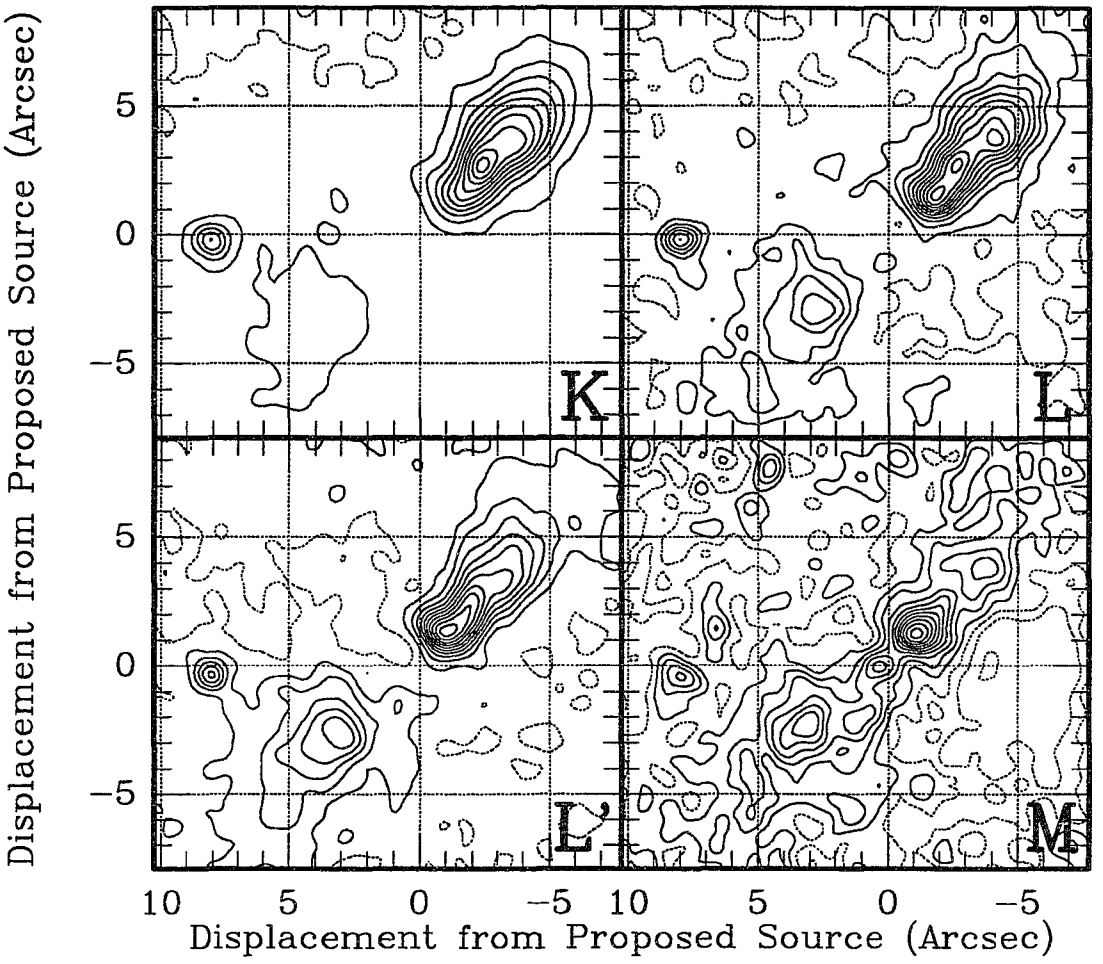

Figure A.7: K, L, L', and M filter images obtained on UT 1991 July 3. The plate scale is approximately 0.31 arcsec/pix. Each image presented here is two coadded, background-subtracted exposures which were registered to the nearest 0.1 pixels using the star A-4, except for M which has three coadded exposures. Total on-source integration times are 240 s at K, 180 s at L, 200 s at L', and 300 s at M. The images have been convolved with a 0.7 arcsec FWHM gaussian to reduce noise at high spatial frequencies in the contour plots.

REFERENCES

Adams, F. C., Lada, C. J., and Shu, F. H. (1987), ApJ, 312, 788

Beichman, C. A., Neugebauer, G., Habing, H. J., Clegg, P. E., and Chester, T. J. (1987), Infrared Astronomical Satellite (IRAS) Catalogs and Atlases Explanatory Supplement, NASA Reference Publication 1190

Blitz, L., Fich, M., and Stark, A. A. (1982), ApJS, 49, 183

Burov, A. B., Kislyakov, A. G., Krasil'nikov, A. A., Kukina, E. P., Lapinov, A. V., Pirogov, L. E., Vdovin, V. F., and Zinchenko, I. I. (1988), Sov. Astron. Lett., 14, 209

Campbell, B., Persson, S. E., Strom, S. E., and Grasdalen, G. L. (1988), AJ, 95, 1173

Casoli, F., Dupraz, C., Gerin, M., Combes, F., and Boulanger, F. (1986), A&A, 169, 281

Castelaz, M. W., Hackwell, J. A., Grasdalen, G. L., Gehrz, R. D., and Gullixson, C. (1985), ApJ, 290, 261

Chini, R. (1981), A&A, 99, 346

Cohen, M. (1973), MNRAS, 164, 395

Crampton, D. and Fisher, W. A. (1974), Pub. D. A. O., 14, 283

Dent, W. R. F. (1988), ApJ, 325, 252

Draine, B. T., and Lee, H. M. (1984), ApJ, 285, 89

Emerson, J. P. (1988), in Formation and Evolution of Low Mass Stars, ed. A. K. Dupree and M. T. V. T. Lago (Boston:Reidel), 193

Georgelin, Y. M. and Georgelin, Y. P. (1976), A&A, 49, 57

Harvey, P. M. and Wilking, B. A. (1984), ApJL, 280, L19

Lada, C. J. (1988), in Formation and Evolution of Low Mass Stars, ed. A. K. Dupree and M. T. V. T. Lago (Boston:Reidel), 93

Lynds, B. T. (1962), ApJS, 7, 1

Minchin, N. R., Hough, J. H., McCall, A., Burton, M. G., McCaughrean, M. J., Aspin, C., Bailey, J. A., Axon, D. J., and Sato, S. (1991), MNRAS, 248, 715

Myers, P. C., Fuller, G. A., Mathieu, R. D., Beichman, C. A., Benson, P. J., Schild, R. E., and Emerson, J. P. (1987), ApJ, 319, 340

Richards, P. J., Little, L. T., Toriseva, M. and Heaton, B. D. (1987), MNRAS, 228, 43

Rydgren, A. E., Strom, S. E., and Strom, K. M. (1976), ApJS, 30, 307

Sugitani, K., Fukui, Y., Mizuno, A., and Ohashi, N. (1989), ApJL, 342, L87

Toomey, D. W., Shure, M. A., Irwin, E. M., and Ressler, M. E. (1990), Instrumentation in Astronomy VII, D. L. Crawford, ed., Proc. SPIE, 1235, 69

Walker, C. K., Adams, F. C., and Lada, C. J. (1990), ApJ, 349, 515

Wilking, B. A., Mundy, L. G., Blackwell, J. H., and Howe, J. E. (1989), ApJ, 345, 257

Wouterloot, J. G. A. and Brand, J. (1989), A&AS, 80, 149

Appendix B: Master Source Photometry Table

In this appendix, the complete set of photometric results is presented. If an entry is blank, the object was not observed through that filter; if it has dashes, the object was not detected, but no upper limit was determined. When two or more observations were made of an object at the same wavelength, a statistical uncertainty is given in parenthesis. All magnitudes without uncertainties should be assumed to have an intrinsic uncertainty of approximately 0.1 magnitudes. Dates of observations are given only for those objects which were found to have varied during the course of these observations.

Object	J	H	K	L	L'	M	2.85μm	3.08μm	3.40μm
SVS 12	>18.34	14.29 (0.15)	11.08 (0.07)	7.41 (0.12)	6.69	5.63 (0.05)			
LDN 1489-IRS	>18.56	13.46 (0.27)	10.09 (0.04)	7.05 (0.18)	6.09	5.15 (0.03)	8.27	10.62 (0.06)	7.35
Haro 6-10:B - 90/11/24	>14.76	>13.11	>11.44	7.71 (0.08)	6.84 (0.03)	5.36 (0.04)			
Haro 6-10:A	9.86	8.34 (0.04)	7.43 (0.01)	5.96 (0.08)	5.48 (0.03)	4.77 (0.07)			
Diff (B-A)	---	---	---	1.756 (0.014)	1.357 (0.034)	0.593 (0.049)			
Haro 6-10:B - 91/01/07			>11.64	7.37 (0.12)	6.61 (0.03)	5.17 (0.07)	9.00	9.09 (0.18)	7.76 (0.10)
Haro 6-10:A			7.40	5.92 (0.10)	5.59 (0.03)	4.81 (0.13)	6.69 (0.05)	6.72 (0.04)	6.10 (0.05)
Diff (B-A)			---	1.441 (0.027)	1.020 (0.026)	0.364 (0.050)	2.310 (0.089)	2.372 (0.142)	1.663 (0.048)
LDN 1551-IRS5	12.66	10.53	8.99	6.85	6.10	4.89	8.26	9.22	7.20
04365+2535	17.19	13.87	10.91	7.84	7.01	6.08			

Object	J	H	K	L	L'	M	2.85μm	3.08μm	3.40μm
HH 43-IRS1:A	>18.68	15.14	11.46	8.43	7.55	6.81			
(0.10) (0.01)									
HH 43-IRS1:B	18.03	15.13	12.84	10.35	9.50	8.47			
	(0.54)	(0.07)	(0.08)						
Diff (A-B)	---	0.007	-1.372	-1.927	-1.957	-1.662			
		(0.179)	(0.065)						
SSV 63:A - 89/11 & 90/03		15.41	12.42	9.03					
		(0.35)							
SSV 63:B		13.78	12.45	---					
		(0.05)	(0.09)						
SSV 63:C		14.85	13.63	---					
		(0.01)	(0.05)						
SSV 63:D		---	---	11.82					
SSV 63:A - 91/01/09	>18.96	14.99	12.04	8.50	7.61	6.49			
				(0.11)	(0.11)	(0.01)			
SSV 63:B	15.54	13.73	12.25	10.15	9.13	7.72			
					(0.26)				
SSV 63:C	16.84	14.83	13.65	>11.73	>11.00	>8.67			
SSV 63:D	>18.96	>16.86	>15.10	10.38	8.90	7.06			
					(0.01)	(0.04)			
S255-IRS1:B	>19.08	17.03	11.27	5.25	4.26	2.59	7.93	7.99	5.85
		(0.05)	(0.08)	(0.09)	(0.07)		(0.25)	(0.09)	(0.01)
S255-IRS1:A	17.06	13.37	10.12	5.90	5.29	4.34	7.55	7.08	6.22
		(0.10)	(0.11)	(0.11)	(0.06)		(0.18)	(0.02)	(0.03)
Diff (B-A)	---	3.627	1.156	-0.662	-1.030	-1.743	0.371	0.915	-0.370
		(0.123)	(0.066)	(0.023)	(0.024)		(0.069)	(0.064)	(0.044)
AFGL 961E - 89/12/22			8.07						
			(0.10)						
AFGL 961W			8.10						
			(0.10)						
Diff (E-W)			-0.030						
			(0.041)						
AFGL 961E - 91/01/07	15.34	11.21	7.71	4.35	3.68	2.74	6.17	7.61	4.84
	(0.01)	(0.06)	(0.01)						
AFGL 961W	12.04	9.64	7.88	5.92	5.57	5.16	6.93	7.38	6.18
	(0.01)	(0.01)	(0.02)						
Diff (E-W)	3.306	1.568	-0.172	-1.571	-1.889	-2.426	-0.762	0.228	-1.339
	(0.008)	(0.042)	(0.022)						
EL-21	16.61	12.46	9.71	6.46	5.98	4.43			
		(0.63)	(0.05)	(0.02)	(0.18)	(0.14)			
WL 16	14.05	10.58	7.88	5.94	5.78	4.69			

EL-29	17.07	11.68	7.19	2.99 (0.20)		
22272+6358B	13.60 (0.05)	10.50 (0.05)	8.30 (0.05)	6.10 (0.05)	5.70 (0.05)	5.00 (0.05)

Additional Mid-IR Photometry taken with Bolo I at the IRTF

Object	7.8μm	8.7μm	9.8μm	10.3μm	11.6μm	12.5μm	N	Q
22272+6358B	3.74 (0.05)	3.43 (0.02)	3.34 (0.02)	3.23 (0.02)	2.63 (0.02)	2.00 (0.03)	3.07 (0.01)	1.20 (0.10)

References

Abt, H. A. 1983, ARAA, 21, 343

Adams, F. C., Lada, C. J., and Shu, F. H. 1987 (ALS), ApJ, 312, 788

Adams, F. C. and Shu, F. H. 1985 (AS85), ApJ, 296, 655

Adams, F. C. and Shu, F. H. 1986 (AS86), ApJ, 308, 836

Aspin, C., McLean, I. S., and Coyne, G. V. 1985, A&A, 149, 158

Beichman, C. A., Becklin, E. E., and Wynn-Williams, C. G. 1979, ApJL, 232, L47

Beichman, C. A., Myers, P. C., Emerson, J. P., Harris, S., Mathieu, R., Benson, P. J., and Jennings, R. E. 1986, ApJ, 307, 337

Beichman, C. A., Neugebauer, G., Habing, H. J., Clegg, P. E., and Chester, T. J. 1987, Infrared Astronomical Satellite (IRAS) Catalogs and Atlases Explanatory Supplement, NASA Reference Publication 1190

Blitz, L., Fich, M., and Stark, A. A. 1982, ApJS, 49, 183

Boss, A. P. 1987, ApJ, 316, 721

Boss, A. P. 1991, Nature, 351, 298

Burov, A. B., Kislyakov, A. G., Krasil'nikov, A. A., Kukina, E. P., Lapinov, A. V., Pirogov, L. E., Vdovin, V. F., and Zinchenko, I. I. 1988, Sov. Astron. Lett., 14, 209

Campbell, B., Persson, S. E., Strom, S. E., and Grasdalen, G. L. 1988, AJ, 95, 1173

Capps, R. W., Gillett, F. C., and Knacke, R. F. 1978, ApJ, 226, 863

Casoli, F., Dupraz, C., Gerin, M., Combes, F., and Boulanger, F. 1986, A&A, 169, 281

Castelaz, M. W., Hackwell, J. A., Grasdalen, G. L., Gehrz, R. D., and Gullixson, C. 1985a, ApJ, 290, 261

Castelaz, M. W., Grasdalen, G. L., Hackwell, J. A., Capps, R. W., and Thompson, D. 1985b, AJ, 90, 1113

Chini, R. 1981, A&A, 99, 346

Clark, F. O. 1992, ApJS, 75, 611

Code, A. D. 1973, in Interstellar Dust and Related Topics. IAU Symp. No. 52, Greenberg and Van de Hulst (eds.), Reidel, Dordrecht, p. 505

Cohen, M. 1973, MNRAS, 164, 395

Cohen, M. & Jones, B. F. 1987, ApJ, 321, 846

Cohen, M. & Schwartz, R. D. 1983, ApJ, 265, 877

Cohen, M., Harvey, P. M., Schwartz, R. D., and Wilking, B. A. 1984, ApJ, 278, 671

Crampton, D. and Fisher, W. A. 1974, Pub. D. A. O., 14, 283

Davidson, J. A., & Jaffe, D. T. 1984, ApJL, 277, 13

Dent, W. R. F. 1988, ApJ, 325, 252

Draine, B. T. & Lee, H. M. 1984, ApJ, 285, 89

Elias, J. A. 1978a, ApJ, 224, 453

Elias, J. A. 1978b, ApJ, 224, 857

Emerson, J. P. 1988, in Formation and Evolution of Low Mass Stars, A. K. Dupree and M. T. V. T. Lago (eds.), Reidel, Boston, p. 193

Forrest, W. J., Pipher, J. L., Ninkov, Z., and Garnett, J. D. 1989, Proc. of the Third Infrared Detector Technical Workshop, NASA Tech. Mem. 102209, p. 157

Georgelin, Y. M. and Georgelin, Y. P. 1976, A&A, 49, 57

Goodrich, R. W. 1986, AJ, 92, 885

Hanner, M. S., Tokunaga, A. T., and Geballe, T. R. 1992, sub. to ApJL

Harvey, P. M. and Wilking, B. A. 1984, ApJL, 280, L19

Heintz, W. D. 1969, J. Royal Astron. Soc. Can., 63, 275

Henning, Th., Pfau, W., and Altenhoff, W. J. 1990, A&A, 227, 542

Heyer, M. H., Ladd, E. F., Myers, P. C., and Campbell, B. 1990, AJ, 99, 1585

Hodapp, K.-W. 1984, A&A, 141, 255

Hodapp, K.-W., Capps, R. W., Strom, S. E., Salas, L. and Grasdalen, G. L. 1988, ApJ, 335, 814

Hough, J. H., Sato, S., Tamura, M., Yamashita, T., McFadzean, A. D., Rouse, M. F., Whittet, D. C. B., Kaifu, N., Suzuki, H., Nagata, T., Gatley, I., and Bailey, J. 1988, MNRAS, 230, 107

Jones, B. F., Cohen, M., Wehinger, P. A., and Gehren, T. 1987, AJ, 94, 1260

Jones, T. W. 1973, PASP, 85, 811

Lada, C. J. 1988, in Formation and Evolution of Low Mass Stars, A. K. Dupree and M. T. V. T. Lago, Reidel, Boston, p. 93

Lada, C. J. and Harvey, P. M. 1981, ApJ, 245, 58

Lada, C. J. and Wilking, B. A 1984, ApJ, 287, 610

Lane, A. P. 1989, in ESO Workshop on Low Mass Star Formation and Pre-Main Sequence Objects, B. Reipurth (ed.), ESO, Garching, p. 331

Leinert, Ch. & Haas, M. 1989, ApJL, 342, L39

Liseau, R., Lorenzetti, D., and Molinari, S. 1992, A&A, 253, 119

Lynds, B. T. 1962, ApJS, 7, 1

Mezger, P. G., Chini, R., Kreysa, E., Wink, J. E., and Salter, C. J. 1988, A&A, 191, 44

Minchin, N. R., Hough, J. H., McCall, A., Burton, M. G., McCaughrean, M. J., Aspin, C., Bailey, J. A., Axon, D. J., and Sato, S. 1991, MNRAS, 248, 715

Moneti, A., Forrest, W. J., Pipher, J. L., and Woodward, C. E. 1988, ApJ, 327, 870

Moneti, A., Pipher, J. L., and Heefer, H. L. 1984, ApJ, 282, 508

Mundt, R., Ray, T. P., and Raga, A. C. 1991, A&A, 252, 740

Myers, P. C., Fuller, G. A., Mathieu, R. D., Beichman, C. A., Benson, P. J., Schild, R. E., and Emerson, J. P. 1987, ApJ, 319, 340

Myers, P. C., Heyer, M., Snell, R. L., and Goldsmith, P, F. 1988, ApJ, 324, 907

Pipher, J. L. & Soifer, B. T. 1976, A&A, 46, 153

Ressler, M. E. and Shure, M. 1991, AJ, 102, 1398

Richards, P. J., Little, L. T., Toriseva, M. and Heaton, B. D. 1987, MNRAS, 228, 43

Rydgren, A. E., Strom, S. E., and Strom, K. M. 1976, ApJS, 30, 307

Shu, F. H., Adams, F. C., and Lizano, S. 1987, A. R. A. A., 25, 23

Simon, M., Chen, W. P., Howell, R. R., Benson, J. A., and Slowik, D. 1992, ApJ, 384, 212

Smith, R. G., Sellgren, K., and Tokunaga, A. T. 1989, ApJ, 344, 413

Solf, J. 1987, A&A, 184, 322

Strom, K. M., Strom, S. E., Wolff, S. C., Morgan, J., and Wenz, M. 1986, ApJS, 62, 39

Strom, K. M., Strom, S. E., Kenyon, S. J., and Hartmann, L. 1988, AJ, 95, 534

Strom, S. E., Strom, K. M., and Edwards, S. 1988, in Galactic and Extragalactic Star Formation, R. Pudritz and M. Fich (eds.), Reidel, Dordrecht

Strom, S. E., Strom, K. M., Grasdalen, G. L., Capps, R. W., and Thompson, D. 1985, AJ, 90, 2575

Sugitani, K., Fukui, Y., Mizuno, Y., and Ohashi, N. 1989, ApJL, 342, L87

Sze, S. M., 1981, The Physics of Semiconductor Devices, 2nd Edition, Wiley & Sons, New York

Tamura, M., Gatley, I., Joyce, R. R., Ueno, M., Suto, H., and Sekiguchi, M. 1991a, ApJ, 378, 611

Tamura, M., Gatley, I., Waller, W., and Werner, M. W. 1991b, ApJL, 374, L25

Terebey, S., Shu, F. H., and Cassen, P. 1984, ApJ, 286, 529

Toomey, D. W., Shure, M. A., Irwin, E. M., and Ressler, M. E. 1990, Proc. SPIE, 1235, 69

Walker, C. K., Adams, F. C., and Lada, C. J. 1990, ApJ, 349, 515

Wilking, B. A. & Lada, C. J. 1983, ApJ, 274, 698

Wilking, B. A., Lada, C. J., and Young, E. T. 1989, ApJ, 340, 823

Wilking, B. A., Mundy, L. G., Blackwell, J. H., and Howe, J. E. 1989, ApJ, 345, 257

Wouterloot, J. G. A. and Brand, J. 1989, A&AS, 80, 149

Zealey, W. J., Mundt, R., Ray, T. P., Sandell, G., Geballe, T., Taylor, K. N. R., Williams, P. M., and Zinnecker, H. 1989, Proc. Astr. Soc. Austr., 8, 62

Zinnecker, H. & Wilking, B. A. 1992, to appear in Binary Stars as Tracers of Stellar Formation, A. Duquennoy and M. Mayor (eds.), Cambridge